Annual Research Briefs – 1989

Center for Turbulence Research

February 1990

NASA

Ames Research Center

LELAND STANFORD JUNIOR UNIVERSITY
ORGANIZED 1891

Stanford University

CONTENTS

Preface

This report contains the 1989 annual progress reports of the Research Fellows of the Center for Turbulence Research. It is intended primarily as a year-end report to the National Aeronautics and Space Administration, Ames Research Center which supports CTR through core funding and by making available its physical and intellectual resources.

The Center for Turbulence Research is devoted to the fundamental study of turbulent flows; its objectives are to stimulate advances in the physical understanding of turbulence, in turbulence modeling and simulation, and in turbulence control. Last year was CTR's third year in operation. CTR now has about fifteen Postdoctoral Fellows, and supports five doctoral students and several short term visitors annually. Several other doctoral students who are supported by grants from the Air Force Office of Scientific Research, the Office of Naval Research, and the National Science Foundation also conduct their research at the CTR. The CTR staff study a wide range of turbulence problems in collaboration with NASA-Ames scientists and Stanford faculty members. The CTR roster for 1989 is provided in the Appendix. Also listed are the members of the Advisory Committee which meets annually to review the Center's program, and the Steering Committee which acts on Fellowship applications.

This year, publication of the CTR Manuscript series was initiated. These are manuscripts prepared for submission to journals that are made available for early dissemination of completed research results by the CTR staff. The reports appearing in the following pages are a brief account of the accomplishments of the CTR Fellows in 1989. They are grouped in the general areas of modeling, experimental research, theory, simulation and numerical methods, and compressible and reacting flows.

Special thanks are due to Debra Spinks, the Center's Administrative Assistant, for her skillful compilation and organization of this report.

Parviz Moin
William C. Reynolds
John Kim

Modeling of compressible turbulence

By O. Zeman

1. Objectives

The work is directed toward understanding and modeling compressibility effects in turbulent flows. The primary objective is to investigate how compressibility influences the basic turbulence processes such as turbulence production and dissipation, length scale modification, spectral energy transfer, etc. The second objective is to develop parameterization schemes and models to incorporate compressibility into one-point closure models and into the subgrid scale models for LES techniques.

The ultimate purpose of this research is to develop compressible turbulence models which are capable of handling the hypersonic regime. Specifically, the emphasis will be on the model capability of predicting a) heat and momentum transfer in hypersonic boundary layers, and b) mixing and growth of high Mach number shear layers, jets and wakes.

2. Accomplishments

The work described in the following section (2.1) is an abbreviated version of the paper Zeman (1989). Section 2.2 is a part of a paper in preparation.

2.1. Dilatation dissipation: the theory and applications in modeling compressible turbulent flows

2.1.1. Abstract

The concept of dilatation dissipation ϵ_d is predicated on the existence of shock-like structures embedded within energetic turbulent eddies. On this assumption a parametric expression for ϵ_d is found $\epsilon_d = (q^3/L)\, F(M_t, K)$ containing calculable parameters of a turbulent field: Favre-averaged turbulence energy $q^2 = \widetilde{u_j u_j}$, length scale L, and r.m.s. (turbulent) Mach number M_t. The function $F(M_t, K)$ is a measure of the probability of ϵ_d with respect to the solenoidal dissipation (q^3/L), and involves integration over the p.d.f. of fluctuating velocity. K is the kurtosis, or intermittency factor, of the fluctuating field. The dilatation dissipation is incorporated in a second-order closure model for compressible mixing layers and the model predictions of mean and turbulence quantities are compared with experiments. The model is capable of predicting the reduction of layer growth rates as a function of the convective Mach number M_c in experiments. The Mach number effect on the turbulence structure is demonstrated by comparing the computed centerline turbulence intensities with the measurements of Samimy and Elliott (1989) and Samimy et al. (1989) for M_c between 0.51 and 0.86.

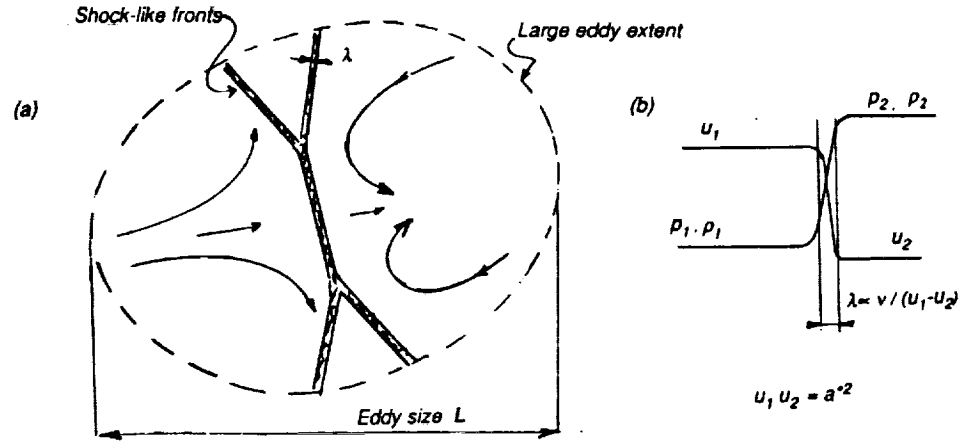

FIGURE 1. (a) Sketch of shock-like structure in a turbulent eddy; (b) normal shock relations.

2.1.2 Theoretical model for dilatation dissipation

The compressible, homogenous, turbulence field can be described in terms of solenoidal and dilatational components of velocity, i.e., $u_i = u_{si} + u_{di}$, where u_s and u_d satisfy the constraints $\nabla \cdot \mathbf{u}_s = 0$, and $\nabla \times \mathbf{u}_d = 0$. Then, in high Reynolds number approximation, the Favre-averaged second-order equations for (decaying) homogeneous turbulence can be written as (Zeman, 1989)

$$1/2 \frac{\partial q^2}{\partial t} = -\nu \overline{\omega_k \omega_k} - 4/3 \nu \overline{\theta^2} + \rho^{-1} \overline{p\theta} \tag{1}$$

$$c_p \frac{\partial T}{\partial t} = -1/2 \frac{\partial q^2}{\partial t} \tag{2}$$

$$\overline{p} = \overline{\rho} R T \tag{3}$$

The viscous term $\nu \overline{\omega_k \omega_k}$ (labeled ϵ_s for future reference) is the traditional solenoidal dissipation due to the energy cascade to small scales and depends only on u_s; the second viscous term in (1) is proportional to the square of fluctuating divergence $\theta = u_{j,j}$, and we shall call it the *dilatation dissipation* ϵ_d. In the energy equation (2), T is the Favre-averaged (mean) temperature and the sum of (1) and (2) yields the enthalpy conservation law $c_p T + \frac{1}{2} q^2 = c_p T_o =$ const. By dimensional analysis, it is then expected that the decay of compressible turbulence be described by

$$\frac{\partial q^2}{\partial t} = -\frac{q^3}{L} f(M_t)$$

where f is a function of the turbulent Mach number $M_t = q/a$ based on the sonic velocity $a = \sqrt{\gamma R T}$, and L is a turbulence length scale so that the solenoidal dissipation $\epsilon_s \propto q^3/L$.

In direct numerical simulation of compressible 2D turbulence, Passot and Pouquet (1987) found that for sufficiently large initial density fluctuation levels $\rho'/\overline{\rho}$ and turbulent Mach number $M_t > 1$ the computed field of initially solenoidal turbulence evolved into a shock-like structure as sketched in Figure 1. Thin regions of steep density gradients (shock-like structures) are embedded in large scale vortices (of length scale L). The shock-like structure may be considered quasi-stationary with the instantaneous dissipation rate $\nu\theta^2 = \nu(\triangle u/\lambda)^2$ where $\triangle u$ is a normal velocity difference across the steep density interface which has a thickness λ. This thickness is determined by the Reynolds number relationship $\lambda\triangle u/\nu = O(1)$ and velocities upstream and downstream of the normal shock are related by the Prandtl-Meyer relation:

$$u_1 u_2 = a*^2 = \gamma R T^* = u_1^2(1 - \triangle u/u_1). \tag{4}$$

where $a*$ is the sonic velocity at the "sonic" temperature $T^* = 2T/(\gamma + 1)$, (with respect to the turbulence frame of reference moving with the local mean flow velocity). The volume fraction occupied by the shocklet structure is λ/L regardless of the flow dimension, thus an instantaneous dilatation dissipation rate (per unit mass) is

$$\epsilon_d' \propto \frac{a*^3}{L}\left(\frac{m_1^2 - 1}{m_1}\right)^3 \tag{5}$$

where $m_1 = u_1/a^*$ is the instantaneous Mach number on the low pressure side of the shock which must be larger than one. We note that the expression (5) does not contain viscosity explicitly and resembles a parametric expression for the solenoidal dissipation at low speeds (except that (5) is applicable only when m_1 is supersonic). Since the model assumes isotropic orientation of the shocklets, u_1 must be proportional to the instantaneous total turbulent velocity $u(t) = \sqrt{u_j u_j}$. In order to obtain an average value ϵ_d, (5) has to be ensemble-averaged with the aid of probability density function for m_1.

There exists experimental evidence that in mixing layers the streamwise fluctuations are highly intermittent with the kurtosis $K = \overline{u^4}/(\overline{u^2})^2$ ranging from 4 up to about 20 at the edges of the layer (Spencer and Jones 1971, Samimy et al. 1989). A convenient expression for non-gaussian p.d.f. $p(u)$ is a Gram-Charlier expansion

$$p(u, K) = \{\frac{1}{\sqrt{2\pi}} + \frac{(K-3)}{4!}\left(3 - 6\left(\frac{u}{\sigma}\right)^2 + \left(\frac{u}{\sigma}\right)^4\right)\}\exp\{-\frac{u^2}{2\sigma^2}\} \tag{6}$$

With the approximation that (6) is the p.d.f. of m_1, i.e. $p(u) \approx p(m_1)$ (with $\sigma = q/a* = M_t$), we obtain

$$\epsilon_d \propto \frac{q^3}{L}[(\frac{1}{M_t^4}\int_1^\infty \left(\frac{m_1^2 - 1}{m_1}\right)^3 p(m_1)dm_1], \quad \text{or,} \tag{7}$$

$$\epsilon_d \propto \left(\frac{q^3}{L}\right) F(M_t, K). \tag{8}$$

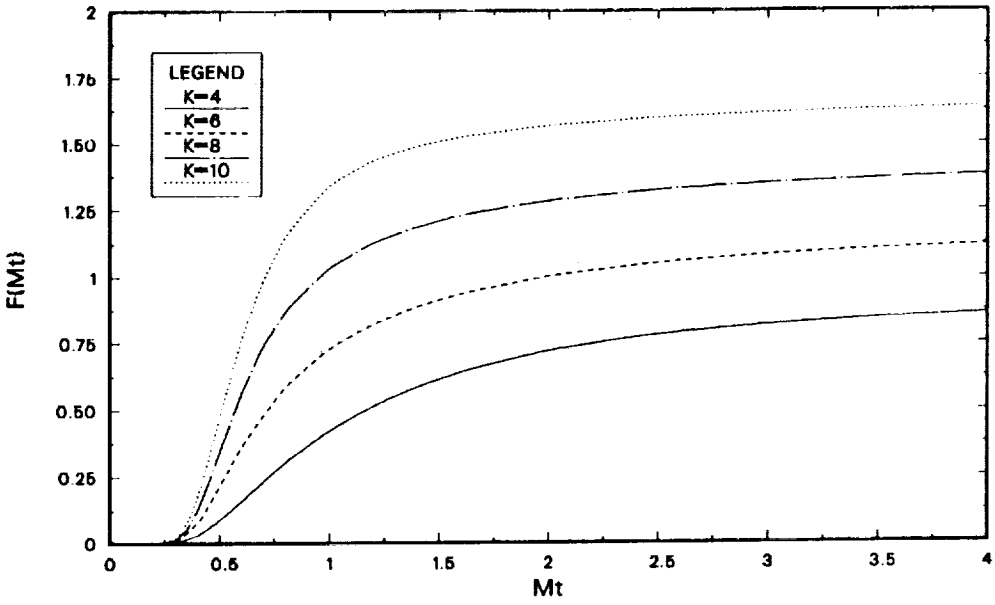

FIGURE 2. Dilatation dissipation function $F(M_t, K)$ for various values of K in the p.d.f. equation (6).

The function $F(M_t, K)$ represents the expression in square brackets above; its values obtained by numerical integration are plotted in Figure 2 for various values of the kurtosis K (in the p.d.f. equation (6). According to (8), ϵ_d is proportional to the solenoidal dissipation since $\epsilon_s \propto q^3/L$. Hence, in a second-order closure model which usually contains an equation for ϵ_s (or for L), ϵ_d is determined merely by the function $F(M_t, K)$, and the total dissipation in (1) and (2) is then

$$\epsilon_{tot} = \epsilon_s(1 + c_d F(M_t, K))$$

as suggested by dimensional analysis mentioned earlier. Apart from the model constant c_d and K (to be estimated from measurements), the total compressible turbulence dissipation is thus determined by (7) and a (standard) model equation for ϵ_s .

2.1.3. Comparison with shear layer experiments

A comparison of the dilatation dissipation model with homogenous turbulence data at sufficiently high Reynolds and Mach numbers is not possible at present. Instead, the model is compared with the experimental data in compressible free shear layers which are the least contaminated by low Reynolds number effects. For this purpose, a computer program for compressible, high Reynolds number

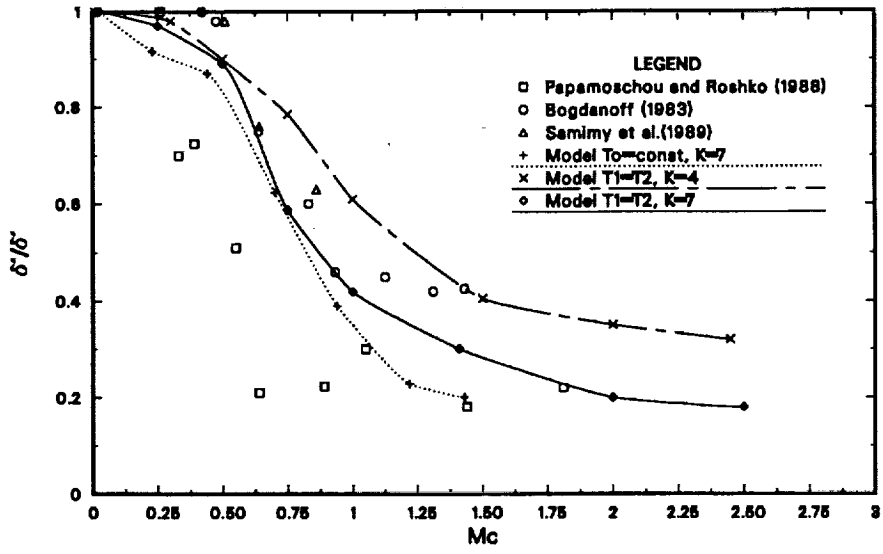

FIGURE 3. Comparison of mixing layer normalized growth rates vs. M_c.

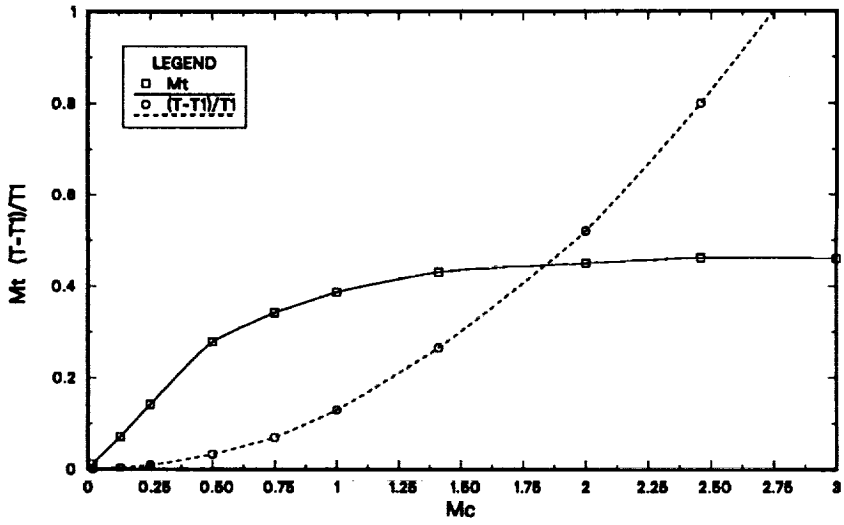

FIGURE 4. Turbulent Mach number M_t and maximum temperature excess as functions of M_c, with $T_1 = T_2$.

shear flows was formulated (Zeman, 1989) to solve transport equations for all non-zero Favre-averaged Reynolds stresses and for the vertical enthalpy flux.

The numerical scheme utilizes the von Mises transformation from (x, y) to

(x, ψ) coordinate system and all transport equations are solved by forward integration in streamwise direction x along streamlines $\psi = const.$

The crucial test of the dilation dissipation model is the prediction of the normalized growth rate δ'/δ'_o as a function of the so-called convective Mach number M_c (δ'_o is the growth rate in the incompressible limit $M_c = 0$). The concept of convective Mach number has been described in Bogdanoff (1983) and Papamoschou and Roshko (1987). With air as the (perfect) fluid, the values of δ'/δ'_o were computed for three cases: a) uniform (freestream) temperature $T_1 = T_2$ (density ratio $s = \rho_2/\rho_1$), and the kurtosis $K = 7$; b) uniform total temperature T_o, and $K = 7$; and c) uniform temperature as in case a) but with low kurtosis $K = 4$. The predicted and experimental growth rates δ'/δ'_o are compared in Figure 3. The comparison shows that the model yields realistic reduction of the shear layer growth rate as a function of the convective Mach number M_c even for small kurtosis. Figure 4 demonstrates how turbulence fluctuations are controlled by the dilatational dissipation: as M_c increases beyond one, the r.m.s. Mach number M_t appears to approach a saturation limit of about 0.5; this is observed in experiments (Samimy 1989). Figures 5, 6, and 7 display model comparisons of mean velocity, and turbulent intensities with experiments of Samimy and Elliott (1989) and Samimy et al. (1989).

Figure 5 compares the computed and experimental mean velocity profiles at two values of M_c. The profiles are shown to be universal functions of the transverse distance $(y - y_c)$ scaled by the vorticity thickness as suggested by Samimy and Elliott.

The streamwise intensity profiles are compared in Figure 6. Considering the uncertainties associated with measurements and modeling of high Mach number flows the model-experiment agreement is relatively good. Note that the measured intensities exterior to the mixing layer are due to the unavoidable background noise levels in supersonic wind tunnels.

Figure 7 compares equilibrium turbulence intensities (at the layer centerline $y = y_c$); although the model overestimates the absolute values of the intensities, the attenuation of velocity fluctuations with increasing M_c is predicted. This comparison corroborates our hypothesis that the reduction in growth rates of high speed mixing layer is a consequence of additional (dilatational) dissipation which arises due to the formation of steep density gradients, or shocklets.

2.1.4. Conclusions

We conclude with the following observations:

(1) As evident from Figure 4, the dilatation dissipation provides the controlling mechanism that suppresses excessive supersonic fluctuations and thus maintains the maximum level of the r.m.s. Mach number M_t below a certain (subsonic) level of about 0.5. This is observed in experiments. Apparently, the local intermittent shock events provide the needed dissipation to maintain, on average, turbulent velocities subsonic.

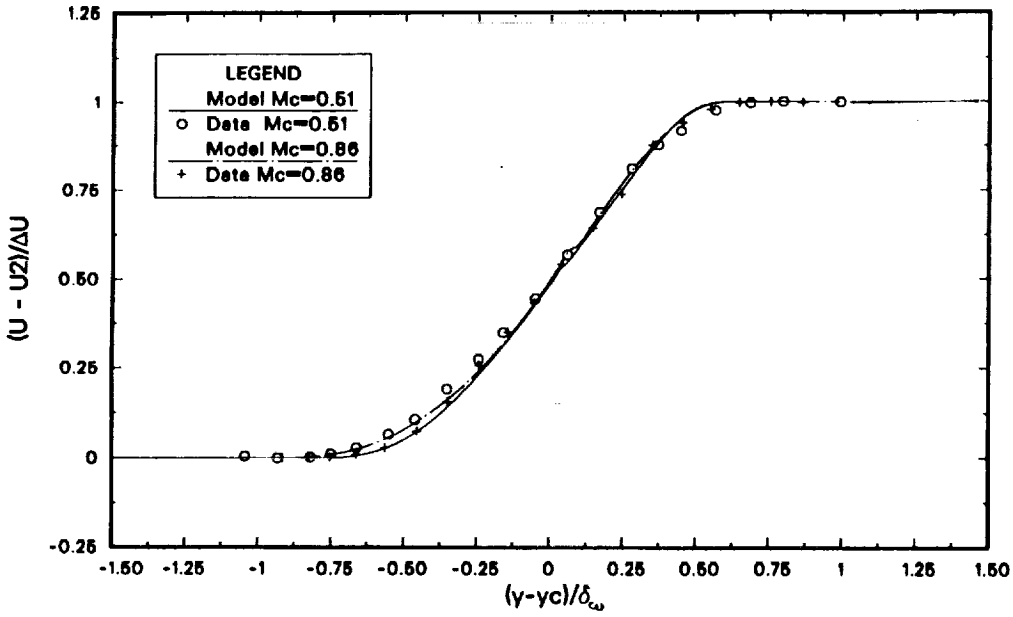

FIGURE 5. Model-experiment comparison: Mean velocity profiles at two values of M_c; abscissa is transverse distance from the layer centerline ($y = y_c$) scaled by the vorticity thickness δ_ω. Data points are from Samimy et al.(1989).

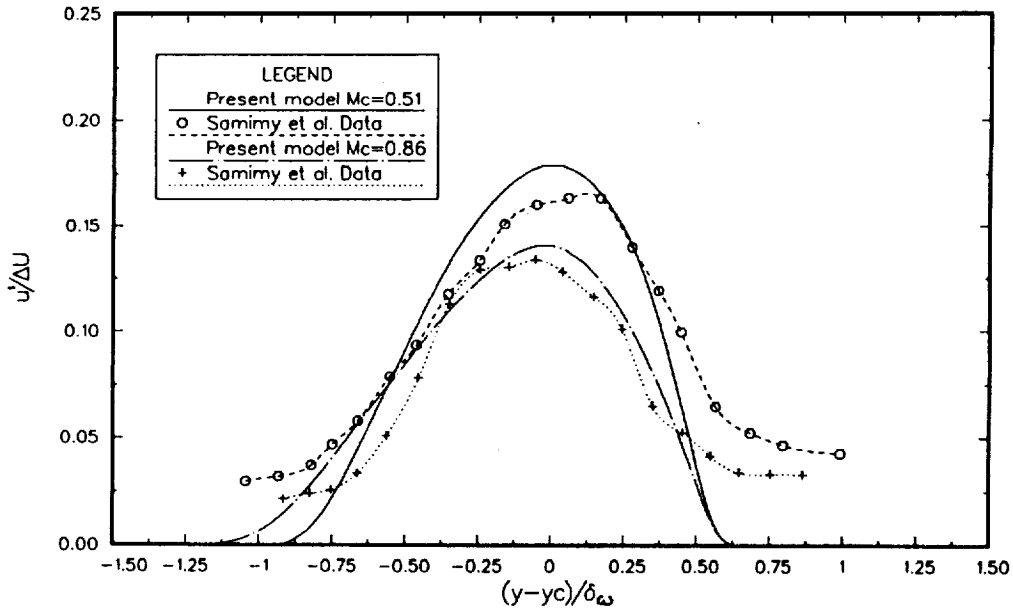

FIGURE 6. Streamwise intensity profiles, otherwise the same as Fig. 5.

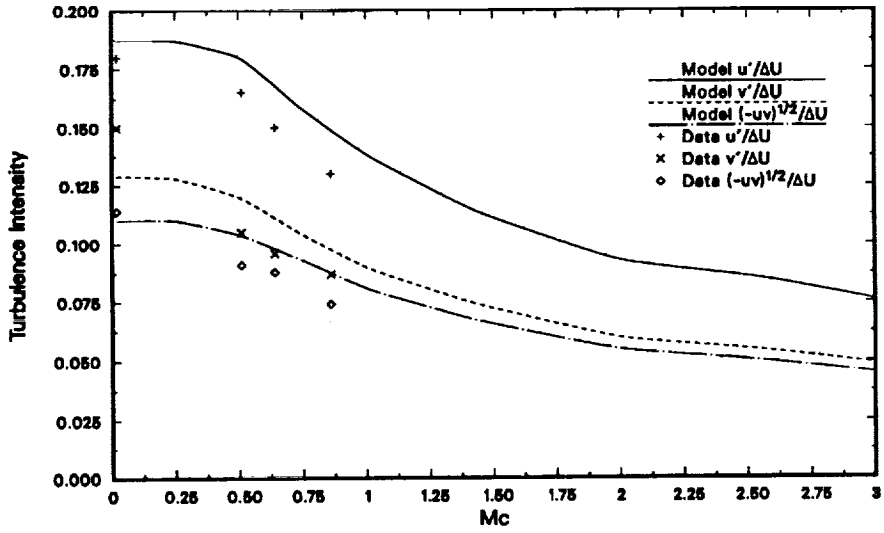

FIGURE 7. Centerline turbulence intensities vs. M_c. u', v' are r.m.s. streamwise and transverse velocities. Lines are from model predictions. Symbols are from experiments of Samimy et al. (1989).

(2) The mechanism of shock formation and dilatation dissipation bypasses the Kolmogorov energy cascade, and the process of spectral energy transfer to small scales is expected to remain unaffected by the formation of shock structures. Hence, the model equation for the solenoidal dissipation is assumed to retain its standard form independent of the dilatation dissipation.

(3) The decomposition of velocities into dilatational and solenoidal components is unique only in a strictly homogeneous turbulence field. In a bounded turbulent flow, the decomposition is not unique because of the boundary conditions. Nevertheless, the concept of the dilatation dissipation is valid, in general. The dilatation dissipation model is Galilean invariant and, therefore, applicable in any high Mach number flows such as wakes, jets, and boundary layers.

2.2 Decay of 2D compressible turbulence

In 2D turbulence the solenoidal dissipation ϵ_s is proportional to $(q^3/L)R_e^{-1}$, where the Reynolds number $R_e = qL/\nu$. Hence, according to equations (1), (2), and (8) in Section 2.1, the governing second-moment equations in 2D compressible decaying turbulence are

$$\frac{\partial q^2}{\partial t} = -\left(q^3/L\right)\{c_s R_e^{-1} + c_d F(M_t, K)\}, \tag{9}$$

$$c_p T + \frac{q^2}{2} = const. \tag{10}$$

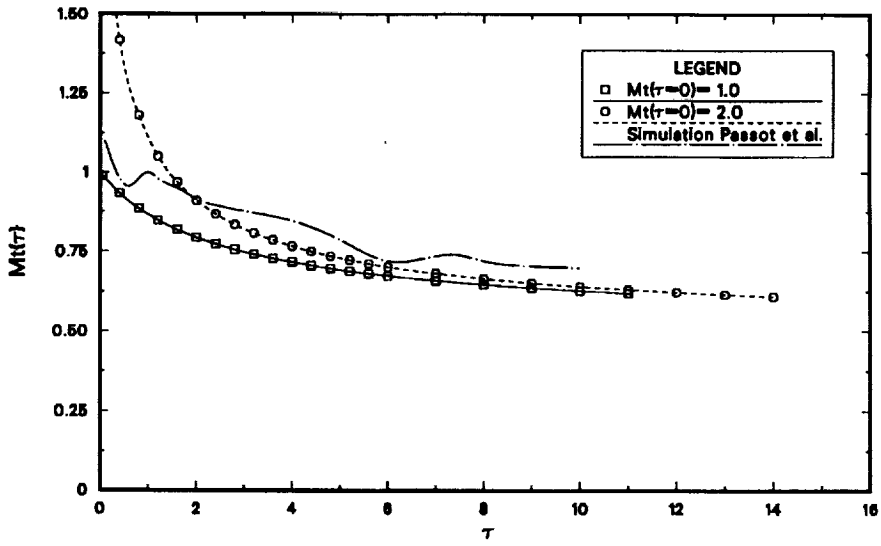

FIGURE 8. Decay of 2D homogeneous turbulence: Comparison of the decay law (11) with DNS results.

Now, (9) and (10) can be combined into a single equation for M_t^2; if, in addition, R_e is assumed to be large, the resulting equation for M_t^2 is

$$\frac{\partial M_t^2}{\partial \tau} = -2c_d M_t^2 F(M_t, K)\{1 + M_t^2 \frac{(\gamma - 1)}{2}\} \tag{11}$$

where $\tau = tq/L$ is a nondimensional time. The above equation can be considered as a *decay law* for 2D compressible turbulence. The equation can be used to verify the dilatation dissipation model when eddy shocklets are limited to 2D motion.

According to (11), for a given value of the kurtosis K, M_t decays as long as $F(M_t)$ remains sufficiently large. Since the homogeneous turbulence p.d.f.'s are gaussian, $K = 3$ and according to Figure 2 $F(M_t, K = 3)$ is negligibly small for $M_t \leq 0.4$. In Figure 8 the evolution of $M_t(\tau)$ according to (11) is tentatively compared with the DNS of 2D turbulence in molecular clouds (where $R_e >> 1$) reported by Passot et al. (1988). For comparison, we used two different initial values for M_t. It is seen that the decay law (11) yields qualitatively the same behavior as the DNS computations. In particular, the asymptotic leveling off of M_t for $\tau > 8$ is well reproduced by (11). Note that the final (asymptotic) value of M_t computed from (11) is independent of the initial conditions. This suggests that in 2D turbulence at high R_e, the dissipation is solely due to the presence of shock-like structures whose formation ceases as M_t drops below certain level. This is in agreement with the proposed theory of dilatation dissipation.

3. Current and future work

Currently, a model is being developed to simulate a hypersonic turbulent boundary layer (TBL) on a flat plate. The major concern here is to formulate a realistic model for the viscous sublayer which, in a hypersonic regime, occupies a significant portion of the total TBL thickness. Furthermore, in the hypersonic regime at freestream Mach numbers, say, $Ma_e > 15$, it is anticipated that pressure and density fluctuations, and shocklet dissipation will play a significant role in the TBL momentum and heat transfer; these issues are presently studied theoretically. Among problems to be addressed in the future are:

1) inclusion of density fluctuation equation in models of compressible and variable density turbulence.
2) Turbulence oblique shock interactions in the compression corner TBL flow.
3) parameterization of shocklet dissipation in subgrid scale models for large eddy simulations of compressible turbulence.

REFERENCES

BOGDANOFF, D.W. 1983 *AIAA J.* **21**, 926

PAPAMOSCHOU, D. & ROSHKO, A. 1988 *J. Fluid Mech* **197**, 453

PAPAMOSCHOU, D. 1986 *Ph. D. Dissertation,* CALTECH, Pasadena, CA

PASSOT, T. & POUQUET, A. 1987 *J. Fluid Mech* **181**, 441

PASSOT, T., A. POUQUET & P. WOODWARD 1988 *Astron. Astrophys* **197**, 228

SPENCER, B. W. & B.G. JONES 1971 *AIAA Paper no. 71-613,* Palo Alto, CA

SAMIMY, M. & G. S. ELLIOTT 1989 to appear in *AIAA J.*

SAMIMY, M., ERWIN, D. E. & ELLIOT, G. S. 1989 *AIAA paper no. 89-2460,* Monterey CA

ZEMAN, O. 1989 to appear in *Phys. Fluids A., Vol. 2, #2*

Turbulence modeling: near-wall turbulence and effects of rotation on turbulence

By T. -H. Shih

1. Motivation and objectives

Many Reynolds averaged Navier-Stokes solvers use closure models (including two-equation models and second-order closure models) in conjunction with "the law of the wall", rather than deal with a thin, viscous sublayer near the wall. However, law of the wall functions are based on assumptions of local equilibrium which are not always valid. For example, flows with separation, reattachment, body forces, strong secondary flows, or streamwise pressure gradient can cause the behavior of the near-wall sublayer to depart from the law of the wall. To solve these problems, the modeled turbulence equations must be carried out in the sublayer in order to capture the non-equilibrium characteristics of the near wall region. Non-equilibrium turbulence models of the two equation type include Jones and Launder (1973), Chien (1982), and Lam and Bremhorst(1981). Second order closure models include Hanjalic and Launder (1976) and Launder and Shima (1989). However, as Patel et al. (1985) pointed out, the damping functions used in the existing k-ϵ models need further modification in order to improve their performance. In addition, analysis of the near-wall behavior of the current second order closure models shows that they do not have the proper asymptotic behavior. Predictions of the normal stresses near the wall are quite poor. This work is motivated by the need for better models to compute near-wall turbulent flows. We will use direct numerical simulation of fully developed channel flow and one of three dimensional turbulent boundary layer flow (Kim et al. (1987), Mansour et al. (1988), and Moin et al. (1989)) to develop new models. These direct numerical simulations provide us with detailed data that experimentalists have not been able to measure directly.

Another objective of this work is to examine analytically the effects of rotation on turbulence, using Rapid Distortion Theory (RDT). This work is motivated by the observation (Reynolds, 1989) that the pressure-strain models in all current second order closure models are unable to predict the effects of rotation on turbulence. All current rapid pressure-strain models in the equation for the invariants of anisotropy tensor are insensitive to pure rotation.

One of the objectives of this work is to develop better models (for both two-equation model and full-Reynolds stress type models) for the near-wall turbulence, using direct numerical simulation data and existing methodologies. The models will be tested using data from direct simulations, experiments and analysis. Another objective of this work is to use RDT to obtain an analytical

solution for pure rotational turbulence, which will hopefully bring us some new understanding of turbulence physics and provide improved turbulence models for rotational flows. Specifically, the objectives of this work can be summarized as follows:

1. Examine the performance of existing two-equation eddy viscosity models and develop better models for the near-wall turbulence using direct numerical simulations of plane channel flow.

2. Use the asymptotic behavior of turbulence near a wall to examine the problems of current second-order closure models and develop new models with the correct near-wall behavior of these models.

3. Use Rapid Distortion Theory to analytically study the effects of mean deformation (especially due to pure rotation) on turbulence. Obtain analytical solutions for the spectrum tensor, Reynolds stress tensor, Anisotropy tensor, and its invariants. Use these results to develop second order closure models.

2. Work accomplished

2.1 k-ϵ model

The k-ϵ model is still the most widely used model for computing engineering flows. In this work, we first examined the near-wall behavior of various eddy viscosity models proposed by different researchers; we then studied the near-wall behavior of terms in the k-equation budget. We found that the modeled eddy viscosity in many existing k-ϵ models does not have correct near-wall behavior, and the pressure transport term in the k-equation is not appropriately modeled. Based on the near-wall asymptotic behavior of the eddy viscosity and the pressure transport term in the k-equation, we proposed a set of new models for them. In addition, a new model for the dissipation rate is derived more rationally. See Shih (1989) for more details.

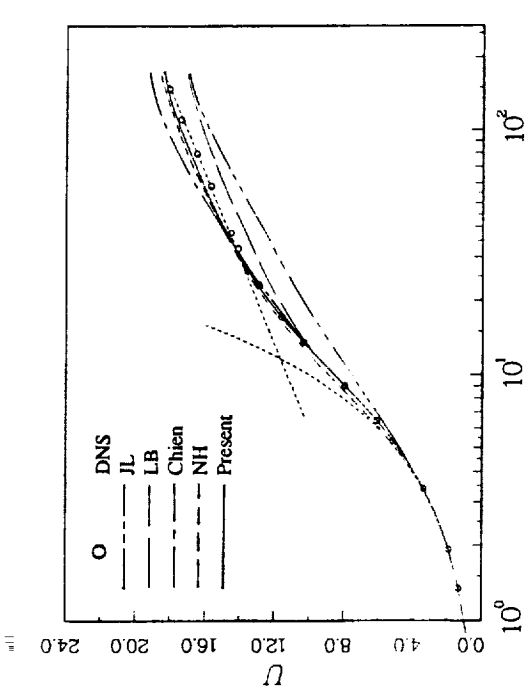

Figure 1. Mean velocity profiles in a channel

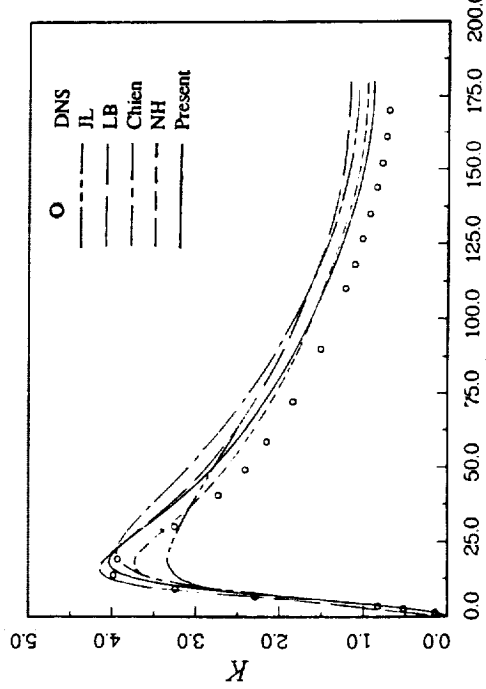

Figure 2. Turbulent energy profiles in a channel

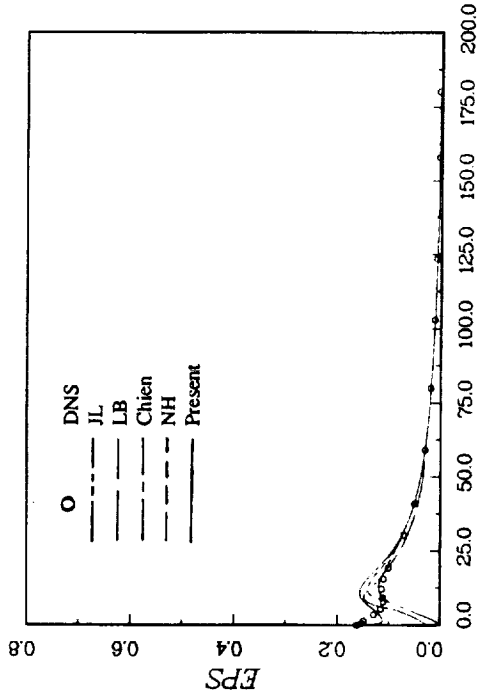

Figure 3. Dissipation rate profiles in a channel

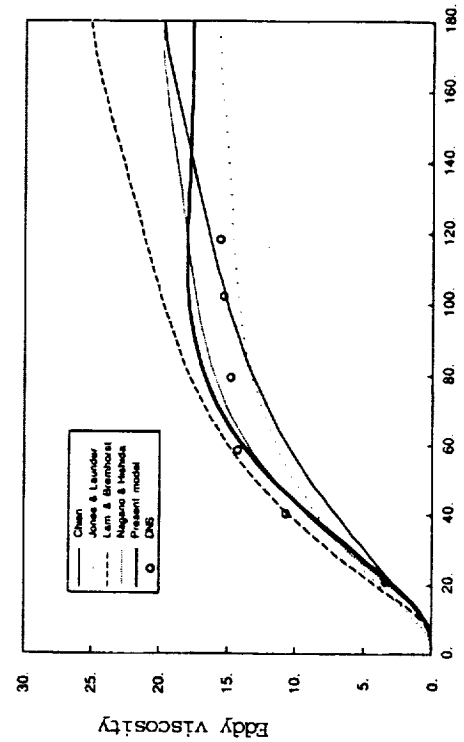

Figure 4. Eddy viscosity profiles in a channel

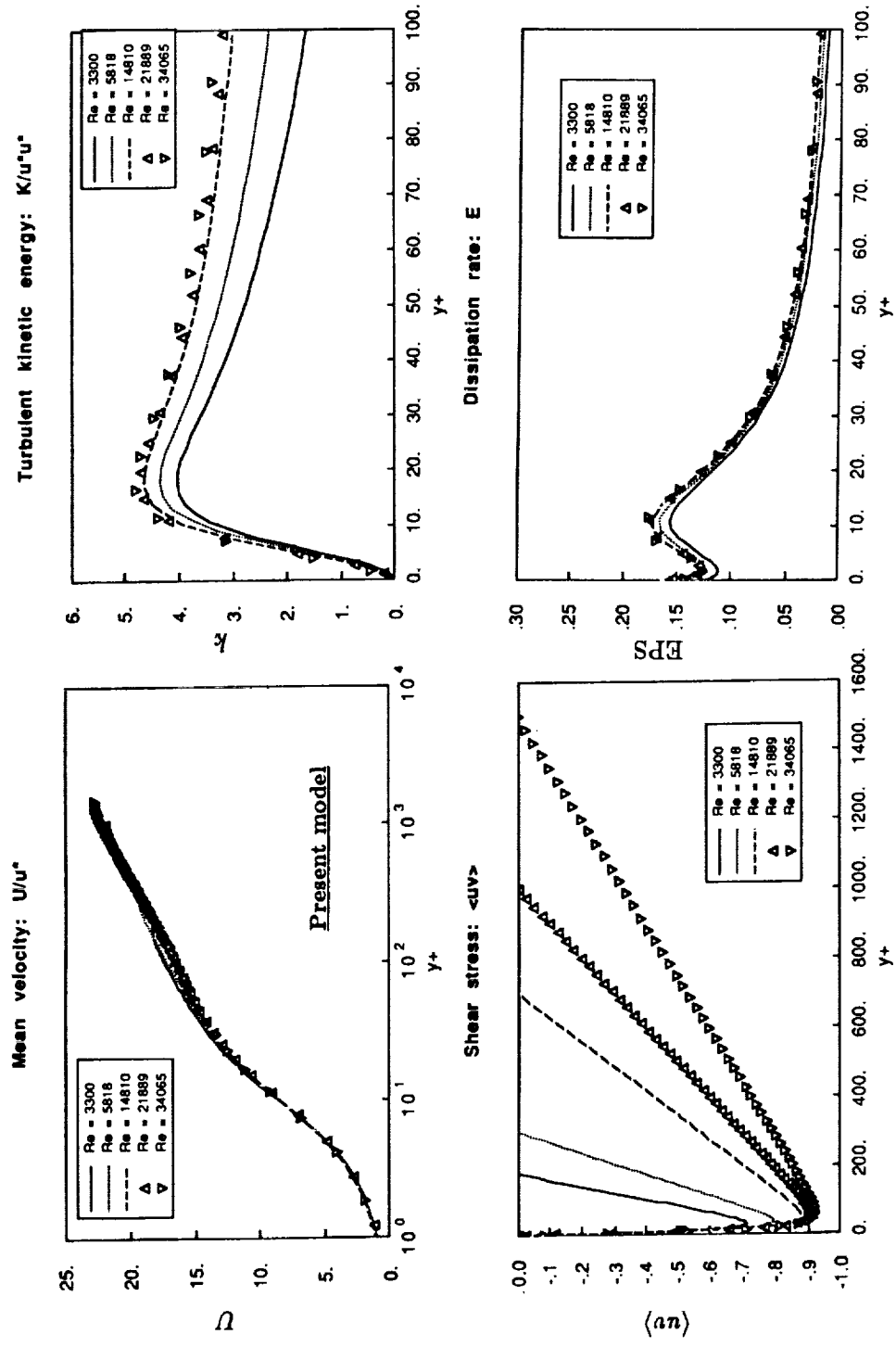

Figure 5. Profiles from present model for channel flows with different Reynolds numbers

The proposed k-ϵ model for the near-wall turbulence has been tested against direct numerical simulations of Kim et al. and compared with other k-ϵ models. The results show that the new model produces significant improvements over existing models, see figures 1 – 5. The modeled equations are given as follows:

$$k_{,t} + U_j k_{,j} = \left[\left((1+C)\frac{\nu_T}{\sigma_k} + \nu \right) k_{,j} \right]_{,j} + \nu_T S_{ij} S_{ij} - \epsilon$$

$$\epsilon_{,t} + U_j \epsilon_{,j} = \left[\left(\frac{\nu_T}{\sigma_\epsilon} + \nu \right) \epsilon_{,j} \right]_{,j} + C_1 \frac{\epsilon}{k} \nu_T S_{ij} S_{ij} - C_2 f_\epsilon \frac{\epsilon\tilde{\epsilon}}{k} + \nu\nu_T U_{i,jm} U_{i,jm}$$

$$\begin{aligned}
\sigma_k &= 1.3 \\
\sigma_\epsilon &= 1.3 \\
C_1 &= 1.45 \\
C_2 &= 2.0 \\
\tilde{\epsilon} &= \epsilon - \phi \\
\phi &= \nu k_{,j} k_{,j} / (2k) \\
\nu_T &= C_\mu f_\mu k^2 / \tilde{\epsilon} \\
C_\mu &= 0.09 \\
f_\mu &= 1 - \exp(-a_1 y^+ - a_2 {y^+}^2 - a_3 {y^+}^3 - a_4 {y^+}^4) \\
a_1 &= 6 \times 10^{-3}, a_2 = 4 \times 10^{-4}, a_3 = -2.5 \times 10^{-6}, a_4 = 4 \times 10^{-9} \\
f_\epsilon &= 1 - \frac{0.4}{1.8} \exp\left(- \left(\frac{k^2}{6\nu\epsilon} \right)^2 \right) \\
C &= \frac{.05}{f_\mu [1 - \exp(-y^+)]} \\
y^+ &= u_\tau y / \nu
\end{aligned}$$

2.2 Second order modeling of near-wall turbulence

Using the near-wall asymptotic behavior of turbulence (Mansour et al. (1988)) as model constraints, we formed a set of modeled transport equations for the Reynolds-stress tensor and the dissipation rate of turbulent kinetic energy. The main emphasis was on developing a model for the "slow term" in the Reynolds-stress equation. A modeled dissipation rate equation is derived more rationally. Near the wall, a reduction in velocity fluctuations normal to the wall become significant. Because of this wall effect, the viscous diffusion term in the Reynolds-stress equations becomes the leading term, and it must be properly balanced by the slow term. We will use this as a model constraint for developing a model for the slow terms. The proposed models in this work do not contain the wall distance; therefore, they are generally suitable for an arbitrary surface. The proposed models also satisfy realizibility which ensures no unphysical behavior will occur. Here, we briefly describe and list the proposed models.

Reynolds stress equation

The exact equation for the Reynolds stress tensor is:

$$\frac{D}{Dt}\langle u_i u_j\rangle = P_{ij} + T_{ij} + D_{ij}^{(\nu)} + \Pi_{ij} - \varepsilon_{ij}$$

where $\langle\ \rangle$ stands for an ensemble average, $D/Dt = \partial/\partial t + U_k \partial/\partial x_k$. The terms P_{ij}, T_{ij}, $D_{ij}^{(\nu)}$, Π_{ij} and ε_{ij} represent the production, turbulent diffusion, viscous diffusion, velocity pressure-gradient correlation, and dissipation tensor and are identified as follows:

$$\begin{aligned}
P_{ij} &= -\langle u_i u_k\rangle U_{j,k} - \langle u_j u_k\rangle U_{i,k} \\
T_{ij} &= -\langle u_i u_j u_k\rangle_{,k} \\
D_{ij}^{(\nu)} &= \nu\langle u_i u_j\rangle_{,kk} \\
\Pi_{ij} &= -\frac{1}{\rho}\langle u_i p_{,j} + u_j p_{,i}\rangle \\
\varepsilon_{ij} &= 2\nu\langle u_{i,k} u_{j,k}\rangle
\end{aligned}$$

The velocity pressure-gradient correlation Π_{ij} is split into the rapid part $\Pi_{ij}^{(1)}$ and the slow part $\Pi_{ij}^{(2)}$:

$$\Pi_{ij} = \Pi_{ij}^{(1)} + \Pi_{ij}^{(2)}$$

The proposed model for the return term, $\Pi_{ij}^{(2)} - \varepsilon_{ij}$ is:

$$\begin{aligned}
\Pi_{ij}^{(2)} - \varepsilon_{ij} = &- \epsilon(\beta b_{ij} + \frac{2}{3}\delta_{ij})(1 - f_w) \\
&- f_w \frac{\epsilon}{\langle q^2\rangle}[2\langle u_i u_j\rangle + 4(\langle u_i u_k\rangle n_j n_k + \langle u_j u_k\rangle n_i n_k) + 2\langle u_k u_l\rangle n_k n_l n_i n_j]
\end{aligned}$$

where n_i is a unit vector normal to the surface, and

$$\begin{aligned}
\beta &= 2 + \frac{F}{9}\{\frac{72}{R_t^{1/2}} + 80.1\ln[1 + 62.4(-II + 2.3III)]\}\exp(-\frac{7.77}{R_t^{1/2}}) \\
F &= 1 + 27III + 9II \\
II &= -\frac{1}{2}b_{ij}b_{ji} \\
III &= \frac{1}{3}b_{ij}b_{jk}b_{ki} \\
b_{ij} &= \langle u_i u_j\rangle/\langle q^2\rangle - \delta_{ij}/3 \\
f_w &= \exp(-(R_t/C_1)^2)
\end{aligned}$$

and $R_t = \frac{\langle q^2\rangle^2}{9\nu\epsilon}$, $C_1 = 1.358 R_{e\tau}^{0.44}$, $R_{e\tau} = u_\tau \delta/\nu$. u_τ is the friction velocity, δ is the thickness of the boundary layer or the half width of the channel.

The rapid part of velocity pressure-gradient, $\Pi_{ij}^{(1)}$ is modeled as follows (Shih and Lumley (1985, 1986)):

$$\begin{aligned}\Pi_{ij}^{(1)} &= (\frac{1}{5} + 2a_5)\langle q^2\rangle(U_{i,j} + U_{j,i}) - \frac{2}{3}(1 - a_5)(P_{ij} - \frac{2}{3}P\delta_{ij}) \\ &+ (\frac{2}{3} + \frac{16}{3}a_5)(D_{ij} - \frac{2}{3}P\delta_{ij}) + \frac{2}{15}(P_{ij} - D_{ij}) + \frac{6}{5}b_{ij}P \\ &+ \frac{2}{5\langle q^2\rangle}[(\langle u_i u_k\rangle U_{j,q} + \langle u_j u_k\rangle U_{i,q})\langle u_k u_q\rangle - \langle u_i u_p\rangle\langle u_j u_q\rangle(U_{p,q} + U_{q,p})]\end{aligned}$$

where,

$$\begin{aligned}P_{ij} &= -\langle u_i u_k\rangle U_{j,k} - \langle u_j u_k\rangle U_{i,k} \\ D_{ij} &= -\langle u_i u_k\rangle U_{k,j} - \langle u_j u_k\rangle U_{k,i} \\ P &= \frac{1}{2}P_{ii} \\ a_5 &= -\frac{1}{10}(1 + C_2 F^{1/2}) \\ C_2 &= 0.8[1 - \exp(-(R_t/40)^2)]\end{aligned}$$

Finally the model for the third moments is modeled as:

$$\langle u_i u_j u_k\rangle = -.07\frac{\langle q^2\rangle}{\epsilon}[\langle u_k u_p\rangle\langle u_i u_j\rangle_{,p} + \langle u_j u_p\rangle\langle u_i u_k\rangle_{,p} + \langle u_i u_p\rangle\langle u_j u_k\rangle_{,p}]$$

Dissipation rate equation

The modeled dissipation rate equation derived in this work is:

$$\begin{aligned}\epsilon_{,t} + U_i\epsilon_{,i} &= (\nu\epsilon_{,i} - \langle\epsilon u_i\rangle)_{,i} - \psi_0\frac{\epsilon\tilde{\epsilon}}{\langle q^2\rangle} \\ &- \psi_1\frac{\tilde{\epsilon}}{\langle q^2\rangle}\langle u_i u_j\rangle U_{i,j} - \psi_2\frac{\nu\langle q^2\rangle}{\epsilon}\langle u_k u_l\rangle(U_{i,jl} - U_{l,ij})U_{i,jk}\end{aligned}$$

where

$$\begin{aligned}\psi_0 &= \frac{14}{5} + 0.98[1 - 0.33\ln(1 - 55II)]\exp(-2.83R_t^{-1/2}) \\ \psi_1 &\approx 2.1 \\ \psi_2 &= -.15(1 - F) \\ \tilde{\epsilon} &= \epsilon - \frac{\nu\langle q^2\rangle_{,i}\langle q^2\rangle_{,i}}{4\langle q^2\rangle}\end{aligned}$$

The turbulent flux term $\langle\epsilon u_k\rangle$ is modeled as:

$$\langle\epsilon u_k\rangle = -.07\frac{\langle q^2\rangle}{2\epsilon}\langle u_k u_p\rangle\epsilon_{,p}$$

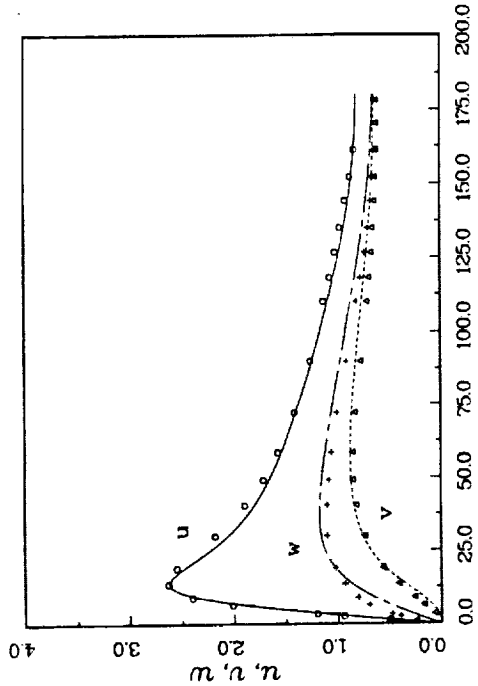

Figure 8. Turbulence intensities in a channel

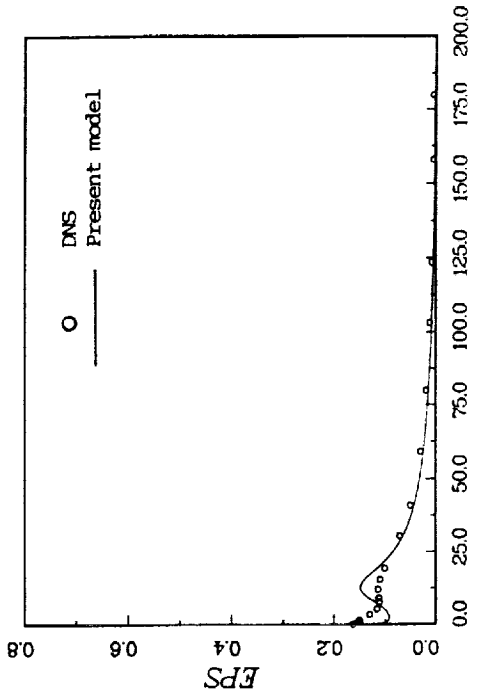

Figure 9. Dissipation rate profile in a channel

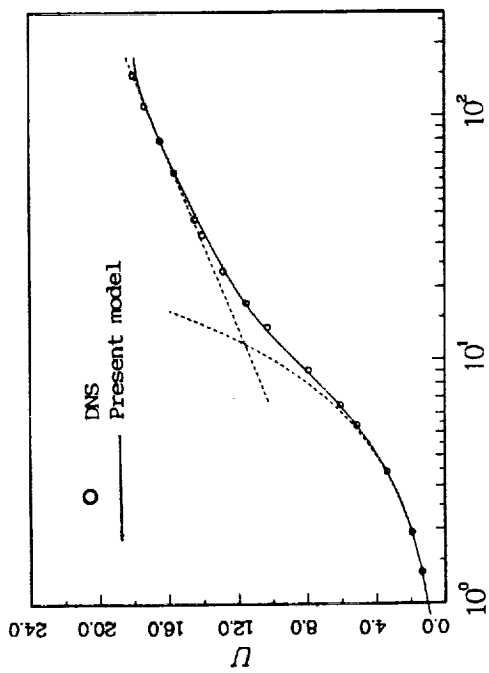

Figure 6. Mean velocity profile in a channel

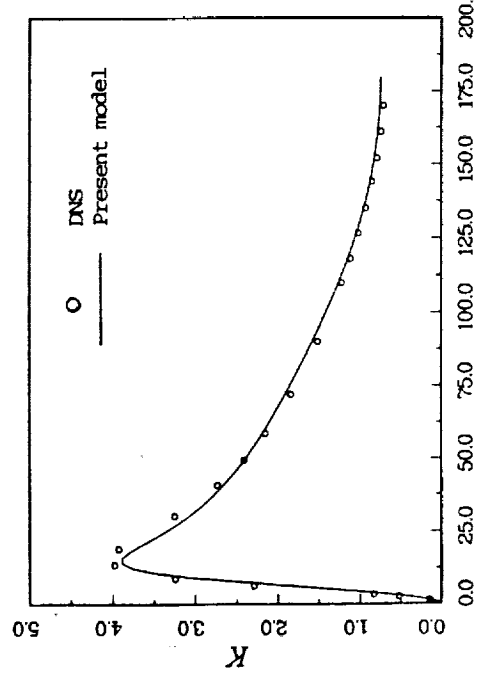

Figure 7. Turbulent energy profile in a channel

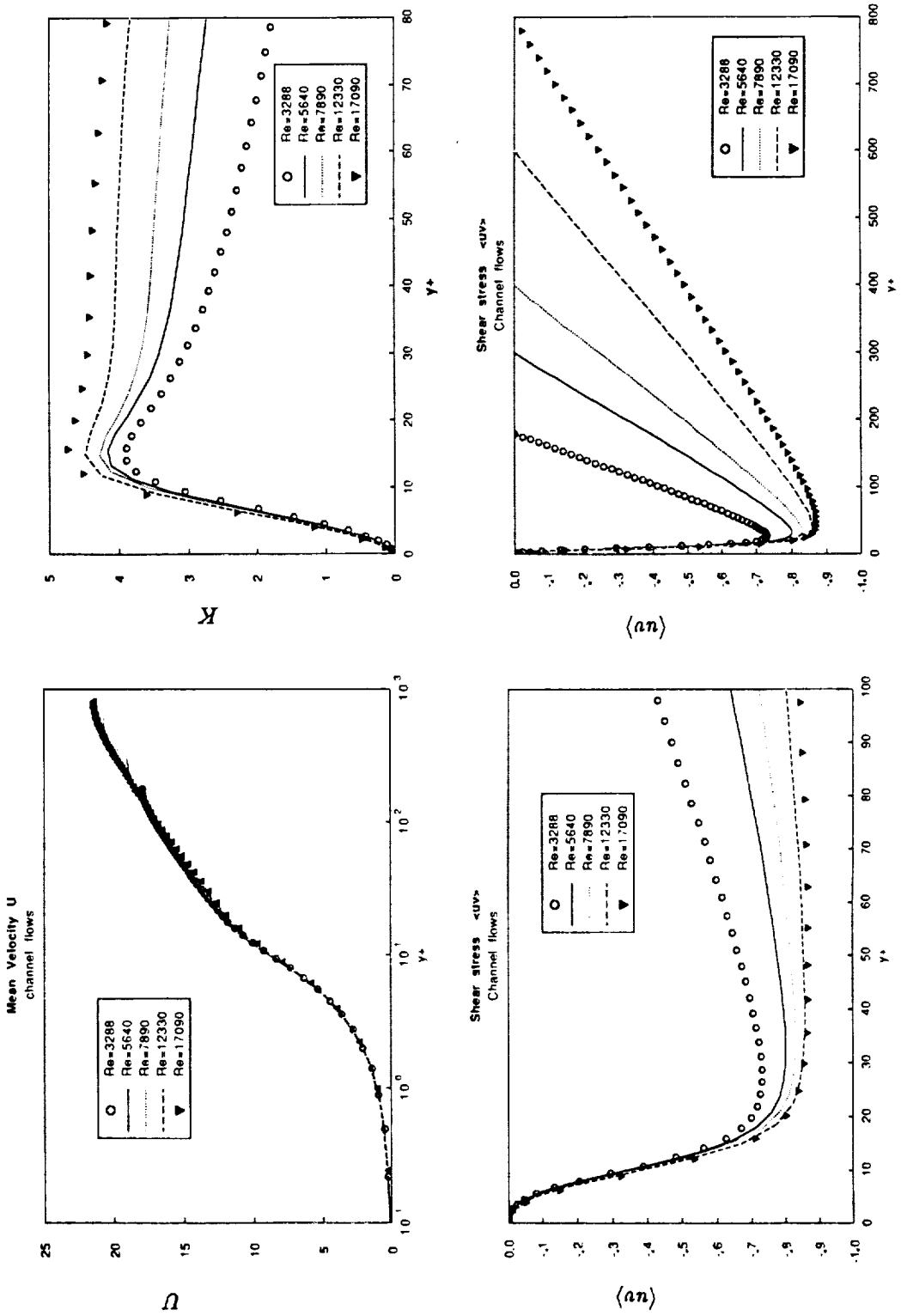

Figure 10. Profiles from present Reynolds-stress model for channel flows with different Reynolds numbers

To test the models developed in this work, we chose a fully developed channel flow as the test flow. The Reynolds number based on friction velocity and channel half width Re_τ is 180, for which direct numerical simulation (Kim et al., 1987) and experimental data (Nishino and Kasagi, 1989) are available for comparison. The modeled Reynolds stress equations for this flow are one-dimensional and steady; therefore, model testing is easy and accurate. The results of the present model compared with direct numerical simulation and other models are shown in figures 6 – 10. As the figures indicate, the proposed models capture the near-wall behavior of the turbulence and show significant improvement over previous second order models and k-ϵ models.

2.3 Second order modeling of a three-dimensional boundary layer

A study of three-dimensional effects on turbulent boundary layer was achieved by direct numerical simulation of a fully developed turbulent channel flow subjected to transverse pressure gradient. The time evolution of the flow was studied. Fourteen realizations, each starting with a different initial turbulence field, were computed and ensemble averaged. The results show that, in agreement with experimental data, the Reynolds stresses are reduced with increasing three-dimensionality and that, near the wall, a lag develops between the stress and the strain rate. In addition, we found that the turbulent kinetic energy also decreased.

To model these three-dimensional effects on the turbulence, we have tried different second order closure models. None of the current second order closure models can predict the reductions in the shear stress and turbulent kinetic energy observed using direct numerical simulations. However, we found that the proposed second order closure models developed in the previous section do at least qualitatively capture these three-dimensional effects, see figures 11 – 14. Detailed studies of the Reynolds-stresses budgets were carried out. One of the preliminary conclusions from these budget studies is that the velocity pressure-gradient term in the normal stress equation $\langle v^2 \rangle$ plays a dominant role in the reduction of shear stress and kinetic energy. These budgets will be used to guide the development of better models for three dimensional turbulent boundary layer flows.

2.4 The effect of rotation on turbulence

In addition to the above studies of second order closure models, we have carried out some RDT analysis on simple homogeneous turbulent flows. An order of magnitude analysis shows that under the condition of $S\langle q^2 \rangle/\epsilon \gg \sqrt{R_t}$, the equations for turbulent velocity fluctuations can be approximated by a linear set of equations, and if $S\langle q^2 \rangle/\epsilon \gg R_t^{3/4}$, then the turbulent velocity equations can be further approximated by an inviscid linear equation. Therefore, RDT can be used to analytically study some very basic turbulent flows such as homogeneous

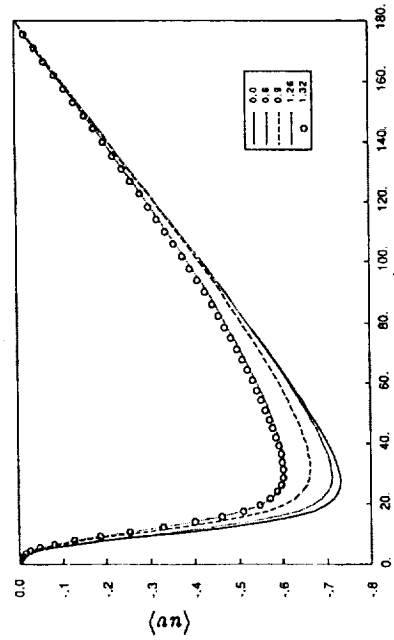

Figure 11. Evolution of shear stress in a 3-D channel

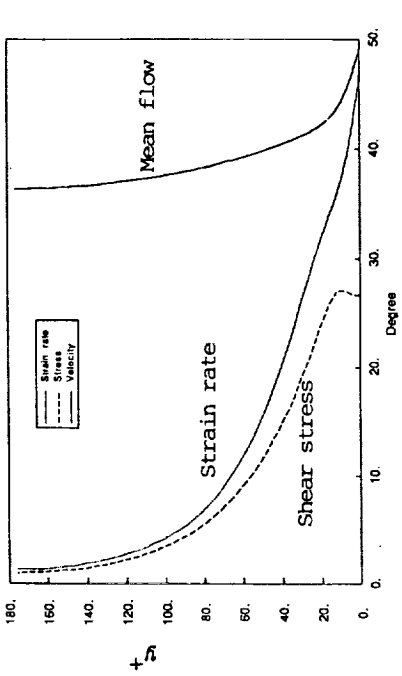

Figure 13. Angles of mean flow, shear stress & strain rate at t=1.2

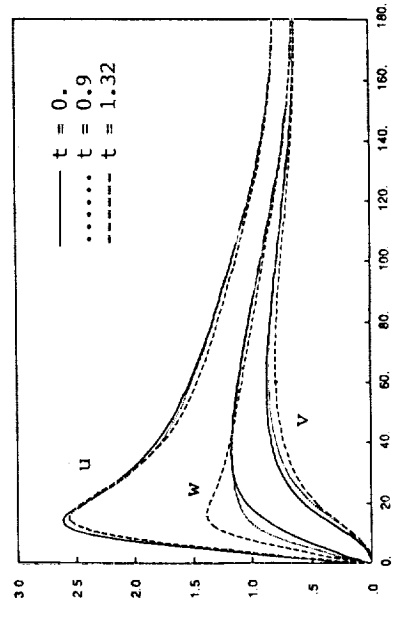

Figure 14. Evolution of mean transverse velocity

Figure 12. Turbulence intensities in a 3-D channel

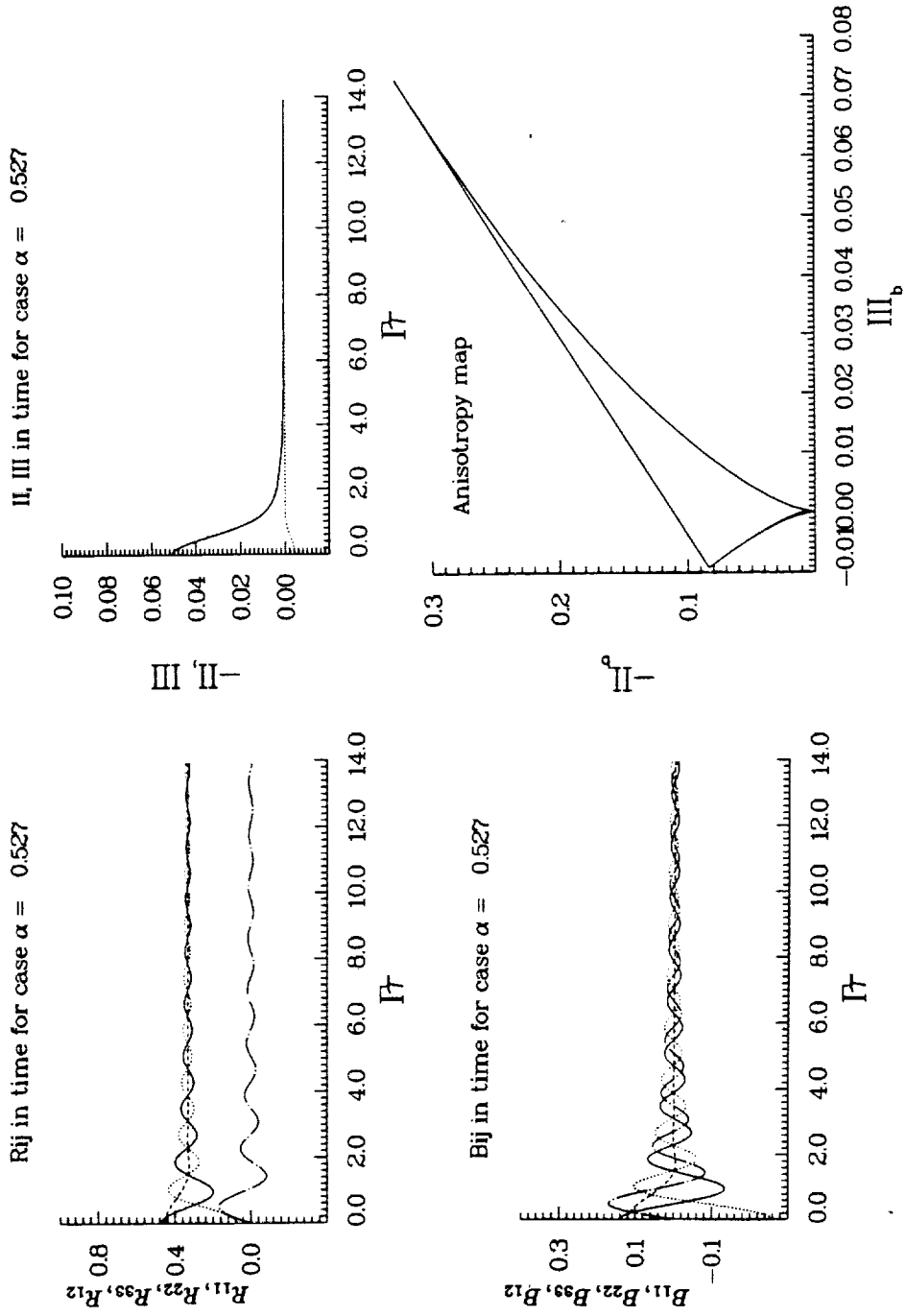

Figure 15. Typical RDT solution for the rotation of initially anisotropic homogeneous turbulence

shear flows, irrotational strain flows, and pure rotational flows. RDT analysis will hopefully bring out some new ideas in turbulence physics and modeling. Reynolds (1989) recently pointed out that all current rapid pressure-strain models are unable to predict the effects of rapid rotation on the turbulence. RDT is certainly an ideal tool to study this kind of basic turbulent flow. It can provide analytical solutions for the details of the flow field, and hence can be used to guide the development of turbulence models.

This work focuses on the effect of rapid rotation on turbulence using RDT. We obtained analytical expressions for velocity, the spectrum tensor, Reynolds-stress, the anisotropy tensor and its invariants. The solutions show that the turbulence is strongly affected by the rapid rotation. A typical case is shown in figure 15. Using RDT, we are calculating the rapid pressure-stain term exactly and we are obtaining very useful information for developing corresponding turbulence models.

3. Future plans

1. Using direct numerical simulation data (Moin et al., 1989 and Spalart, 1989), we are planning to improve the second-order closure models proposed in this work for three dimensional boundary layers.

2. Extend second order closure models to near-wall turbulent heat fluxes.

3. Use the information obtained from RDT to model the effects of rapid rotation on the turbulence. It appears that at least the quadratic terms of mean velocity gradient are necessary in the rapid pressure-stain model.

4. Modeling the effects of buoyancy on the turbulence.

5. Third order modeling of shearless turbulent mixing layer — using moment generating function method. This type of model will be needed when third order moments play a dominant role in transferring of momentum and energy, such as in a convective planetary boundary.

6. Explore the potential of the RNG method in one-point turbulence closure models.

REFERENCES

CHIEN, K.-Y. 1982 Predictions of channel and boundary-layer flow with a low-Reynolds-number turbulence model. *AIAA Journal.* **20,** 33-38.

HANJALIC, K. & LAUNDER, B. E. 1976 Contribution towards a Reynolds-stress closure for low-Reynolds-number turbulence. *J. Fluid Mech.* **74,** 593-619.

JONES, W. P. & LAUNDER, B. E. 1973 The calculation of low-Reynolds number phenomena with a two-equation model of turbulence. *International Journal of Heat and Mass Transfer.* **16,** 1119-1130.

KIM, J., MOIN, P. & MOSER, R. 1987 Turbulent statistics in fully developed channel flow at low Reynolds number. *J. Fluid Mech.* **177**, 133–166.

LAM, C. K. G. & BREMHORST, K. 1981 A modified form of the $K - \epsilon$ model for predicting wall turbulence. *ASME Transactions, Journal of Fluids Engineering.* **103**, 456-460.

LAUNDER, B. E. & SHIMA, N. 1989 Second-moment closure for the near-wall sublayer: development and application. *AIAA Journal.* **27**, 1319-1325.

MANSOUR, N. N., KIM, J. & MOIN. P. 1988 Reynolds–stress and dissipation rate budgets in a turbulent channel flow. *J. Fluid Mech.* **194**, 15–44.

MOIN, P., SHIH, T. -H., DRIVER, D. & MANSOUR, N. N. Numerical simulation of a three-dimensional turbulent boundary layer AIAA 89-0373.

NISHINO, K. & KASAGI, N. 1989 Turbulent statistics measurement in a two dimensional channel flow using a three-dimensional particle tracking velocimeter. *Seventh Symposium on Turbulent Shear Flows.* Stanford University

PATEL, V. C., RODI, W. & SCHEUERER, G. 1985 Turbulence models for near–wall and low–Reynolds–number flows: A Review. *AIAA Journal.* **23**, 1308–1319.

REYNOLDS, W. C. 1989 Effects of rotation on homogeneous turbulence. Tenth Australasian Fluid Mechanics Conference, the University of Melbourne, Australia, Dec. 11-15, 1989

SHIH, T. -H. & LUMLEY J. L. 1986 Second-order modeling of near-wall turbulence. *Phys. Fluids.* **29**, 971–975.

SHIH, T. -H. & LUMLEY, J. L. 1985 Modeling of pressure correlation terms in Reynolds–stress and scalar flux equations. *Rept. FDA-85-3, Sibley School of Mech. and Aerospace Eng., Cornell University.*

SHIH, T. H. 1989 An improved $k - \epsilon$ model for near-wall turbulence and comparison with direct numerical simulations. NASA-Stanford Center for Turbulence Research, Stanford, California.

SPALART, P. R. 1989 Theoretical and numerical study of a three-dimensional turbulent boundary. *J. Fluid Mech.* **205**, 319-340.

Center for Turbulence Research
Annual Research Briefs – 1989

An experimental study of scalar mixing in curved shear layers

By P. S. Karasso AND M. G. Mungal

This report describes the work being undertaken to study the scalar mixing in curved shear layers. First, the motivation for this work and its objectives are described. Second, a description of the experimental rig that has been built is given. Third, some preliminary results (flow visualizations) are discussed, and finally, future steps that will be taken to complete the study are outlined.

1. Introduction

Straight mixing layers have been the object of considerable study over the last twenty years. Curved mixing layers have seen less investigation. Here, we will provide a brief description of the aspects that are important to this work. The characterization of a curved shear layer depends upon the sense of the curvature: if the high speed stream is on the inside of the curvature, it is referred to as the unstable case; the reverse is referred to as the stable case (Fig. 1). For such shear layers, with equal density fluids, two kinds of instability modes are encountered. First, the Kelvin-Helmholtz (K-H) instability which is due to the shear per se and manifests itself with spanwise vortical structures. Second, the Taylor-Görtler (T-G) instability, associated with the centripetal forces due to the streamlines' curvature, which creates streamwise vortical structures. The Taylor-Görtler instability is enhanced in the unstable case and suppressed in the stable one. Plesniak & Johnston (1989) have provided detailed measurements of the turbulence properties of curved mixing layers.

Wang (1984) studied a curved shear layer to determine the flow structure for the stable and the unstable case. He used spatially averaged shadowgraph pictures which can easily mask the real physics of the flow. He found evidence of organized motion for the stable case but more 3-dimensionality and loss of the large-scale (K-H) motion for the unstable case.

Koochesfahani (1984) made concentration field measurements in a plane shear (mixing) layer, where the K-H instability is dominant, producing a non-marching probability density function (pdf) of mixture fraction; a similar result was obtained earlier by Konrad (1976). A new, more plausible model for mixing by Broadwell & Breidenthal (1982) based on the large-scale structures was thus supported.

The existence of streamwise vortical structures in a lower Reynolds number plane shear layer was investigated by Bernal (1981). Image reconstruction by

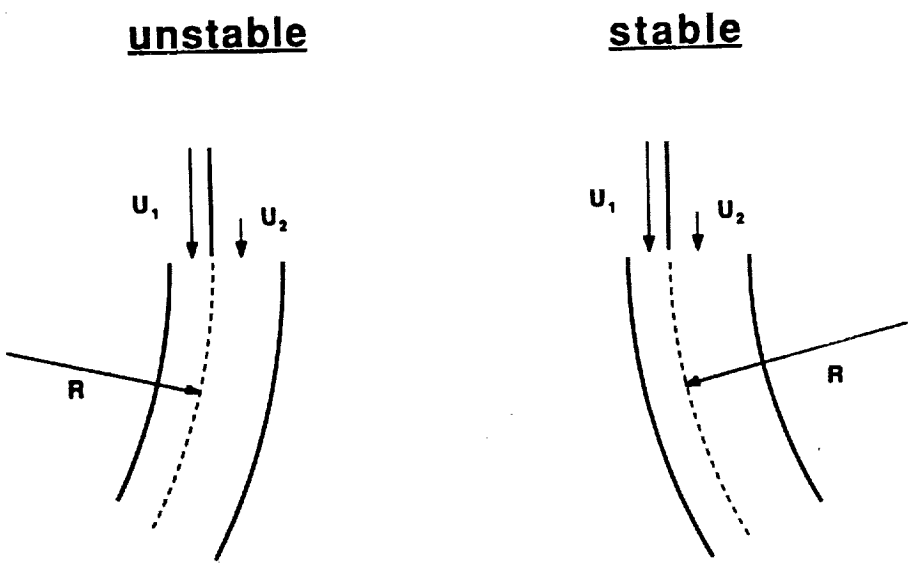

FIGURE 1. Definition of stable vs. unstable curvature

Jimenez, Cogollos and Bernal (1985) revealed the flow structure and suggested possible growth mechanisms.

It is the purpose of this study to understand the flow physics, the molecular mixing and growth rate in curved shear layers at high Reynolds numbers past the mixing transition (up to 80,000 based on velocity difference and visual thickness). The curvature offers a way to "dissociate" the effect of the two instability modes: in the unstable case both K-H and T-G are present and strong whereas in the stable the K-H is strong and the T-G is weak. A detailed quantitative description of the composition field in the fully developed region is sought via pdf measurements. The flow physics is investigated via detailed image reconstruction approaches.

Instantaneous, spatially resolved pictures of high Reynolds numbers curved shear layers do not exist in the literature, so we have chosen to begin there in order to address the question of organized motion. Volume rendering in the $y-z-t$ space has proven to be a most powerful tool to investigate the evolution of structures in flows (Cruyningen, Lozano, Mungal, Hanson, 1989) and will be attempted in the curved layer. It is again noted that Schlieren pictures or shadowgraphs are incompatible with the above ideas and that only instantaneous planar cuts of the layer can reveal the real mechanisms of mixing.

2. Experimental facility & technique

A schematic of the facility that was built for this study is shown in Fig 2. It is a blow-down water tunnel made entirely out of plexiglass which allows full

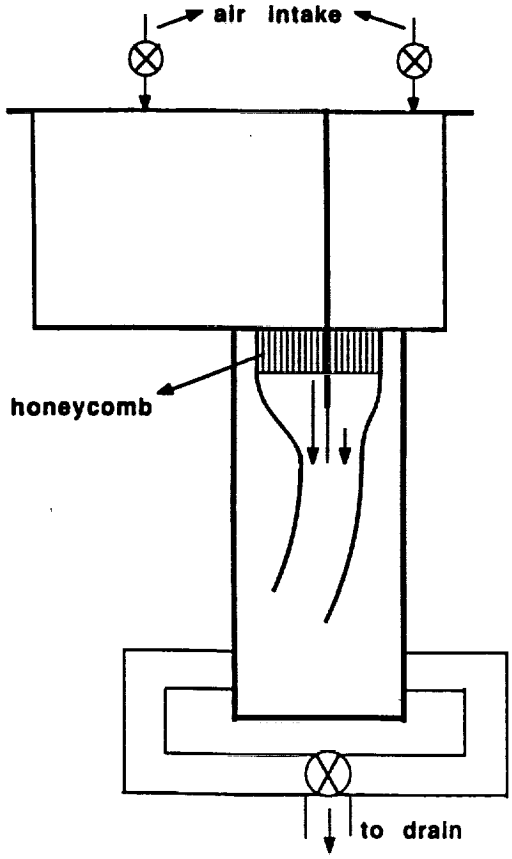

FIGURE 2. Layout of Rig

optical access. The overhead tank is partitioned so that one side (usually the low-speed) can be totally dyed. The velocity ratio of the two streams and the flow rates can be controlled by means of a draining valve and air-admittance valves. The facility is operated at a velocity ratio of 4:1. A speed of 2 m/s can be achieved on the high speed side, which gives a Reynolds number of about 80,000 towards the end of the test section. The test section size is 16 cm (span) x 10 cm (height) x 30 cm (length). The facility has been mounted over a recently refurbished floor and underground sump tank.

The test section (curved walls, shown in the unstable configuration in Fig. 2) was modelled after Wang's facility and it is considered to be of mild curvature. The run-time of the tunnel ranges from 15 to 30 seconds, depending on the velocity magnitudes.

Flow visualizations are effected with planar laser induced fluorescence (PLIF). A fluorescent dye (sodium fluorescein) is diluted in the low-speed side and the layer is excited with a laser sheet from a 2-Watt Argon-ion laser. The sheet can

be directed in the $x - y$ plane (side view), the $x - z$ plane (plan view), and the $y - z$ plane (end view) to give the whole flow field. Fast photography (exposure time 1/1000 sec) with 3200 ASA film was then used, minimizing smearing of the flow field.

3. Present results

Some high Reynolds number flow visualizations are shown below, using the techniques described earlier. The high and low speed streams are at 2 and 0.5 m/s respectively.

Figure 3 shows side views for the stable and the unstable case (flow is from left to right). The K-H rolls are very well defined throughout the whole test section for both cases. The two fiducial marks on each picture are at 15 and 25 cm downstream from the splitter plate (corresponding to Reynolds numbers of approximately 35,000 and 60,000). The large-scale organized motion of the flow prevails into the fully developed region of the shear layer. This photo immediately shows the advantage over spatially integrated measures such as shadowgraphy when compared to Wang's results. The growth of the structures was in general found to be larger for the unstable case. To clarify the overall growth rates, time-averaged pictures are shown in Fig.4 (flow here is from top to bottom). The dots are put there to help the reader follow the mixing layer. It can be seen that the layer grows about 50% more for the unstable case than for the stable one.

In order to investigate the 2-D aspect of the K-H vortices, plan views of both cases are presented. Bands of mixed and unmixed fluid are observed (Fig. 5). Bands were found to be much more defined in the stable case, whereas much more streakiness was evidenced in the unstable case. We believe that this is due to the enhanced T-G instability which creates streamwise structures. Another rather striking event is the fact that the spanwise rolls are seen to occur tilted with respect to the flow direction. This, to our knowledge, has never been reported before and would again show the difficulties in shadow techniques. Various runs were performed to further investigate this fact for a case of a plane 2-D layer at the same high Reynolds number (straight walls can also be easily mounted in the experimental rig). The skewness of the structures was again evidenced.

End views of the layers are not presented here. The reason has to do with the fact that single pictures of this view cannot easily reveal any structures. This view, however, will be heavily emphasized during our upcoming image reconstruction which is addressed in the next section.

We have emphasized here the importance of instantaneous cuts, especially for such high speed flows, in order to understand the real physics underlying the evolution of the structures. Also it is crucial to see that all three views are needed and are complementary to each other. For instance, a side view capturing a tilted object may look very ambiguous, whereas a plan view might reveal it.

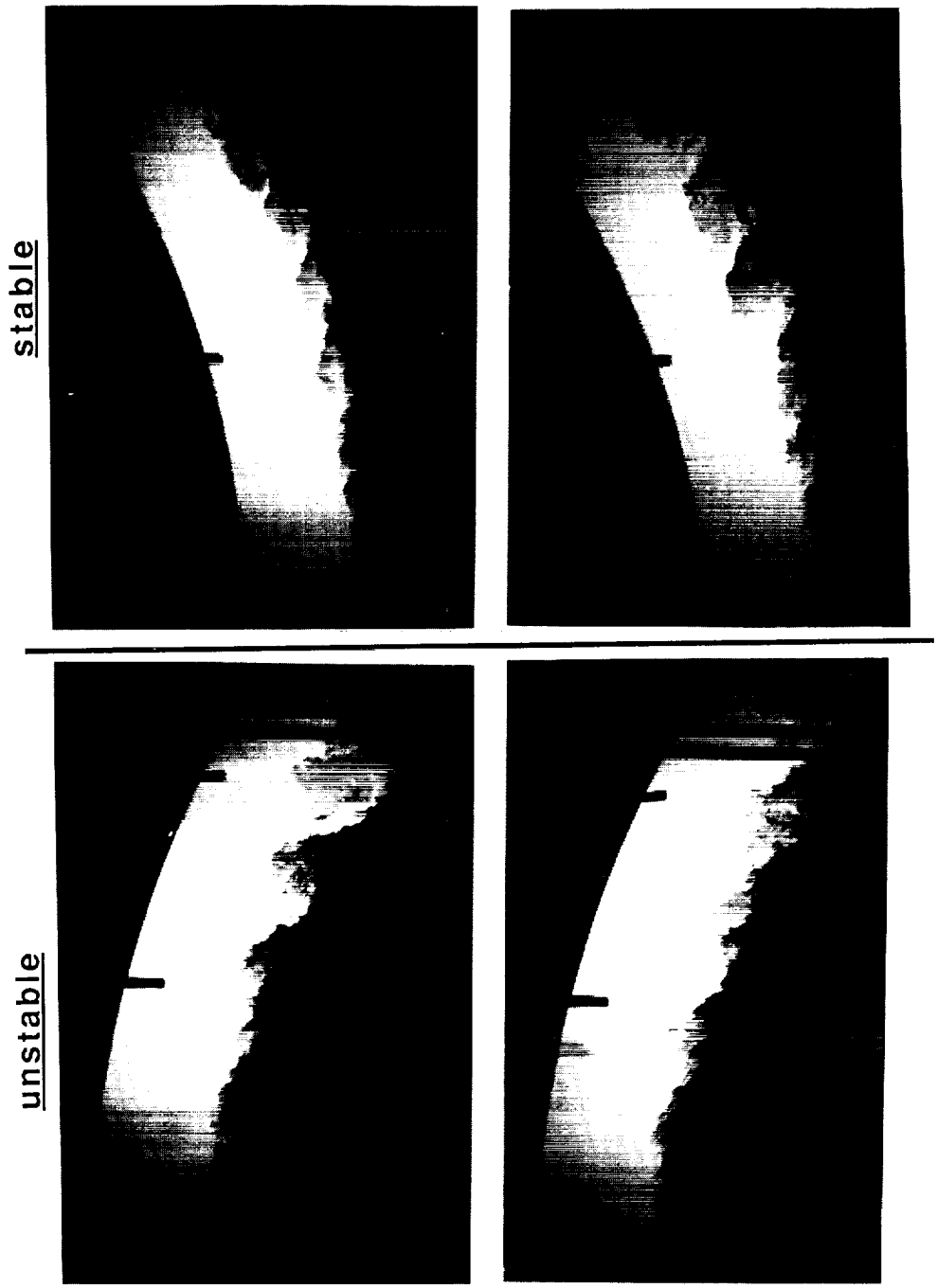

FIGURE 3. Side views of mixing layer, using PLIF. Time exp. 1/1000 sec.

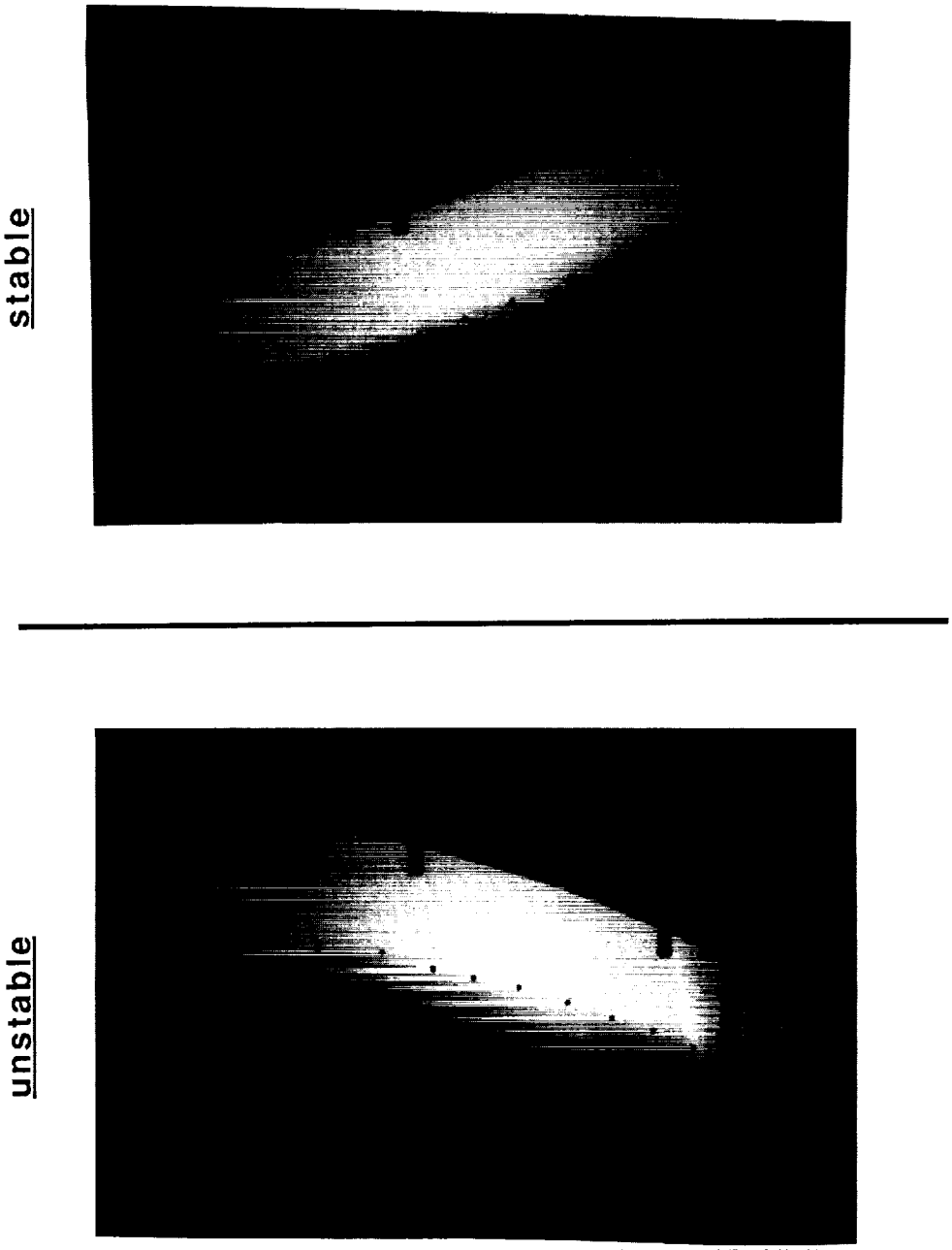

FIGURE 4. Time averaged side views of mixing layer, using PLIF. Time exp. 0.5 sec.

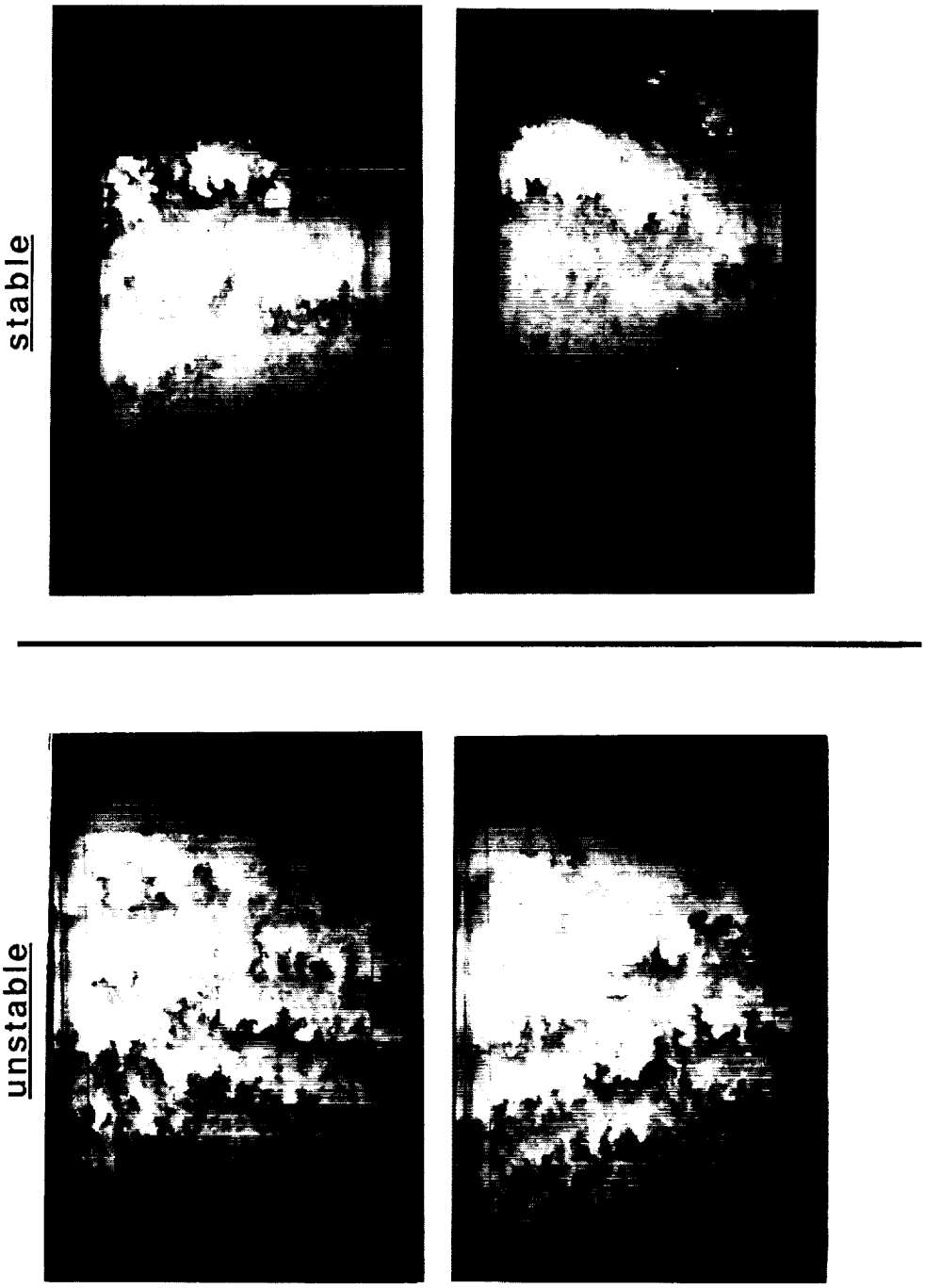

FIGURE 5. Plan views of mixing layer, using PLIF. Time exp. 1/1000 sec.

Similarly a plan view of K-H structures captured while pairing would not show any organization of motion.

4. Future work

The future work has two main objectives: i) Perform image reconstruction of the layer for both curved cases and for a straight case in order to compare the changes in the flow structures and ii) Perform detailed quantitative measurements of the concentration field.

The end view of the mixing layers will be used to get a $y - z - t$ space reconstruction of the flow field. This will be done by using the Pixar computer available at the High Temperature Gasdynamics Laboratory at Stanford University. Sequential digitized images will come from video recording of the flow. It is important that each frame consist of a truly instantaneous cut; therefore, a pulsed 20-Watt Copper-vapor laser will be used. The framing rate must also be sufficient to have sufficient cut planes through a structure. To this end, video framing rates will first be used, followed possibly by the higher framing rate of a Spin Physics recording system, should it be necessary. First reconstructions should occur in the Spring.

The final task is generating the concentration field pdf. For this, the imaging system will consist of a self-scanning linear array camera. The laser source will either be the Copper-vapor laser or the Argon-ion laser. The frame grabber in this case is not a trivial issue because of the extremely high framing rates needed to resolve the flow and the amount of data generated. At this point the hardware problem seems to be resolved and the various components' interfacing problems are being tackled. Once components are bought (computer, A/D board and optics), first results will occur within 3 to 6 months.

5. Summary

Instantaneous planar visualizations of high Reynolds number curved mixing layers were presented. These cuts revealed that the K-H structures are existent and well defined in the fully developed region. Additional views suggest that these structures may occur tilted with respect to the flow. More streakiness in the unstable case suggests a strong T-G instability. The growth rate was found to be about 50% larger for the unstable case. Image reconstruction of the flow field and detailed concentration measurements of the layer will constitute the bulk of our future work.

REFERENCES

BERNAL, L. P. 1981 The Coherent Structure of Turbulent Mixing Layers: I. Similarity of the Primary Vortex Structure. II. Secondary Streamwise Vortex Structure. Ph.D. Thesis, Caltech.

BROADWELL, J. E., & BREIDENTHAL, R. E. 1982 A Simple Model of Mixing and Chemical Reaction in a Turbulent Shear Layer. *J. Fluid Mech.* **125**, 397-410.

DIMOTAKIS, P. E., & BROWN, G. L. 1976 The Mixing Layer at High Reynolds Numbers: Large Structure Dynamics and Entrainment. *J. Fluid Mech.* **78**, 535-560.

JIMENEZ, J., COGOLLOS, M., & BERNAL, P. L. 1985 A Perspective view of the Plane Mixing Layer. *J. Fluid Mech.* **152**, 125-143.

KONRAD, J. H. 1976 An experimental investigation of mixing in two-dimensional turbulent shear flows with application to diffusion limited chemical reactions. Ph.D. Thesis, Caltech.

KOOCHESFAHANI, M. M. 1984 Experiments on Turbulent Mixing and Chemical Reaction in a Liquid Mixing Layer., Ph.D. Thesis, Caltech

PLESNIAK, M. W. & JOHNSTON, J. P. 1989 Reynolds stress evolution in curved two-stream turbulent mixing layers, Seventh Symp. on Turbulent Shear Flows, Stanford, August 1989.

VAN CRUYNINGEN, I., LOZANO, A., MUNGAL, M. G., & HANSON, R. K. 1989 3D Visualization of Temporal Flow Sequences, submitted to AIAA Journal.

WANG, C. 1984 The Effects of Curvature on Turbulent Mixing Layers, Ph.D. Thesis, Caltech.

An experimental investigation of a low Reynolds number turbulent boundary layer subject to an adverse pressure gradient

By J. H. Watmuff

The evolution of a low Re_θ turbulent boundary layer in an adverse pressure gradient (APG) is being studied for comparison with direct numerical simulations by Spalart. A short region of favorable pressure gradient (FPG) is applied first to establish a self-preserving layer with $Re_\theta \approx 600$, which is a suitable initial condition for the simulations. The APG is then applied rapidly such that $\beta \approx 2$ at $Re_\theta \approx 1500$. The streamwise extent of the measurements exceeds the current capabilities of direct simulations so that the results should also serve as a useful data base for Reynolds-averaged boundary layer prediction methods and in the future for direct simulation schemes as computer technology evolves.

1. Relationship between the experiment and CFD simulations

An important feature of the numerical method of Spalart (1988) is that there is no turbulence modelling. A high non-dimensional grid density is needed which restricts the simulations to low Reynolds numbers, i.e. $R_\theta < 1500$ at present. The key assumptions in Spalart's 1988 method are that the streamwise evolution of the flow is slow and that the straining of the turbulence by the mean-flow can be neglected. These assumptions will inevitably cause the method to breakdown in a large APG. Spalart has developed a new technique that should overcome these difficulties, and preliminary results are coming to hand. One of the objectives of this experiment is to obtain accurate measurements for comparison with the simulations.

There are three requirements in the relationship between the experiment and the simulation. Firstly, the Reynolds number must be matched precisely. Secondly, the experiment and simulation must have closely matched initial conditions. Following a suggestion by Inman and Bradshaw (1981), a mildly favorable pressure gradient is used to very closely approximate a self-preserving layer, i.e. by careful experimental design the boundary layer is maintained at almost constant thickness over some streamwise distance before being subjected to the APG. The FPG region allows the simulated layer and the experimental layer to approach each other without incurring a large increase in Re_θ which would reduce the streamwise extent of the simulations in the APG. In the experiment the additional development length has the added advantage of allowing upstream trip effects to decay before the region of interest. Finally, accurate experimental pressure coefficient (C_p) measurements with high spatial resolution are required

as an input for the simulation. A suitable flow configuration for the computations would be one in which the boundary layer experienced a non-dimensional pressure gradient $\beta = \frac{\delta^*}{\tau_w}\frac{dP}{dx} \approx 2$ at a maximum $R_\theta \approx 1500$. This design goal has been achieved.

2. Apparatus and methods

2.1. Tunnel and traverse

The layer develops on a 1m wide aluminium plate forming the test-section floor of a small open-return wind tunnel. The plate is supported above an optics table which also serves as an extremely flat and rigid mounting platform for a high-speed computer controlled 3D probe traverse. A flexible ceiling is contoured to produce the pressure distribution and two plexiglass sidewalls complete the test-section.

Selection of a transition device was performed in the absence of the PG. The incoming layers are laminar and closely follow the Blasius profile over an entrance velocity range from 6 to 12m/s. Various transition devices were tried, including 3D roughness, but a d=2.4mm wire located at X=0.15m was best, producing a "normal" turbulent boundary by X=0.35m. The Reynolds number per unit length based on the entrance velocity to the test section is 4.28×10^5 1/m giving a nominal entrance velocity of around 6.5 m/s. The Reynolds number was maintained constant to within $\pm 1\%$ during all measurements. The free-stream turbulence intensity in the test-section near the exit of the contraction is 0.25%.

The Y-axis (normal to the wall) of the traverse is carried by the (spanwise) Z-axis which is supported within the test-section by a gantry constructed of carbon-fiber composite. The Y- and Z- axes use linear stepping motors for positioning. Rubber strips are used to seal the gaps between the edges of the plate and the sidewalls. These gaps provide access for mounting the gantry to carriages underneath the plate. A brushless linear d.c. motor is attached to one of these carriages for positioning of the (streamwise) X-axis. The coordinate origin is on the wall at the centerline of the contraction exit. The size and repeatability of the measurement volume and the maximum traversing speeds are 2100 $\pm$ 0.1 mm at 2.0 m/s in the X-direction, 95 $\pm$ 0.05mm at 1m/s in the Y-direction and 500 $\pm$ 0.05mm at 1m/s in the Z-direction. These traversing speeds are sufficient for "flying hot-wire" measurements in regions of high turbulence intensity (see Watmuff, Perry and Chong 1983), but this capability has not been exploited yet.

2.2. Probes

Three round Pitot tubes with o.d. ranging from 1mm to 2mm are used to measure the mean velocity (U), and nine different Preston tubes with diameters ranging from 1.5mm to 7.9mm are used for skin friction coefficient (C_f) measurements.

Modified Dantec normal and cross-wire probes are used for the turbulence measurements. The distance between the prongs is reduced, and the prongs are stiffened with the addition of a small web. Platinum filaments 2.5 μm diameter and 0.5mm long are used. Perry, Lim, Henbest and Chong (1983) found substantial differences between profiles of $\overline{uv}$ measured in a rough-wall boundary layer where large turbulence intensities exist. The differences in $\overline{uv}$ were found to depend on the included angle between the cross-wire filaments and on whether the probe was stationary or "flying" upstream. The differences between the stationary and flying results were substantial only for conventional probes where the included angle is nominally 90°. Only small differences were observed when the included angle was increased to 120°. By tilting the probes in a uniform stream, Perry et al. found that a flow angle of 45° could be imposed on the probe with the 120° included angle without appreciable error, but that the probe with a 90° included angle started to show errors at flow angles as low as 20°.

Since relatively high turbulence intensities are also experienced in the APG region in this experiment, the included angle between the cross-wire filaments was increased to 110° which is about the maximum possible angle considering the probe geometry. Estimates of the Probability Density Function of the instantaneous flow angle (θ) relative to $\overline{V}$ have been measured at various positions in the layer and $\Pr[-20° < \theta < 20°] > 0.995$ in the most strongly turbulent regions. Thus, the errors described by Perry et al. should be small in this experiment.

Wall distances are set using the electrical contact of a needle with the test plate. This distance is calibrated by focussing a telescope on the filament and its image in the wall.

2.3. Methods

The small pressure differences in the test section (0.100 inches of water maximum) are measured using a high accuracy commercially available pressure transducer with an advertised accuracy of better than 0.001 inches of water and a range of 0.5 inches of water. The 44 static wall taps, pitot tube and reference total and static pressures are connected to the transducer *via* a 48 port Scanivalve under computer control. A pause of 5 seconds is used after the connection before reading the transducer, and all averages are obtained over at least 90 seconds.

The C_p variation is shown in figure 1, and it acts as a simple data base for inferring the local static wall pressure for all pressure probe measurements. The C_p data base was created by simply averaging the results of a number of runs performed several months apart. There is no discernible trend in the data taken at the different times. Averaging periods of up to 15 minutes were found to be necessary to achieve smooth data.

When the pressure probes are on the wall, the pressure difference between the probe and the local static pressure can be very small owing to the low velocities

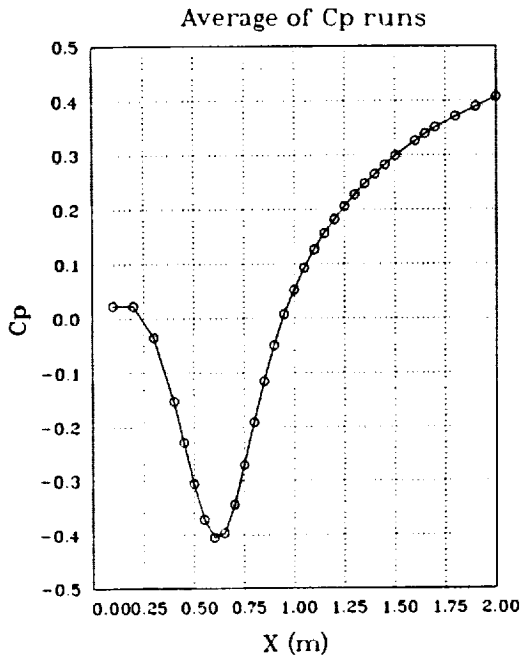

FIGURE 1. Variation of pressure coefficient C_p with X.

in the test-section. Further, the pressure difference is obtained by subtraction of two relatively large numbers. For the Preston tube C_f measurements, long time averaging periods were also necessary for smooth results.

Hot-wire probes must be calibrated frequently in a uniform stream. Using a conventional single-axis traversing system in this experiment would require the removal and reinstallation of fragile and expensive probes from the measurement region for the purpose of calibration. This would be time consuming and risk probe breakage. One advantage of the computer-controlled 3D traverse is that this operation occurs in a matter of seconds while minimizing the chances of probe damage. The system also acts as a shaker for imposing accurately known velocity perturbations on the cross-wire probes for calibration purposes.

A high-speed 15 bit Tustin A/D converter and a microVAX II computer are used for double-buffered data acquisition. A 32K hardware buffer is located between the Tustin and the computer and high speed DMA data transfers need only occur when the buffer is nearly full. While waiting for the new data the CPU is free to process data obtained during the previous data acquisition cycle using newly developed high-speed algorithms for reducing hot-wire data to Reynolds stresses, i.e. there is a high degree of parallelism between data acquisition and data processing. A system throughput of 25K/s for single wires and 10K/s for cross wires can be sustained indefinitely despite the fact that the calculations are performed in double-precision.

Total computer control of tunnel speed, probe traversal, and data acquisition allows all procedures to be automated. Sophisticated software enables long

duration experiments to be performed continuously over many days without manual intervention. This mode of operation required several significant new developments. For example, large and complex 3D measurement grids can be programmed and viewed ahead of time. Hot-wire calibration drift is monitored and new calibrations are performed (automatically) if the drift exceeds some tolerance. Other features that have proved vital for long duration unattended experimental runs include automatic error detection/recovery schemes and the provision of "emergency" asynchronous manually initiated software interrupts for hardware checkouts and to provide access to approximately 125 menu settable control variables.

Automation of the experiment allows massive quantities of data to be processed on-line over a relatively short period. Spatially dense mean-flow and Reynolds stress profiles are measured along the tunnel centerline at 50mm intervals from X=0.2m to X=2.0m, i.e. 37 profiles. The close spacing of the profiles is needed in the region of FPG to examine the recovery from upstream trip effects and the approach to self-similarity and in the region of APG where there is rapid growth with streamwise distance. The spacing of the profiles also provides a sensitive means for detecting anomalous data.

The greatest obstacle in obtaining high quality data has been hot-wire calibration drift caused by extremely large changes in ambient temperature. Variations of up to $40°F$ are typical over a 24 hour period while changes of up to $10°F$ have been observed over a period as short as 5 minutes. Automation of the experiment has provided a "brute force" solution to this frustrating problem, i.e. hot-wire profiles are repeated until the drift check obtained after measuring a profile is within a certain tolerance of a drift reference taken immediately after the wires have been calibrated. Setting the drift tolerance at 0.5% (larger tolerances introduce too much scatter in the data) has meant that on average a profile must be measured 5 times before it is acceptable. At the time of writing over 600 normal- and cross-wire profiles have been measured.

3. Results

3.1. Skin friction

The streamwise distribution of C_f at 37 streamwise locations along the tunnel centerline has been measured with 9 different diameter Preston tubes ranging in diameter from 1.5mm to 7.9mm In the FPG the larger diameter tubes protrude into the region where the mean flow deviates from the law of the wall. Downstream towards the end of the APG region the pressure difference ΔP between the smallest diameter probes and the local static pressure inferred from the C_p data base can be as small as 0.006 inches of water. Therefore, errors of 1% in the reference total head ($\approx$ 0.1 inches of water) or in the C_p data base lead to errors of $\approx$ 15% in ΔP. Consequently, the estimates from the 9 tubes have been averaged using the criteria that the nondimensional diameter $d^+ < 100$ and that

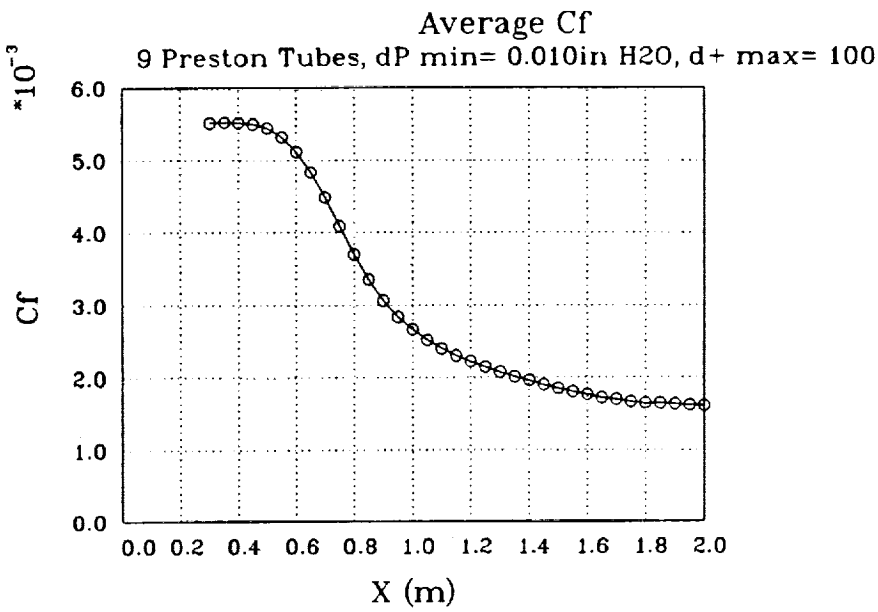

FIGURE 2. Skin friction coefficient C_f with X. Average of 9 different Preston tubes.

$\Delta P > 0.01$ inches of water. The averaged data are shown in figure 2. High values of $C_f (> 5.5 \times 10^{-3})$ are maintained in the FPG region. With application of the APG the C_f falls rapidly at first but for X>1.5m C_f approaches a constant value.

The accuracy of the C_f measurements needs to be considered since the pressure gradients in both the FPG and APG regions exceed the limits suggested by Patel (1965). Hirt and Thomann (1986) compared the wall shear stress τ_w measured directly with a floating element to values inferred from Preston tubes in axisymmetric boundary layers subject to sudden application and removal of adverse pressure gradients, i.e. the layers were far from equilibrium. Preston tube errors of up to 10% were observed. They found that the Preston tube readings indicated velocities below the law of the wall in decreasingly adverse pressure gradients. However, no parameters could be found to correlate the errors, so it is difficult to apply their results to this flow.

McDonald (1968) used empirical information combined with similarity arguments based on mixing length concepts to examine the effect of pressure gradient on the law of the wall. Deviations from the law of the wall were expressed as a function of a stress gradient $\alpha_0 = (\nu/\rho U_\tau^3) dP/dX$. In this experiment $-0.009 < \alpha_0 < 0.02$ and his results indicate that the deviations from the law of the wall may be as high as 8%. However, for a sink-flow the predictions indicate a negative deviation while the experiment of Jones and Launder (1972) and the numerical study by Spalart (1986) both indicate positive deviations from the law of the wall. Therefore, the accuracy of McDonald's predictions is questionable.

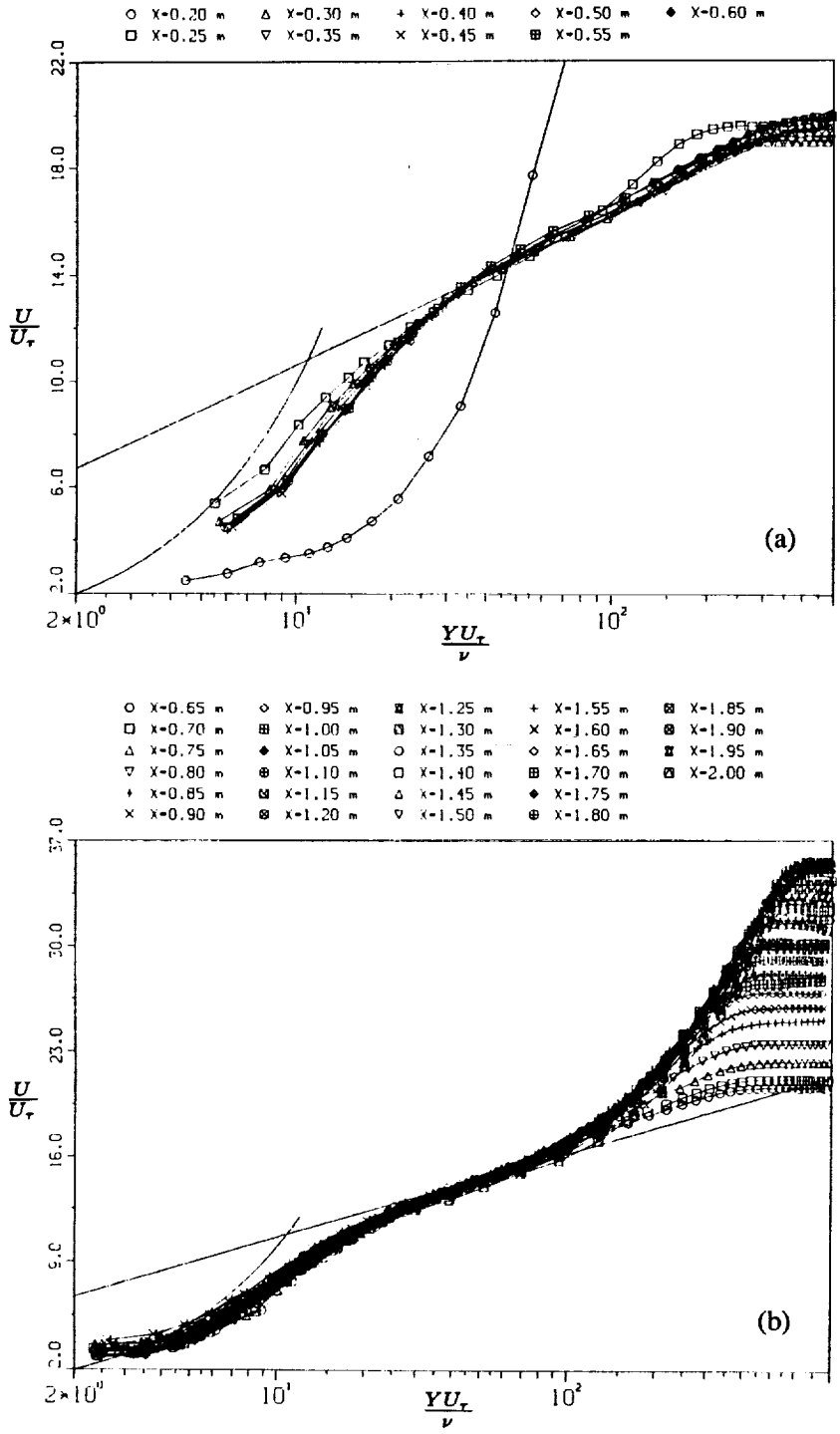

FIGURE 3. Mean velocity profiles with wall-scaling in (a) FPG region and (b) APG region. Hot-wire data.

In this experiment, the results from the 9 Preston tubes satisfying the averaging criteria described above cover the range $20 > d^+ > 100$ and the C_f estimates agree to within $\pm$ 3%. Moreover, the mean velocity profiles in the APG region shown in figure 3(b) (where $Y^+_{min} \approx 3$) fairly closely follow both the sublayer profile and the logarithmic law. The most significant anomalies appear in the FPG region, figure 3(a), where there are deviations from both the sublayer profile and the logarithmic law.

3.2. Mean velocity

It is well known that Pitot tubes suffer from wall proximity effects and a variety of correction schemes exist. However, it is uncertain which is the most appropriate for boundary layer data. Local static pressures have not been measured, and the Pitot tube data is reduced using the static pressure at the wall. The local static pressure throughout the layer could differ substantially from the wall static pressure owing to mean streamline curvature. Also, the Pitot tube mean flow data shows some scatter, especially in the near wall region, owing to the small pressure differences. For these reasons the normal hot-wire mean flow data are presented here.

The mean-velocity profiles in the FPG region are shown in figure 3(a). The first profile at X=0.2m (50mm downstream of the trip wire) is strongly contaminated by the trip. At X=0.25m the pressure gradient is small and the profile here has the appearance of a typical low Re_θ zero pressure gradient layer. Note the wake component. Also, this profile follows both the sublayer profile and the logarithmic law more closely than the other profiles. From X=0.3m onwards the profiles are essentially identical for about 20δ in the streamwise direction. The layer thicknesses $\delta \approx$ 12.0mm, $\delta^* \approx$ 1.75mm and $\theta \approx$ 1.2mm remain very nearly constant. At the end of the FPG the C_f is uniform to within $\pm 1\frac{1}{4}\%$ over a span of 40δ. These results provide strong evidence that the design goal of producing a highly 2D self-similar sink-like flow condition for compatibility with the initial conditions of Spalart's CFD simulations has been closely achieved. The small value of $Re_{\theta_{max}} = 650$ at the end of the FPG increases the size of the APG region which can be treated by the simulations.

Application of the APG increases the growth rate and the profiles become less full, resulting in large values of the strength of the wake component as shown in figure 3(b). The profiles appear to follow the law of the wall, but the region of logarithmic velocity variation remains small ($Y^+ < 100$). The layer thicknesses δ, δ^* and θ (not shown) increase almost linearly with streamwise distance and the profile shape factor H (not shown) is a weak indicator of the change. At the end of the region corresponding to Spalart's simulations (X=1m) $\delta \approx$ 28mm. The spanwise variation in C_f is within $\pm$3% over 12δ, and the momentum balance is within 5%. These results indicate that the layer is acceptably two-dimensional. The flow will provide an excellent test case for Spalart's new method since at X=1m, $Re_\theta \approx 1500$ and $\beta = \frac{\delta^*}{\tau_w}\frac{dP}{dx} \approx 2$.

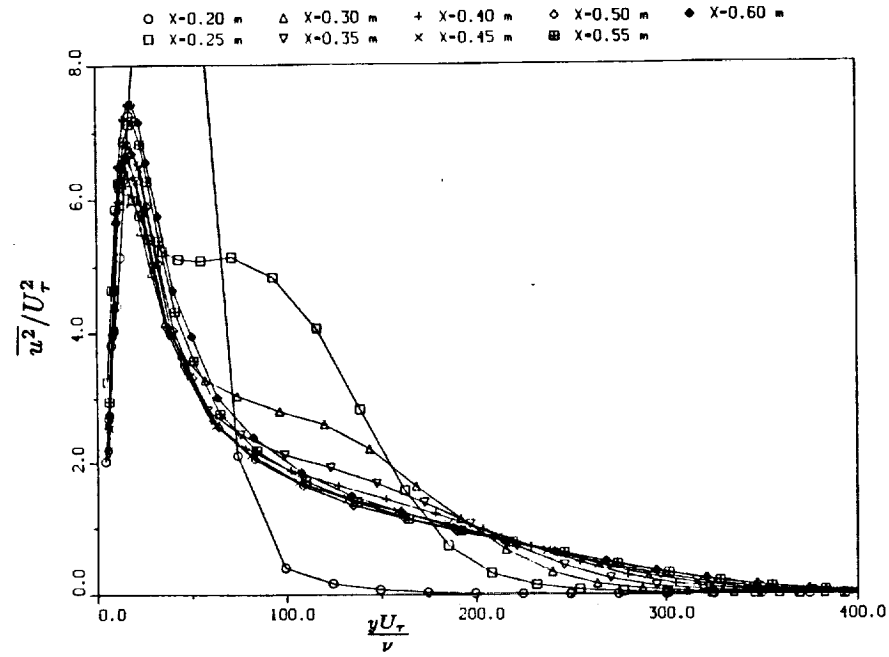

FIGURE 4. Streamwise development of $\overline{u^2}/U_\tau^2$ in the FPG region with wall scaling.

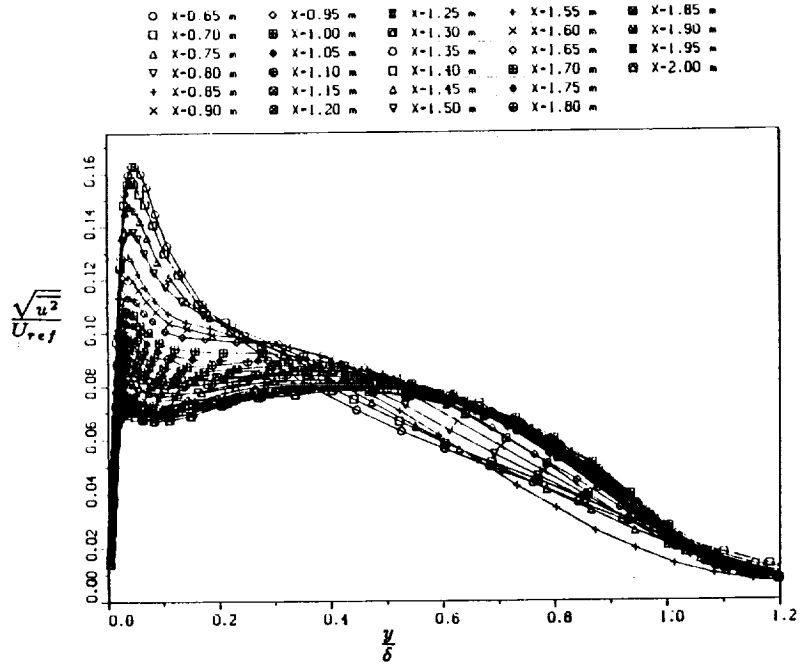

FIGURE 5. Streamwise development of $\frac{\sqrt{u^2}}{U_{ref}}$ against $\frac{Y}{\delta}$.

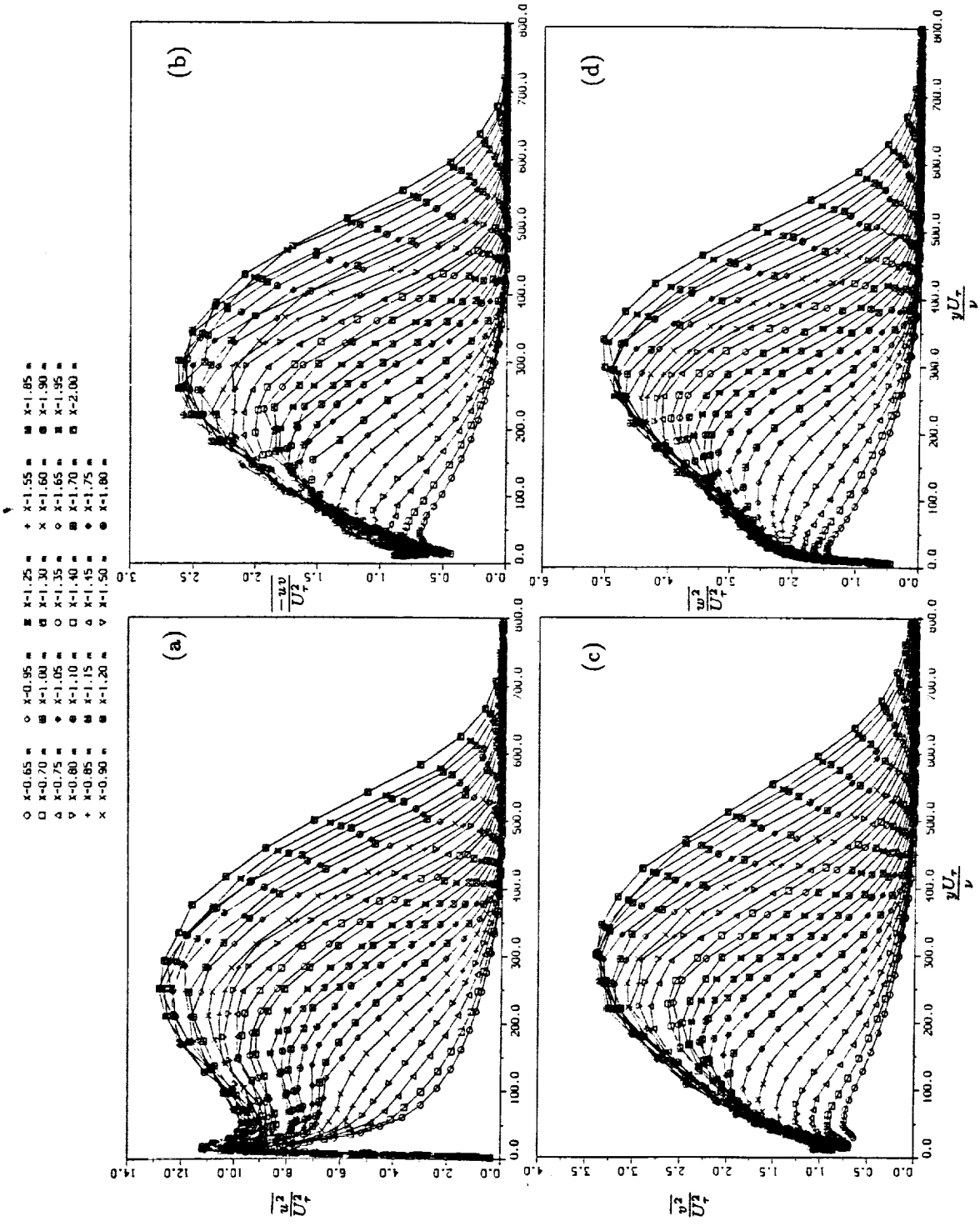

FIGURE 6. Streamwise development of Reynolds stresses in APG region in wall coordinates. (a) $\frac{\overline{u^2}}{U_\tau^2}$ (b) $\frac{\overline{-uv}}{U_\tau^2}$ (c) $\frac{\overline{v^2}}{U_\tau^2}$ (d) $\frac{\overline{w^2}}{U_\tau^2}$

Further downstream, in the region beyond the current capabilities of direct CFD simulations, there is evidence to suggest that the layer finally reaches a new self-preserving condition. Near the wall, the data follow the law of the wall, and in the outer region profiles of the velocity defect collapse. β approaches a constant value which is a necessary condition for self-preserving layers. Also, the strength of the wake component asymptotes to a constant value of around 14. Unfortunately, the two-dimensionality of the mean-flow is poorer in this region since the spanwise variation in C_f increases to $\pm 6\%$ and the momentum imbalance rises to about 9%.

3.3. Reynolds stress

The normal hot-wire measurements in the FPG region shown in figure 4 indicate that the trip effects decay rapidly in the near wall and outer regions but that a longer development length is required for recovery in the central region of the layer. However, the profiles have a marked similarity over the last 20δ of the FPG region. The same behaviour is observed for the cross-wire data $\frac{\overline{-uv}}{U_\tau^2}$, $\frac{\overline{v^2}}{U_\tau^2}$ and $\frac{\overline{w^2}}{U_\tau^2}$ but these results are not shown here. The observations provide further evidence that the layer is in a state of equilibrium before application of the APG.

Profiles of turbulence quantities in the APG region are shown with wall scaling in figures 6(a) to (d). The close spacing of the profiles provides a sensitive means of detecting inconsistencies in the data (assuming that the profiles should develop smoothly and monotonically with X). Large values of all the fluctuating quantities emerge in the central region of the layer with increasing streamwise distance. Note that $\frac{\overline{u^2}}{U_\tau^2}$ in the central region of the layer is larger than the peak value near the wall for $x > 1.5$m, in sharp contrast with channel flow and zero PG boundary layers.

Profiles of $\frac{\sqrt{\overline{u^2}}}{U_{ref}}$ are plotted against Y/δ in figure 5. Note that in the outer half of the layer the profiles are essentially identical for X > 1.1m. Similar observations apply for cross-wire data but these are not shown. It appears that the turbulent fluid in the outer region of the layer is convecting downstream almost without change. The peak values of the Reynolds stresses possess a locus which is linear with X, being inclined to the wall. The locus of maximum $\frac{\sqrt{\overline{u^2}}}{U_{ref}}$ can be clearly seen in the contour plot shown in figure 7(a). Contours of $\frac{\overline{u^2}}{U_\tau^2}$ are shown in figure 7(b). The disparity between the two sets of contours illustrates that the relationship between the turbulence structure at the wall and the outer flow varies widely in response to the pressure gradient. This is one of the most interesting aspects of this boundary layer.

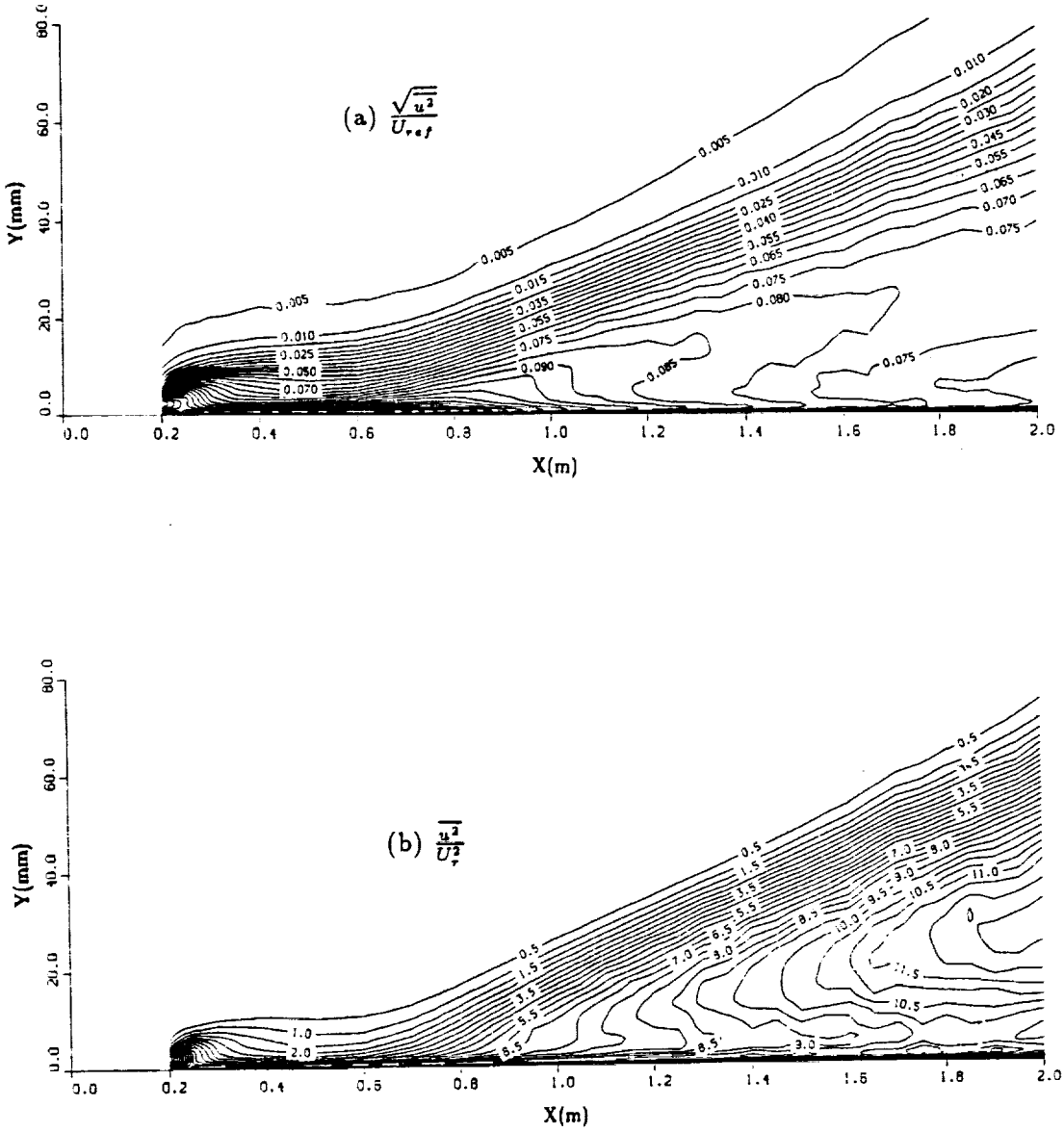

FIGURE 7. Contours of (a) $\frac{\sqrt{u^2}}{U_{ref}}$, and (b) $\frac{\overline{u^2}}{U_\tau^2}$, throughout entire layer.

REFERENCES

HIRT, F. & THOMANN, H. 1986 Measurement of wall shear stress in turbulent boundary layers subject to strong pressure gradients. *J. Fluid Mech.* **171**, 547- 562.

INMAN, P. N. & BRADSHAW, P. 1965 Mixing length in low Reynolds number turbulent boundary layers. *AIAA J. Vol. 19, No. 5.* 653-655.

JONES, W. P. & LAUNDER B. E. 1972 Some properties of sink-flow turbulent boundary layers. *J. Fluid Mech.* **56**, 337-351.

MCDONALD, H. 1968 The effect of pressure gradient on the law of the wall in turbulent flow. *J. Fluid Mech.* **35**, 311-336.

PATEL, V. C. 1965 Calibration of Preston tube and limitations of its use in pressure gradients. *J. Fluid Mech.* **23**, 185-208.

PERRY A. E., LIM K. L., HENBEST S. M. & CHONG M. S. 1983 Rough- and smooth-walled shear flows. Fourth Symposium on Turbulent Shear Flows, Karlsruhe, F. R. G.

SPALART, P. R 1986 Numerical study of sink-flow boundary layers. *J. Fluid Mech.* **172**, 307-328.

SPALART, P. R. 1988 Direct simulation of a turbulent boundary layer up to Re_θ=1410. *J. Fluid Mech.* **187**, 61-98.

WATMUFF, J. H., PERRY, A. E. & CHONG, M. S. 1983 A Flying Hot-Wire System. *Experiments in Fluids.* Vol. 1. 1983.

An experimental study of the effects of rapid rotation on turbulence

By S. V. Veeravalli

1. Introduction

Experiments (Traugott, 1958, Wigeland & Nagib, 1978 and Jacquin et al., 1988), large eddy simulations (Bardina et al., 1985) and direct numerical simulations (Bardina et al., 1985 and Speziale et al., 1987) all show that rapid rotation (i.e. the rotation time scale $(1/\Omega)$ << the turbulence time scale) has a striking effect on homogeneous nearly isotropic turbulence. The cascade process is effectively inhibited by rotation, and thus dissipation is greatly reduced. Some attempts have been made to incorporate this effect in turbulence models (Bardina et al., 1985 and Speziale et al., 1987). Numerical simulations further showed the somewhat surprising result that anisotropic homogeneous turbulence subjected to rotation tended towards an isotropic state; however, the residual anisotropy was not zero. Reynolds (1989) performed a detailed analysis using Rapid Distortion Theory (RDT) and showed that a reduction in the anisotropy is indeed expected and if the anisotropy is produced by irrotational strain then the anisotropy tensor b_{ij} is asymptotically driven to half its initial value.

Our objective is to extend the work of the experiments mentioned above to lower turbulent Rossby numbers ($R_{o\lambda} \equiv (\frac{1}{3}q^2)^{\frac{1}{2}}/(\lambda\Omega) \approx 0.07$ to match those used in the numerical simulations — λ is the Taylor microscale and q^2 is twice the turbulent kinetic energy) and to confirm some of the results obtained by Reynolds (1989) for anisotropic turbulence.

2. Previous work

Experimental studies of rotating turbulence can be broadly classified into two groups: *a*) rotating tank experiments and *b*) wind tunnel experiments.

The work of Ibbetson & Tritton (1975) and Hopfinger et al. (1982) belong to category *a* . Ibbetson & Tritton dropped a grid into a rotating tank and found that the turbulence behind the grid decayed much faster in the presence of rotation. Hopfinger et al. (1982) used a shaking grid to generate turbulence and found that away from the grid the flow exhibited a strong tendency towards 2-dimensionality and essentially consisted of columnar vortices aligned with the axis of rotation.

Traugott (1958), Wigeland & Nagib (1978) and Jacquin et al. (1988), on the other hand, imposed solid body rotation on grid turbulence in a wind tunnel and thus these experiments approximate homogeneous turbulence better. The smallest value of $R_{o\lambda}$ achieved in the Wigeland & Nagib (1978) experiment

was approximately 0.4 while Jacquin et al. (1988) obtained a value of 0.3. These experiments showed that the mildly anisotropic grid turbulence tended towards isotropy and that the kinetic energy decay was greatly reduced due to an inhibition of the cascade process. The flows did not exhibit a strong tendency towards 2-dimensionality; however, the length scales along the axis of rotation grew at a much faster rate compared to the non-rotating case and showed departures from the behaviour expected in isotropic flow (the direct numerical simulation results of Bardina et al., 1985 show a similar behaviour for the length scales).

Large eddy simulations and direct numerical simulations (Bardina et al., 1985 and Speziale et al., 1987) also showed the dramatic suppression of the spectral transfer term observed in experiments. In particular, Speziale et al. (1987) found that the development of the energy spectrum $E(\underline{\kappa}, t)$ agreed extremely well with,

$$E(\underline{\kappa}, t) = E(\underline{\kappa}, t_o)\, exp[-2\nu\kappa^2(t - t_o)] \tag{1}$$

which is what is expected for purely viscous decay with the spectral transfer term equal to zero. (ν is the kinematic viscosity, $\underline{\kappa}$ the wave number vector and the development is for $t > t_o$.) Speziale et al. (1987) also showed that homogeneous (unbounded) turbulence does not undergo Taylor-Proudman reorganization — the analysis is outlined below. The results of Reynolds (1989) are also summarized below.

3. Theory

In the equations to follow, the mean velocity is constant, $\underline{u}$, represents the instantaneous velocity, $\underline{\Omega}$ the rotation vector, p the instantaneous pressure, and ρ the density. The Navier-Stokes equations in a frame rotating with the mean rotation $\underline{\Omega}$ and moving with the mean speed are,

$$\frac{\partial u_i}{\partial t} + \frac{\partial u_i u_j}{\partial x_j} = -\frac{1}{\rho}\frac{\partial p}{\partial x_i} - 2\epsilon_{ijk}\Omega_j u_k + \nu\frac{\partial^2 u_i}{\partial x_j \partial x_j} \tag{2a}$$

(the centrifugal acceleration term has been included in the pressure) and the continuity equation is

$$\frac{\partial u_i}{\partial x_i} = 0. \tag{2b}$$

If the Rossby number $\epsilon/(\Omega q^2)$ is $<< 1$ (where $\Omega = |\underline{\Omega}|$) and the Ekman number $\nu/(\Omega L^2)$ is also $<< 1$ (where L is a typical length scale) and the flow is nearly steady, then we have,

$$\frac{\partial p}{\partial x_i} = -2\epsilon_{ijk}\Omega_j u_k \tag{3}$$

The curl of equation (3) then yields the Taylor-Proudman theorem

$$\Omega_j \frac{\partial u_k}{\partial x_j} = 0, \tag{4}$$

indicating that velocity gradients along the axis of rotation are suppressed.

However, for unbounded flows, the inviscid linearized equations (RDT equations),

$$\frac{\partial u_i}{\partial t} = -\frac{1}{\rho}\frac{\partial p}{\partial x_i} - 2\epsilon_{ijk}\Omega_j u_k, \tag{5}$$

admit travelling wave solutions of the form (Greenspan, 1968 and Phillips, 1963),

$$u_i = A_i \, exp[i(\underline{\kappa} \cdot \underline{x} - \alpha(\underline{\kappa})\,\Omega\, t)]. \tag{6}$$

Thus,

$$\frac{\partial u_i}{\partial t} = -\alpha(\underline{\kappa})\,\Omega\, A_i \, exp[i(\underline{\kappa} \cdot \underline{x} - \alpha(\underline{\kappa})\,\Omega\, t)]. \tag{7}$$

And hence (Speziale et al., 1987),

$$\left|\frac{\partial u_i}{\partial t}\right| \Big/ |\epsilon_{ijk}\Omega_j u_k| = O(1) \tag{8}$$

always. Hence, equation (3) is not applicable and no Taylor-Proudman reorganization occurs for homogeneous turbulent flows undergoing rapid rotation. Equation (7) indicates that the time scale of the velocity fluctuations is $O(1/\Omega)$; however, the non-linear term in equation (2a) is still negligible as $\epsilon/(\Omega q^2)$ is $<< 1$.

Reynolds (1989) showed, using the inviscid RDT equations (5), that for isotropic homogeneous turbulence, the spectrum tensor $E_{ij}(\underline{\kappa})$ is unchanged under rotation. He also studied the effect of rotation on anisotropic turbulence by defining the following 'structure' tensor,

$$Y_{ij} \equiv \int \frac{\kappa_i \kappa_j}{\kappa_n \kappa_n} E_{mm}(\underline{\kappa}) d\underline{\kappa}, \tag{9a}$$

with the corresponding anisotropy 'structure' tensor

$$y_{ij} \equiv \frac{Y_{ij} - q^2\delta_{ij}/3}{q^2}. \tag{9b}$$

(Note that if the turbulence is independent of x_1 then $Y_{11} = 0$ and $y_{11} = -\frac{1}{3}$.) It can then be shown (Reynolds, 1989) that Y_{ij} and consequently y_{ij} is unaffected by rotation. Further,

$$b_{ij} \to -\frac{y_{ij}}{2} \;\; as \;\; t \to \infty. \tag{10}$$

Reynolds (1989) also showed that 2-D 1-C (two-dimensional one-component) turbulence and 2-D 2-C turbulence tended to 2-D 3-C turbulence with the asymptotic state given by equation (10).

The turbulence generated in the laboratory is necessarily bounded and not strictly homogeneous due to the presence of the tunnel walls. It is unclear whether relations (8) and (10) would be strictly valid in such a case. If the turbulence does tend towards 2-dimensionality, then there are two regimes of interest:

$$\text{a)} \qquad \frac{\epsilon}{\Omega q^2} << 1 \text{ but } R_{o\eta} \equiv \frac{v}{\Omega \eta} > 1$$

where η and v are the Kolmogorov length and velocity scales respectively and

$$\text{b)} \qquad \frac{\epsilon}{\Omega q^2} << 1 \text{ and } \frac{v}{\Omega \eta} << 1.$$

(Jacquin et al., (1988) observed that when $v/(\Omega\eta) = O(1)$, then the turbulence decay rate changes sharply from $q^2 \sim x^{-1.3}$ to $q^2 \sim x^{-1}$, indicating that a third regime could exist between 'a' and 'b'.) If the dissipation scales do become axisymmetric for very small $R_{o\eta}$, then one would expect different decay rates for the axial and transverse velocity components (Batchelor, 1946) and the turbulence could then become anisotropic.

4. Experiments

The experiments will be carried out in three stages. Preliminary measurements will be done in a 15.2 cm diameter tunnel operated at a maximum speed of 10 m/s and capable of rotation rates up to 200 rad/s. The second series of experiments would be conducted in a 76 cm diameter facility capable of a peak speed of 30 m/s and a peak rotation rate of 80 rad/s. Finally, the 76 cm facility would be placed in a pressure vessel and operated at a pressure of approximately 16 atmospheres (and at approximately 8 m/s) in order to significantly increase the turbulent Reynolds number.

The design of the 15.2 cm rotating rig is complete and a schematic diagram is shown in Figure 1. The design is similar to the one used by Wigeland & Nagib (1978). The flow is provided by a centrifugal blower; it is then passed through a settling chamber and a contraction before entering the rotating section. The rotating section consists of a honeycomb of sufficient pressure drop to induce solid body rotation in the flow and a turbulence generating grid. The rotating turbulent flow is then studied in the stationary test section. The in-house constant temperature anemometers (Microscale HWM-100) were thoroughly tested and were found to be adequate for the initial measurements. The software necessary for data acquisition and analysis is being developed. A calibration set-up for x-wires will be fabricated. We are also currently working on the design of the larger (76 cm) facility.

The types of the experiments and the measurements of interest are described below.

Detailed measurements of decaying nearly isotropic grid generated turbulence will be made in the rotating rig and compared with the non-rotating case. The quantities of interest would be the Reynolds stresses, dissipation rates and length scales. Two point correlation functions $R_{\alpha\alpha}(r,0,0)$ and $R_{\alpha\alpha}(0,r,0)$, (no sum on α) could be measured to compare the growth rates of the length scales obtained from axial and transverse separations (the axis of rotation has been assumed to be along x, see figure 1) — none of the previous measurements shows a comparison of the type; $R_{33}(r,0,0)$ vs. $R_{33}(0,r,0)$. In addition the spectral transfer term could be measured, both directly and from the decay of the energy spectrum (c.f. Yeh & Van Atta, 1973).

The Rossby number used in the numerical simulations ($R_{o\lambda} \approx 0.07$) was chosen as the principal design parameter for the 15.2 cm facility; however, it should be capable of operating in regime 'b' discussed above. The expression for $R_{o\eta}$ when $q^2 \approx AU^2(x/M)^{-1}$ is given by

$$R_{o\eta} = \frac{(\frac{1}{2}A)^{\frac{1}{2}} M^{\frac{1}{2}} U^{\frac{3}{2}}}{2\nu^{\frac{1}{2}} \Omega x}. \tag{11}$$

(Here, M is the mesh size, U is the mean axial velocity and x is the downstream distance). Thus, with a judicious choice of M, U, Ω it should be possible to obtain $R_{o\eta} \approx 0.2$ within the test section (approximately 0.75 m long). (Note that one can't simply increase Ω to decrease $R_{o\eta}$ because when $\Omega/(RU) \approx 1$, where R is the radius of the tunnel, the vortex exiting the tunnel could breakdown (Dellenback et al., 1988), creating disturbances in the test section.)

A second set of experiments will be conducted to study the effect of rotation on anisotropic turbulence. It would not be possible to verify all the results presented in Reynolds (1989), especially those pertaining to 1C and 2C turbulence, in the laboratory; however, one could examine the validity of equation (10). The intensity of the axial velocity fluctuations could be reduced with respect to the transverse components by passing the flow through a contraction and the behaviour of b_{ij} downstream of the contraction could be studied. Additionally, a small difference in the intensities of the transverse fluctuations could be introduced by using a parallel bar array instead of a bi-planar grid to generate the turbulence (Veeravalli & Warhaft, 1989).

Finally, it would interesting to study the dispersion of a passive scalar in this flow with a view to examining the difference in mixing rates along the axis and in the transverse plane.

REFERENCES

BATCHELOR, G. K. 1946 The theory of axisymmetric turbulence. *Proc. Roy. Soc. London.* **186A**, 480-502

BARDINA, J., FERZIGER, J. H. & ROGALLO, R. S. 1985 Effect of rotation on isotropic turbulence: computation and modeling. *J. Fluid Mech.* **154,** 321-336

DELLENBACK, P. A., METZGER, D. E. & NEITZEL, G. P. 1988 Measurements in turbulent swirling flow through an abrupt axisymmetric expansion. *AIAA Journal.* **26,** No.6, 669-681

GREENSPAN, H. P. 1968 *The theory of rotating fluids.* Cambridge University Press.

HOPFINGER, E. J., BROWAND, F. K. & GAGNE, Y. 1982 Turbulence and waves in a rotating tank. *J. Fluid Mech..* **125,** 505-534

IBBETSON, A. & TRITTON, D. J. 1975 Experiments on turbulence in a rotating fluid. *J. Fluid Mech..* **68,** 639-672

JACQUIN, L., LEUCHTER, O. & GEFFROY, P. 1988 Experimental study of homogeneous turbulence in the presence of rotation. *Turbulent Shear Flows 6,* ed. by L.T.S. Bradbury et al., 46-57

PHILLIPS, O. M. 1963 Energy transfer in rotating fluids by reflection of inertial waves. *Phys. of Fluids.* **6,** 513-520

REYNOLDS, W. C. 1989 Effects of rotation on homogeneous turbulence. Proc. 10th Australian Fluid Mech. Conf., University of Melbourne, Dec. 11- 15

SPEZIALE, C. G., MANSOUR, N. N. & ROGALLO, R. S. 1987 Decay of turbulence in a rapidly rotating frame. In *Studying Turbulence Using Numerical Simulation Databases.* Proc. 1987 Summer Program, Center for Turbulence Research, Stanford U., Report CTR-S87, 205-212

TRAUGOTT, S. C. 1958 Influence of solid-body rotation on screen-produced turbulence. ACA Tech. Note 4135

VEERAVALLI, S. V. & WARHAFT, Z. 1989 The shearless turbulence mixing layer. *J. Fluid Mech.* **207,** 191-229

WIGELAND, R. A. & NAGIB, H. M. 1978 Grid-generated Turbulence with and without rotation about the streamwise direction. IIT Fluids and Heat Transfer Rep.. **R78-1,** Illinois Inst. of Tech., Chicago, Illinois

YEH, T. T. & VAN ATTA, C. W. 1973 Spectral transfer of scalar and velocity fields in heated-grid turbulence. *J. Fluid Mech..* **58,** 233-261

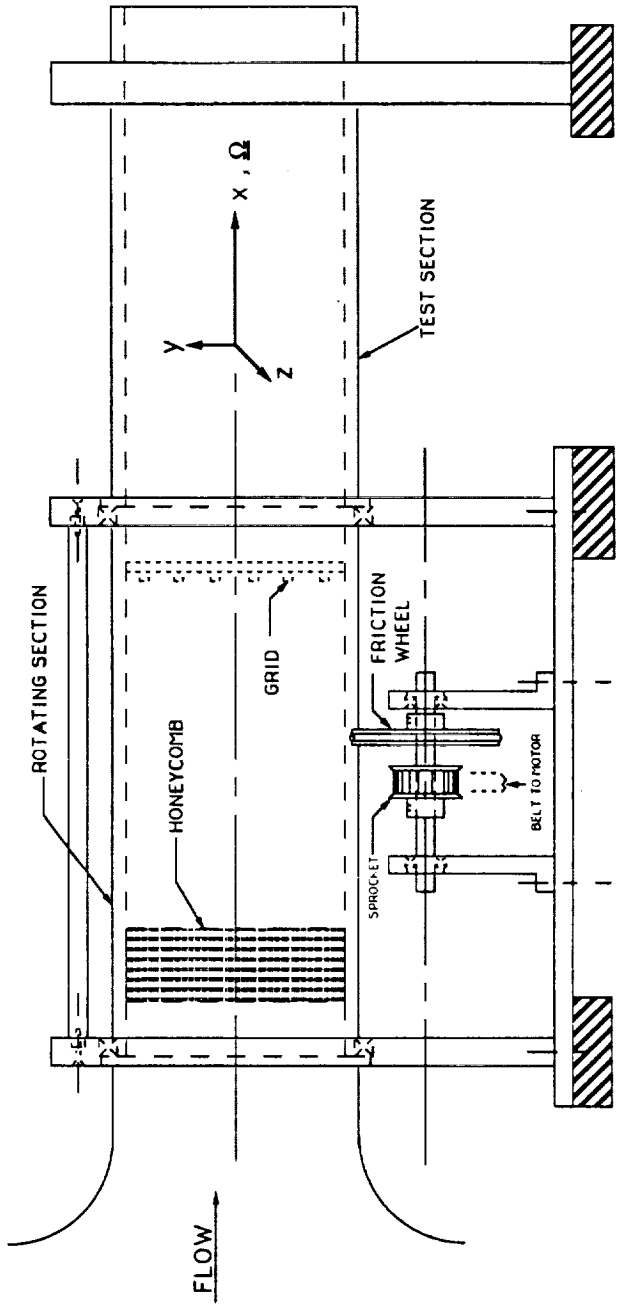

FIGURE 1. Schematic diagram of the Rotating Flow Rig.

An experimental study of secondary vortex structure in mixing layers

By J. H. Bell

1. Introduction

This report covers the first eight months of an experimental research project on the secondary vortex structure in plane mixing layers. The aim of the project is to obtain quantitative data on the behavior of the secondary structure in a turbulent mixing layer at reasonable Reynolds numbers ($Re_{\delta_\omega} \sim 50{,}000$. In particular, we hope to resolve the questions of how the scale of the secondary vortex structure changes with the scale of the mixing layer, and whether the structures are fixed in space, or whether they "meander" in the spanwise direction. Co-investigator for this project is Rabi Mehta, a JIAA research associate.

2. Background

It is well known that the development of plane mixing layers is largely influenced by the formation and interaction of large-scale spanwise vortices (Brown & Roshko 1974). Many of the earlier studies which first determined the important role played by the spanwise vortices also showed the existence of a second organized and persistent vortex structure in the mixing layer. Initial experiments showed that this vortex structure was oriented mostly in the *streamwise* direction, and suggested that its appearance might be related to the appearance of small scales within the flow (Konrad 1977, Breidenthal 1981).

A fairly clear picture of the streamwise vortex structure was produced by subsequent flow visualization experiments (Bernal 1981, Jimenez *et al.* 1985, Lasheras *et al.* 1986, Bernal & Roshko 1986, and Lasheras & Choi 1988), and this is described below. The structure is sketched in figure 1, which is taken from Lasheras *et al.* (1986). It appears that the streamwise vortex structure arises in the braid region of the mixing layer, between the spanwise structures. Residual spanwise vorticity in this region is stretched by the strain field produced by the spanwise structures. The extensional principle axis of the strain field is along a line perpendicular to the spanwise direction and is oriented at an angle to the streamwise direction. The result is the formation of a vortex tube which winds back and forth between adjacent spanwise rollers. When viewed from above, this structure appears to be a row of alternating-sign streamwise vortices embedded in the mixing layer. This picture of the structure has been confirmed by the results of numerical simulations using both the Biot-Savart law (Ashurst & Meiberg, 1988) and the direct Navier-Stokes method (Metcalfe *et al.* 1987).

Despite these results, many features of the streamwise vortex structure are not well understood. This is mostly due to a lack of quantitative information

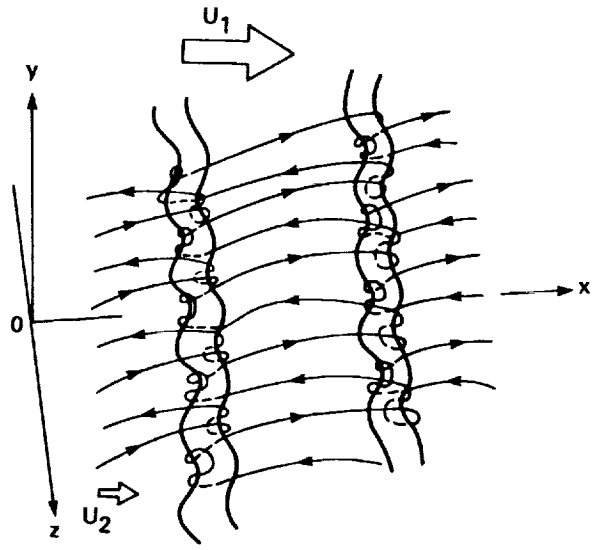

FIGURE 1. Sketch of vortex structure in mixing layers. Thick lines outline the spanwise structures, and the thin lines looping between them represent the streamwise vortex structure. (Taken from Lasheras *et al.* 1986.)

on the development of this structure, which in the past has usually been studied through flow-visualization. Fortunately, the streamwise vortex structure is sufficiently stable that it shows up in the mean flow and can be examined through measurements of mean streamwise vorticity in the mixing layer. This approach was used by the authors in a recent study, which investigated the presence and role of "naturally occurring" streamwise structures in a mixing layer (Bell & Mehta 1989a). A plane, two-stream mixing layer was generated, with a fixed velocity ratio of 0.6 and both initial boundary layers laminar and nominally two-dimensional. Measurements indicated that small spanwise disturbances in the upstream boundary layer on the high speed side of the splitter plate were amplified prior to the roll-up of the spanwise vortex sheet. Actual streamwise vortices were first observed slightly farther downstream, prior to the estimated location of the spanwise vortex roll-up. The streamwise vortices first appeared in widely spaced clusters of 3-4 vortices of both signs, but further downstream, the vortices re-organized to form counter-rotating pairs. The spacing between individual streamwise vortices was found to grow in a stepwise fashion as the mixing layer developed, with the location of the steps corresponding to the estimated locations of pairing of the spanwise vortices. Overall, the streamwise vortex structure scaled approximately with the mixing layer vorticity thickness. The streamwise vortex structures appeared to weaken with streamwise distance, with

the maximum mean vorticity diffusing as approximately $1/X^{1.5}$. The streamwise vorticity was found to be strongly correlated in position, strength, and scale with the secondary shear stress ($\overline{u'w'}$). The $\overline{u'w'}$ data suggested that the streamwise structures persisted through to the self-similar region, although they were very weak by this point and the mixing layer appeared to be nominally two-dimensional.

The present study is an extension of Bell & Mehta (1989a), using more sophisticated instrumentation to examine the role of the streamwise vortex structure in mixing layer development. One particularly interesting question raised by the experimental results relates to the observed decay of the mean streamwise vortex strength with X. This finding is in conflict with the results of direct Navier-Stokes simulations, which show no sign of streamwise vorticity decay (Rogers & Moser 1989). It has been suggested that the discrepancy occurs because the vortices tend to wiggle, or "meander" from side to side in the spanwise direction with increasingly greater amplitude as the flow moves downstream. The increasing amplitude of the meander would presumably reflect the transition of the mixing layer to an increasing turbulent state as the local Reynolds number increased. Once the amplitude of the meander became greater than the spacing between adjacent vortices, the structure would essentially average itself out of the mean flow. However, the streamwise vortex structure should still be detectable by more sophisticated means, such as spatial or temporal correlations. In the present study, it is proposed to apply these techniques to examine the behavior of the secondary vortex structure.

3. Experimental apparatus and techniques

3.1. Pre-existing experimental apparatus

The *Mixing Layer Wind Tunnel* located in the Fluid Mechanics Laboratory at the NASA Ames Research Center was used for all of the work described in this progress report (Fig. 2). The wind tunnel consists of two separate legs which are driven individually by centrifugal blowers connected to variable speed motors. The two blower/motor combinations are sized such that one has three times the flow capacity of the other, although the components downstream of the wide-angle diffusers are identical on the two legs. The two streams are allowed to merge at the sharp edge of the tapered splitter plate. The included angle at the splitter plate edge, which extends 15 cm into the test section, is about 1°, and the edge thickness is approximately 0.25 mm. The test section is 36 cm in the cross-stream direction, 91 cm in the spanwise direction and 366 cm in length. One side-wall is slotted for probe access and flexible for pressure gradient control.

The free-stream velocities within the test section are typically found to remain constant to within 1% of the set value. The measured streamwise turbulence level (u'/U_e) is about 0.15% and the transverse levels (v'/U_e and w'/U_e) are

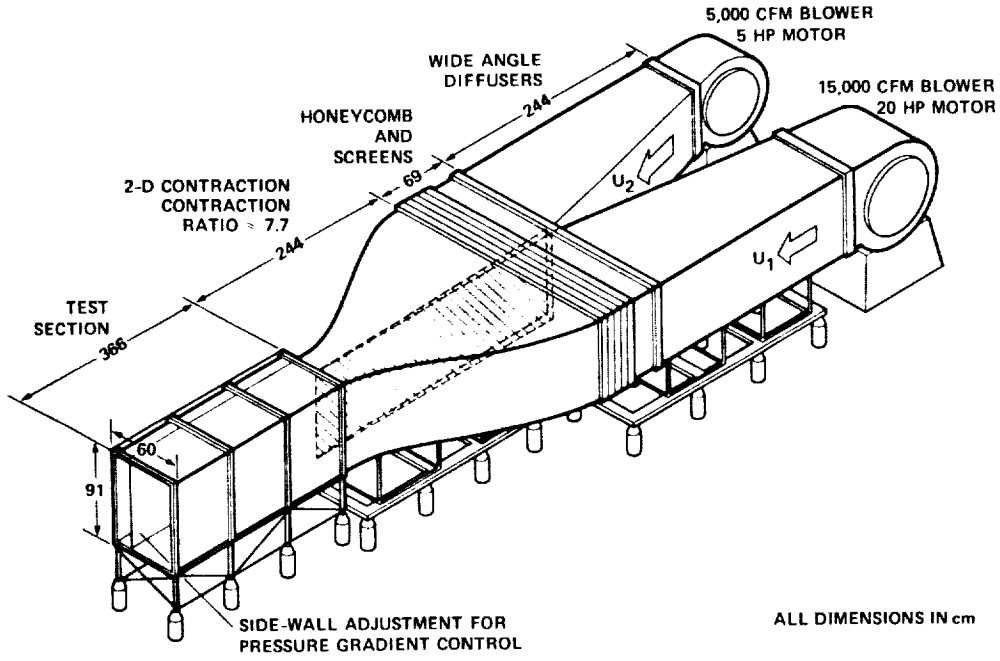

FIGURE 2. Mixing Layer Wind Tunnel.

about 0.05%. The mean core-flow is found to be uniform to within 0.5%, and cross-flow angles are less than 0.25°. Further details of the mixing layer wind tunnel design and calibration are given by Bell & Mehta (1989b).

In the studies described in section 4, measurements were made using a single rotatable cross-wire probe held on a 3-D traverse and linked to a fully automated data acquisition and reduction system controlled by a MicroVax II computer. The cross-wire probe had two 5 μm diameter tungsten sensing elements, each about 1 mm long and positioned about 1 mm apart. The probe was calibrated statically in the potential core of the flow assuming a 'cosine-law' response to yaw, with the effective angle determined by calibration. The analog signals were filtered (low pass at 30 Khz), DC offset, and amplified ($\times$10) before being fed into a NASA-built computer interface. The interface contained a fast sample-and-hold A/D converter with 12 bit resolution and a multiplexer for connection to the computer. Individual statistics were averaged over 5,000 samples obtained at a rate of 400 samples per second.

3.2. New experimental apparatus

As indicated in section 2, single-point, time-averaged measurements are insufficient to fully address the question of how secondary vortex structure develops

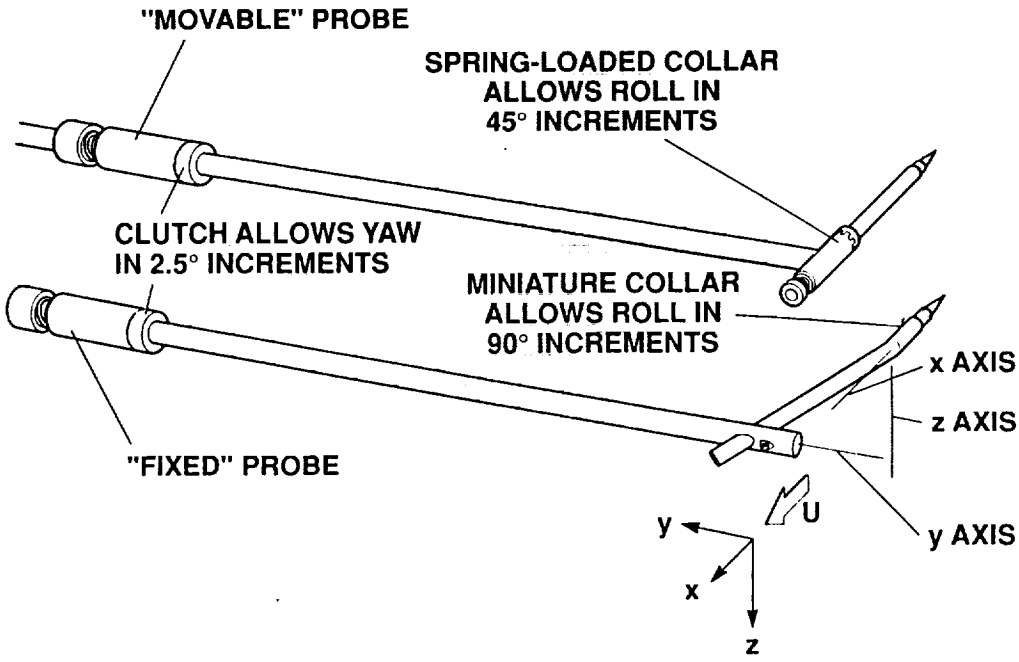

FIGURE 3. Sketch showing new probe holders made for spatial correlation measurements.

in the mixing layer. Accordingly, considerable time has been spent on the construction of new equipment and software for measuring spatial and temporal correlations. The new equipment consists of a pair of new hot-wire probe holders, a second, independent, 2-D traverse system, and a new traverse table. New software has been written to acquire two-point data and compute the correlations, as well as to increase the degree of automation in the data acquisition process.

The two new hot-wire probe holders are sketched in figure 3. Both probe holders allow the crossed hot-wire probes to be yawed at 2.5° intervals for precise angle calibrations. The larger "movable" probe can be rolled at 45° intervals, allowing measurements of all six independent components of the Reynolds stress tensor, as well as the three components of mean velocity. The smaller "fixed" probe can be rolled at 90° intervals. Both probe holders will be capable of moving independently on separate traversing systems. In practice, however, the "fixed" probe holder will be left at one point in the flow, while the "movable" probe holder is traversed automatically around it, to obtain correlation measurements. The movable probe holder is designed primarily for ease of use, and is mounted on the original computer-controlled 3-D traverse system. The fixed probe holder is designed with an angled head, so that the two hot-wire probes can be brought as close together as possible. The minimum probe separation is 6 mm, which, in the region under investigation, is approximately 1/10th the mixing layer thickness,

and 1/5th the radius of the streamwise vortices. The fixed probe is mounted on a 2-D traverse system, which rests within the 3-D traverse for the movable probe.

A new table for the combined probe traversing mechanism has been constructed. The old traverse table, made from wood, had to be laboriously shifted and re-leveled at each new measurement station. Careful leveling is necessary because the angle the probe makes with the flow must be carefully maintained from one station to the next in order to make consistent measurements of the secondary velocities, which are comparatively small. The new traverse table is more stable than the old one, and has a more effective leveling system. This allows the probes to be shifted between measurement stations much more quickly and accurately, increasing both the overall rate at which data is acquired and its repeatability.

Under the old system, velocity data from the crossed hot-wire was reduced on-line. Raw data was not stored. The greater volume of data produced by the dual probes makes real-time data reduction impractical, while the recent acquisition by the Fluid Mechanics Lab of an Exabyte EXB-8200 8mm helical scan tape drive makes it considerably easier to store large quantities of raw data. As a result, new software has been written to allow the raw data to be stored and transferred to tape with extensive off-line data reduction. The stored raw data will form a database from which any temporal or spatial correlation implicit in the original measurements can be retrieved. Another major aim of the software upgrade has been to further automate the data acquisition procedure. The new probe holder design allows the crossed hot-wire calibration procedure to be partially automated. As a result, the calibrations can be automatically checked at periodic intervals during a run. This will result in longer running times, a lower level of operator intervention, and lower errors due to hot-wire drift.

3.3. New measurement techniques: application to the problem

A simple relationship between spatial correlation data and the actual coherent structures in a turbulent flow can rarely be established. Considerable care must be exercised in postulating the form of a turbulent structure from the correlation data, and in fact some controversy has arisen in the past concerning the interpretation of correlation measurements in mixing layers (Chandrsuda *et al.* 1978, Wygnanski *et al.* 1979, Wood 1980). In the present case, the task is considerably easier. The general shape of the coherent structures has already been discovered through flow visualization, and it is only necessary to determine their scale and strength. Thus, it is reasonable to search for the particular correlation which is most likely to give unambiguous data concerning the behavior of the structures.

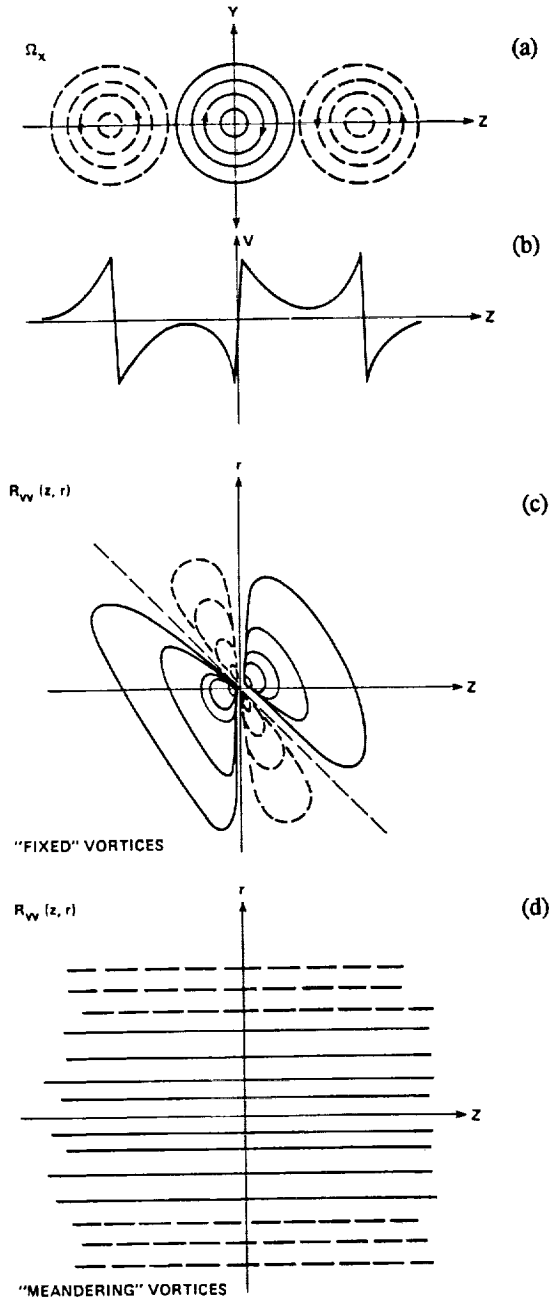

FIGURE 4. Sketches showing details of proposed spatial correlation measurements. z is the spanwise location of the fixed probe, r is the spanwise separation between probes. a) Sketch of streamwise vorticity field in mixing layer. b) Level of cross-stream velocity along a line through the centers of the vortices. c) Sketch of spatial correlation R_{vv} for the case of fixed streamwise vortices. d) Sketch of spatial correlation R_{vv} for the case of meandering streamwise vortices.

To address the question of spanwise meander of the streamwise vortex structures, the best quantity to examine appears to be the variation of the cross-stream velocity correlation in the spanwise direction, i.e., $R_{vv}(0,0,r)$. Imagine that the shear layer contains a row of alternating-sign streamwise vortices, as diagrammed in figure 4a. A distinctive pattern of cross-stream velocity is produced. This is demonstrated in figure 4b, which shows the variation of V with Z along a line drawn through the vortex centers. The cross-stream velocity rapidly changes sign across the core of a streamwise vortex. If correlation measurements are made along a line passing through the streamwise vortex cores in the spanwise direction, there will be a zero-crossing at a separation corresponding to the radius of the vortices. This correlation will be observed even if spanwise meander has reduced the *mean* streamwise vorticity to zero. The amplitude of the meander can also be determined from the variation of R_{vv} with both the spanwise location of the fixed probe (z) and the spanwise separation of the probes (r). If the streamwise vortex structure is fixed in the spanwise direction, the variation of R_{vv} with z and r can be easily calculated from the V vs z curve shown in figure 4b. The resulting contour plot is shown in figure 4c. If the structure meanders over a distance larger than the radius of the streamwise vortices, the very different correlation shown in figure 4d will be obtained. In this case, while there is no dependence on the location of the fixed probe (i.e. z) and no detectable mean vorticity, the variation with probe separation r suffices to establish the presence and radius of the streamwise structures.

4. Effect of initial conditions on mixing layer structure

As an interim study while the new instrumentation was designed and built, it was decided to examine the effects of initial conditions on streamwise vorticity in mixing layers. The results of Bell & Mehta (1989a), for a mixing layer originating from a splitter plate with laminar initial boundary layers, were used as a base case for comparison. Hereinafter, this case is referred to as the *undisturbed* case. The second case was that of a mixing layer originating from turbulent initial boundary layers, but with the same operating conditions as Bell & Mehta (1989a). This case is referred to as the *tripped* case. No mean streamwise vorticity was found in the tripped mixing layer, and a difference between the far-field growth rates of the tripped and undisturbed cases was noted. It was speculated that the difference in growth rates, which has been observed by previous researchers (Browand & Latigo 1979, and Mehta & Westphal 1986) was related to the absence of mean streamwise vorticity in the tripped case. Accordingly, a third or *vortex generator* case was studied, in which streamwise vorticity was injected into the tripped mixing layer by means of a row of vortex generators mounted on one side of the splitter plate.

4.1. Experimental setup

In all three cases, the free-stream velocities were set at 15 m/s on the high-speed side and 9 m/s on the low-speed side, thus giving a mixing layer with velocity ratio $U_2/U_1 = 0.6$. In the tripped case, the boundary layers on the splitter plate were perturbed using round wire trips about 0.75 mm diameter on the high-speed side and 1.2 mm diameter on the low-speed side. The wire trips were installed 15 cm upstream of the trailing edge to allow the boundary layers to recover from the perturbation. Well-developed turbulent boundary layers were produced on both sides of the splitter plate; details of the boundary layers for the first two cases are summarized below in Table 1.

Table 1. Initial Boundary Layer Properties

Condition	U_e (m/s)	δ_{99} (cm)	θ (cm)	Re_θ	H	C_f $\times 10^3$
High-Speed Side, Undisturbed	15.0	0.398	0.0526	525	2.52	0.87
Low-Speed Side, Undisturbed	9.0	0.441	0.0606	362	2.24	1.56
High-Speed Side, Tripped	15.0	0.758	0.0820	804	1.49	5.30
Low-Speed Side, Tripped	9.0	0.851	0.0941	567	1.50	4.86

In the vortex generator case, streamwise vortices were injected into the mixing layer by a row of half-delta wing vortex generators placed on the high-speed side of the splitter plate, 2.54 cm ahead of the trailing edge. Both initial boundary layers had been tripped with round wires as described in the second case. The vortex generators were installed at alternating positive and negative angles of attack with their trailing edges spaced 1.91 cm apart, so as to produce an evenly-spaced row of counter-rotating streamwise vortices. Each vortex generator had a 6.4 mm semi-span, a 68° sweep angle, and was placed at an angle of attack of $\pm 17°$. The vortex generator spacing was chosen to be comparable to the Kelvin-Helmholtz wavelength, and the semi-span was chosen to be approximately equal to the local boundary layer thickness.

Data were obtained in the uv- and uw-planes with a cross-wire probe at nine streamwise stations for the undisturbed case and at eight stations each for the two other cases. In each case, measurements were made at corresponding positions within the test section, located between X $\sim$ 10 to 250 cm downstream of the splitter plate. In the undisturbed case, the last station is $4760\theta_1$ downstream of the splitter plate trailing edge, where θ_1 is the momentum thickness of the high-speed side splitter plate boundary layer. In the two cases with turbulent initial boundary layers, the last station is $3050\theta_1$ downstream of the trailing edge. At each station, data were obtained in a cross-sectional plane which typically extended over 20 points in the cross-stream direction and 60 points in

the spanwise direction. The spanwise extent of the data set ranged from three to ten mixing layer thicknesses, depending on the streamwise location. All the global properties presented below were *spanwise-averaged* for all cases. The measurements of U, W and $\overline{u'w'}$ were corrected for mean streamwise velocity gradient ($\partial U/\partial Y$) effects, assuming a linear variation in U between the cross-wire sensors (Bell & Mehta 1989a). The streamwise component of mean vorticity ($\omega_x = \partial W/\partial Y - \partial V/\partial Z$) was computed using the central difference method. The overall circulation was defined as the surface integral of the streamwise vorticity over the cross-flow plane with vorticity levels less than 10% of the maximum value being set to zero in order to provide immunity from "noise".

4.2. Results and discussion

Contour plots of mixing layer properties at a representative station show clear differences in the three cases. Figures 5-7 show selected properties measured at $X = 57.3$ cm, which is just downstream of the estimated location of the second vortex pairing. The mean streamwise vorticity contours show the most marked difference between the three cases. In the undisturbed case (figure 5a), an irregular row of $8 - 10$ streamwise vortices of varying strengths can be easily made out. In contrast, the tripped case (figure 5b) has a much lower level of vorticity in an irregular pattern, not at all suggestive of concentrated streamwise vortices. In the vortex generator case, a single row of 11 round, well-defined counter-rotating vortices are clearly observed, with the magnitudes of the peak levels approximately the same. The spacing between the vortices is 2 cm, approximately the same as the spacing between the vortex generator trailing edges. In the undisturbed and vortex generator cases, the mean streamwise vorticity is strongest at the first measurement station ($X = 7.8$ cm), and its effects on the other flow quantities are greatest at this location.

The presence of mean streamwise vorticity leads to spanwise variation of the mixing layer properties. Contours of mean streamwise velocity are shown for the three cases in figure 6. In the undisturbed case (figure 6a), there is an irregular distortion of the mean flow, corresponding to the presence of the streamwise vortices. The tripped case (figure 6b) displays very little spanwise variation — the flow appears essentially two-dimensional. The contours for the vortex generator case (figure 6c) give an idea of the strength of the injected vortices. A very regular, well-defined spanwise wavelength can be observed in the contours, the "peaks" and "valleys" of which mark regions of common flow up or down, in between the vortices. Similar behavior is seen in the turbulence quantities, as shown in figure 7, which plots contours of twice the turbulent kinetic energy ($\overline{q^2}$). The undisturbed case (figure 7a) displays an irregular variation associated with the streamwise vortices while the tripped case (figure 7b) turbulence distribution is essentially two-dimensional. In the vortex generator case (figure 7c), the pattern is quite well-marked and similar to that of the mean velocity, with the presence of local peaks of $\overline{q^2}$ near the centerline.

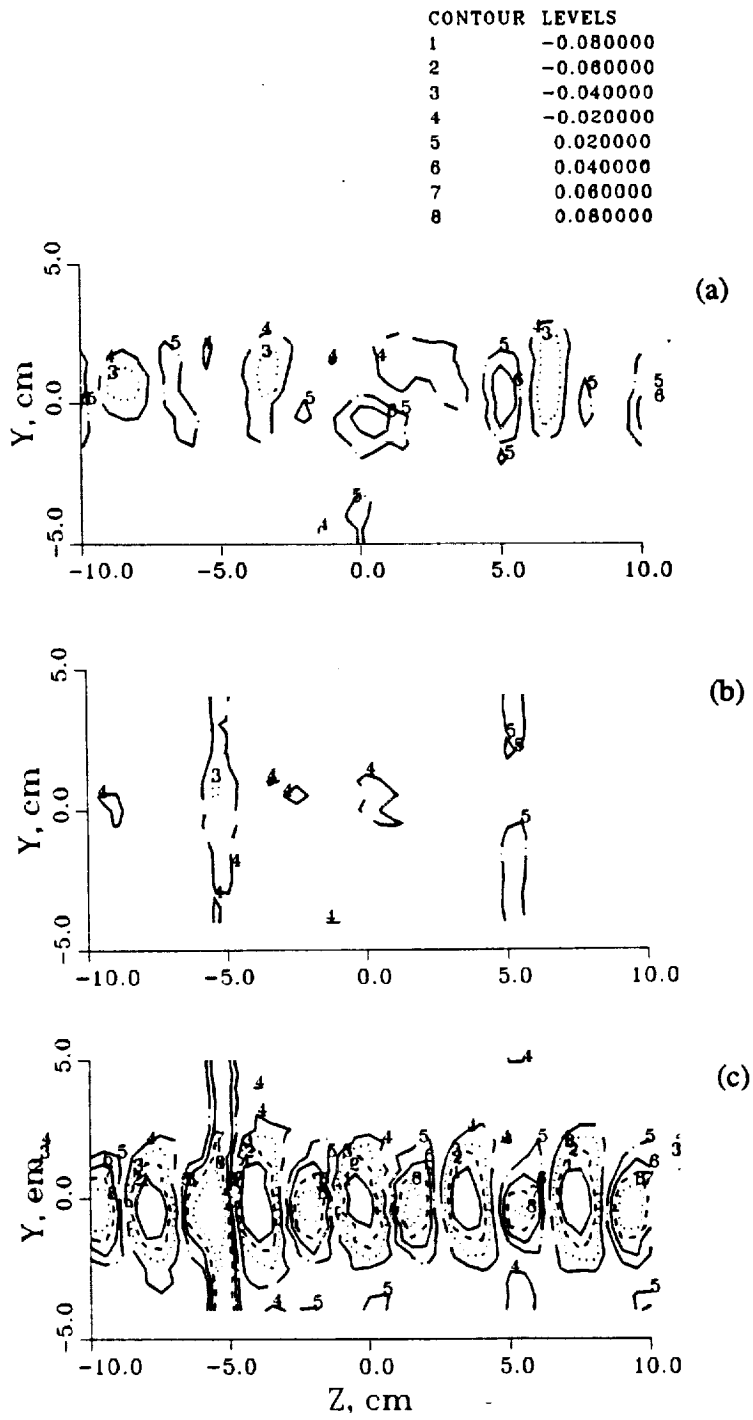

FIGURE 5. Contours of mean streamwise vorticity Ω_x/U_0 (cm^{-1}) at $X = 57.3$ cm. a) Undisturbed case, b) Tripped case, c) Vortex generator case.

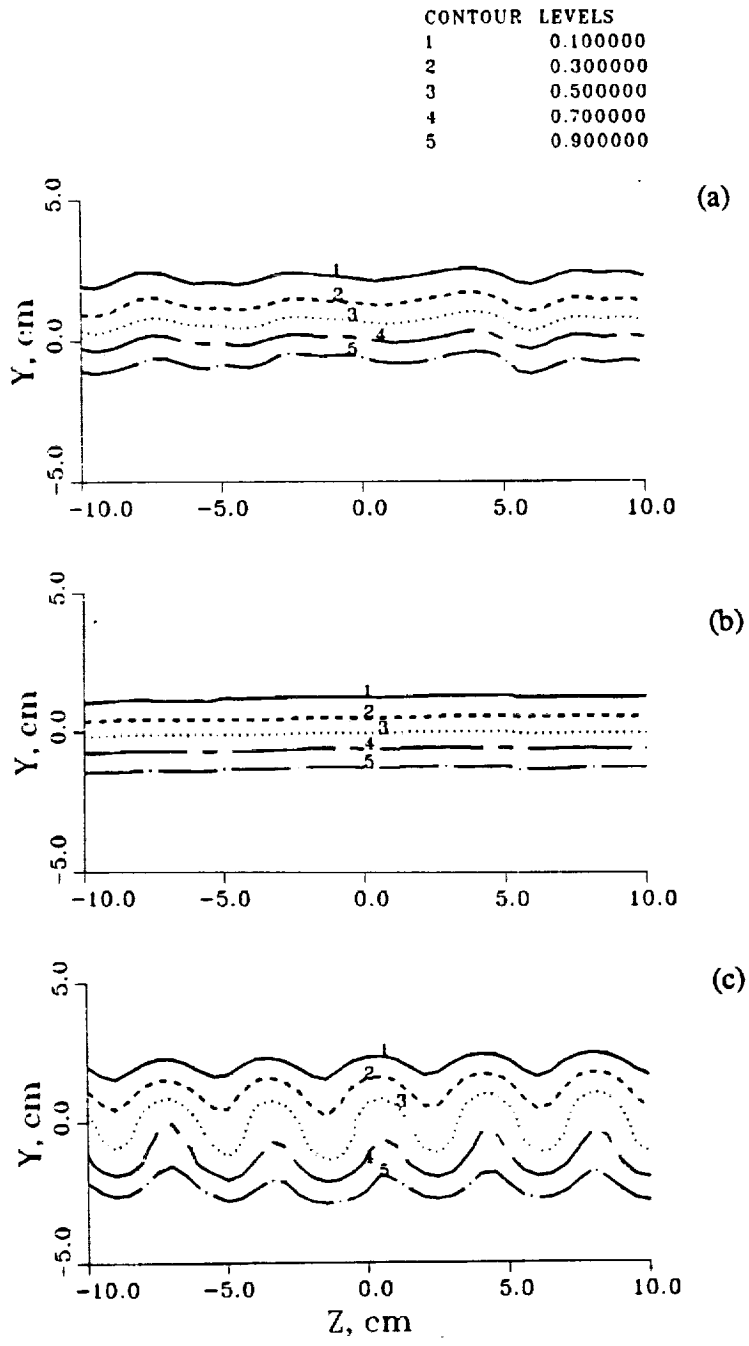

FIGURE 6. Contours of mean streamwise velocity U/U_0 at $X = 57.3$ cm. a) Undisturbed case, b) Tripped case, c) Vortex generator case.

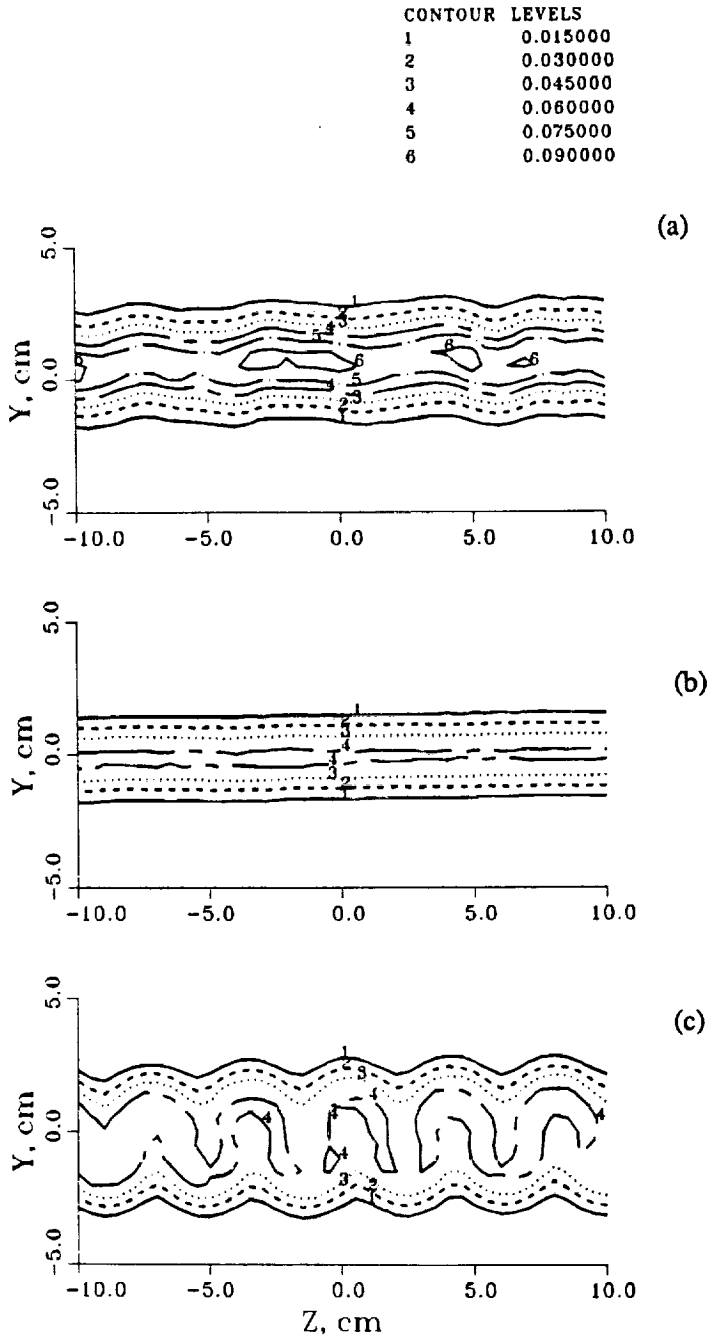

FIGURE 7. Contours of turbulent kinetic energy $\overline{q^2}/U_0{}^2$ at $X = 57.3$ cm. a) Undisturbed case, b) Tripped case, c) Vortex generator case.

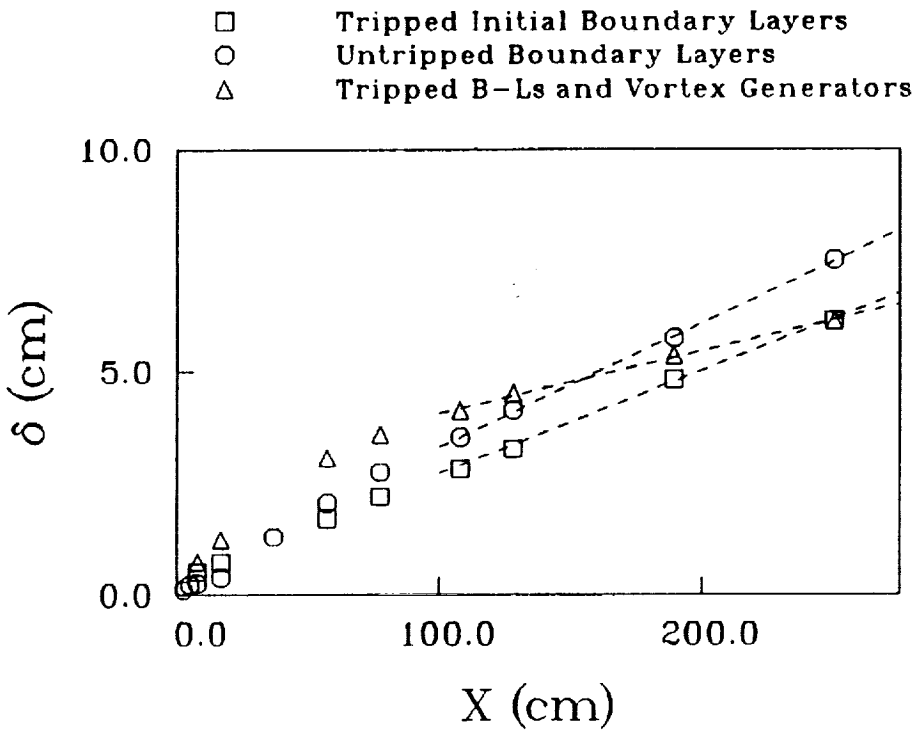

FIGURE 8. Mixing layer thickness (determined as described in text), versus streamwise distance.

The differences between the three cases shown in the contour plots reflect a difference in the global mixing layer properties. Figure 8 shows the mixing layer thickness δ, determined by fitting the mean velocity profile to an error function, for all three cases. (Mixing layer thickness has been determined by fitting the normalized mean velocity data to an error function profile shape: $U/(U_1-U_2) = [1+erf(\zeta)]/2$, where ζ is the normalized cross-stream coordinate: $\zeta = (y-y_0)/\delta$. The values of δ and y_0 are taken to be the mixing layer thickness and centerline location, respectively.) The three cases have very different growth rates, especially in the far-field, where linear growth is expected. The tripped case growth rate in the linear region is $d\delta/dx = 0.023$, quite close to the accepted value for a mixing layer with this velocity ratio. But the far-field growth rate for the undisturbed case is 20% higher than that for the tripped case. As noted above, similar differences in growth rate have been reported previously in the literature. Spanwise averaging of the mixing layer properties, employed for the first time in this study, shows that the difference in growth rates persists across the mixing layer span.

Since the undisturbed case contains significant mean streamwise vorticity while the tripped case does not, it was expected that the injection of streamwise

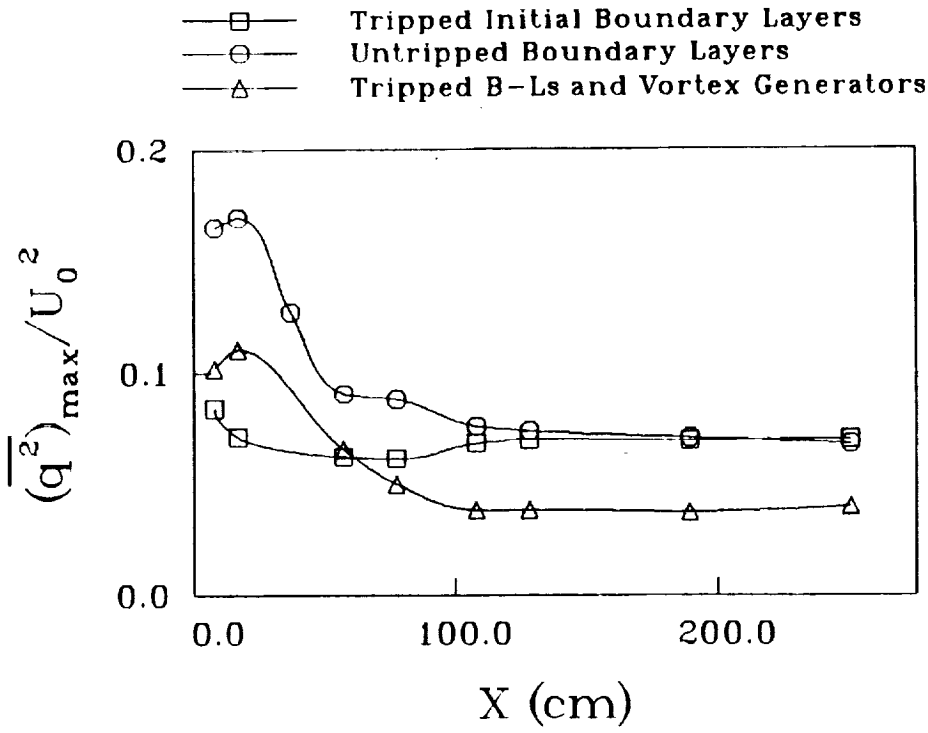

FIGURE 9. Maximum turbulent kinetic energy versus streamwise distance.

vorticity would increase the growth rate. But, although the growth is high initially in this case (for $X \leq 60$ cm), the far-field growth rate is extremely low — only 61% of the tripped case growth rate. Since the mixing layer growth rate is so drastically affected by the vorticity injection, the Reynolds stresses would be expected to show a comparable effect. This is indeed the case as seen in the streamwise development of the peak turbulent kinetic energy, $\overline{q^2}_{max}$ (figure 9). The tripped and undisturbed cases asymptote to about the same constant level beyond $X \sim 125$ cm. The vortex generator case also achieves a constant level by that streamwise location, but the asymptotic level is significantly lower. This is not too surprising given the lower cross-stream velocity gradients in this case. At the last station, a very slight upturn in the $\overline{q^2}_{max}$ level for the vortex generator case is noticeable. Measurements at a station some 30 cm farther downstream (not shown) also show a slightly higher turbulence level, but their accuracy is suspect due to test section end effects. This behavior *may* indicate that at some distance farther downstream, this case will recover to a higher level of Reynolds stresses, and presumably a higher growth rate as well.

The behavior of the injected streamwise vorticity in vortex generator case is compared to that of the "naturally occurring" vorticity, measured in the undisturbed case, in figure 10. The peak vorticity and circulation data presented in

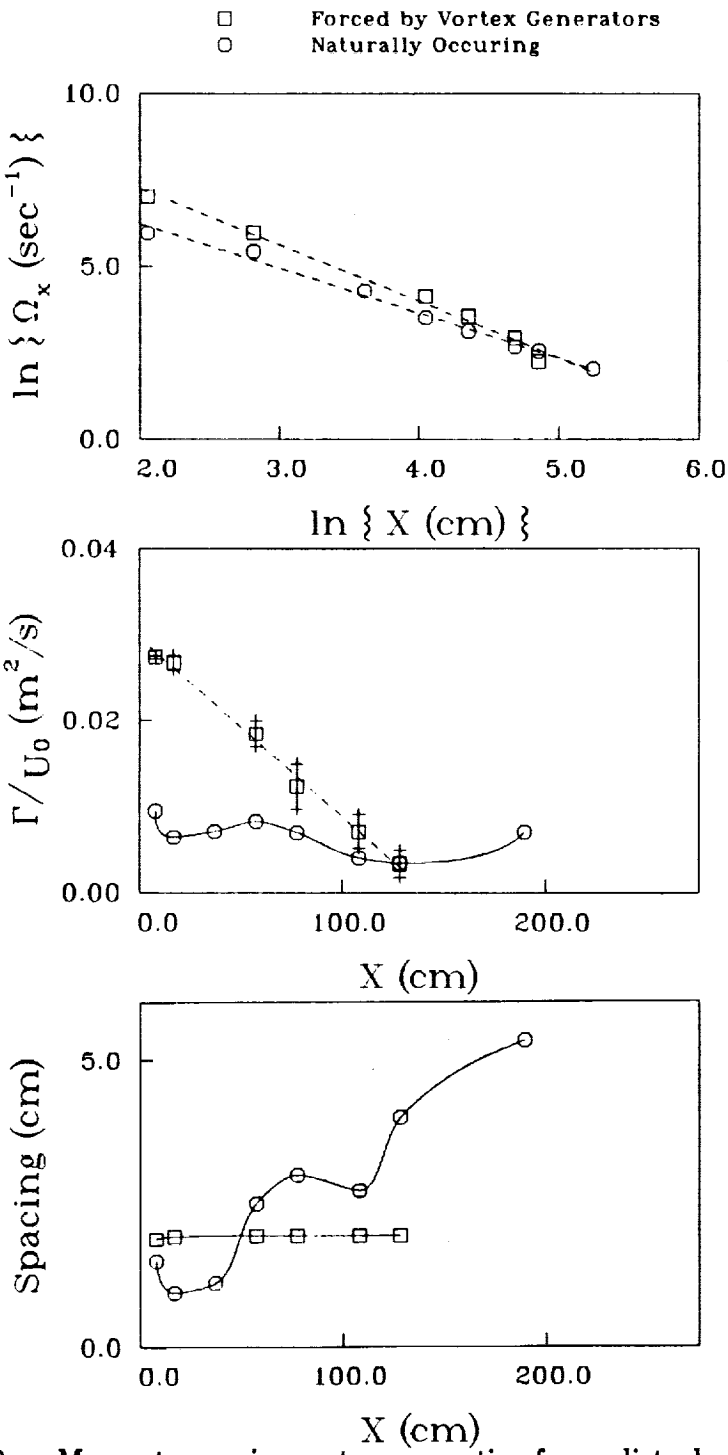

FIGURE 10. Mean streamwise vortex properties for undisturbed and vortex generator cases. a) Peak streamwise vorticity vs X, log-log scale, b) Streamwise vortex circulation vs X, c) Streamwise vortex spacing vs X.

figure 10 are left unnormalized. The most appropriate normalizing parameters — the initial strength and circulation of the spanwise structures — can only be estimated in the present study. Mean spanwise vorticity, $\Omega_z = (\frac{\partial V}{\partial x} - \frac{\partial U}{\partial y})$ was estimated by assuming the $\frac{\partial V}{\partial y}$ term is negligible. Spanwise vortex circulation was estimated using an initial streamwise wavelength determined by the convection velocity and the measured natural frequency of the mixing layer. (For the undisturbed case, the estimated values at about the location of the first roll-up are: $\Omega_{z_{max}} = 1400$ s$_1$ and $\Gamma_z = 0.11$ m^2/s. For the vortex generator case, the estimate is made more uncertain by the highly distorted state of the mixing layer and the lack of a clearly observable natural frequency. In this case, the estimated values are: $\Omega_{z_{max}} = 1100$ s$_1$ and $\Gamma_z = 0.11$ m^2/s.)

The streamwise development of the peak mean vorticity for two cases is presented on a log-log scale in Fig. 10a. The decay is roughly linear on this scale, indicating a power-law decay rate. Although the peak initial levels for the injected vorticity are considerably higher, the decay rate is also faster; the naturally occurring vorticity was found to decay as $1/X^{1.5}$, whereas the injected vorticity decays as $1/X^{1.8}$. Beyond the station at $X \sim 100$ cm, the peak levels for the two cases are seen to be comparable. As discussed previously, this apparent reduction in vortex strength may actually be due to the increasingly large meander of vortices of constant strength; spatial correlation measurements will be conducted in the future to establish whether or not this is the case. The vortex circulation (Fig. 10b) shows very different behavior for the two cases. The naturally occurring vortex circulation shows a very slow decrease, with a small intermediate peak at $X \sim 60$ cm — this was associated with the change in scale of the streamwise vortex structure (described below). However, the injected vortex circulation shows a relatively fast linear decay and by $X \sim 125$ cm, the level is comparable to that of the naturally occurring vortices. The mean spacing of the streamwise vortices can be easily found by counting the number of vortices present at each station. The vortex spacing in the undisturbed case increases in a step-wise fashion, scaling approximately as the mixing layer vorticity thickness (Fig. 10c). On the other hand, the spacing for the injected vortices is *constant* within the measurement domain. This may simply be due to the fact that the injected vortices are of equal strength and spacing, unlike the naturally occurring structures, and so there is no tendency for self-induced motion. Another possibility, related to the pairing of the *spanwise* structures, is discussed below.

4.3. Conclusions

The original purpose of injecting the streamwise vorticity into the tripped mixing layer was to try and increase its growth rate to a level more comparable to that of the undisturbed layer. The initial ($X \leq 60$ cm) growth rate is indeed increased significantly due to the extra entrainment provided by the streamwise structures. However, the growth rate further downstream ($X \geq 100$ cm) is

reduced drastically over both the tripped and untripped cases. A possible explanation for this change can be made by postulating that the streamwise vortex structure affects the pairing of the spanwise vortices. Most of the growth of a mixing layer occurs due to entrainment during the pairing process of the nominally two-dimensional spanwise vortical structures (Sandham *et al.* 1988). If the spanwise structures were altered so as to reduce the pairing rate, entrainment by the mixing layer, and thus its growth rate, would be decreased.

The naturally occurring streamwise vorticity in the undisturbed case first appears in the regions of maximum extensional strain, in the braid region. The two structures become interlaced in such a way that, in flow-visualizations, it appears that the only effect of the streamwise structure on the spanwise is to produce a regular, gentle undulation in the latter (Lasheras *et al.* 1986). Therefore, the entrainment due to the spanwise structures proceeds undisturbed; total growth may in fact be enhanced by the additional entrainment in the braids due to the streamwise structures. However, the injected vorticity in the vortex generator case imposes its own pattern on the spanwise structures, as indicated by the gross distortions in the mean velocity contours. It is possible that this changes the pairing process, reducing the pairing rate. In the near-field, entrainment by the streamwise structures more than makes up for this deficit. However, entrainment due to the streamwise vortices decreases much faster than the spanwise structures recover, so at some point the overall entrainment rate is reduced, and hence the growth rate of the mixing layer drops. This hypothesis is also consistent with differences noted in the behavior of the streamwise vortices in the two cases. Previous investigations have suggested that the scale change in the streamwise vortices occurs during the pairing of the spanwise rollers (Jimenez *et al.* 1985, Bell & Mehta 1989a). The fact that a scale change is not observed in the vortex generator case suggests that the pairing of the spanwise rollers has been suppressed.

The mixing layer with vorticity injection maintains a lower growth rate and turbulence levels out to the end of the measurement region in the current study. Although there is some evidence of an upward trend at the last measurement station, the data is not sufficiently extensive to determine when, if ever, the vortex generator case will recover to a higher turbulence level and growth rates. The absence of such a recovery would, of course, indicate that more than one asymptotic structure is possible in mixing layers.

5. Future plans

The equipment and software for spatial correlation measurements is currently in the final test phase. Once the checkout is complete, work will commence on:

- A study of the variation of $R_{vv}(0,0,r)$ in the undisturbed mixing layer. An examination of this quantity will show the extent of spanwise meander of the streamwise vortex structure.

- A similar study of the tripped mixing layer. In this case, the mean streamwise vortex structure is entirely absent. Correlation measurements will determine if it is actually present, but masked by a high level of meander.
- A study of the vortex generator case, which will attempt to determine what sort of turbulence structure is responsible for the lower growth rate. Correlation measurements should be able to determine the extent to which the streamwise vortex structure influences the development of the spanwise rollers.

In addition to these studies, which are designed to take advantage of the new instrumentation, two additional cases are being considered:

- A repeat of the vortex generator case, at twice the original free-stream velocities, but with the same velocity ratio. This would approximately double the nondimensionalized development distance, as determined by either Reynolds number or initial mixing layer thickness. Thus, it should be possible to determine when, if ever, the effect of initial conditions relaxes, and a more "normal" growth rate is recovered. Requiring no complex measurements, this study can be accomplished fairly quickly.
- A study of a mixing layer originating from a splitter plate with a corrugated end. Such a splitter plate would inject cross-stream vorticity into the mixing layer, in a manner analogous to the way that the vortex generator case injects streamwise vorticity. Thus, this study would form a natural complement to the vortex generator case. Although this flow has been previously studied at low Reynolds numbers through flow-visualization (Lasheras & Choi, 1988), the unusual behavior of the vortex-generator case suggests that it merits a second, more intensive look.

Acknowledgments

I would like to thank my co-investigator, Dr. Rabindra D. Mehta. Although not associated with the C.T.R., Dr. Mehta has participated wholeheartedly in this project, and it owes much to his expertise and assistance, for which I am very grateful. Dr. Mehta was supported by NASA Grant NCC-2-55 from the Fluid Dynamics Research Branch, NASA Ames Research Center.

REFERENCES

ASHURST, W. T., & MEIBURG, E. 1988 Three-Dimensional Shear Layers via Vortex Dynamics.. *J. Fluid Mech.* **189**, 87-116.

BELL, J. H. & MEHTA, R. D. 1989a Three-Dimensional Structure of a Plane Mixing Layer. AIAA Paper 89-0124. Also, JIAA Report TR-90, Dept. of Aero/Astro, Stanford University.

BELL, J. H. & MEHTA, R. D. 1989b Design and Calibration of the Mixing Layer Wind Tunnel. JIAA Report TR-89, Dept. of Aero/Astro, Stanford University.

BERNAL, L. P. 1981 The Coherent Structure of Turbulent Mixing Layers. Ph.D. Thesis, California Institute of Technology.

BERNAL, L. P. & ROSHKO, A. 1986 Streamwise Vortex Structure in Plane Mixing Layers. *J. Fluid Mech.* **170**, 499-525.

BREIDENTHAL, R. 1981 Structure in Turbulent Mixing Layers and Wakes using a Chemical Reaction. *J. Fluid Mech.*, **109**, 1-24.

BROWAND, F. K. & LATIGO, B. O. 1979 Growth of the Two-Dimensional Mixing Layer from a Turbulent and Nonturbulent Boundary Layer. *Phy. Fluids*, **22**, pp. 1011-1019.

BROWN, G. L. & ROSHKO, A. 1974 On Density Effects and Large Structure in Turbulent Mixing Layers. *J. Fluid Mech.*, **64**, pp. 775-816.

CHANDRSUDA, C., MEHTA, R. D., WEIR, A. D., & BRADSHAW, P. 1978 Effect of Free-stream Turbulence on Large Structures in Turbulent Mixing Layers. *J. Fluid Mech.*, **85**, pp. 693-704.

JIMENEZ, J., COGOLLOS, M., & BERNAL, L. P. 1985 A Perspective View of the Plane Mixing Layer, *J. Fluid Mech.*, **152**, pp. 125-143.

KONRAD, J. H. 1977 An Experimental Investigation of Mixing in Two-Dimensional Turbulent Shear Flows with Applications to Diffusion-Limited Chemical Reactions, Ph.D. Thesis, California Institute of Technology, and Project SQUID Technical Report CIT-8-PU, Dec. 1976.

LASHERAS, J. C., CHO, J. S. & MAXWORTHY, T. 1986 On the Origin and Evolution of Streamwise Vortical Structures in a Plane, Free Shear Layer. *J. Fluid Mech.*, **172**, pp. 231-258.

LASHERAS, J. C. & CHOI, H. 1988 Stability of a Plane Turbulent Shear Layer to Axial Perturbations. *J. Fluid Mech.*, **189**, pp. 53-86.

MEHTA, R. D. & WESTPHAL, R. V. 1986 Near-Field Turbulence Properties of Single- and Two-Stream Plane Mixing Layers. *Exp. in Fluids*, **4**, pp. 257-266.

METCALFE, R. W., ORSZAG, S. A., BRACHET, M. E., MENON, S., & RILEY, J. J. 1987 Secondary Instability of a Temporally Growing Mixing Layer. *J. Fluid Mech.*, **184**, pp. 207-243.

ROGERS, M. M., & MOSER, R. D. 1989 The Development of Three-Dimensional Temporally-evolving Mixing Layers. Proceedings of the 7th Symposium on Turbulent Shear Flows, Aug. 21-23, Stanford University, *vol.* 1, pp 9.3.1-9.3.6.

SANDHAM, N. D., MUNGAL, M. G., BROADWELL, J. E., & REYNOLDS, W. C. 1988 Scalar Entrainment in Mixing Layers. Proceedings of the 1988 Summer Program, Center for Turbulence Research, CTR-S88, Dec. 1988, pp. 69-76.

WOOD, D. H. 1980 A Reattaching, Turbulent, Thin Shear Layer, Ph.D. Thesis, Dept. of Aeronautics, Imperial College, University of London.

WYGNANSKI, I., OSTER, D., FIEDLER, H., & DZIOMBA, B. 1979 On the Perseverance of a Quasi-Two-Dimensional Eddy-Structure in a Turbulent Mixing Layer. *J. Fluid Mech.*, **93**, pp. 325-335.

Development of renormalization group analysis of turbulence

By L. M. Smith

1. Introduction

The renormalization group (RG) procedure for nonlinear, dissipative systems is by now quite standard (Ma, 1976). The successes of its application to the problem of hydrodynamic turbulence are also becoming well-known (Forster, Nelson and Stephen, 1977, Fournier and Frisch, 1983, Yakhot and Orszag, 1986). Much progress has been made towards an understanding of what is, and what is not, accessible via RG analysis. In summary, the RG method isolates self-similar behavior and provides a systematic procedure to describe scale-invariant dynamics in terms of large scale variables only. The parameterization of the small scales in a self-consistent manner has important implications for sub-grid modeling. The limiting forms of such parameterizations are often universal, i.e. independent of the numerical coefficients in the original model.

Recognizing its limitations, the renormalization group technique is a powerful tool. RG methods will predict characteristics of the dynamics of a model that are approximately scale-invariant. Applied to the Navier Stokes equations, RG provides an expression for the eddy-damping of the large scales by the small scales. Other scale-dependent dynamics, such as sweeping, are not addressed (Chen and Kraichnan, 1989).

Skepticism has surrounded the RG predictions for turbulence because the detailed mathematics involved is not yet well understood. The method is justified mostly by its success: universal scaling laws derived using RG methods are quite accurate. Observed scaling laws are reproduced for a diverse set of problems, from population dynamics (Feigenbaum, 1979), to turbulence, to nonlinear spin dynamics near a ferromagnetic critical point (Wilson, 1974).

The deduction of experimentally known scaling laws gives credibility to the RG method. The merit of any theory, however, must be based on its predictive power. To date, the most important predictions from RG analysis of turbulence have been low Reynolds number corrections to traditional high Reynolds number models. For examples, RG formulas provide smooth transition between the Smagorinsky eddy viscosity and the molecular viscosity, and deduced modifications to the traditional $\kappa - \varepsilon$ model (Yakhot and Orszag, 1986, hereafter referred to as I). In the latter case, however, ambiguities remain with respect to procedure and interpretation. This is not surprising given the pioneering nature of the mathematics.

The RG model for homogeneous, isotropic turbulence is developed in Section 2. The steps of the RG procedure for nonlinear equations are reviewed. The meaning and consequences of the ϵ-expansion are addressed in Section 3 using the work of Fournier and Frisch (1978, 1983). Their results are given in terms of the expansion parameter ϵ. Inertial range statistics and scaling laws are recovered for the case of $\epsilon = 4$ (I). Section 4 gives some results of the theory for homogeneous, weakly anisotropic turbulence ($\epsilon = 4$ and no mean flow). Extension of the theory to include a weak mean flow is discussed in Section 5. In Section 6, errors in the Yakhot-Orszag RG $\kappa - \varepsilon$ equations are corrected. Consistency between direct numerical simulation data for channel flow, the standard $\kappa-\varepsilon$ model and the RG-based model requires a reinterpretation of the contributions to the ε-equation. Finally, Section 7 proposes application of the RG method to a sequence of model equations that converges to the Navier Stokes equations. The solutions of these particular model equations are known to have self-similar solutions.

2. The RG procedure

The renormalization group symmetry transformation consists of two steps (Ma, 1976). First, course graining is achieved by averaging over small scales. Second, space is rescaled. New independent variables are defined in the original domain by the rescaling. In most cases, the dependent variables are also rescaled.

It is not clear how to course-grain a nonlinear system in which the large scales are coupled to the small scales. This is, of course, the closure problem of turbulence. The RG technique was developed for the equations of nonlinear spin dynamics, the time-dependent Ginzburg-Landau equations. It is based on expansion about an equilibrium basic state whose Gaussian statistics are known from the theory of statistical mechanics. Although this procedure is sensible for near-equilibrium dynamics, it is not obviously relevant to turbulence. Nevertheless, the basic state in the RG analysis of turbulence is also assumed Gaussian. The meaning of the expansion will be explored using the work of Fournier and Frisch (1978, 1983) in Section 3.

The RG transformation of a nonlinear system is illustrated with homogeneous, isotropic turbulence driven by a Gaussian random force. The model equations in Fourier space are

$$\hat{v}_i[\hat{\mathbf{k}}] = G^o[\hat{\mathbf{k}}]\hat{f}_i[\hat{\mathbf{k}}] - \frac{i\lambda_o}{2}P_{imn}[\mathbf{k}]\int_{-\infty}^{\infty}\frac{d\omega}{2\pi}\int_{q=0}^{\Lambda_o}\frac{d\mathbf{q}}{(2\pi)^d}\hat{v}_m[\hat{\mathbf{q}}]\hat{v}_n[\hat{\mathbf{k}}-\hat{\mathbf{q}}] \qquad (1)$$

$$\left\langle \hat{f}_i[\hat{\mathbf{k}}]\hat{f}_j[\hat{\mathbf{k}}']\right\rangle = (2\pi)^{d+1}2D_o\frac{F[k]}{2\pi k^2}P_{ij}[\mathbf{k}]\delta[\hat{\mathbf{k}}+\hat{\mathbf{k}}'] \qquad (2)$$

where $\hat{v}_i$ and $\hat{f}_i$ are the i^{th}-components of the Fourier amplitudes of the velocity and force vectors, $\hat{\mathbf{k}} = [\mathbf{k},\omega]$ is a four-vector, and $G^o[\hat{\mathbf{k}}] \equiv (-i\omega + \nu_o k^2)^{-1}$

with $k \equiv |\mathbf{k}|$ and ν_o the kinematic viscosity. The tensor $P_{imn}[\mathbf{k}]$ results from elimination of the pressure using the continuity condition $k_i \hat{v}_i[\hat{\mathbf{k}}] = 0$: $P_{imn}[\mathbf{k}] \equiv k_m P_{in}[\mathbf{k}] + k_n P_{im}[\mathbf{k}]$ with projection operator $P_{ij}[\mathbf{k}] \equiv \delta_{ij} - k_i k_j / k^2$, where δ_{ij} is the Kronecker delta function. The cutoff Λ_o is the wavenumber above which viscosity wipes out all motion, $\lambda_o = 1$ is an ordering parameter and d is the number of dimensions. The brackets $<>$ denote an ensemble average. The force, and thus the zeroth-order velocity (in λ_o), is homogeneous and isotropic, defined by the scalar correlation function $F[k]$.

Course graining is achieved with the following steps:

1. Define $\hat{v}_i^< \equiv \hat{v}_i[0 \leq k < k_c]$ and $\hat{v}_i^> \equiv \hat{v}_i[k_c \leq k \leq \Lambda_o]$ (with analogous definitions for $\hat{f}_i^<$ and $\hat{f}_i^>$) where k_c is the low wavenumber cutoff of the band to be eliminated.

2. In the nonlinear term let $\hat{v}_m[\hat{\mathbf{q}}]\hat{v}_n[\hat{\mathbf{k}} - \hat{\mathbf{q}}] = \hat{v}_m^<[\hat{\mathbf{q}}]\hat{v}_n^<[\hat{\mathbf{k}} - \hat{\mathbf{q}}] + 2\hat{v}_n^<[\hat{\mathbf{k}} - \hat{\mathbf{q}}]\hat{v}_m^>[\hat{\mathbf{q}}] + \hat{v}_m^>[\hat{\mathbf{q}}]\hat{v}_n^>[\hat{\mathbf{k}} - \hat{\mathbf{q}}]$.

3. Iteratively substitute for $\hat{v}_i^>$ in the equation for $\hat{v}_i^<$. Iterate a number of times equal to the order of the nonlinearity, i.e. keep terms to order λ_o^2.

4. Ensemble average over $\hat{f}_i^>$ and evaluate all four-dimensional $^>$-integrals. These are integrals whose integrand has wavenumber defined in the interval $[k_c, \Lambda_o]$. All $^>$-integrals are calculated to lowest order in the distant interaction limit. This is the limit in which $^<$-wavenumbers are small compared to $^>$-wavenumbers.

Steps 1-4 eliminate the wavenumber band $k_c \leq k \leq \Lambda_o$.

In addition to terms obtained by replacing $\hat{v}_i$ by $\hat{v}_i^<$ in the original equations, correction terms are generated. They are

a. force renormalization terms. These terms are zeroth-order in $\hat{v}_i^<$ and redefine the force correlation.

b. viscosity renormalization terms. These are linear in $\hat{v}_i^<$ and define an eddy viscosity, $\nu_T = \nu_o + \delta\nu$.

c. vertex renormalization terms. These are second-order in $\hat{v}_i^<$ and redefine the vertex, $\lambda_T = \lambda_o + \delta\lambda$. These terms must vanish in the infrared limit $k \to 0$ by Galilean invariance (Forster et. al., 1977).

d. higher order terms in $\hat{v}_i^<$.

To focus on scale-invariant behavior inherent in the original equations, one justifies neglect of new terms. Then one proceeds to the second half of the RG transformation, the rescaling. In this case the scale-invariant behavior is the balance between forcing and eddy damping and the new terms are higher order in $\hat{v}_i^<$.

One iterates the two-part RG symmetry transformation until the equations converge to a 'fixed point'. At a fixed point, the parameters in the model no longer change; the equations are invariant under the RG transformation and

describe self-similar physics. The scaling laws at a fixed point are often independent of the initial parameter values and capture 'universal' physics contained the original model.

3. The ϵ-expansion

Fournier et. al., (1983) examined the general class of force-correlation functions $F[k] = 2\pi k^{3-\epsilon}$ for $\epsilon > 0$. (The parameter ϵ here simply defines $F[k]$ and is not the dissipation rate, traditionally denoted by the same symbol. In this paper we denote the dissipation rate of the turbulent field by ε to avoid confusion.) They found for the eddy viscosity, after elimination of the wavenumber band $k_c \leq k \leq \Lambda_o$,

$$\nu_T[k_c] = \nu_o(1 + 3\frac{\sigma_1[\epsilon]D_o}{\nu_o^3}(\frac{k_c^{-\epsilon} - \Lambda_o^{-\epsilon})}{\epsilon})^{1/3}. \tag{3}$$

where $\sigma_1[\epsilon] = (d^2 - d - \epsilon)/(4d(d+2)\pi^2)$.

At the fixed point, which is found in the limit $\Lambda_o >> k_c$, $k_c \to k \to 0$, the following asymptotic relations hold:

$$\nu_T[k] \sim (\frac{3\sigma_1[\epsilon]}{\epsilon})^{1/3} D_o^{1/3} k^{-\epsilon/3} \tag{4}$$

$$E[k] \sim (\frac{3\sigma_1[\epsilon]}{\epsilon})^{1/3} D_o^{2/3} k^{1-2\epsilon/3} \tag{5}$$

$$\bar{\lambda} \equiv \frac{\lambda_o D_o^{1/2}}{(\nu_T^{3/2} k_c^{\epsilon/2})} \sim (3\sigma_1[\epsilon])^{-1/2} \epsilon^{1/2} \tag{6}$$

where $\bar{\lambda}$ is the non-dimensionalized expansion parameter (Reynolds number). Relations (4)-(6) are universal in the sense that they do not depend on ν_o.

If $\epsilon < 0$, the fixed point energy spectrum (5) results from force-correlation function $F[k] = 2\pi k^{3-2\epsilon/3}$. The case $\epsilon = -2/3$ was considered by Forster et. al., (1977), and reproduces $E[k] \propto k^2$ for low wavenumbers. This is the power law predicted by Saffman (1967) for homogeneous, isotropic turbulence. For $\epsilon < 0$, the dynamics are not universal at the fixed point.

The point $\epsilon = 0$ is called a crossover point: for $\epsilon < 0$, higher-order terms in $\hat{v}_i^<$ decay exponentially as k_c is decreased and statistics are essentially Gaussian; for $\epsilon > 0$, higher-order terms in $\hat{v}_i^<$ become important and statistics are no longer Gaussian (Fournier et. al., 1978, Kraichnan, 1987, 1989). Neglect of the higher-order terms is rigorously justified only for $\epsilon < 0$. For all $\epsilon > 0$, the higher-order terms in $\hat{v}_i^<$ are marginal (neither grow nor decay exponentially) as k_c is decreased.

For ϵ positive and near zero, the expansion in powers of $\bar{\lambda}$ is likely, but not guaranteed, to be asymptotic by relation (6). Unfortunately, ϵ near zero corresponds to an energy spectrum near $E[k] \sim k$, which is not often observed in nature.

Despite the mathematical uncertainties associated with positive values of ϵ away from zero, Yakhot et. al., (I), applied the RG procedure to the forced Navier Stokes equations (1) and (2) with $\epsilon = 4$. This case models the physically relevant spectrum $E[k] \sim k^{-5/3}$. Their results are exactly equations (3)-(6) with $\epsilon = 4$ everywhere except in the coefficient σ_1. The value $\epsilon = 0$ is used to evaluate σ_1. By relating the parameter D_o to the flow-averaged dissipation rate $\bar{\varepsilon}$, they found the universal scaling law $E[k] = 1.617\bar{\varepsilon}^{2/3}k^{-5/3}$ (Leslie, 1973, I, Dannevik, Yakhot, and Orszag, 1987).

The prediction for Kolmogorov's constant 1.617 is very close to the observed values, which are in the range 1.4-1.6. It is found using $\sigma_1[0] = 1/(10\pi^2)$. If $\sigma_1[4] = 1/(30\pi^2)$ is used, the RG value of Kolmogorov's constant is 1.11. It is not apparent why the coefficient at the fixed point should be evaluated at $\epsilon = 0$ instead of $\epsilon = 4$. Indeed, the general procedure advocated in I is to evaluate all coefficients at the fixed point using $\epsilon = 0$. This procedure is supported by most of the RG results for turbulence. As another example, the Obukhov-Corrsin constant derived using $\epsilon = 0$ is 1.16, while the value derived using $\epsilon = 4$ is 0.41. However, we show in Section 6 that evaluating coefficients in the RG equation for the dissipation rate at $\epsilon = 0$ leads to results that are inconsistent with direct numerical simulations and the traditional model. Paper I does not explain why amplitudes of a k^1-spectrum are used for the theory of a $k^{-5/3}$-spectrum.

If we are only interested in scale-invariant physics, the RG-expansion is likely to reflect its essential features, regardless of the value of ϵ. The difference between ϵ from its crossover value gives a rough idea of the importance of the dynamics that are being neglected and the departure from Gaussian statistics. For high Reynolds number turbulence, with a well-developed $k^{-5/3}$-spectrum, the eddy viscosity (3) with $\epsilon = 4$ may capture the eddy-damping effect of small scales even though all other effects are ignored in the RG analysis. Numerical tests will be decisive (Karniadakis, Yakhot, Rakib, Orszag and Yakhot, 1989).

To summarize, the RG-expansion probably provides an accurate description of self-similar physics. The difference between the expansion parameter and its crossover value is a measure of the importance of other dynamics and of non-Gaussianity. It is not clear if and/or why amplitudes should always be evaluated at the crossover value of the renormalized expansion parameter.

4. Weakly anisotropic turbulence

A model for weakly anisotropic turbulence can be developed by extending the force correlation to depend linearly on the anisotropy tensor b_{ij},

$$< \hat{f}_i[\hat{\mathbf{k}}]\hat{f}_j[\hat{\mathbf{k}}'] >= (2\pi)^{d+1}\delta[\hat{\mathbf{k}}+\hat{\mathbf{k}}']D_o\frac{F[k]}{2\pi k^2}\{2P_{ij}[\mathbf{k}]+$$

$$+\psi\{b_{ij}-\frac{(b_{in}k_nk_j+b_{jn}k_nk_i)}{k^2}+\frac{b_{nm}k_nk_mk_ik_j}{k^4}+$$

$$+\alpha_o(\frac{b_{nm}k_nk_m\delta_{ij}}{k^2}-\frac{b_{nm}k_nk_mk_ik_j}{k^4})\}\} \tag{7}$$

where α_o and ψ are constants. The anisotropy tensor is defined as $b_{ij} \equiv (< v_i[\mathbf{x},t]v_j[\mathbf{x},t] > -(1/3)\kappa\delta_{ij})/\kappa$ where $\kappa \equiv (1/2) < v_i[\mathbf{x},t]v_i[\mathbf{x},t] >$. Relation (7) is the most general weakly anisotropic correlation (i.e. linear in b_{ij}) that satisfies continuity and the required symmetry conditions (Reynolds, 1987). Note that b_{ij} is a matrix of constants because the flow is assumed homogeneous.

In anticipation of an anisotropic eddy viscosity, let

$$G^o[\hat{\mathbf{k}}] = (-i\omega+\nu_o k^2+\beta_o k_m k_n b_{mn})^{-1} \tag{8}$$

in the forced Navier Stokes equations (1), where $\beta_o = 0$. The model given by (1), (7) and (8) has no mean flow.

The RG steps 1-4 result in renormalized equations with correction terms a-d (Section 2) where the eddy damping is now defined by $\nu_T = \nu_o + \delta\nu$ and $\beta_T = \beta_o + \delta\beta$. In addition, a fifth type of term is generated which couples the equation for $\hat{v}_i[\hat{\mathbf{k}}]$ to the equation for $\hat{v}_j[\hat{\mathbf{k}}]$:

e. linear coupling terms. In the equation for $\hat{v}_i[\hat{\mathbf{k}}]$, these are linear in $\hat{v}_j[\hat{\mathbf{k}}]$ and have the form $(k^2b_{ij}-k_ik_mb_{mj})\hat{v}_j^<[\hat{\mathbf{k}}] \equiv M_{ij}\hat{v}_j^<[\hat{\mathbf{k}}]$.

The linear coupling terms show that the small scales can force $\hat{v}_i$ through interaction with $\hat{v}_j$.

One can suppress this forcing by choosing α such that it vanishes at each iteration of the RG scale elimination. The choice

$$\alpha^{(n)} = 1+\psi\frac{7\beta^{(n)}}{2\nu^{(n)}} \tag{9}$$

makes the coefficient of the linear coupling terms zero. The superscript n is the iteration number.

With constraint (9), $F[k] = 2\pi k^{3-\epsilon}$ and $\epsilon = 4$ ($E[k] \sim k^{-5/3}$), one finds

$$\nu_T^{(n+1)} = \nu_T^{(n)}+\sigma_1[\epsilon]\frac{D_o}{(\nu_T^{(n)})^2}\frac{1}{(\Lambda[nr])^4}\frac{(e^{4r}-1)}{4} \tag{10}$$

$$\beta_T^{(n+1)} = \beta_T^{(n)}+\sigma_2[\epsilon]\frac{D_o}{(\nu_T^{(n)})^2}(\frac{\beta_T^{(n)}}{\nu_T^{(n)}}+\psi)\frac{1}{(\Lambda[nr])^4}\frac{(e^{4r}-1)}{4} \tag{11}$$

where $\sigma_1[0] = 1/(10\pi^2)$ as above, $\sigma_2[0] = 1/(40\pi^2)$ and $\Lambda[nr] = \Lambda_o e^{nr} = k_c$. The cutoff k_c is now the last eliminated wavenumber.

The differential equations appropriate for repeated elimination of infinitesimal bands ($r \to 0$) are

$$\frac{d\nu_T[\eta]}{d\eta} = \sigma_1 \nu_T[\eta](\bar{\lambda}[\eta])^2 \tag{12}$$

$$\frac{d\beta_T[\eta]}{d\eta} = \sigma_2(\beta_T[\eta] + \psi\nu_T[\eta])(\bar{\lambda}[\eta])^2 \tag{13}$$

where $\eta \equiv nr$ and $\bar{\lambda}$ is the renormalized expansion parameter given by (6). The solution of (12) subject to $\nu_T[0] = \nu_o$ is equation (3) with $k_c = \Lambda_o e^{-\eta}$; the solution of (13) subject to condition $\beta_T[0] = 0$ is

$$\beta_T[k_c] = \frac{(\sigma_2/\sigma_1)\psi}{(1-\sigma_2/\sigma_1)}(\nu[k_c] - \nu_o^{(1-\sigma_2/\sigma_1)}\nu_T^{\sigma_2/\sigma_1}[k_c]). \tag{14}$$

As in the isotropic theory given in Sections 2 and 3, the fixed point is at $\eta \to \infty$, which corresponds to $k_c \to k \to 0$. According to the theory of Yakhot et. al., one evaluates the coefficients σ_1 and σ_2 at the crossover $\epsilon = 0$. Then $\nu_T[k]$, $E[k]$ and $\bar{\lambda}$ are given by (4)-(6), $\beta_T[k] \sim (1/3)\psi\nu_T[k]$ and

$$\alpha \sim \frac{13}{6}. \tag{15}$$

The parameter α defines the turbulent states that are energetically possible in the model. As α increases, the function space of realizable states decreases (Shih et. al., *to be submitted to J. Fluid Mech.*). The value of α for the Reynolds-stress model of Launder, Reece and Rodi, (1975), is $\alpha_{LRR} = .527$; the value for the Reynolds stress model that matches Rapid Distortion Theory (RDT) is $\alpha_{RDT} = 3/2$. Both models have small regions of realizability around the isotropic turbulence point.

If we suppress the linear coupling terms in the RG analysis, α increases from 1 to 13/6 as more and more scales are eliminated from the problem. In view of the large values of α necessary to prevent linear coupling, turbulence models based on RG theory which includes this coupling seem more promising. The extension is relatively simple: the model equations become

$$\hat{v}_i[\hat{\mathbf{k}}] = G^o[\hat{\mathbf{k}}]\hat{f}_i[\hat{\mathbf{k}}] + \Theta_o M_{ij}[\mathbf{k}]\hat{v}_j[\hat{\mathbf{k}}] - \frac{i\lambda_o}{2}P_{imn}[\mathbf{k}]\int \frac{d\hat{\mathbf{q}}}{(2\pi)^{d+1}}\hat{v}_m[\hat{\mathbf{q}}]\hat{v}_n[\hat{\mathbf{k}}-\hat{\mathbf{q}}] \tag{16}$$

where M_{ij} is defined above and $\Theta_o = 0$. Two special cases were treated by Rubinstein and Barton (1987). This is a possible area of further research. The equations of a passive scalar are amenable to similar analysis.

5. Homogeneous turbulence with a weak mean flow

A formulation of the RG theory of turbulence without an artificial external force would be appealing. One might think that providing an internal production mechanism by including a mean flow would alleviate the necessity of an external force. However, if the zeroth-order turbulent velocity field is sustained by interaction with the mean, then wavenumbers are changing in time as quickly as Fourier amplitudes. For the RG analysis to be meaningful, one requires that wavenumbers stay constant at least in the turnover time of a large eddy.

Thus we continue to assume that the turbulence is sustained by an external force. The homogeneous mean must be considered weak and corrects the zeroth-order solution given by the balance of external forcing and viscous diffusion. Our model equations for the fluctuations $\hat{v}_i'$ are

$$\hat{v}_i'[\hat{\mathbf{k}}] = G^o[\hat{\mathbf{k}}]\hat{f}_i[\hat{\mathbf{k}}] + N_{ij}[\mathbf{k}]\hat{v}_j'[\hat{\mathbf{k}}] - \frac{i\lambda_o}{2}P_{imn}[\mathbf{k}]\int \frac{d\hat{\mathbf{q}}}{(2\pi)^{d+1}}\hat{v}_m'[\hat{\mathbf{q}}]\hat{v}_n'[\hat{\mathbf{k}}-\hat{\mathbf{q}}] \quad (17)$$

$$N_{ij}[\mathbf{k}] = \Pi_{mn}k_m\frac{\partial}{\partial k_n}\delta_{ij} - \Pi_{ij} + 2\frac{k_m k_i}{k^2}\Pi_{mj} \quad (18)$$

where $\hat{v}_i = U_i + \hat{v}_i'$, $U_i \equiv <\hat{v}_i> = \Pi_{ij}x_j$ and Π_{ij} is constant (Leslie, 1973).

For simplicity, one may first consider isotropic, homogeneous forcing given by the correlation (2). The RG procedure is carried out as in Section 2, by repeated substitution of $(\hat{v}_i')^>$ in the equation for $(\hat{v}_i')^<$. For consistent asymptotics, terms of order $\Pi_{ij}^2\lambda_o$ and $\Pi_{ij}\lambda_o^2$ must be retained, while terms of order λ_o^3 may be dropped. One anticipates interesting changes in the RG eddy viscosity.

The RG analysis for homogeneous shear should reproduce the universal scalar spectrum of the Reynolds stress in the inertial range. For shear in the x_2 direction, $U_i = U\delta_{i1}x_2$, RG should predict $4\pi k^2 < \hat{v}_1'[\hat{\mathbf{k}}]\hat{v}_2'[\hat{\mathbf{k}}] > \propto k^{-7/3}$.

One immediately notices the similarity between the model equations with a mean flow (17) and the renormalized model equations due to anisotropic external forcing (16). This similarity can be exploited to reduce the amount of work in the problem with a weak mean flow. It is a straightforward extension to flow with a homogeneous mean driven by a weakly anisotropic external forcing.

6. The RG $\kappa - \varepsilon$ model

The most important RG contribution to turbulence modeling has thus far been low Reynolds number corrections to previously established high Reynolds number equations. The RG corrections are derived, unlike their ad-hoc predecessors.

Unfortunately, there remain unresolved issues in the high Reynolds number RG $\kappa - \varepsilon$ model. These should be reconciled before study of the low Reynolds number corrections. For better understanding of the RG $\kappa - \varepsilon$ equations, the traditional model is reviewed. The Yakhot-Orszag RG model is then discussed. We give a corrections to, and a reinterpretation of, the results cited in I.

6.1. The traditional $\kappa - \varepsilon$ model

The dissipation rate of fluctuations in homogeneous turbulence is $\varepsilon \equiv \nu_o < (\nabla_j v_i')^2 >$ where $v_i'[\mathbf{x}, t]$ are the zero-averaged fluctuations from the mean. As in Section 5, $v_i = U_i + v_i'$, $U_i \equiv < v_i >= \Pi_{ij} x_j$ where Π_{ij} is constant. The time rate of change of ε is

$$\frac{\partial \varepsilon}{\partial t} = -\overbrace{2\nu_o^2 < (\nabla_j \nabla_m v_i')^2 >}^{1} - \overbrace{2\nu_o < (\nabla_j v_i')(\nabla_m v_i') > \nabla_j U_m}^{2} -$$

$$-\overbrace{2\nu_o < (\nabla_j v_i')(\nabla_j v_m') > \nabla_m U_i}^{3} - \overbrace{2\nu_o < (\nabla_j v_i')(\nabla_j v_m')(\nabla_m v_i') >}^{4}. \qquad (19)$$

In the standard, high Reynolds number model of equation (19), the total dissipation of ε is represented by the combination of the dissipation term 1 and the turbulent transport term 4,

$$-2\nu_o^2 < (\nabla_j \nabla_m v_i')^2 > -2\nu_o < (\nabla_j v_i')(\nabla_j v_m')(\nabla_m v_i') > \sim -C_\varepsilon^2 \frac{\varepsilon^2}{\kappa} \qquad (20)$$

where C_ε^2 is an adjustable constant. A typical value of C_ε^2 is 1.8. The total production is traditionally modeled by the sum of the two remaining terms, 2 and 3,

$$-2\nu_o < (\nabla_j v_i')(\nabla_m v_i') > \nabla_j U_m - 2\nu_o < (\nabla_j v_i')(\nabla_j v_m') > \nabla_m U_i$$

$$\sim -C_\varepsilon^1 \frac{\varepsilon}{\kappa} \nabla_j U_i < v_i' v_j' > . \qquad (21)$$

The constant C_ε^1 is also adjustable. A typical value for C_ε^1 is 1.4.

The simplest model of ε for inhomogeneous turbulence simply restores diffusion and advection by the mean,

$$\frac{\partial \varepsilon}{\partial t} + U_j \nabla_j \varepsilon = C_\varepsilon^1 \frac{\varepsilon}{\kappa} P_\kappa - C_\varepsilon^2 \frac{\varepsilon^2}{\kappa} + \nabla_j \chi_T \nabla_j \varepsilon \qquad (22)$$

where χ_T is an eddy diffusivity and $P_\kappa = -\nabla_j U_i < v_j' v_i' >$. The Reynolds stress $< v_i' v_j' >$ is usually modeled by $- < v_i' v_j' >= \nu_T \nabla_j U_i + 2\kappa \delta_{ij}/3$.

Though the parameterizations in (22) are for high Reynolds number turbulence, their signs and general trends are supported by direct numerical simulations of turbulent channel flow (Mansour, Kim, and Moin, 1988). The simulations are necessarily at low Reynolds numbers. In section 6.3, consistency with the simulation data is used to reinterpret the RG-based ε-equation.

6.2. The Yakhot-Orszag RG ε-equation

The goal is to calculate the effect of the small scale velocity field on the large scale variations of ε. The strategy is to assume that the high wavenumber velocity field obeys forced Navier Stokes equations, for examples (1) or (18). The model worked out in I assumes that the high wavenumbers are governed by (1) with homogeneous, isotropic forcing given by (2).

The steps used in I to derive the RG ε-equation are given in CTR Manuscript 106 (Smith, 1989). Many assumptions of the procedure are not explicitly addressed by the authors of I. A large amount of second guessing is required to understand their interpretation of the results. Due to the complexity and vagueness of their method, the steps will not be presented here.

Here we simply state the results reported in I and give corrections. The corrections are to purely mechanical errors and do not address assumptions or interpretation. These more important issues are discussed in section 6.3.

The Yakhot-Orszag high Reynolds number, RG ε-equation is

$$\frac{\partial \varepsilon}{\partial t} + U_j \nabla_j \varepsilon = -1.063 \frac{\varepsilon}{\kappa} P_\kappa - 1.7215 \frac{\varepsilon^2}{\kappa} + \nabla_j \chi_T \nabla_j \varepsilon \tag{23}$$

where $P_\kappa = -\nabla_j U_i < v_i' v_j' >$ as above. The Reynolds stress is again modeled by $- < v_i' v_j' > = \nu_T \nabla_j U_i + 2\kappa \delta_{ij}/3$. The RG theory gives ν_T and χ_T as functions of ε and κ.

The corrected model, based on the same method, assumptions and interpretation, is

$$\frac{\partial \varepsilon}{\partial t} + U_j \nabla_j \varepsilon = 1.594 \varepsilon (a_\infty + \varepsilon b_\infty) + 0.9 \frac{\varepsilon^2}{\kappa} + \nabla_j \chi_T \nabla_j \varepsilon \tag{24}$$

where the coefficient of the production term is identically zero (CTR Manuscript 102, 1989). The constants a_∞ and b_∞ are defined by integrals,

$$a_\infty = -2 \int_0^\infty d\eta \, \nu_T[\eta] \Lambda[\eta]$$

$$b_\infty = 0.2 \int_0^\infty d\eta \, \frac{1}{\nu_T^2[\eta] \Lambda^2[\eta]} \tag{25}$$

where $\nu_T[\eta]$ is given by (3) with $k_c = \Lambda[\eta] = \Lambda_o e^{-\eta}$. The term $1.594\varepsilon(a_\infty + \varepsilon b_\infty)$ has the same scaling as the term $10.5\varepsilon^2/\kappa$, but is of the opposite sign and larger in magnitude. All coefficients in models (23) and (24) are evaluated at the crossover value of the renormalized expansion parameter, $\epsilon = 0$. Models (23) and (24) should be compared with the standard model (22).

6.3. Corrected results reinterpreted

In paper I, the starting point to derive the RG ε-equation is the equation for $\phi \equiv \nu_o(\nabla_j v_i[\mathbf{x},t])^2$. The average of ϕ is the dissipation rate in homogeneous turbulence. The exact equation for ϕ is

$$\frac{\partial \phi}{\partial t} = -v_j \nabla_j \phi + \nu_o \nabla_j \nabla_j \phi - 2\nu_o (\nabla_m \nabla_j v_i)^2 -$$

$$-2\frac{\nu_o}{\rho}(\nabla_j v_i)(\nabla_j \nabla_i P) - 2\nu_o (\nabla_j v_i)(\nabla_j v_m)(\nabla_m v_i) \tag{26}$$

The origin in (26) of the terms in model (24) suggests a reinterpretation consistent with the standard model (22) and direct numerical simulation data for turbulent channel flow. The RG analysis is actually performed on the transform of equation (26) with $\hat{v}_i = \hat{v}_i^< + \hat{v}_i^>$, $\hat{\phi} = \hat{\phi}^< + \hat{\phi}^>$ and $\hat{P} = \hat{P}^< + \hat{P}^>$. The following list gives the origin, Fourier integral and final contribution in real space in the format

*). origin in equation (27)

Fourier integral

$\rightarrow$ final contribution to RG model

a.) a renormalized diffusion term, generated by the $-v_j \nabla_j \phi$ term:

$$-ik_j \int \frac{d\hat{\mathbf{q}}}{(2\pi)^{d+1}} \hat{v}_j^>[\hat{\mathbf{q}}]\hat{\phi}^>[\hat{\mathbf{k}} - \hat{\mathbf{q}}]$$

$$\rightarrow \nabla_j \chi_T \nabla_j \phi^<. \tag{27}$$

b.) a contribution from $-2\nu_o(\nabla_m \nabla_j v_i)^2$:

$$-2\nu_o \int \frac{d\hat{\mathbf{q}}}{(2\pi)^{d+1}} q_m q_j (k-q)_m (k-q)_j \hat{v}_i^>[\hat{\mathbf{q}}]\hat{v}_i^>[\hat{\mathbf{k}} - \hat{\mathbf{q}}]$$

$$\rightarrow \tilde{B}_d \varepsilon (a_\infty + 3\nu_T \Lambda_f^2). \tag{28}$$

c.) contributions from $-2\nu_o(\nabla_j v_i)(\nabla_j v_m)(\nabla_m v_i)$:

$$2i\nu_o \int \frac{d\hat{\mathbf{q}}\, d\hat{\mathbf{r}}\, d\hat{\mathbf{p}}}{(2\pi)^{2d+2}} \delta[\hat{\mathbf{k}} - \hat{\mathbf{q}} - \hat{\mathbf{r}} - \hat{\mathbf{p}}] q_j \hat{v}_i^>[\hat{\mathbf{q}}] p_m \hat{v}_i^>[\hat{\mathbf{p}}] r_j \hat{v}_m^<[\hat{\mathbf{r}}] \quad +$$

$$+ \quad 2i\nu_o \int \frac{d\hat{\mathbf{q}}\, d\hat{\mathbf{r}}\, d\hat{\mathbf{p}}}{(2\pi)^{2d+2}} \delta[\hat{\mathbf{k}} - \hat{\mathbf{q}} - \hat{\mathbf{r}} - \hat{\mathbf{p}}] q_j \hat{v}_i^>[\hat{\mathbf{q}}] r_j \hat{v}_m^>[\hat{\mathbf{r}}] p_m \hat{v}_i^<[\hat{\mathbf{p}}]$$

$$\rightarrow \tilde{B}_d \varepsilon \nu_T (\nabla_j v_i^<)^2 (b_\infty + \frac{3}{2} \frac{(d^2 + d + \epsilon - 6)}{2d(d+2)} \frac{1}{\nu_T^2 \Lambda_f^2}). \tag{29}$$

In b.) and c.), Λ_f is the integral scale. The relationships between Λ_f, ν_T, ε and κ are

$$\nu_T \Lambda_f^2 = \frac{3}{2} C_K \gamma[\epsilon] \frac{\varepsilon}{\kappa}$$

$$\nu_T = c_\nu[\epsilon] \frac{\kappa}{\varepsilon} \tag{30}$$

where $\tilde{A}_d = (d^2 - d - \epsilon)/(2d(d+2))$, $\tilde{B}_d = 1.5\tilde{A}_d/.1904$, $\gamma[\epsilon] = (3\tilde{A}_d \tilde{B}_d/8)^{1/3}$, $c_\nu[\epsilon] = (4\gamma[\epsilon])/(9C_K^2[\epsilon])$ and $C_K[\epsilon]$ is the RG prediction for Kolmogorov's constant.

In the corrected Yakhot-Orszag model described by (24) and (25), the constants were evaluated at the crossover value of the renormalized expansion parameter ϵ. Here the ϵ-dependence is shown explicitly. The definition of b_∞ as a function of ϵ is

$$b_\infty = -\frac{(d^2 + d + \epsilon - 6)}{2d(d+2)} \int_0^\infty d\eta \, \frac{1}{\nu_T^2[\eta] \Lambda^2[\eta]}. \tag{31}$$

The expression (3) for $\nu_T[\eta]$ and $\Lambda[\eta] = \Lambda_o e^{-\eta}$ may still be used to evaluate a_∞ and b_∞. The coefficient defining a_∞ is not a function of ϵ. The renormalized diffusivity χ_T is a function of ϵ.

The division into $^>$ and $^<$ functions identifies the sub-equation in (26) that generates the renormalized ε-equation. The derivation in I associates $v_i^>$ with v_i', $v_i^<$ with U_i and $\varepsilon = \nu_o < (\nabla_j v_i^>)^2 >= \nu_T < (\nabla_j v_i^<)^2 >$. The contributing sub-equation is then

$$\frac{\partial \varepsilon}{\partial t} = -U_j \nabla_j \varepsilon + \nabla_j \chi_T \nabla_j \varepsilon - 2\nu_o^2 < (\nabla_j \nabla_m v_i')^2 > -$$

$$-2\nu_o < (\nabla_j v_i')(\nabla_m v_i') > \nabla_j U_m - 2\nu_o < (\nabla_j v_i')(\nabla_j v_m') > \nabla_m U_i. \tag{32}$$

Equation (32) is the exact equation (19) for ε without the turbulent transport term and with advection and diffusion restored.

The simulation data for channel flow indicates that the contribution c.) should be a production term. If the Reynolds stress is modeled by $- < v_i' v_j' >= \nu_T \nabla_j U_i$, then $P_\kappa = \nu_T (\nabla_j U_i)^2 = \nu_T < (\nabla_j v_i^<)^2 >= \varepsilon$. Thus, in the context of RG and traditional modeling, we may label $\nu_T < (\nabla_j v_i^<)^2 >$ either P_κ or ε, depending on the sign of its coefficient.

The sign of contribution c.) is positive, in accord with the numerical simulation data. Thus we should identify c.) as

$$1.594\varepsilon P_\kappa (b_\infty[0] - \frac{4.8}{\kappa}), \tag{33}$$

where b_∞ is larger in magnitude than the $1/\kappa$ term and has the opposite sign.

The interpretation (33) is consistent with standard model (22) and the simulation data for channel flow, and gives

$$\frac{\partial \varepsilon}{\partial t} + U_j \nabla_j \varepsilon = 1.594\varepsilon(a_\infty[0] + \varepsilon b_\infty[0]) +$$

$$+5.7\frac{\varepsilon^2}{\kappa} - 4.8\frac{\varepsilon}{\kappa}P_\kappa + \nabla_j \chi_T \nabla_j \varepsilon. \tag{34}$$

In equations (33) and (34) all coefficients have been evaluated at $\epsilon = 0$.

7. RG analysis of optimal equations

The Euler-Lagrange (EL) equations governing the optimization of a mean field moment, subject to constraints derived from the Navier Stokes equations, have smooth, ordered solutions. The EL solutions better approximate the ordered features of turbulent flow with each additional constraint. A particular class of EL equations that approximates the equations of shear turbulence has solutions of self-similar, downstream rolls (Busse, 1970). This scale-invariant structure suggests that RG analysis of EL equations may be fruitful.

Well chosen EL equations may adequately capture 'order within disorder' and predict the organized motions observed in real turbulent flows. For example, the size of the smallest downstream roll in the above mentioned solutions is a prediction for the spacing of the streaks near the wall in shear flows. The fact that these EL equations capture self-similar physics indicates that optimal theory and RG theory are different approaches that may sometimes isolate the same phenomena. Perhaps they are complimentary when applied to the turbulence problem.

Optimal theory has until now been restricted to semi-analytically tractable EL equations. Thus, the constraints have been limited to the boundary conditions, continuity and the integral statement of energy balance. A joint project with F. Waleffe is an upper bound formulation based on additional constraints which impose the balance of vorticity. Such a formulation requires numerical solution, but will unquestionably provide better and more accurate information about the ordered structures in turbulent shear flows. (See the CTR 1989 Annual Report by F. Waleffe.)

The optimal equations constrained by the boundary conditions, continuity and the integral statement of energy have the same linear terms as the Navier Stokes equations and different nonlinear terms. Only the nonlinear terms are

affected by the addition of more constraints. The existence of nonlinear terms which represent only the ordered, self-similar physics inherent in the Navier Stokes nonlinear terms would be intriguing. The RG method is not limited by nonlinearity, however complicated. Features such as the streak spacing and the slope of the logarithmic layer should be products of RG analysis.

8. Conclusions

There remain unanswered questions about the Yakhot-Orszag theory of turbulence based on renormalization group techniques. Among them are 'What is the meaning of evaluating coefficients at the crossover value of the nondimensionalized expansion parameter?' and 'What is the correct procedure for deriving a model equation for the dissipation rate?'. Extension of the theory to weakly anisotropic flow, and to flow with a mean, may help answer these questions as well as improve eddy viscosity/diffusivity models. Finally, RG analysis of optimal equations may help isolate the ordered features of turbulent flows.

REFERENCES

BUSSE, F., 1970 *J. Fluid Mech.* **41**, 219.

CHEN, S. & KRAICHNAN, R. H. 1989 *Phys. Fluids A.* **1** 2019.

DANNEVIK, P., YAKHOT, V., & ORSZAG, S. A. 1987 *Phys. Fluids* **30**, 2021.

FEIGENBAUM, M. J. 1979 *Journal of Statistical Physics* **21**, no. 6, 669.

FORSTER, D., NELSON, D. R., & STEPHEN, M. J. 1977 *Physical Review A* **16**, no. 2, 732.

FOURNIER, J.-D. & FRISCH, U. 1977 *Physical Review A* **17**, no. 2, 747.

FOURNIER, J.-D. & FRISCH, U. 1983 *Physical Review A* **28**, no. 2, 1000.

KARNIADAKIS, G., YAKHOT, A., RAKIB, S., ORSZAG, S., & YAKHOT, V. 1989 7^{th} Symposium on Turbulent Shear Flows, Stanford University.

KRAICHNAN, R. H., 1987 *Phys. Fluids* **30**, 2400.

KRAICHNAN, R. H., 1989 *Physica D* **37**, 160.

LAUNDER, B. E., REECE, G. L., & RODI, W. 1975 *J. Fluid Mech.* **68**, 537.

LESLIE, D. C. 1973 *Developments in the Theory of Turbulence*, Clarendon Press, Oxford.

LUMLEY, J. L. 1978 *Advances in Applied Mathematics* **18**, Academic Press, New York, 123-176.

MA, S.-K. 1976 Modern Theory of Critical Phenomena, (Frontiers in Physics; 46).

MANSOUR, N. N., KIM, J., & MOIN, P 1988 *J. Fluid Mech.* **194**, 15.

REYNOLDS, W. C. 1987 Fundamentals of Turbulence for Turbulence Modeling and Simulation, Von Karman Institute lecture notes.

RUBINSTEIN, R. & BARTON, J. M. 1987 *Phys. Fluids* **30**, 2987.

SAFFMAN, P. G. 1967 *J. Fluid Mech.* **27**, 581.

SHIH, T.-S. & REYNOLDS, W. C. *to be submitted to J. Fluid Mech.*

SMITH, L. M. 1990 CTR Manuscript 106.

WILSON, K. G. & KOGUT, J. 1974 *Phys. Rep.* **12**, 75.

YAKHOT, V. & ORSZAG, S. A. 1986 *Journal of Scientific Computing* **1**, no. 1, 3.

Short-time Lyapunov exponent analysis

By J. A. Vastano

A new technique for analyzing complicated fluid flows in numerical simulations has been successfully tested. The analysis uses short-time Lyapunov exponent contributions and the associated Lyapunov perturbation fields. A direct simulation of Taylor-Couette flow just past the onset of chaos demonstrated that this new technique marks important times during the system evolution and identifies the important flow features at those times. This new technique will now be applied to a "minimal" turbulent channel.

1. Introduction

Numerical simulations of turbulence are increasing in number and quality each year. These simulations provide a wealth of information about the structure of turbulent flows. The analysis of these flows must start, therefore, by discovering when and where to look at the system in order to see the important events in the flow evolution. Short-time Lyapunov exponent analysis is a new technique that shows promise for finding these events. Research at the Center for Turbulence Research over the past year has shown that this technique can successfully locate the times during a flow evolution when important chaos-producing mechanisms are operating. At these times, the structure of the perturbation fields associated with the Lyapunov exponent computation give a picture of those flow features in which the exponential growth of perturbations is occurring. This report will define the Lyapunov exponent spectrum, describe the short-time contributions and fields used in the analysis, and discuss the numerical tests that have been performed.

2. Lyapunov exponent analysis

The asymptotic motion of a bounded, dissipative system is on some attracting set in its phase space (Eckmann and Ruelle 1985). Attractors range from simple fixed points to chaotic strange attractors. The Lyapunov exponent spectrum provides a fundamental description of the geometric and dynamical properties of an attractor. Lyapunov exponents measure the long-term average exponential growth rate of perturbations to the system trajectory in phase space. More precisely, if the time evolution of the system x is given by

$$\dot{x} = F(x),$$

then a perturbation δx evolves according to

$$\dot{\delta x} = J(x)\delta x;$$

where $J(x)$ is the linearized form of $F(x)$, $J(x) = dF/dx$. For a given initial condition $x(0)$ on the attractor and an initial perturbation $\delta x(0)$,

$$\delta x(t) = M(t, x(0))\delta x(0),$$

where

$$M = \int_0^t J(x(s))ds$$

The long-time evolution of perturbations will be governed by the eigenvalues of M^*M. The eigenmodes specify perturbation fields $\delta x_i(0)$ that will grow at the rates given by the eigenvalues. We define the Lyapunov exponents λ_i by

$$\lambda_i = \lim_{t\to\infty} \frac{1}{t} \log(|\delta x_i(t)|/|\delta x_i(0)|).$$

The exponents are ordered so that λ_1 is largest. There are an infinite number of Lyapunov exponents for a spatially-extended system. Each exponent corresponds, roughly, to a separate direction in phase space. The Kaplan-Yorke conjecture (Frederickson et al. 1983) gives a simple formula that relates the Lyapunov exponents of an attractor to its dimension. Initial perturbations in almost any direction will grow at the rate λ_1, but there exist subspaces of the initial tangent space for which perturbations grow at the rates given by the other Lyapunov exponents as well. In computing the exponents, one follows N perturbations to estimate N Lyapunov exponents. A standard technique exists for evolving the perturbations for long times and obtaining estimates of all N exponents (Benettin et al. 1980) The basic procedure is the Gram-Schmidt reorthogonalization, which removes from the i-th perturbation field those components corresponding to growth at rates λ_1 through λ_{i-1}.

The greatest difficulty in computing Lyapunov exponent spectra for model systems is that the convergence of the running estimates to the long-time average exponents is slow (like $1/t$) and cannot be accelerated. On the other hand, it has been argued (Goldhirsch et al. 1987, Greene and Kim 1987) that the evolving perturbation fields $\delta x_i(t)$ decay exponentially fast to the eigenmodes of $M(t, 0)$ and, furthermore, that these functions are themselves a smooth field over the attractor. In other words, the Lyapunov perturbation fields are local properties on the attractor. If this is the case, then the short-time contributions to the long-time average exponent,

$$\Delta\lambda_i(t) = \frac{1}{\Delta t} \log(|\delta x_i(t + \Delta t)|/|\delta x_i(t)|)$$

are also local properties on the attractor.

The growth of perturbations to the system at any time can be measured by projecting the perturbation onto the local Lyapunov perturbation fields and

checking the short-time expansion rates. Clearly, when these short-time rates are much smaller or larger than average, perturbation will either be damped or expand at large rates. In addition, if the perturbation fields themselves have structure, they indicate where in physical space the mechanisms driving the instability are located, and the form of the instability.

3. A test case

To test the utility of the short-time exponent analysis, numerical simulations were performed on Taylor-Couette flow just past the onset of chaos in that system. This system was chosen because there is experimental evidence that the flow is low-dimensionally chaotic at computationally accessible Reynolds numbers. A code for computing the base flow already existed (Moser et al. 1985) and could be easily extended to the computation of N Lyapunov exponents. Although there had been a great deal of previous experimental, theoretical, and numerical work on this system, the transition to chaos was not understood. In particular, no physical mechanism or instability underlying the transition from quasiperiodic to chaotic flow had been determined.

The particular Taylor-Couette flow studied was chosen to match the most complete experiment to date on the transition to chaos in this system (Brandstater et al. 1985, Brandstater and Swinney 1987). For this case, the outer cylinder is fixed and the inner rotates at a constant frequency. At Reynolds numbers R near zero, the flow state is Couette flow, axially and azimuthally homogeneous. At a critical Reynolds number R_c, a bifurcation to another steady flow occurs. This is Taylor vortex flow, consisting of an axial stack of ring vortices, still azimuthally homogeneous. Neighboring vortices rotate in the opposite sense, so that vortices are separated by alternating inflow and outflow boundaries. The axial wavelength is defined by a pair of Taylor vortices. In the experiment of Brandstater and Swinney, the average axial wavelength was 2.5 times the gap between cylinders. The numerical simulation assumes axial periodicity; the axial period is set to 2.5 gaps.

At higher Reynolds numbers, first one and then a second azimuthal travelling wave appear on the vortices. Each travelling wave introduces an independent frequency of motion to the flow. The waves have integer azimuthal wavenumber: in the experiment of Brandstater and Swinney, both travelling waves had wavenumber four. This is convenient for the simulations, since the state is four-fold symmetric in the azimuthal direction and it is only necessary to simulate a quarter of the azimuthal extent. In the experiment, the onset of quasiperiodic (two-frequency) flow occurred at $R/R_c = 10.0$, and a chaotic flow was observed at $R/R_c = 11.7$. The dimension of chaotic attractors can be determined from time series data. Experimental time series yielded dimension estimates between two and three for Reynolds numbers as high as $R/R_c = 15$.

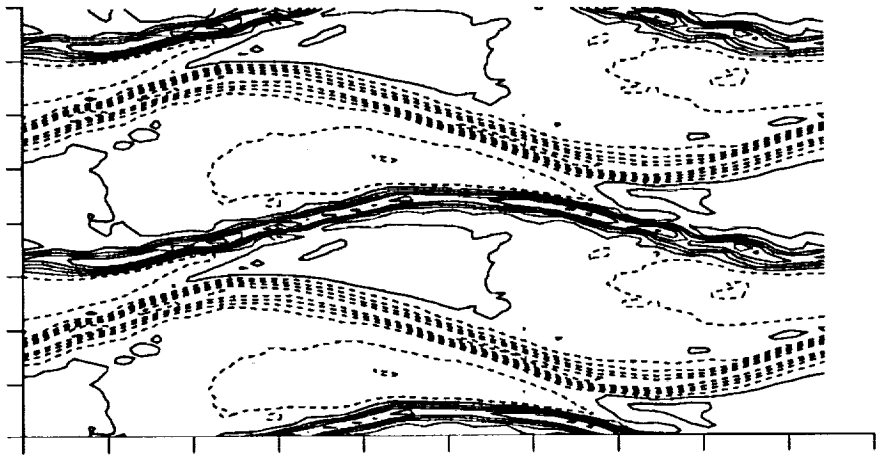

FIGURE 1. Contours of azimuthal velocity at a midplane in r for $R/R_c = 12.0$. The horizontal axis is the azimuthal direction and the vertical axis is the axial direction. One-quarter of the cylinder is shown azimuthally, and two axial wavelengths (twice the computational grid) are shown axially.

4. Results

To convert the code of Moser et al. to estimate N, Lyapunov exponents required following $N + 1$ times as many fields. The linear part of the time evolution operator is identical for the base flow and the perturbations. The nonlinear term of the evolution operator for the base flow is $u \times \omega$. For the perturbations, this term becomes $\delta u \times \omega + u \times \delta\omega$. The only other addition to the code was the Gram-Schmidt reorthogonalization procedure, which is done every few time steps, primarily to give smooth short-time contribution curves. Since computing N Lyapunov exponents requires $(N+1)$ times as many grid points as does the base simulation, it was essential to use the lowest resolution possible. The resolution used in the simulations was 16 Chebyshev modes radially by 32 Fourier modes in the axial and azimuthal directions. This resolution was sufficient to capture the flow in the quasiperiodic regime immediately prior to the onset of chaos with good accuracy. The travelling wave frequencies were predicted to within 2% of the values seen in experiment at $R/R_c = 11$. Increasing the number of radial modes to 32 dropped the discrepancy to less than a percent, but did not otherwise alter the flow.

A sample flow visualization, at $R/R_c = 12$, is shown in Figure 1. This is a picture at an instant of time of a chaotic flow. The quantity shown is the azimuthal velocity component of the flow at a radial midplane. The more focused, higher velocity jet is the radial outflow boundary jet, while the more diffuse

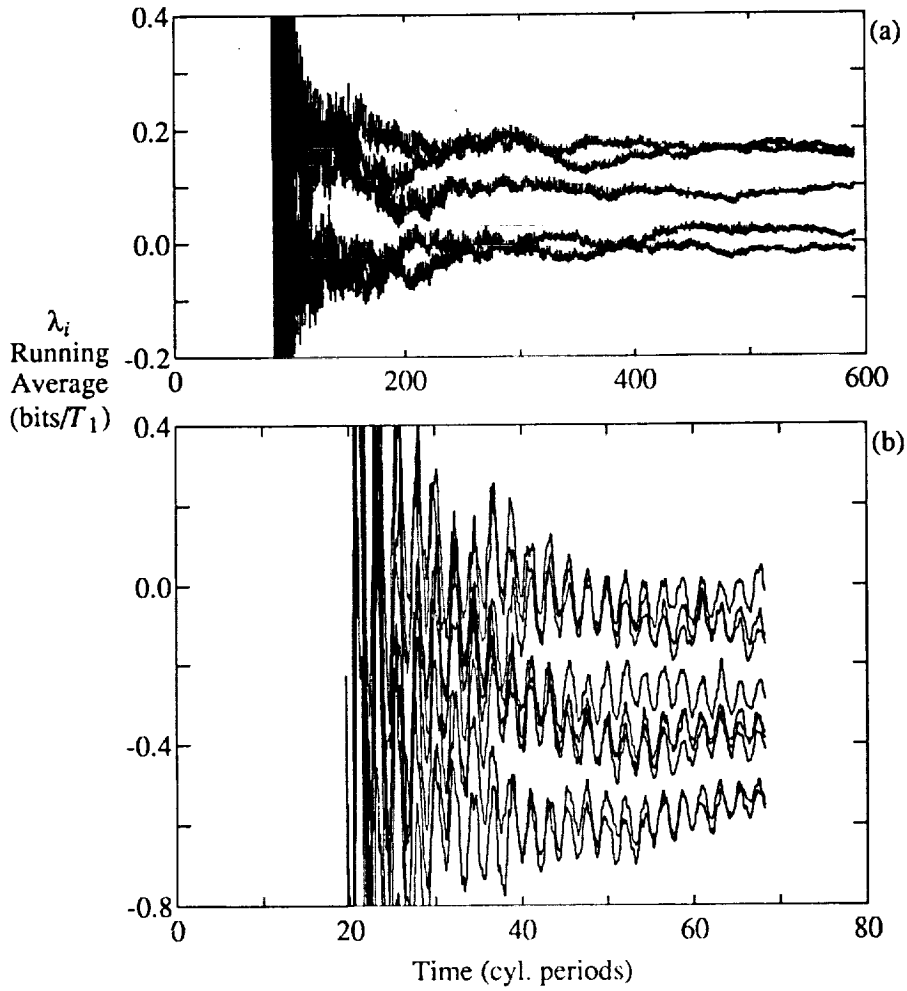

FIGURE 2. Convergence of the Lyapunov exponents at $R/R_c = 11.32$ for (a) the first five exponents, (b) exponents six through fourteen.

jet is the radial inflow boundary jet. The jets are labelled by their radial components, but the dominant velocity component in both jets is azimuthal, not radial. Chaos appeared in the simulations at about $R/R_c = 11.1$, earlier than had been observed in experiments. A power spectral analysis of a numerically computed time series showed that the travelling wave peaks in the spectrum corresponding to the travelling wave frequencies were about 8 decades above the broadband noise component at $R/R_c = 11.3$. The experiments had only six decades of signal-to-noise separation; thus, it is probable that the chaos was already present in the experiment at this Reynolds number, but was masked by the instrumental noise.

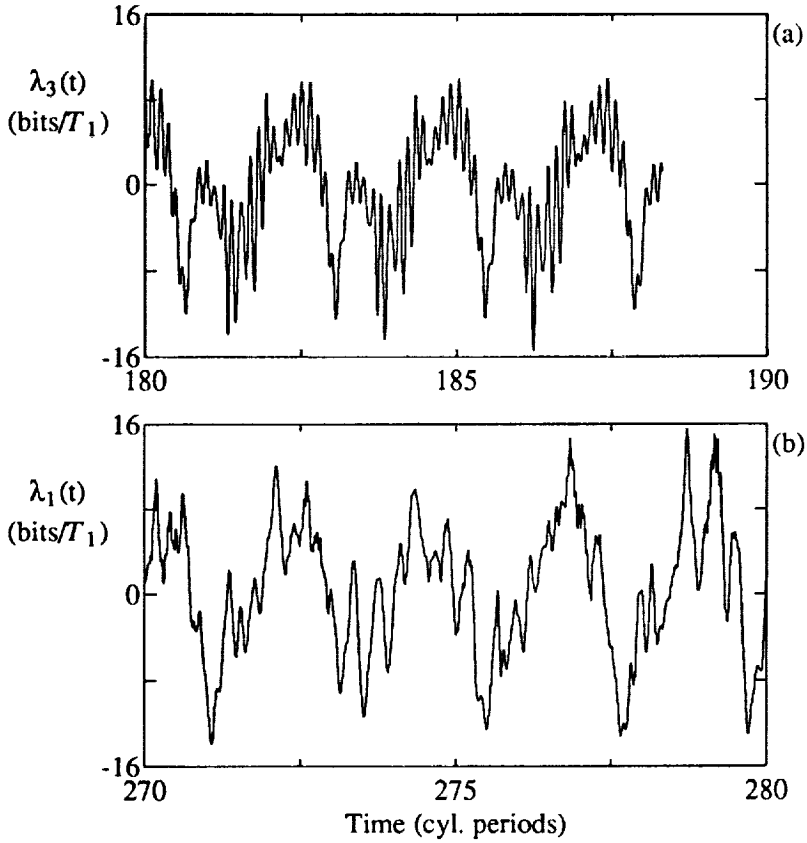

FIGURE 3. Short-time contributions to the first nonzero Lyapunov exponent for (a) $R/R_c = 9.71$ (quasiperiodic), and (b) $R/R_c = 11.32$ (chaotic).

The convergence of the Lyapunov exponents in the simulation is shown in Figure 2. The first five exponents were computed for almost 600 cylinder revolutions, but clearly from the figure they are just converging. The next nine exponents were followed for a much shorter time, and there is still a large uncertainty in their estimates. The trend in the exponents is clear, however, and the Kaplan-Yorke formula gives an attractor dimension of about nine. This is higher than the values between 2 and 3 determined from experimental data. It would appear that low amplitude structure unresolved in the experiments adds significantly to the dimension of the chaos.

Computation of well-converged Lyapunov exponent spectra is expensive: the runs described above used more than 500 hours of CPU time on a Cray-YMP computer. This is in contrast to the short-time Lyapunov exponent contributions, shown in Figure 3 for a quasiperiodic and a chaotic case. The perturbation fields, started from random initial conditions, evolved very rapidly towards

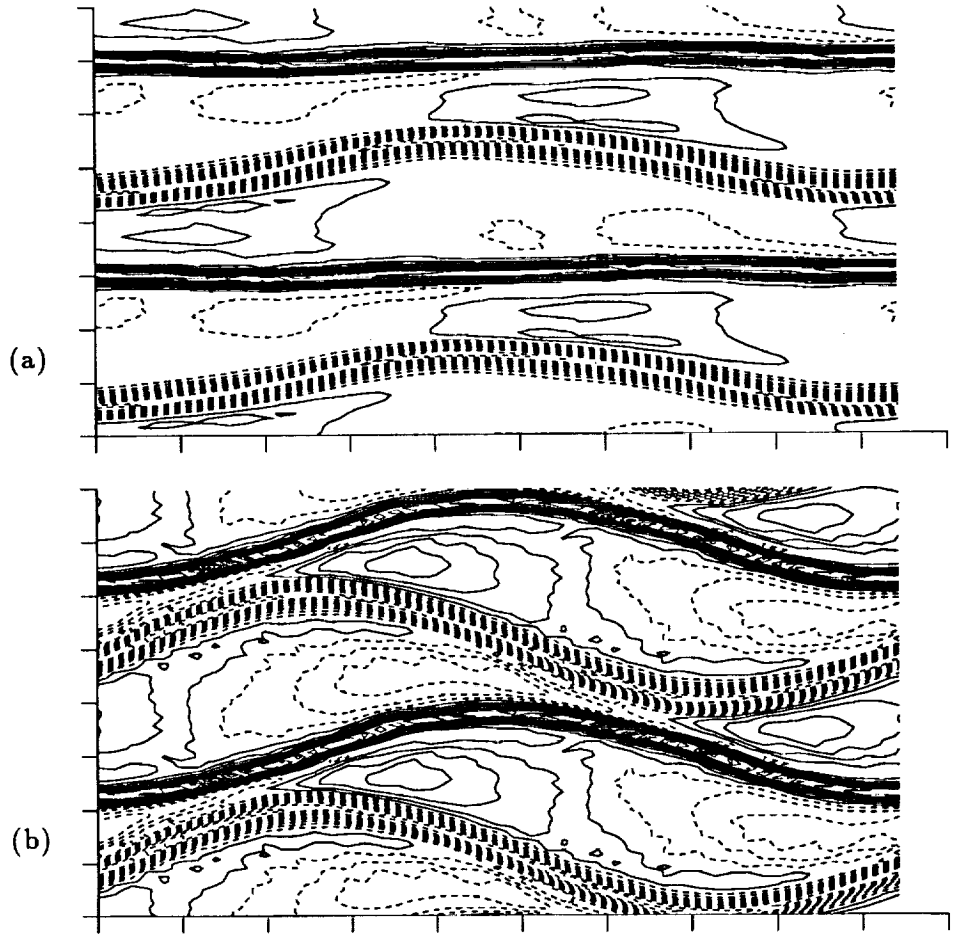

FIGURE 4. The chaotic flow at $R/R_c = 11.32$. Shown are the azimuthal velocity contours at a midplane in r for (a) a minimum in the short-time contributions to λ_1, and (b) a maximum.

asymptotic forms that are displayed at selected times for the chaotic case in Figure 5. The short-time contributions settled down somewhat more slowly than the gross form of the perturbation fields, but were qualitatively similar to the time traces shown in Figure 3 within 40 cylinder revolutions.

The first thing to notice about the short-time contributions is the enormous variation of the contributions compared to the long-time average exponents. For the quasiperiodic case, the contributions are to the first negative exponent, which has a value of -0.4 bits/T_1, where T_1 is the period of the primary travelling wave. For the chaotic case, the contributions shown are for the first exponent, which has a value of 0.35 bits/T_1. The short-time contributions can be forty times or

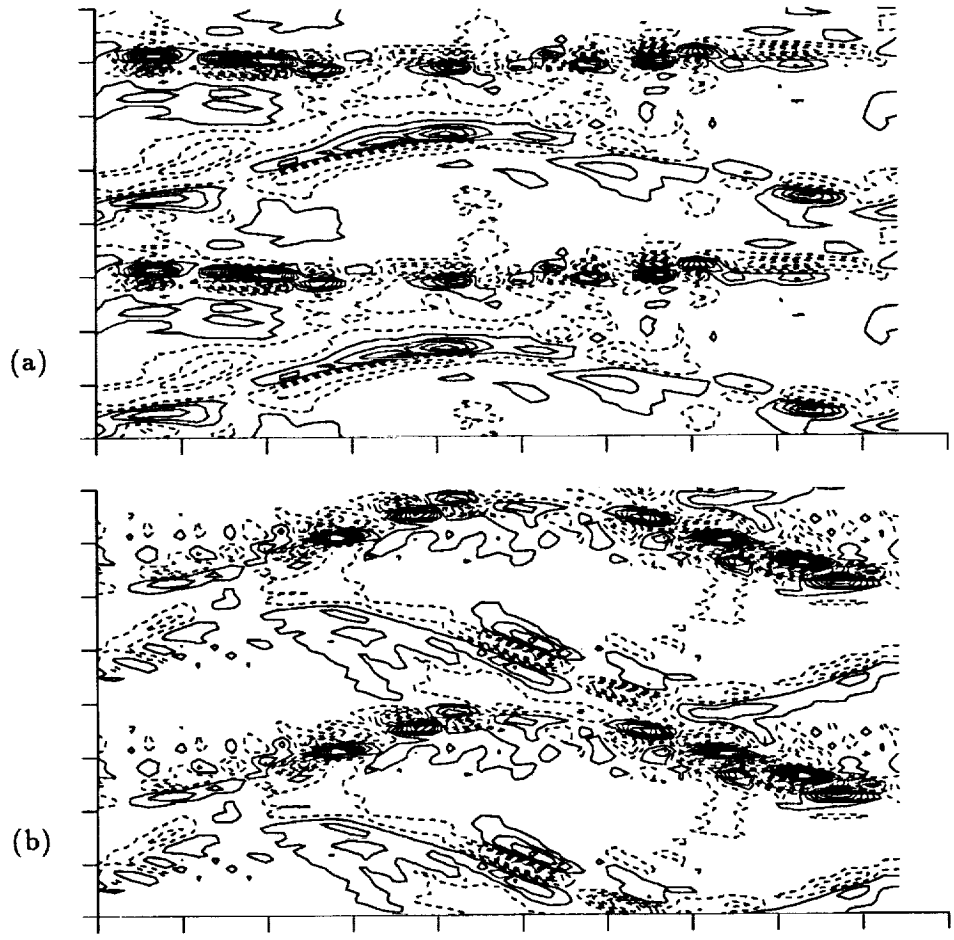

FIGURE 5. The perturbation field corresponding to λ_1 for the flow of Fig. 4. Shown are the azimuthal velocity contours at a midplane in r for (a) a minimum in the short-time contributions to λ_1, and (b) a maximum.

more the size of the long-time average, and of either sign. There are fairly rapid, small oscillations in the contributions that are not yet understood; they may be related to the evolution of structures in the perturbation fields. The large scale oscillations on a time scale of two cylinder periods are the important features for understanding the flow. At minima, perturbations to the flow are crushed, while at maxima they can expand at an enormous rate (for a short time). Figure 4 shows the chaotic flow at times corresponding to a minimum and the succeeding maximum of the short-time contributions to λ_1. The large-scale change in the wave-forms is the quasiperiodic part of the flow. The separation of the outflow and inflow jets at closest approach is much smaller at the maximum time than at

the minimum time. This seems to be what triggers the instability of the flow that causes the chaos. The jet profiles have been followed as they evolve, and there does not appear to be any change in the jets other than their separation. The nature of the instability that is triggered can be seen in Figure 5, which displays the perturbation field at the same times. All of the energy in the perturbation is concentrated on the outflow boundary jet at both times, and it has the same general form: the outflow jet is rolling up. Examination of the perturbation field at other radial locations shows no important radial effects, so while the jet is not two-dimensional, the instability is very much a Kelvin-Helmholtz type phenomenon.

The instability scenario gleaned from the short-time analysis is this: as the quasiperiodic evolution of the flow proceeds, the outflow jet is destabilized by the close approach of the inflow boundary jet. For some part of the overall evolution, a perturbation of the outflow jet in the form of a roll-up of the jet can grow. This produces the chaos in the system. Examination of Figure 1 shows that at higher Reynolds numbers, the roll-up becomes more apparent in the base flow itself. The same type of perturbation field is also observed for the quasiperiodic case, indicating that prior to the instability, the same mechanism is present as a damped mode.

5. Future plans

The test case has shown that short-time Lyapunov exponent analysis can be a useful tool for examining chaotic flows. The next step will be to apply this tool to a fully turbulent flow. The plane channel case studied by Keefe (1987) has an extremely high dimension, requiring the evolution of many hundreds of perturbation fields. This will not be possible in an economical way. A better alternative is the "minimal" channel studied by Jiménez (1989): not only will the dimension and thus the number of requisite perturbations be lower, but the number of structures in the flow will be reduced, simplifying the task of identifying which of them are important to the turbulence evolution

REFERENCES

BENETTIN, G., GALGANI, L., GIORGILLI, A., & STRELCYN, J.-M. 1980 Lyapunov Characteristic Exponents for Smooth Dynamical Systems . *Meccanica.* **15,** 9.

BRANDSTATER, A., SWIFT, J., SWINNEY, H. L., WOLF, A., FARMER, J. D., JEN, E., & CRUTCHFIELD, J. P. 1983 Low-Dimensional Chaos in a Hydrodynamic System. *Phys. Rev. Lett.* **51,** 1442.

BRANDSTATER, A. & SWINNEY, H. L. 1987 Estimating the dimension of strange attractors. *Phys. Rev. A.* **35,** 2207.

ECKMANN, J.-P. & RUELLE, D. 1985 Ergodic theory of chaos and strange attractors. *Rev. Mod. Phys.* **57**, 617.

KEEFE, L., MOIN, P., & KIM, J. 1987 The Dimension of an Attractor in Turbulent Poiseuille Flow. *APS Bull.*. **32**, 2026.

FREDERICKSON, P., KAPLAN, J. L., YORKE, E. D., & YORKE, J. A. The Liapunov Dimension of Strange Attractors J. Diff. Equ. *49*. **185.**

GOLDHIRSCH, I., SULEM, P.-L., & ORSZAG, S. A. 1987 Stability and Lyapunov Stability of Dynamical Systems: A Differential Approach and a Numerical Method. *Physica.* **27D**, 311.

GREENE, J. M., & KIM, J.-S. 1987 The Calculation of Lyapunov Spectra. *Physica.* **24D**, 213.

JIMÉNEZ, J. 1989 Transition to turbulence in two dimensional Poiseuille flow. *J. Fluid Mech.* , (to appear).

MOSER, R. D., MOIN, P., & LEONARD, A. 1983 A Spectral Numerical Method for the Navier-Stokes Equations with Applications to Taylor-

COUETTE FLOW J. Comp. Phys 52. *524*.

Center for Turbulence Research
Annual Research Briefs - 1989

Organized motions underlying turbulent shear flows

By F. Waleffe

1. Introduction

The objective of this project is to determine the nature and significance of the organized motions underlying turbulent shear flows. There is considerable experimental evidence for the existence of such motions. In particular, one consistently observes longitudinal streaks with a spacing of about 100 in wall units in the near-wall region of wall-bounded shear flows. Recently, an analysis based on the *direct resonance* mechanism has predicted the appearance of streaks with precisely such a spacing. Also, the *minimum channel* simulations of Jimenez and Moin have given a strong dynamical significance to that spanwise length scale. They have shown that turbulent-like flows can not be maintained when the spanwise wavelength of the motion is constrained to be less than about that critical number.

A critical review of the direct resonance ideas and the non-linear theory of Benney and Gustavsson is presented first. It is shown how this leads to the later *mean flow-first harmonic* theory of Benney. Finally, we note that a different type of analysis has led to the prediction of streaks with a similar spacing. This latter approach consists of looking for *optimum fields* and directly provides deep insights into why a particular structure or a particular scale should be preferred. Extension of past work is proposed.

2. The Direct resonance concept

The full velocity field is separated into a mean $\bar{u}(y)$ and a perturbation. The equation for the mean is obtained by averaging the incompressible Navier-Stokes equations over x, z, t:

$$\frac{1}{R}\frac{d^2}{dy^2}\bar{u} = \frac{\partial}{\partial x}\bar{P} + \frac{d}{dy}\overline{uv} \tag{1}$$

The equations for the perturbations are then derived by subtracting the averaged equations from full Navier-Stokes. Eliminating the pressure and using continuity leads to a set of equations for the remaining 2 degrees of freedom, which correspond to the vertical velocity v and the vertical vorticity η. One finds:

$$(\frac{\partial}{\partial t} + \bar{u}\frac{\partial}{\partial x} - \frac{1}{R}\nabla^2)\nabla^2 v - \bar{u}''\frac{\partial}{\partial x}v = NL_v \tag{2}$$

$$(\frac{\partial}{\partial t} + \bar{u}\frac{\partial}{\partial x} - \frac{1}{R}\nabla^2)\,\eta + \bar{u}'\frac{\partial}{\partial z}v = NL_\eta \tag{3}$$

where the non-linear terms, NL_v, NL_η, are given in Jang, et al. (1986). The boundary conditions are $v = \frac{\partial}{\partial y} v = \eta = 0$ at the walls ($y = \pm 1$ say), together with some periodicity conditions in the x and z directions.

In the linear case, one looks for normal mode solutions of the form:

$$v = \hat{v}(y) e^{i(\alpha x + \beta z - \omega t)} \tag{4}$$

$$\eta = \hat{\eta}(y) e^{i(\alpha x + \beta z - \omega t)} \tag{5}$$

The equation for the vertical velocity v, which decouples from the vertical vorticity, is known as the Orr-Sommerfeld (OS) equation. It constitutes an eigenvalue problem. The vertical vorticity is then obtained as the solution of a forced ODE. This can be done by expanding $\hat{\eta}$ in a series based on the eigenmodes of the homogeneous problem (also known as the *Squire* equation). Each term in the expansion is proportional to $(\omega - \omega_i)^{-1}$, where ω is an eigenvalue of the OS equation and ω_i an eigenvalue of the Squire equation associated to an eigenmode $\eta_i(y)$. Of course, this procedure breaks down if any eigenvalue of the Squire equation is identical to the OS eigenvalue. This situation corresponds to a *direct resonance*. The free modes of the vertical vorticity equation are always damped (that equation is simply advection-diffusion with zero boundary conditions and no forcing). In consequence, a direct resonance can only occur for damped modes. But even in the case of near-resonance, there is the possibility that the vertical vorticity attains high amplitudes before the final viscous decay.

The general solution of the time dependent problem for a vertical vorticity of the form $\eta(y,t)e^{i(\alpha x + \beta z)}$ is given by:

$$\eta(y,t) = \beta \lambda_0 \, \frac{e^{-i\omega t} - e^{-i\omega_0 t}}{\omega - \omega_0} \, \eta_0(y) + R(y,t) \tag{6}$$

where

$$\lambda_0 = \frac{\int \bar{u}' \hat{v} \, \eta_0^* \, dy}{\int \eta_0 \eta_0^* dy} \tag{7}$$

The function $R(y,t)$ contains terms of the same form for other eigenmodes η_i plus homogeneous solutions so as to satisfy the initial conditions. We are interested in the amplitude of the forced response:

$$A(t) = \beta \lambda_0 \, \frac{e^{-i\omega t} - e^{-i\omega_0 t}}{\omega - \omega_0} \tag{8}$$

For a direct resonance one gets $A(t) = \beta \lambda_0 \, t e^{-i\omega t}$. After a time $t_* = |Im(\omega)|^{-1}$, the amplitude reaches its maximum value given by :

$$max|A| = \frac{\beta |\lambda_0|}{e \, |Im(\omega)|} \tag{9}$$

where the vertical bars denote an absolute value or the norm of a complex number and $Im(\omega)$ is the imaginary part of ω. For near-resonance, a good estimate of the maximum amplitude is given by

$$max|A| \simeq \frac{\beta|\lambda_0|}{e\ max\{|Im(\omega)|, |Im(\omega_0)|\} + |Re(\omega) - Re(\omega_0)|/2} \tag{10}$$

After reaching this maximum, the amplitude decays viscously. The most amplified modes are those for which the phase velocities are nearly equal and *both* damping rates are small.

The interest in this mechanism is that if the gain in amplitude is significant non-linear effects will start to play a role. The direct resonance mechanism might then bridge the gap between linear theory and the observed 3-D non-linear instability in shear flows. This is especially relevant to Couette flow for which there is no known 2-D instability while direct resonances are present for any wavenumber (and correspond to modes moving with the average velocity).

2.1. Non-linear effects

Whether direct resonance is an important mechanism or not depends on the nature of the non-linear interactions which can be triggered. Non-linearity must act quickly enough to prevent the linear viscous decay. One must realize that only the vertical vorticity is amplified by the direct resonance and this limits the possible non-linear effects. The non-linear implications of direct resonances have been investigated by Benney and Gustavsson (1981). The situation is quite different depending on whether one has a single 3-D wave or several.

For a single wave, the vertical velocity remains decoupled from the vertical vorticity. The only non-linear terms in the vertical vorticity equation have the form of an interaction between the vertical velocity and vorticity, but there is no self-interaction of the vertical vorticity. This imposes strong limitations on the non-linear effects. Benney and Gustavsson conclude that if ϵ is a measure of the amplitude of the vertical velocity perturbation, the time scale for the non-linear interactions is ϵ^{-2}, exactly as in classical weakly non-linear analyses of OS waves. This time scale must be shorter than the viscous and phase decorrelation time scales for the finite amplitude effects to act (i.e. one needs $|Im(\omega)|, |Im(\omega_0)|, |Re(\omega) - Re(\omega_0)| < \epsilon^2$, a strong restriction). However, their deduction ignores the interaction between the vertical velocity and vorticity through the mean flow. That interaction occurs on a time scale of $O(\epsilon^{-1})$, much faster than $O(\epsilon^{-2})$. That process is well illustrated by the following exact viscous non-linear solution in an unbounded domain. Consider the flow: $u = \omega_y(t)z - \omega_z(t)y$, $v = -1/2\ \omega_x(t)z$, $w = 1/2\ \omega_x(t)y$, which is a linear flow with time-dependent vorticity. The u-velocity is given by the superposition of two Couette flows. The v and w velocities are that of a rigid

body rotation around the x-axis at a rate $1/2\omega_x$. The full vorticity equation, $D_t\vec{\omega} = \vec{\omega}.\vec{\nabla}\vec{v} + \nu\nabla^2\vec{\omega}$, becomes:

$$\begin{aligned} \dot{\omega}_x &= 0 \\ \dot{\omega}_y &= -\frac{1}{2}\omega_x\omega_z \\ \dot{\omega}_z &= \frac{1}{2}\omega_x\omega_y \end{aligned} \tag{11}$$

which implies that $\omega_x(t) = \omega_x(0)$ stays constant. Then if initially the flow is a Couette flow, $\omega_z(0) = -a$, $\omega_y(0) = 0$, on which a small downstream vortex is introduced, $\omega_x(0) = 2\epsilon$, the solution is:

$$\begin{aligned} \omega_y(t) &= a\ \sin(\omega_x(0)t/2) \\ \omega_z(t) &= -\ a\ \cos(\omega_x(0)t/2) \end{aligned}$$

For small times, one has:

$$\begin{aligned} \omega_y(t) &\sim a\ (\epsilon t - (\epsilon t)^3/6) \\ \omega_z(t) &\sim -\ a\ (1 - (\epsilon t)^2/2) \end{aligned}$$

The time scale is indeed of order ϵ^{-1}. In a domain bounded by two infinite horizontal planes the rigid rotation given by ω_x would be replaced by a periodic array of downstream rolls. These downstream rolls would decay on a slow viscous time scale due to the presence of the walls. The initial Couette flow would be maintained by viscous action at the same walls. As a result, one would observe a very "turbulent-looking" mean profile together with some associated streaks.

If there is a direct resonance for (α, β), there is also one for $(\alpha, -\beta)$. It is then necessary to consider the evolution when both waves are present. When several modes are present simultaneously, there is the possibility of a non-linear feedback on the vertical velocity. In that case, Benney and Gustavsson reason that the time scale for the non-linear processes is $\epsilon^{-1/2}$, which is very fast. On that time scale the vertical vorticity and the associated horizontal motions reach an amplitude of order $\epsilon^{1/2}$. Benney and Gustavsson rescale the equations assuming that the horizontal motions are of order $\epsilon^{1/2}$ while the vertical vorticity is of order ϵ. At lowest order, the resulting system consists of the homogeneous vorticity equation and a non-homogeneous equation for the vertical velocity. Although the derivation of these scalings is not available in their paper, one suspects that they proceeded as follows. Starting with a vertical velocity $\epsilon\, v(\alpha, \pm\beta)$, the vertical vorticity is "directly forced" and behaves initially as $\epsilon t\, \eta(\alpha, \pm\beta)$. The non-linear distortions are at least of order $\epsilon^2 t^2$. These distortions might interact with $\eta(\alpha, \pm\beta)$ to induce a feedback on $v(\alpha, \pm\beta)$ of order $\epsilon^3 t^4$, which introduces an $\epsilon^3 t^5$ modification of $\eta(\alpha, \pm\beta)$. Schematically, one gets:

$$v(\alpha, \pm\beta) = \epsilon\ (1 + \epsilon^2 t^4 + \ldots) e^{i(\alpha x \pm \beta z - \omega t)}$$

$$\eta(\alpha, \pm\beta) = \epsilon t(1 + \epsilon^2 t^4 + \ldots)e^{i(\alpha x \pm \beta z - \omega t)}$$

However, due to the necessary requirement of small damping for the direct resonance to lead to significant amplification, one can expect more resonances to appear. In the worst case, the vertical vorticity could resonantly force a $v(0, 2\beta)$ mode (downstream roll with half spanwise wavelength), which then induces a $\eta(0, 2\beta)$ mode (streaks). The non-linear feedback on $v(\alpha, \pm\beta)$ could be as high as order $\epsilon^3 t^6$. This cascade of interactions is represented in the following diagram.

$$\begin{aligned}
\epsilon\, v(\alpha, \pm\beta) &\longrightarrow \epsilon t\, \eta(\alpha, \pm\beta) \\
\epsilon^2 t^2\, \eta\eta^* &\longrightarrow \epsilon^2 t^3\, v(0, 2\beta) \\
\epsilon^2 t^3\, v(0, 2\beta) &\longrightarrow \epsilon^2 t^4\, \eta(0, 2\beta) \\
\epsilon^3 t^5\, \eta(\alpha, \pm\beta)\eta(0, 2\beta) &\longrightarrow \epsilon^3 t^6\, v(\alpha, \pm\beta)
\end{aligned}$$

The first and third interactions are linear and correspond to "near direct resonances". The second interaction was observed by Jang, Benney and Gran, it is further discussed below. The fourth interaction has not yet been explicitly established. If this scenario takes place, the correct expansion would rather be:

$$v(\alpha, \pm\beta) = \epsilon\,(1 + \epsilon^2 t^6 + \ldots)e^{i(\alpha x \pm \beta z - \omega t)}$$

$$\eta(\alpha, \pm\beta) = \epsilon t(1 + \epsilon^2 t^6 + \ldots)e^{i(\alpha x \pm \beta z - \omega t)}$$

implying a non-linear time scale of order $\epsilon^{-1/3}$.

3. Applications

Gustavsson has looked for and found direct resonances for laminar Couette, plane, and pipe Poiseuille flows. No exact resonances were found for laminar boundary layer profiles; however, Jang, Benney and Gran (1986) found one for a *turbulent* boundary layer profile. The use of the theory for a turbulent profile is more delicate to justify, as in that case finite perturbations must exist to maintain the turbulent mean. Yet, considering the linear perturbation equations around a turbulent mean can be seen as an effort to determine a "proper eigenmodal decomposition" of the fluctuating field. Kim has located several near-resonances in the case of a turbulent channel flow profile. We are now confronted with a selection problem. Which of these near resonances, if any, is the relevant one?

The first, and only, resonance found by Jang, Benney and Gran corresponds to a wavenumber intriguingly close from the peak of experimentally measured power spectral distributions. In addition, the vertical velocity motion induced by the non-linear interaction of the vertical vorticity with itself corresponds to a downstream roll with a spacing of 90 in wall units. This is a very interesting non-linear process which gives a mechanism to generate streamwise vorticity from vertical vorticity. Longitudinal streaks are then introduced by the interaction

of this streamwise vortex with the mean profile. Physically, the large horizontal motions coming from the large vertical vorticity induced by the direct resonance create downstream and spanwise vorticity ($\frac{\partial}{\partial y}w$ and $\frac{\partial}{\partial y}u$) as a consequence of the no-slip condition at the walls. These vorticity components are stretched ($\frac{\partial}{\partial y}w\frac{\partial}{\partial x}u$) and rotated ($-\frac{\partial}{\partial x}w\frac{\partial}{\partial y}u$), respectively, as can be deduced from the equation for the x-vorticity:

$$\frac{D}{Dt}\omega_x = \omega_x\frac{\partial}{\partial x}u + \omega_y\frac{\partial}{\partial y}u + \omega_z\frac{\partial}{\partial z}u + \nu\nabla^2\omega_x$$

neglecting $\frac{\partial}{\partial z}v$ and $\frac{\partial}{\partial x}v$ in the expressions for ω_x and ω_z, one finds:

$$\frac{D}{Dt}\omega_x \simeq \frac{\partial}{\partial y}w\frac{\partial}{\partial x}u - \frac{\partial}{\partial x}w\frac{\partial}{\partial y}u + \nu\nabla^2\omega_x$$

Mathematically this process translates into the non-linear forcing of a $v(0,2\beta)$ vertical velocity mode. This mechanism is particularly relevant to the studies of John Kim (1983). One emphasizes that according to the mechanism explained above, the downstream vorticity is generated from the vertical vorticity rather than from a "splatting" effect (Kim, 1983).

From the nature of the non-linear interactions, the streamwise vortex always has twice the spanwise wavenumber of the 3-D vertical vorticity which generated it. Thus *double* pairs of counter-rotating vortices should be observed if this process is relevant. The "minimum channel" simulations of Jimenez and Moin, show that "turbulence" can be maintained with only *one* pair of counter-rotating streamwise vortices. This would imply that the mechanism for their generation can not come from the non-linear interaction of the vertical vorticity with itself as proposed by Jang, Benney and Gran. More cautiously, there must be another mechanism for their creation.

4. Mean flow-first harmonic model

The appearance of the new resonances discussed above imposes some significant modifications to the non-linear theory of Benney and Gustavsson. It is necessary to reformulate the problem in order to account for the intrinsic spanwise modulation of the mean flow. Steps in that direction have been taken by Benney and Chow (1989). These authors have formulated a *mean flow-first harmonic* theory where the mean varies in both the vertical and spanwise direction and the perturbation is composed of only one downstream fourier mode. No extensive analysis of the solutions of these equations have yet been made. This self-contained theory is still in a primitive state. It seems that some careful numerical simulations could test the validity of this approach. This mean flow-first harmonic theory is in some sense based on an idea of triad resonances between modes of the form $(\alpha, \pm\beta)$ and $(0, 2\beta)$, but it could also describe interaction

between $(\alpha, \pm 2\beta)$, $(0, \pm 2\beta)$ and $(\alpha, 0)$. In other words, in the case of a mean + a spanwise mode $(0, 2\beta)$, one might find both *fundamental* and *subharmonic* instabilities (just as for a mean + a 2-D Tollmien-Schlichting $(\alpha, 0)$ wave). The fundamental instability could be relevant to the minimum channel simulations. Such instabilities of a spanwise periodic basic state might be the other side of the 3-D instability of a downstream periodic basic flow. The question is which basic state should be studied? Laminar Couette flow modified by its slowest decaying downstream roll eigenmode is a good candidate. The same basic state could be chosen for channel flow, or, alternatively, a state generated from the computed turbulent profiles could be used. This state would be obtained by averaging the full-field over the downstream x direction and time.

In the mean flow-first harmonic theory, one hopes that the waves developing on a spanwise varying basic state are such that their non-linear interactions maintain the mean and especially the downstream rolls. It seems more likely to the present author that the downstream structures would rather be formed by a 3-D instability of the developing wave (i.e. the 3-D instability of a mean + a downstream mode $(\alpha, 0)$; the elliptical instability).

5. Optimum fields

A related investigation is to determine *optimum* perturbation fields maintaining the mean and being chosen so as to maximize various mean moments (e.g. production) under some critical constraints derived from Navier-Stokes. In this approach as in the mean field-first harmonic theory, the mean flow equations are exact while approximations are made on the fluctuation equations. Busse (1978), for instance, showed that the field which maximizes the averaged Reynolds stresses, while maintaining the mean and satisfying the boundary conditions, the incompressibility constraint and an energy constraint, corresponds to a downstream roll-streak structure with a spacing of about 50 in wall units. Without a doubt, a numerical investigation including additional constraints will improve this value. The advantages of this approach is that it is mathematically rigorous and gives some definite physical insights such as what are the important constraints on the real motions, and why a particular structure is observed. It is an excellent way of getting the organized motions in a turbulent field. Once a solution is found, it can then serve as the basis for a new expansion or analysis. Busse's solution, for instance, could serve as the basic state in the 3-D stability calculations referred to above.

The following question could be quite relevant to the minimum channel simulations. Given the computed turbulent velocity profile, what is the most "efficient" way of maintaining it? By "efficient" we mean, for example, that the ratio of the total average turbulent energy production to the total average kinetic energy of the fluctuations is maximized. Of course, one could look for other optima (such as max average Reynolds stresses over rms fluctuations). Mathematically, the

problem is that of determining the maximum of:

$$\frac{- < \overline{uv}\frac{d}{dy}\bar{u} >}{< u^2 + v^2 + w^2 >} \tag{12}$$

where the brackets $< . >$ stand for an average over all variables x, y, z, t. The overbar, as before, is an average over x, z, t. We request that this optimum fluctuating field maintains the mean, that is :

$$\frac{1}{R}\frac{d^2}{dy^2}\bar{u} = \frac{\partial}{\partial x}\bar{P} + \frac{d}{dy}\overline{uv} \tag{13}$$

The optimum field should satisfy the incompressibility constraint: $\vec{\nabla}.\vec{u} = 0$, and the boundary conditions. Finally, we impose that it also satisfies the energy constraint that, for a statistically steady state, the turbulent energy production is equal to the dissipation rate. This reads:

$$- < \overline{uv}\frac{d}{dy}\bar{u} >= \frac{1}{R} < (\vec{\nabla}u)^2 + (\vec{\nabla}v)^2 + (\vec{\nabla}w)^2 > \tag{14}$$

As the turbulent profile and the Reynolds number are imposed, this last constraint implies that we are maximizing the functional:

$$\frac{< (\vec{\nabla}u)^2 + (\vec{\nabla}v)^2 + (\vec{\nabla}w)^2 >}{< u^2 + v^2 + w^2 >} \tag{15}$$

For this type of problem, one knows from Busse's work that the optimum field corresponds to x-independent structures, thus we are really maximizing the spanwise wavenumber. The question has thus become: what is the smallest spanwise wavelength which could maintain the turbulent mean? The equations for the optimum fluctuating field are obtained from variational calculus, after some manipulations they read:

$$[\lambda - \frac{1}{R}(\frac{d^2}{dy^2} - \beta^2)]\,(\frac{d^2}{dy^2} - \beta^2)\,\hat{v}(y) = \beta^2\lambda_2(y)\hat{u}(y) \tag{16}$$

$$[\lambda - \frac{1}{R}(\frac{d^2}{dy^2} - \beta^2)]\,\hat{u}(y) = -\lambda_2(y)\hat{v}(y) \tag{17}$$

with the boundary conditions: $\hat{v} = d\hat{v}/dy = \hat{u} = 0$ at $y = \pm 1$. The *Lagrange multipliers* λ and $\lambda_2(y)$ are determined from the constraints that $< (\vec{\nabla}\vec{u})^2 >$ and $\overline{uv}$ have fixed values. This is a fairly simple numerical problem. One will note the strong similarity between this system and the OS and vertical vorticity equations. The most important difference is that we now have a production term for the downstream roll (v). This term models some optimum process maintaining the rolls.

5.1. Improvements

The most efficient way of subtracting energy from the mean flow corresponds to x-independent structures. Conservation of energy was insured but no further constraint was imposed on how this energy should be spread among the 2 degrees of freedom v and u, i.e. among downstream rolls and streaks. However, we know that there are strong constraints on such a process. Indeed, if one introduces downstream rolls into the flow they are very efficient at taking energy out of the mean, but all that energy goes into the streaks. These streaks are themselves precisely determined by the mean profile and the rolls.

One way of improving the results is to proceed as in the mean field-first harmonic theory and recognize that the mean should have an intrinsic spanwise variation ($u(y,z)$), with associated downstream rolls (v,w motions). The problem is then to determine what optimum fluctuations could maintain such a mean. The fluctuations will now be x-dependent. This problem will predict a mean profile, streak spacing *and* an optimum x-scale.

A simpler alternative has been proposed by Malkus (1967). Instead of considering a different mean, the idea is to impose more constraints on the fluctuations. Malkus' suggestion is to include the equation for the total streamwise enstrophy. This should give insight into the mechanism of production of streamwise vorticity. Yet another way is to split *a priori* the fluctuating field into its 2 degrees of freedom and impose energetic constraints for both of them simultaneously. In this way, the repartition of the turbulent energy production among the 2 degrees of freedom would be imposed from Navier-Stokes, instead of being freely determined by the variational problem.

Dr. Leslie Smith has been working on related topics, and these optimum fields projects will be realized with her collaboration.

REFERENCES

JANG, P. S., BENNEY, D. J. & GRAN, R. L. 1986 *J. Fluid Mech.*, **169**, 109.

BENNEY, D. J. & GUSTAVSSON, L. H. 1981 *Studies in Appl. Math.*, **64**, 185.

BENNEY, D. J. & CHOW, K. 1989 *Studies in Appl. Math.*

BUSSE, F. H. 1978 *Advances in Applied Mech.*, **18**, 77.

KIM, J. 1983 *Phys. Fluids*, **26**, 2088, and 1985, **28**, 52.

MALKUS, W. V. R. 1967 Private Communication

Center for Turbulence Research
Annual Research Briefs - 1989

Turbulence dynamics in the wavelet representation

By C. Meneveau

The phenomenon of small-scale intermittency is shown to motivate the decomposition of the velocity field into modes that exhibit both localization in wavenumber and physical space. We review some basic properties of such a decomposition, called the wavelet transform. The wavelet-transformed Navier-Stokes equations are derived, and we define a new quantity $\Pi(r, \vec{x}, t)$, which is the flux of kinetic energy to scales smaller than r at position $\vec{x}$ (at time t). Then, the main goals of this research are summarized.

1. Introduction

One of the most important features of a turbulent flow is the transfer of kinetic energy from large to small scales of motion. For isotropic and homogeneous turbulence, the three-dimensional energy spectrum $E(k,t)$ obeys

$$\frac{\partial E(k,t)}{\partial t} = T(k,t) - 2\nu k^2 E(k,t), \tag{1}$$

where $T(k,t)$ is the net transfer of energy through wavenumbers of magnitude k. The total spectral flux of energy through wavenumber k to all smaller scales is given by

$$\Pi(k,t) = \int_k^\infty T(k',t)dk'. \tag{2}$$

Usually the mechanism of energy transfer is visualized by simplified models such as the successive break-down of 'eddies', or as the creation of small scales by the stretching and folding of vortical elements. One then argues that through scales of motion of size k^{-1}, there is a net flux of kinetic energy to smaller scales, which is equal to the time average of $\Pi(k,t)$. Notice that $\Pi(k,t)$ does not depend on position because of the Fourier representation used to obtain Eq. (2). If one now wishes to reconcile this definition of a 'flux' of energy to smaller scales with the phenomenological picture of breakdown of eddies, one needs to tacitly make the assumption that its average value is indeed physically representative of the underlying physics in any regions of space. In some loose sense, this then corresponds to the theory of Kolmogorov (1941), which neglects the phenomenon of intermittency. Of course, it has been known for a long time that the rate of dissipation $\varepsilon(x,t)$ is distributed very intermittently (Batchelor and Townsend

1949), a behavior which increases with the Reynolds number of the flow. Also, its moments increase with Reynolds number according to power-laws in the inertial range of turbulence. Among others, this permits a self-consistent statistical and geometrical representation of ε in terms of multifractals (Kolmogorov 1962, Novikov 1971, Mandelbrot 1974, Frisch and Parisi 1985, Meneveau and Sreenivasan 1987a, 1987b, 1989). The observation of power-law behavior of spatial moments of the dissipation can be modelled again rather naturally within the framework of breakdown of eddies, but now assuming that the flux of energy to smaller scales exhibits spatial fluctuations. These fluctuations accumulate as the scales of motion become smaller, and can lead to very intermittent distributions of the dissipation displaying power-law behavior. This suggests the need for defining a flux of kinetic energy to smaller scales which, as opposed to Eq. 2, should retain some degree of spatial locality.

In a very interesting paper, Kraichnan (1974) proposed to decompose the velocity field into band-limited contributions according to

$$u_i^m(\vec{x},t) = (2\pi)^{-d} \int_{|k|=2^m}^{2^{m+1}} \hat{u}_i(\vec{k},t) e^{i\vec{k}\cdot\vec{x}} d^3k, \tag{3}$$

where

$$\hat{u}_i(\vec{k},t) = \int_{-\infty}^{\infty} u_i(\vec{x},t) e^{-i\vec{k}\cdot\vec{x}} d^3x. \tag{4}$$

The equation of motion of $u_i^m(\vec{x},t)$ can be deduced from the Navier-Stokes equations, and multiplying the result by $u_i^m(\vec{x},t)$ gives the evolution equation of $[u_i^m(\vec{x},t)]^2$ which can be interpreted as the kinetic energy occurring in a wavenumber band around 2^m, at position $\vec{x}$. The result is

$$(\frac{\partial}{\partial t} - \nu\nabla^2)[u_i^m(\vec{x},t)]^2 = T^m(\vec{x},t), \tag{4}$$

where

$$T^m(\vec{x},t) = \frac{-i}{2(2\pi)^d} u_i^m(\vec{x},t) \int_{|k|=2^m}^{2^{m+1}} P_{ijk}(\vec{k}) e^{i\vec{k}\cdot\vec{x}} \int_{\vec{q}} \hat{u}_j(\vec{q}) \hat{u}_k(\vec{k}-\vec{q}) d^3q d^3k. \tag{5}$$

Here $P_{ijk}(\vec{k})$ is the usual divergence-free projection operator. In analogy to Eq. (2), Kraichnan (1974) then defined a flux of kinetic energy to smaller scales as

$$\Pi^m(\vec{x},t) = \sum_{n=m}^{\infty} T^n(\vec{x},t), \tag{6}$$

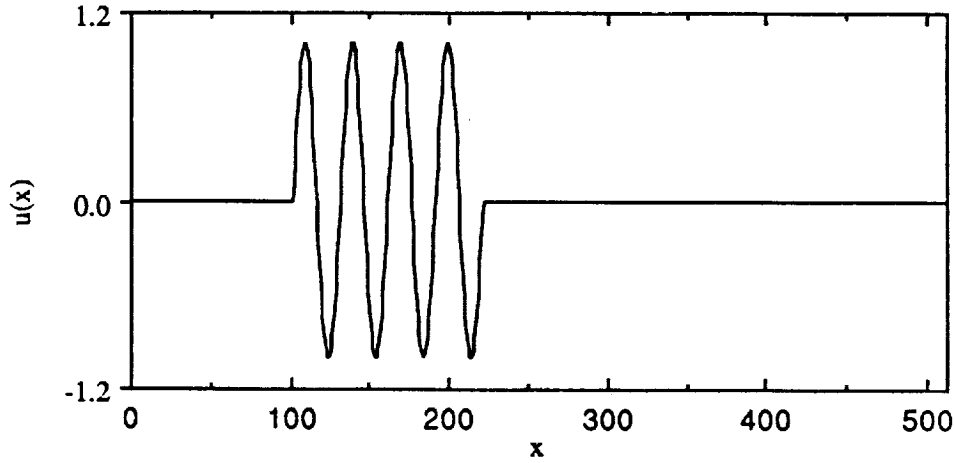

FIGURE 1 (A). Signal $u(x)$ displaying oscillations of a single scale in a confined spatial region.

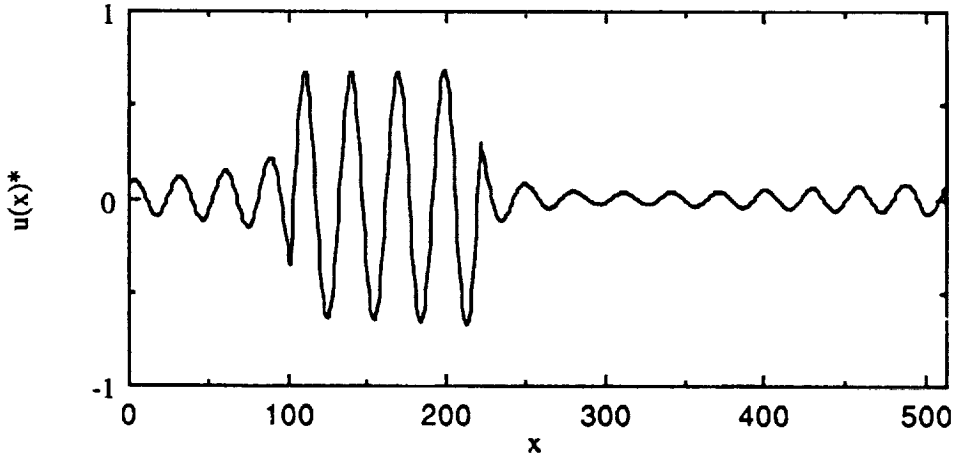

FIGURE 1 (B). High-pass filtered version of the signal $u(x)$. The filtering here consists of cutting off all discrete Fourier modes of scales larger than 30.

which is now a position-dependent quantity because of the band-pass filtering.

However, filtering using Fourier modes can be dangerous in the following sense. Take for instance the signal of Fig. (1a), where an oscillation of wavelength $\lambda = 30$ is confined to a certain region of space. This could be thought of as an extreme case of intermittency, where at a given scale λ all activity is confined to a subregion of space only. If we now high-pass filter the signal up to scales equal to ~ 30, we get the signal of Fig. (1b). It is apparent that the elimination of modes at scales larger than 30, some of which were needed to cancel the

oscillations outside the domain of activity, has resulted in spreading the 'activity' everywhere. This is because of the non-local nature of the Fourier modes.

This motivates the study of bases that retain locality both in wavenumber and position space. Their use in describing turbulence dynamics is the primary goal of this research, with special emphasis on the spatial characteristics of the transfer of energy to smaller scales and the implications on intermittency. The formalism will then be applied to numerical data bases of turbulent flows.

The theory and applications of the so-called wavelet bases, which are local in wavenumber and position space, has recently generated much interest (for a detailed account, see Daubechies 1988). Wavelets are currently used for speech and image processing (Mallat 1989, Kronland-Martinet et al. 1987), and can be used to describe affine coherent states in quantum mechanics (Paul 1985). The work of Siggia (1977) and Nakano (1988) attempt to describe turbulence using wavepackets, which display several similitudes with wavelets. Explicitly, the potential use of wavelets in turbulence has been pointed out in the context of coherent structures (Farge and Rabreau 1988) as well as in studies of its fractal nature (Argoul et al. 1989), even though their claim that it has proven the Richardson cascade based on single hot-wire measurements appears to be premature.

Section 2 defines the (continuous) wavelet transform of a signal, and reviews several of its properties. Section 3 defines the flux of kinetic energy to smaller scales using the wavelet representation, and also derives the wavelet-transformed Navier-Stokes equations. Section 4 contains some practical considerations related to the implementation of the discrete version of the wavelet transform, and its generalization to three dimensions. Section 5 summarizes the future objectives of the present research.

2. The wavelet transform

Given a signal $u(x)$, its wavelet transform is defined as

$$W(r,x)\{u\} = C_g^{-\frac{1}{2}} r^{-\frac{1}{2}} \int_{-\infty}^{\infty} g(\frac{x'-x}{r}) u(x') dx', \tag{7}$$

where $g(s)$ is a function called wavelet, satisfying the admissibility condition

$$C_g = \int |\omega|^{-1} |\hat{g}(\omega)|^2 d\omega < \infty. \tag{8}$$

Here $\hat{g}(\omega)$ is the Fourier transform of $g(s)$. $g(s)$ is of zero mean, will have some oscillations and will usually be real. A typical example is the mexican hat $g(s) = (1-s^2)e^{-s^2/2}$, which can approximately be viewed (Coifman 1989) as the difference between two exponentials of different sizes centered around $s = 0$. Therefore, $W(r,x)$ can be regarded as the relative contribution of scales r to the

signal at position x. If $g(s)$ obeys the above conditions, the wavelet transform can be inverted (Grossmann and Morlet 1984). The inversion formula for the wavelet transform reads

$$u(x) = C_g^{-\frac{1}{2}} \int_0^\infty \int_{-\infty}^\infty r^{-\frac{5}{2}} g(\frac{x - x'}{r}) W(r, x')\{u\} dx' dr. \tag{9}$$

$W(r, x)$ can also be obtained from $\hat{u}(k)$, the Fourier transform of u(x) according to

$$W(r, x)\{u\} = C_g^{-\frac{1}{2}} (2\pi)^{-1} r^{\frac{1}{2}} \int_{-\infty}^\infty \hat{g}(rk)^* \hat{u}(k) e^{ixk} dk, \tag{10}$$

where $\hat{g}(\omega)$ is the Fourier transform of $g(s)$. The total energy of the signal is given by

$$\int u(x')^2 dx' = C_g^{-1} \int_0^\infty \int_{-\infty}^\infty r^{-2} [W(r, x)\{u\}]^2 dr dx. \tag{11}$$

One can also compute $\hat{u}(k)$ from $W(r, x)\{u\}$ using

$$\hat{u}(k) = C_g^{-\frac{1}{2}} (2\pi)^{-1} \int_0^\infty \int_{-\infty}^\infty r^{-\frac{3}{2}} \hat{g}(rk) e^{ixk} W(r, x)\{u\} dx dr. \tag{12}$$

The wavelet transform commutes with differentiation in the spatial variable, namely

$$\frac{\partial}{\partial x} W(r, x)\{u\} = W(r, x)\{\frac{\partial}{\partial x'} u(x')\} \tag{13}$$

For vector functions $\vec{u}(x)$ with components $u_i(x)$, the transform is a vector $\vec{W}(r, x)$ whose components are the transforms of the components of $\vec{u}(x)$.

For functions defined in higher dimensions, it is recommendable to use decomposable wavelets. In three dimensions we use

$$g(\vec{s}) = g(s_1, s_2, s_3) = g_1(s_1) g_2(s_2) g_3(s_3). \tag{14}$$

One can then prove the following useful relations:

$$\vec{\nabla}_{\vec{x}} \cdot \vec{W}(r, \vec{x})\{\vec{u}(\vec{x}')\} = W(r, \vec{x})\{\vec{\nabla}_{\vec{x}'} \cdot \vec{u}(\vec{x}')]\} \tag{15}$$

and

$$\vec{\nabla}_{\vec{x}} \vec{W}(r, \vec{x})\{\vec{u}(\vec{x}')\} = W(r, \vec{x})\{\vec{\nabla}_{\vec{x}'} \vec{u}(\vec{x}')\}. \tag{16}$$

3. Wavelet representation of turbulence dynamics

Let us define $W_i(r,\vec{x},t)$ as the wavelet transform of the velocity field $u_i(\vec{x},t)$. (From here on we simplify the notation by using $W_i(r,\vec{x},t)$ instead of $W_i(r,\vec{x},t)\{u_i\}$). Because of Eq. (15), the incompressibility condition reads

$$\vec{\nabla}_{\vec{x}} \cdot \vec{W}(r,\vec{x},t) = 0. \tag{17}$$

Multiplying the Fourier-transformed Navier-Stokes equations by $C_g^{-\frac{1}{2}} r^{\frac{d}{2}} (2\pi)^{-d} \times \hat{g}(r\vec{k})^* e^{i\vec{x}\cdot\vec{k}}$, integrating over wavenumber space and using Eq. (12) gives

$$\left(\frac{\partial}{\partial t} - \nu\nabla^2\right)[W_i(r,\vec{x},t)] =$$

$$\int_{r'}\int_{r''}\int_{\vec{x}'}\int_{\vec{x}''} W_j(r',\vec{x}',t) W_k(r'',\vec{x}'',t) I_{ijk}(r,\vec{x};r',r'',\vec{x}',\vec{x}'')\, dr'\, dr''\, d^3x'\, d^3x'', \tag{18}$$

where

$$I_{ijk}(r,\vec{x};r',r'',\vec{x}',\vec{x}'') =$$

$$-\frac{i r^{\frac{d}{2}}}{2 C_g^{\frac{1}{2}} (2\pi)^{3d} (r' r'')^{\frac{1+d}{2}}} \int_{\vec{k}} \hat{g}(r\vec{k})^* P_{ijk}(\vec{k}) e^{i\vec{k}\cdot(\vec{x}+\vec{x}'')} \times \int_{\vec{q}} \hat{g}(r'\vec{q}) \hat{g}(r''(\vec{k}-\vec{q})) e^{i\vec{q}\cdot(\vec{x}'-\vec{x}'')} d^3q\, d^3k. \tag{19}$$

This illustrates that there are now interactions of the $W_i(r,\vec{x},t)$ occurring at different positions as well as different scales. These non-local and inter-scale interactions are dictated by the properties of $I_{ijk}(r,\vec{x};r',r'',\vec{x}',\vec{x}'')$. Additionally, one can, of course, apply the wavelet transform in time.

Of more immediate interest is to define a quantity analogous to Eq. (6) in the wavelet representation. For this we start with Eq. (19) and multiply by $W_i(r,\vec{x},t)$ and express the right-hand-side as a function of the velocity field. We obtain

$$\left(\frac{\partial}{\partial t} - \nu\nabla^2\right)[W_i(r,\vec{x},t)]^2 = T(r,\vec{x},t), \tag{20}$$

where

$$T(r,\vec{x},t) =$$

$$-\frac{i r^d}{2(2\pi)^{2d}} \left[\int_{\vec{p}} \hat{g}(r\vec{p})^* \hat{u}_i(\vec{p}) e^{i\vec{p}\cdot\vec{x}} d^3p\right] \int_{\vec{k}} P_{ijk}(\vec{k}) \hat{g}(r\vec{k})^* e^{i\vec{k}\cdot\vec{x}}$$

$$\times[\int_{\vec{q}} \hat{u}_j(\vec{q})\hat{u}_k(\vec{k}-\vec{q})d^3q]d^3k. \tag{21}$$

The flux of kinetic energy to all smaller scales can then be defined as

$$\Pi(r,\vec{x},t) = \int_0^r T(r',\vec{x},t)dr'. \tag{22}$$

Therefore, given the Fourier transform of the velocity field, the quantity $\Pi(r,\vec{x},t)$ can be computed. Other quantities whose spatial distribution is of interest is the dissipation term

$$\varepsilon(r,\vec{x},t) = \frac{\nu}{2}[\frac{\partial W_i}{\partial x_j} + \frac{\partial W_j}{\partial x_i}]^2. \tag{23}$$

Assuming constant mean shear, the production term is

$$P(r,\vec{x},t) = W_i(r,\vec{x},t)W_j(r,\vec{x},t)S_{ij}, \tag{24}$$

where S_{ij} is the mean rate of strain.

4. Wavelet bases and discretization

There are many possible choices for the wavelet $g(s)$. The simplest is the Haar function $g(s) = 2^{\frac{1}{2}}$ for $0 \leq s \leq \frac{1}{2}$ and $g(s) = -2^{\frac{1}{2}}$ for $\frac{1}{2} < s \leq 1$. Another is the mexican hat mentioned in section 2. In terms of the discretization of the transform, assume that one has a signal on a discrete grid consisting of N points. One possibility is to space r logarithmically and 'slide' the spatial variable over all N points of the signal. In such a case one obtains of the order of $NlogN$ values of the transform. This is what has generally been used in qualitative studies, such as by Kronland-Martinet et al. (1987) and Argoul et al. (1989). The fact that the transform consists of more points than the original signal comes from the non-orthogonality of the wavelet functions in such a case.

Intuitively, for larger values of r one could use a coarser spatial grid than for smaller values of r. This observation has led (see Mallat 1989) to the definition of basis functions of the form

$$g^{m,i}(x) = g(\frac{x - ib_0a_0^m}{a_0^m}) = g(a_0^{-m}x - ib_0), \tag{25}$$

where a_0 and b_0 are dilation and translation steps. Notice that now the translation depends on the dilation, both being logarithmically spaced. Choices for a_0 and b_0 are not completely arbitrary (Daubechies 1988); here we will use the simplest case $a_0 = 2$ and $b_0 = 1$. Notice that the Haar basis with such a choice of a_0 and b_0 constitutes an orthonormal system, because

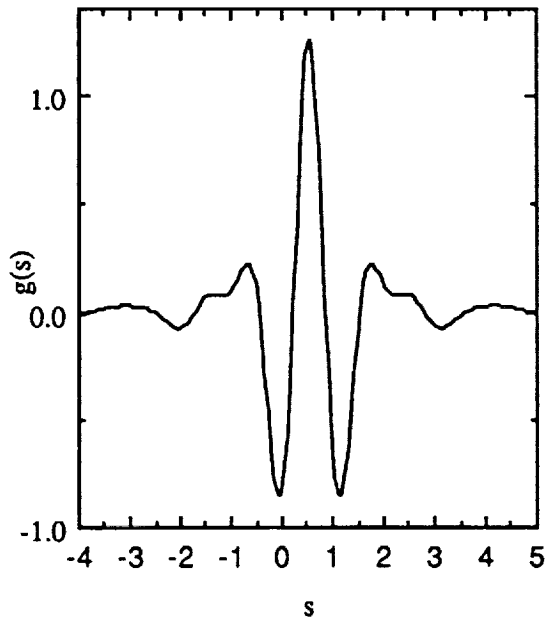

FIGURE 2. Lemarie-Battle wavelet with exponential decay in physical space. For a method of constructing such a wavelet, see Mallat(1989).

$$\int g^{m,i}(x)g^{n,j}(x)dx = \delta_{mn}\delta_{ij}. \tag{26}$$

The discrete wavelet coefficients of a continuous function u(x) are defined as

$$W^{m,i} = \int g^{m,i}(x)u(x)dx, \tag{27}$$

and the (discrete) reconstruction formula is the wavelet series expansion of $u(x)$

$$u(x) = C_g^{-\frac{1}{2}} \sum_m \sum_i 2^{-\frac{m}{2}} W^{m,i} g^{m,i}(x). \tag{28}$$

In practice, $u(x)$ itself is discrete and the integration in Eq. (27) needs to be replaced by a sum. In the formulation to be adopted here, the discrete samples $u(x_n)$ are viewed (Mallat 1989, Daubechies 1988) as resulting from the convolution of $u(x)$ with a function $\phi_{0,n}(x)$ according to

$$u(x_n) = \int u(x)\phi_{0,n}(x)dx. \tag{29}$$

It turns out that the conditions of orthonormality of the entire wavelet basis (as well as several other considerations) are related to the properties of $\phi_{0,n}(x)$

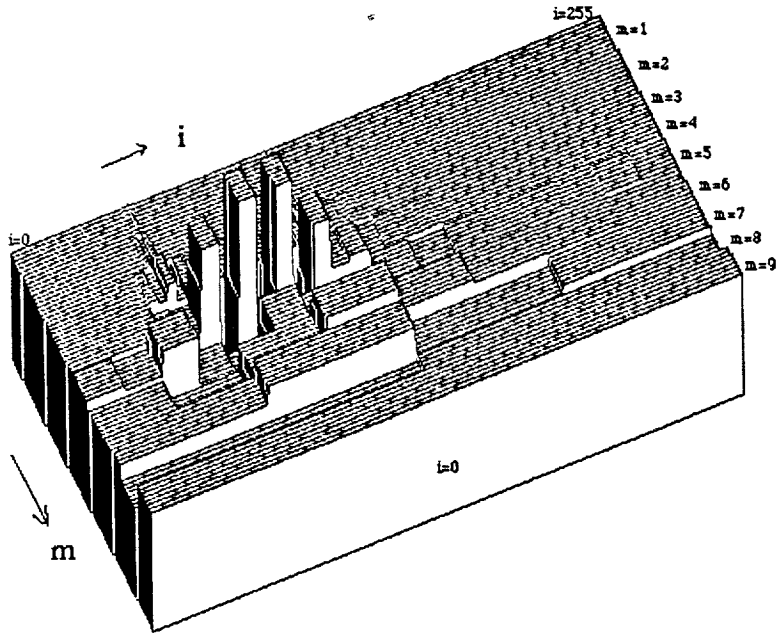

FIGURE 3. Wavelet transform of the signal of Fig. 1(a) using the Lemarie-Battle wavelet and the fast algorithm of Mallat (1989). The index m denotes the scale and runs from $m = 1$ to $m = log_2 N = 9$. The index i runs from 0 to $2^{-m}N - 1$. The spatial resolution thus decreases as m increases. The total number of values of the transform is $N - 1$, and for the decomposition to be complete, one also needs to know, say, the mean of the signal.

(Mallat 1989, Daubechies 1988). For instance, the use of such a formulation naturally leads to an algorithm to compute fast wavelet transforms (FWT).

Several issues other than orthonormality need to be taken into account when deciding which wavelets to use. One very important issue is the degree of locality. The Haar system is very well localized in space (it has compact support in $[0, 1]$), but has very poor spectral locality. This is a disadvantage, because we would like the wavelet coefficients corresponding to a certain scale r to be large only when the signal actually contains oscillations of that scale. In other words, one is interested in fast decay both in wavenumber and position space. A very convenient function complying with the conditions of discrete orthonormality was discovered by Lemarie and Battle (see Mallat 1989). This function decays as k^{-4} in wavenumber space and exponentially in physical space, and was used by Mallat (1989) for image analysis. Figure 2 shows this function. Figure 3 displays the discrete wavelet transform of the signal of Fig. 1a. Notice the spacing that becomes more coarse-grained as the dilation factor $r = 2^m$ increases. The transform peaks near $m = 5$ (corresponding to a scale $\lambda = 32$) only in the vicinity of the oscillations of the signal. Inverting the transform for scales up to 32 ($m = 0$ to 5) gives the signal of Fig. 4. Since the wavelet coefficients away

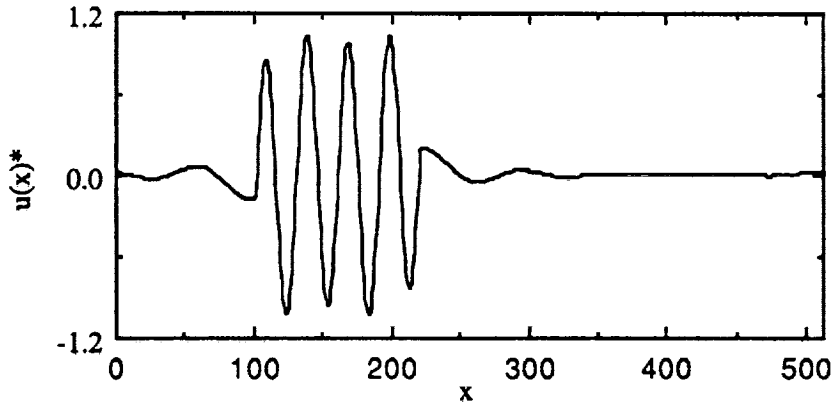

FIGURE 4. High-pass filtered version of the signal of Fig. 1(a) using scales corresponding to $m = 1$ to 5. Here we have applied the (discrete) inverse-wavelet transform algorithm of Mallat (1989).

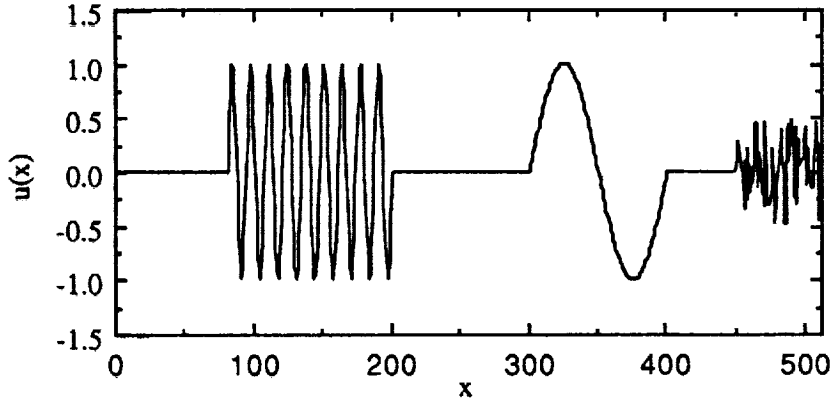

FIGURE 5. Signal displaying oscillations of different frequencies at different locations, as well as random numbers (right portion).

from the activity are very small, there is little risk in incurring the problems that occurred with the Fourier representation (see Fig. 1b).

Figure 5 shows another function consisting of oscillations of different scales located at different positions. Figure 6 is its discrete wavelet transform. Figures 7 and 8 correspond to high-pass and low-pass filtered versions of the signal. The wavelet transform is seen to separate events of different scales in a fashion which respects their location in space.

Even though $g(s)$ of the Lemarie-Battle wavelets has fast decay in space, it has non-local support (i.e. $g^{m,i}(x) \neq 0$ even at large $\mid x \mid$). If one were to

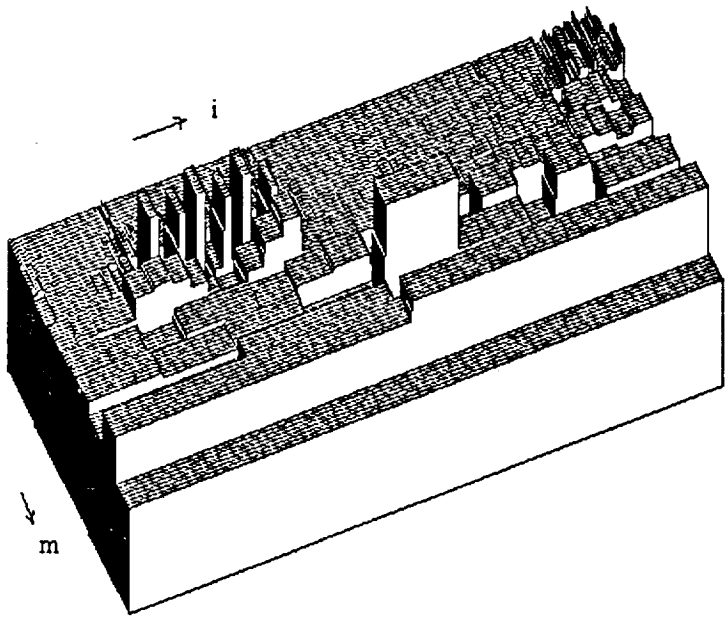

FIGURE 6. Wavelet transform of Fig. 5 using the Lemarie-Battle wavelet and the fast algorithm of Mallat (1989). Notice the localization in both wavenumber and physical space of the different events.

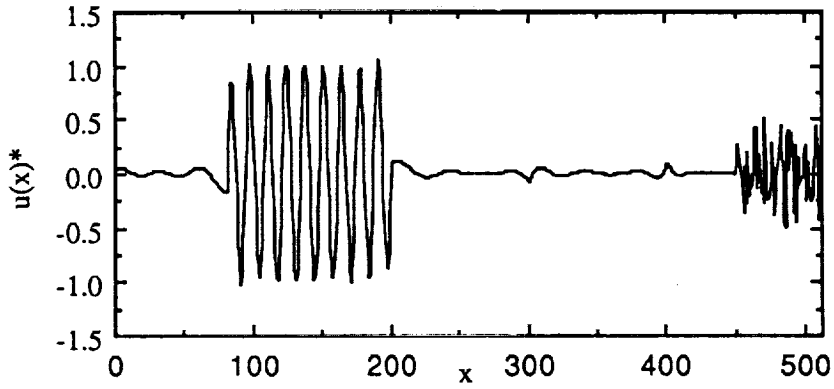

FIGURE 7. Reconstruction of the signal using scales between $m = 1$ and $m = 4$ (high-pass filtering).

set it to zero after some value of $| x |$, then the discrete orthonormality is not exactly obeyed. In other words, finite domain truncation leads to a loss of discrete orthonormality. Daubechies (1988) shows that one can construct orthonormal wavelets of compact support which are different from the Lemarie-Battle wavelets. However, such wavelets do not possess symmetry (Daubechies

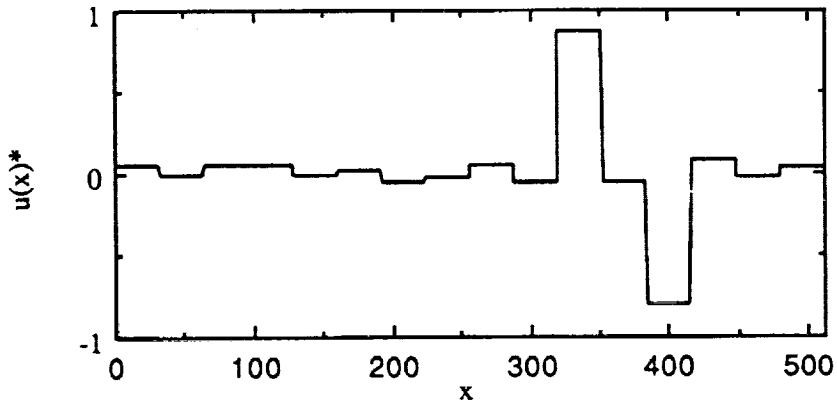

FIGURE 8. Reconstruction of the signal using scales between $m = 5$ and $m = 9$ (low-pass filtering). Since the reconstruction only uses modes down to scales of size 32, the result is a coarse-grained version of the signal.

(1988) even proves that the Haar basis is the *only* system with symmetry). It turns out that non-symmetric bases are a problem in many respects for the applications envisaged in this work. Essentially, the coefficients corresponding to some portion of the signal appear shifted from that position. Therefore, in the present work we will use the Lemarie-Battle wavelets. It is necessary to point out that the deviations from exact orthonormality due to truncation are negligible in practice. Also, the fast transform procedure of Mallat (1989) is implemented. A generalization of the algorithm to three dimensions will be done.

5. Future plans

The main objective of this work is to compute $\Pi(r, \vec{x}, t)$ of Eq. (22) from full numerical solutions of turbulent flows that are available in data bases at certain times t_0. Then the degree of spatial intermittency of $\Pi(r, \vec{x}, t_0)$ will be quantified for different values of r. We will compare the statistics of $\Pi(r, \vec{x}, t)$ with ε_r, the rate of dissipation averaged over a domain of size r, which is the quantity usually used for studies of intermittency. This is a dissipative quantity, whose integral over domains of sizes pertaining to the 'inertial range' is usually thought to represent statistical features of the inertial range. By comparing the dynamically relevant quantity $\Pi(r, \vec{x}, t)$ with ε_r, we hope to clarify this issue. Also, the statistics of 'breakdown' coefficients defined as

$$M = \frac{\Pi(r_1, \vec{x}, t)}{\Pi(r_2, \vec{x}, t)} \tag{30}$$

will be quantified. It will be tested whether a cascade model constructed in such a way as to display the measured statistics of M is consistent with our present

knowledge of intermittency of the dissipation. A similar study will be made in the context of scalar dissipation and flux of scalar variance to smaller scales. This will lead to a better physical and statistical understanding of the energy cascade and of intermittency.

Other more long-term objectives are the study of Eq. (18) and in particular of the quantity $I_{ijk}(r, \vec{x}; r', r'', \vec{x}', \vec{x}'')$. The problem of subgrid modelling in the present context is to find approximations to the right-hand side of Eq. (18) whenever there are interactions between the resolved scales (say $r \geq r_0$) and the smaller ones. A guide to such considerations could be given by the work of Nakano (1988), who applied DIA to the wave-packet representation. Another line of inquiry could be to attempt a real-space renormalization group analysis of Eq. (18).

In general, the hope is that models deduced from the behavior of wavelet coefficients may capture the physics of turbulence in a more natural way than those based on Fourier modes. However, at this point the manipulations appear to be much more complicated in the wavelet representation, and so its real usefulness remains to be proven.

REFERENCES

ARGOUL F., ARNEODO A., GRASSEAU G., GAGNE Y., HOPFINGER E., & FRISCH U. 1989 **338,** *51*

BATCHELOR G. K. & TOWNSEND A. A. 1949 Proc. R. Soc. Lond. **A199,** 238

COIFMAN R. 1989 Preprint Yale University

DAUBECHIES I. 1988 *Comm. Pure Appl. Math.* **XLI,** 909

FARGE M. & RABREAU G. 1988 *C. R. Acad. Sci. Paris* **II 307,** 1479

FRISCH & PARISI 1985 in *Turbulence and Predictability in Geophysical Fluid Dynamics and Climate Dynamics. North-Holland, New York. p. 84*

GROSSMANN A. & MORLET J. 1984 *SIAM J. Math. Anal.* **15,** 723

KOLMOGOROV A. N. 1941 *C. R. Acad. Sci. U.S.S.R.* **30,** 301

KOLMOGOROV A. N. 1962 *J. Fluid Mech.* **13,** 82

KRAICHNAN H. 1974 *J. Fluid Mech.* **62,** 305

KRONLAND-MARTINET R., MORLET J. & GROSSMANN A. 1987 Int. J. Patt. Rec. and Art. Int. **1,** 97

MALLAT S. J. 1989 *IEEE Patt. Anal. and Mach. Int.* **11,** 674

MANDELBROT B. B. 1974 *J. Fluid Mech.* **62** 331

MENEVEAU C. & SREENIVASAN K. R. 1987 *Phys. Nucl. B (Proc. Suppl.)* **2,** 49

MENEVEAU C. & SREENIVASAN K. R. 1987 *Phys. Rev. Lett.* **59** 1424

MENEVEAU C. & SREENIVASAN K. R. 1989 preprint
NAKANO T. 1988 *Phys. Fluids* **31**, 1420
NOVIKOV E. A. 1971 *Appl. Math. Mech.* **35**, 231
PAUL T. 1985 *J. Math. Phys.* **25**, 3252
SIGGIA E. D. 1977 *Phys. Rev. A* **15**, 1730

Direct simulation of turbulent combustion

By T. J. Poinsot

Problem background and objectives

Understanding and modeling of turbulent combustion are key-problems in the computation of numerous practical systems. Because of the lack of analytical theories in this field and of the difficulty of performing precise experiments, direct simulation appears to be one of the most attractive tools to use in addressing this problem.

The present work can be split into two parts:

1. Development and validation of a direct simulation method for turbulent combustion.

2. Applications of the method to premixed turbulent combustion problems.

The goal of part 1 is to define and to test a numerical method for direct simulation of reacting flows. A high level of confidence should be attached to direct simulation results, and this can only be achieved through extensive validation tests. We have considered two major questions :

1.1. Which equations should be solved? Contrary to cold-flow turbulence, the choice of equations to solve for turbulent reacting systems is still an open question. At the present time, it is not reasonable to compute time-dependant solutions of Navier-Stokes equations with complex chemistry in multi-dimensional configurations. A reduction in the number of equations to be solved is needed. This also leads to a loss of information which must be estimated.

1.2. Which configurations should be studied and what boundary conditions are necessary? A second problem is the choice of the configurations to study and of the associated boundary conditions. Most direct simulations of cold-flow turbulence are performed for temporal situations with periodic boundary conditions. This approach is not convenient for many reacting flows, and spatial simulations are required. These simulations can not be done without adequate boundary conditions.

In part 2, direct simulation is used to address some of the many critical problems related to turbulent combustion. At the present time, I have limited this work to premixed combustion and considered only four basic issues :

2.1. The effect of pressure waves on flame propagation.

2.2. The interaction between flame fronts and vortices. This is the basic problem of turbulent combustion. The goal here is to gain more insight into the fundamental interaction mechanisms between flame fronts and vortices.

2.3. The influence of curvature on premixed flame fronts.

2.4. The validation of flamelet models for premixed turbulent combustion.

Questions 2.1 to 2.3 concern fundamental processes in turbulent premixed combustion which are not well understood at the present time. Part 2.4 is related to modeling and its goal is to use results obtained in sections 2.2 and 2.3 to construct and validate a flamelet model for turbulent premixed flames.

1. Development and validation of a direct simulation method for reacting flows

1.1. The equations to solve

The amount of complexity to include in direct simulations of reacting flows requires difficult compromises. Taking into account the variations of thermodynamical properties with temperature and chemical compositions as well as solving for all species present in a reacting compressible flow will typically lead to codes slower by at least three orders of magnitude than the codes used presently for cold flows. This is due to the high number of additional equations to solve (around 30 for a propane flame) but also to the stiffness of the resulting equations which will need very dense computation grids. On the other hand, using constant density assumptions, infinitely fast chemistry approximation or oversimplified equations for species concentrations (like assuming that the Lewis number is equal to unity, in which case the species concentration may be obtained directly from the temperature) will lead to faster codes but will not tell us much about real mechanisms. The choice which was made here is the following (Poinsot and Lele 1989):

- solve the complete Navier-Stokes equations, including variable density and compressibility effects,
- use an elementary reaction for premixed combustion (*Reactants* $\rightarrow$ *Products*) and finite rate chemistry (Arrhenius law). The reaction rate $\dot{w}_R$ is expressed as:

$$\dot{w}_R = B\rho Y_R \ \exp\left(-\frac{T_{ac}}{T}\right) \tag{1}$$

where T_{ac} is the activation temperature and Y_R is the local mass fraction of reactants.

- solve separately for species concentration and temperature (non-unity Lewis number),
- take into account the variations of species diffusion, viscosity and conductivity with temperature,
- take into account heat losses.

This choice is accompanied by certain limitations:

- the Schmidt, Prandtl and Lewis numbers are fixed,
- most cases are run in two-dimensional geometries,
- only premixed combustion has been considered.

Extensions to three-dimensional or to diffusion flames are straightforward. At the present stage, the following mechanisms can be described:

- dynamic effect of the flame front on the flow (this requires variable density),
- effects of the flow on the inner structure of the flame front (this requires finite-rate chemistry),
- extinction of the flame by stretch and influence of curvature (this requires non-unity Lewis numbers and non-zero heat losses),
- influence of pressure waves on combustion, triggering of combustion instabilities (this requires compressibility).
- mixing, ignition, and quenching mechanisms in supersonic combustion (this requires compressibility, non-unity Lewis number, and finite-rate chemistry).
- flame-generated vorticity and flame/vortex interactions (this requires non-constant density and viscosity).

All these mechanisms are key-processes in many combustion phenomena and few of them are well understood in a general sense. Before going to three-dimensional cases with more complex chemistry, the present approach can lead to many original and important results.

1.2. Configurations and boundary conditions

A second problem is the choice of the configurations to study and of the associated boundary conditions. An extensive study of appropriate boundary conditions for spatial direct simulation has been performed. This effort goes beyond the scope of reacting flows, and its goal is to provide a satisfactory method to specify boundary conditions in cases where periodicity can not be assumed. Periodicity has been used in most direct simulations of reacting or non-reacting flows because it suppresses the need of boundary conditions (The domain is folded on itself). When more realistic problems are considered (involving inflows and outflows, for example) the problem of boundary conditions becomes crucial. On the basis of methods proposed for the Euler equations (Thompson 1987), a general formulation for the Navier Stokes equations has been derived (Poinsot and Lele 1989). This method called Navier-Stokes Characteristic Boundary Conditions (NSCBC) applies for most boundaries (inlet, outlet, adiabatic slip-wall, no-slip adiabatic, or isothermal wall). It has been implemented in the high-order finite-difference code of Dr. Lele and tested in the following configurations (all of them concern spatially evolving flows) :

1/ Non-reacting shear layers (confined by walls or unconfined).
2/ Premixed flames in a shear layer.
3/ Acoustic waves leaving the computation domain (subsonic and supersonic).
4/ Vortices leaving the computation domain (subsonic and supersonic).
5/ Very low Reynolds number flows (Poiseuille flow).

As an example, Figs. 1 and 2 show results obtained from test 4. A vortex is generated at time $t = 0$ in a supersonic flow and is convected downstream. The mean flow is uniform, from left to right at a Mach number of $u_0/c = 1.1$ (c is the sound speed). The maximum velocity induced by the vortex is small ($0.0018u_0$). The plots on the left side of Figs. 1 and 2 give the vorticity field

while the plots on the right side display the longitudinal velocity perturbations $(u - u_0)/u_0$. The right boundary is supposed to be 'non-reflecting'. It should let the vortex pass through without generating any perturbation. Two methods were used for the outlet boundary:

- Method 1 is a reference method proposed by Rudy and Strikwerda (1981) which can be viewed as the prototype of methods used by many other authors (Yee 1981, Jameson and Baker 1984). It uses extrapolation for the velocities and the density. The pressure is then obtained by solving for a Riemann invariant and relaxing the pressure to some value at infinity.
- Method 2 is the 'non-reflecting' version of the NSCBC method.

Supersonic outlet boundary conditions are supposed to be easy to implement because no information can travel upstream towards the inlet. All errors created at the outlet should be convected outwards. In fact, physical information satisfies this assumption but numerical instabilities do not (Vichnevetsky and Pariser 1986). Using extrapolation at the outlet generates numerical waves which travel upstream much faster than the sound speed and interact with the inlet to generate other perturbations (Poinsot, Colonius and Lele 1989). This coupling is very strong with method 1 (Fig. 1). Not only is the vorticity field near the outlet strongly modified but the inlet field is also affected and additional vorticity is introduced into the computation. The total vorticity and the maximum vorticity in the domain do not go to zero after the vortex has left the domain (Fig. 3). This numerical feedback between outlet and inlet can lead to non-physical instabilities similar to the one described by Buell and Huerre for incompressible flows (1988) and could make the final results of the simulation dubious.

When the NSCBC method is used, the vortex leaves the domain without any perturbation. The total vorticity and the maximum vorticity in the computation box both go to zero (Fig. 3). The improvement over the reference method is clear.

Although the method is based on inviscid characteristic theory, it also works very well for viscous flows, like the Poiseuille flow. All tests are presented in Poinsot and Lele (1989).

2. Applications to premixed turbulent flames

2.1. The effect of pressure waves on flame propagation

The effects of pressure waves on combustion and especially the effects of acoustic waves on the stability of a reacting flow are not well understood at the present time although their practical importance is evident in many situations (Yang and Culick 1986, Poinsot et al 1987, 1988). Some of these effects can be simulated numerically. One of the most interesting configurations is the premixed flame in a shear layer (Fig. 4 to 6). This case illustrates also the importance of the boundary conditions which control the acoustics. Depending on the boundaries, the flame will behave very differently:

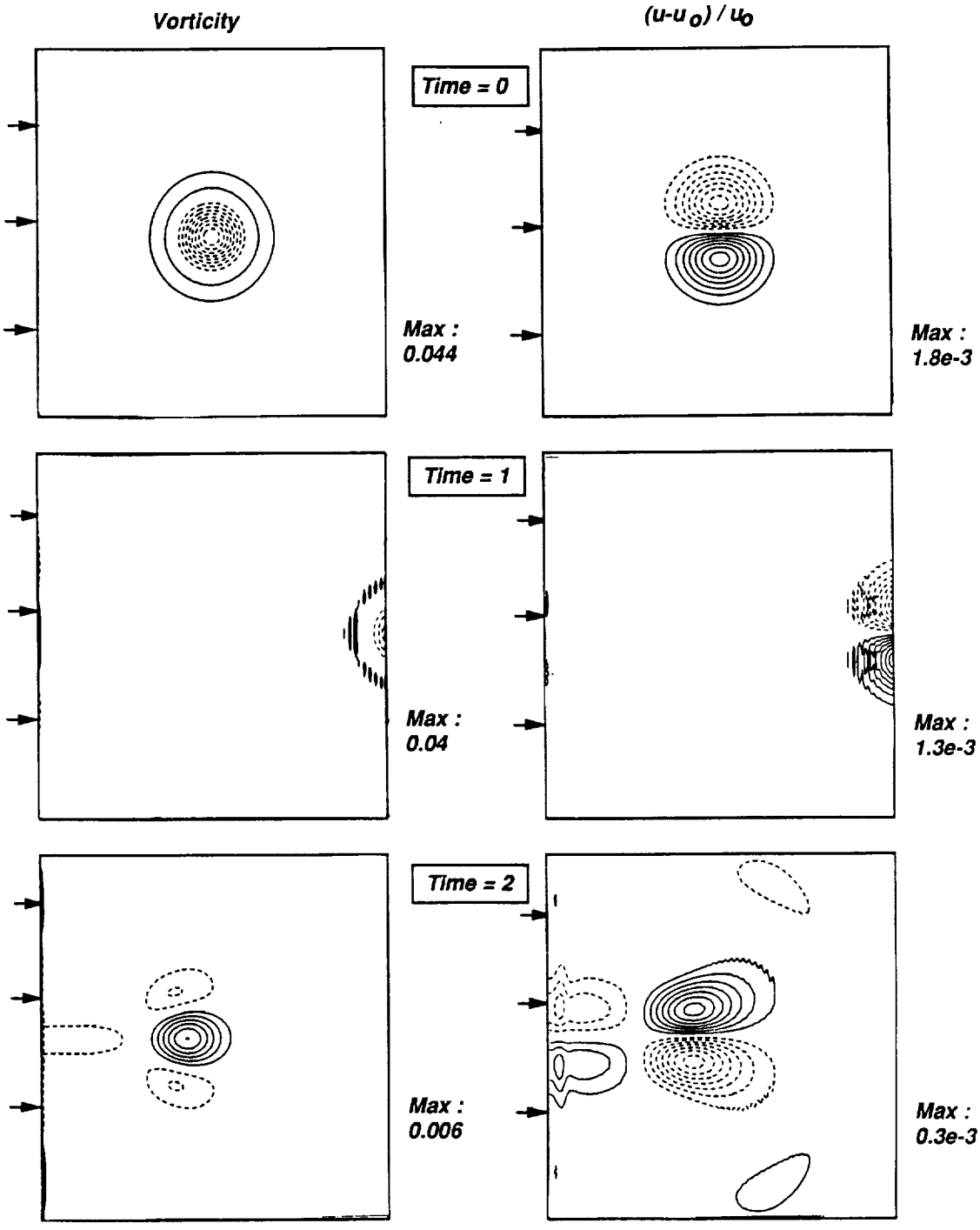

FIGURE 1. Transmission of a vortex through a non-reflecting boundary. Reference method.

- if all boundaries are non-reflecting (Fig. 4), acoustic waves will leave the domain and no coupling may take place between combustion and acoustic waves. The total reaction rate in the computation box will reach a constant value after a finite time and a steady state is obtained.

- if the flame is placed in an infinite duct, where no reflection is allowed at the downstream end but where walls are placed on each side of the shear layer, no steady state is obtained (Fig. 5). The reaction rate oscillates and the frequency of oscillation (obtained by a non-linear spectral method (Veynante and Candel 1988)) is the frequency f_{2t} of the second transverse acoustic mode of the duct. This mode has a pressure antinode near the duct axis, where the flame is spreading, and this condition, known as the Rayleigh criterion, is necessary to have coupling between combustion and acoustic waves.

- finally, if the flame is placed in a 'real' duct with walls and reflection on a downstream end of the tube, the reaction rate oscillations are dominated by the quarter-wave mode of the duct at frequency f_{1L} (Fig. 6). The second transverse mode of the duct (frequency f_{2t}) is also present as indicated by spectral analysis (Fig. 7a). Although the reaction rate and the quarter-wave mode are directly coupled, the vorticity oscillations are insensitive to the quarter-wave mode (Fig. 7b). They depend only on the transverse modes f_{1t} and f_{2t}. The flow structure in this case is displayed in Fig. 8. The fuel concentration field (Fig. 8a) shows that the flame front is wrinkled. (These wrinkles do not appear when no acoustic wave is present, for example for the case of Fig. 4). Structures are convected along the flame front at the flow speed. The vertical velocity contours (Fig. 8b) reveal that they are formed at the duct inlet by the sloshing motion due to the acoustic transverse oscillations.

This simple example shows that a strong coupling may occur between acoustic waves and combustion. This interaction is believed to be even stronger when the flame front reaches a wall. More studies of these mechanisms will be performed in the coming year.

2.2. The interaction between flame fronts and vortices

The modeling of turbulent premixed combustion is still largely based on empiricism because of the complexity of flame/turbulence interactions. The first step in building a turbulent combustion model is to determine in which combustion regime the reacting flow will be. Diagrams defining combustion regimes versus length and velocity scales ratios have been proposed by Borghi (1984), Peters (1986), Bray (1980) and Williams (1985). Knowing the integral turbulence scale and the turbulent kinetic energy, these diagrams indicate if the flow will contain flamelets, pockets or distributed reaction zones. Each of these regimes requires specific modeling.

In the 'flamelet' domain, chemical times are small compared to turbulence times (Bray 1980). Eddies stretch and convolute the flame front, but they do not destroy its internal structure. The flame front can be described as a laminar

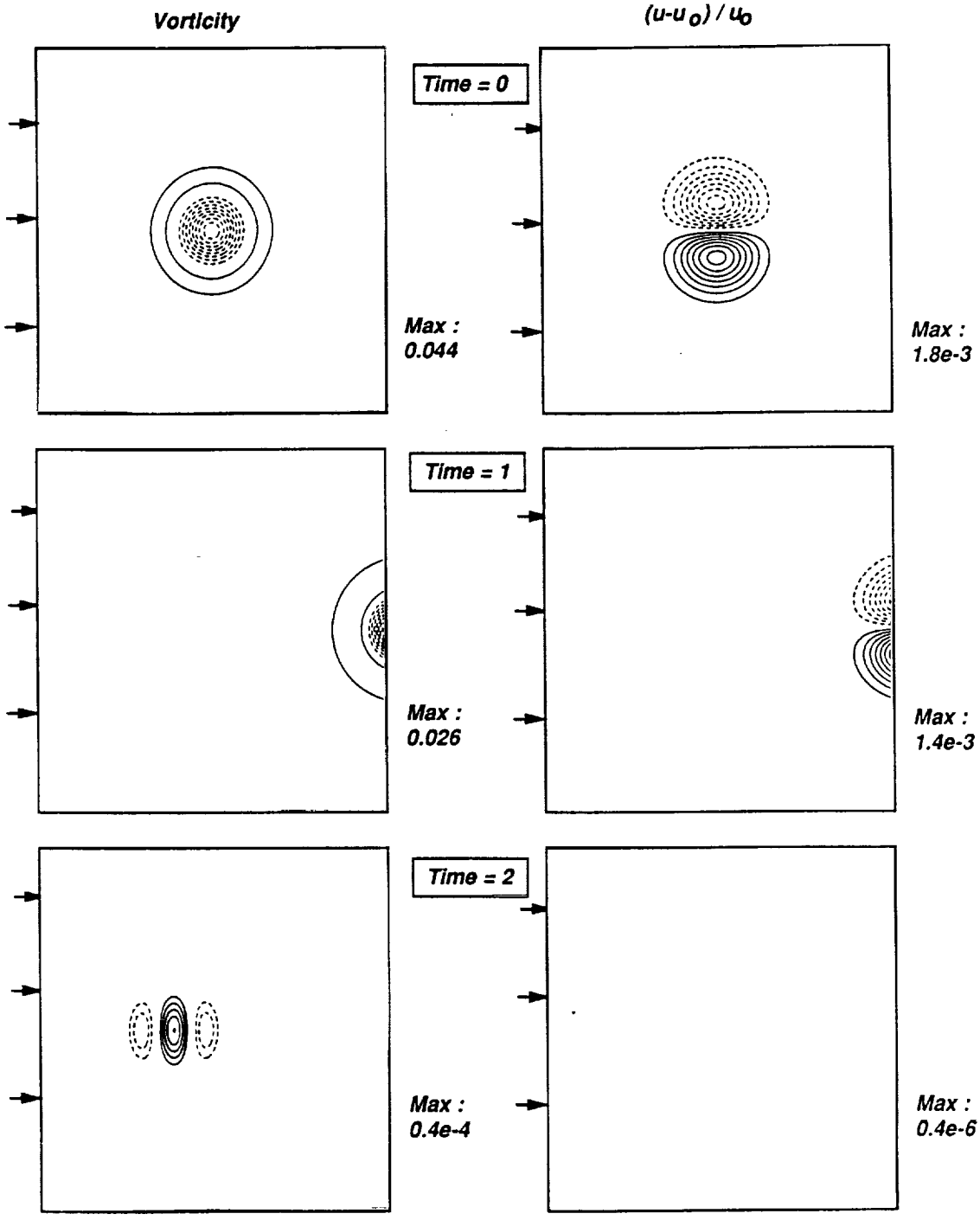

FIGURE 2. Transmission of a vortex through a non-reflecting boundary. NSCBC method.

flame between fresh and burnt gases. The modeling of such a flow is done by tracking the area of this interface (Candel et al 1988, Veynante et al 1989).

In distributed reaction regimes, the turbulence is very intense, and the flame is shred in small elements. No laminar flame front can be identified any more. Statistical models (Pope and Cheng 1987, Borghi 1984) are likely to be better adapted.

Therefore, knowing which regime corresponds to the flow to be modelled is a necessary and important step in turbulent combustion modeling. Unfortunately, the dimensional analysis which is used to construct these diagrams is rather crude and neglects important effects such as flame front curvature, transient or viscous effects. The basic reason for this situation is that these mechanisms are not well understood and, therefore ,are ignored in this first-order analysis.

It is possible to construct realistic turbulent combustion diagrams. The technique which was used here is based on a detailed analysis of the physical mechanisms controlling turbulent premixed combustion and uses direct numerical simulation to quantify them (Poinsot, Veynante and Candel 1990). This is done by constructing a 'spectral' diagram describing the interaction between one isolated vortex and a laminar flame front. This information is used afterwards to infer the behavior of a complete turbulent reacting flow and construct more quantitative diagrams.

2.2.1. Turbulent combustion diagrams

Classical turbulent combustion diagrams suppose that a reacting flow can be parameterized using two non-dimensionalized numbers: the ratio of the turbulence integral scale l to the flame front thickness l_F and the ratio of root-mean-square velocity fluctuations u' to the laminar flame speed s_L. Using the notations and assumptions of Peters (1986), different transitions can be associated to specific lines in this diagram (Fig. 9a).

- The line $u'/s_L = 1$ indicates the transition between wrinkled flames and corrugated flames (flames where turbulence can form pockets of fresh gases in burnt gases).
- The limit between flamelets and distributed reaction zones is reached when the stretch $\frac{1}{A}\frac{dA}{dt}$ (A is the flame surface) imposed on the flame becomes larger than the critical stretch for extinction and creates local quenching. The critical stretch depends on the flame characteristics but may be estimated by s_L/l_F (Peters 1986). Defining the Karlovitz number by:

$$Ka = \frac{\frac{1}{A}\frac{dA}{dt}}{s_L/l_F}, \tag{2}$$

we expect local quenching and distributed reaction zones if $Ka > 1$.

The flame stretch $\frac{1}{A}\frac{dA}{dt}$ can be expressed as a function of the Taylor scale Λ and of u' as

$$\frac{1}{A}\frac{dA}{dt} \simeq u'/\Lambda.$$

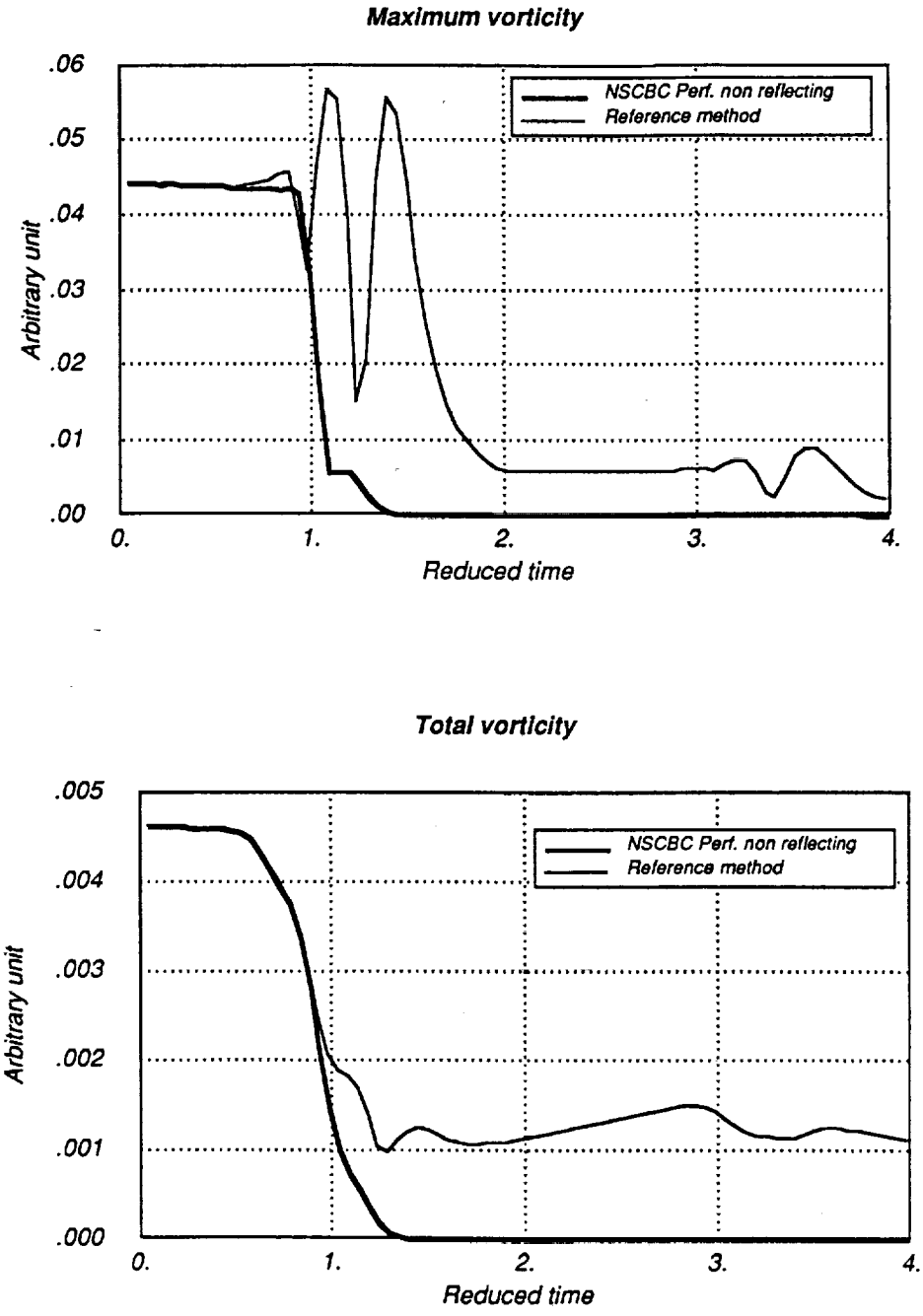

FIGURE 3. Transmission of a vortex through a non-freflecting boundary. Comparison between reference and NSCBC methods.

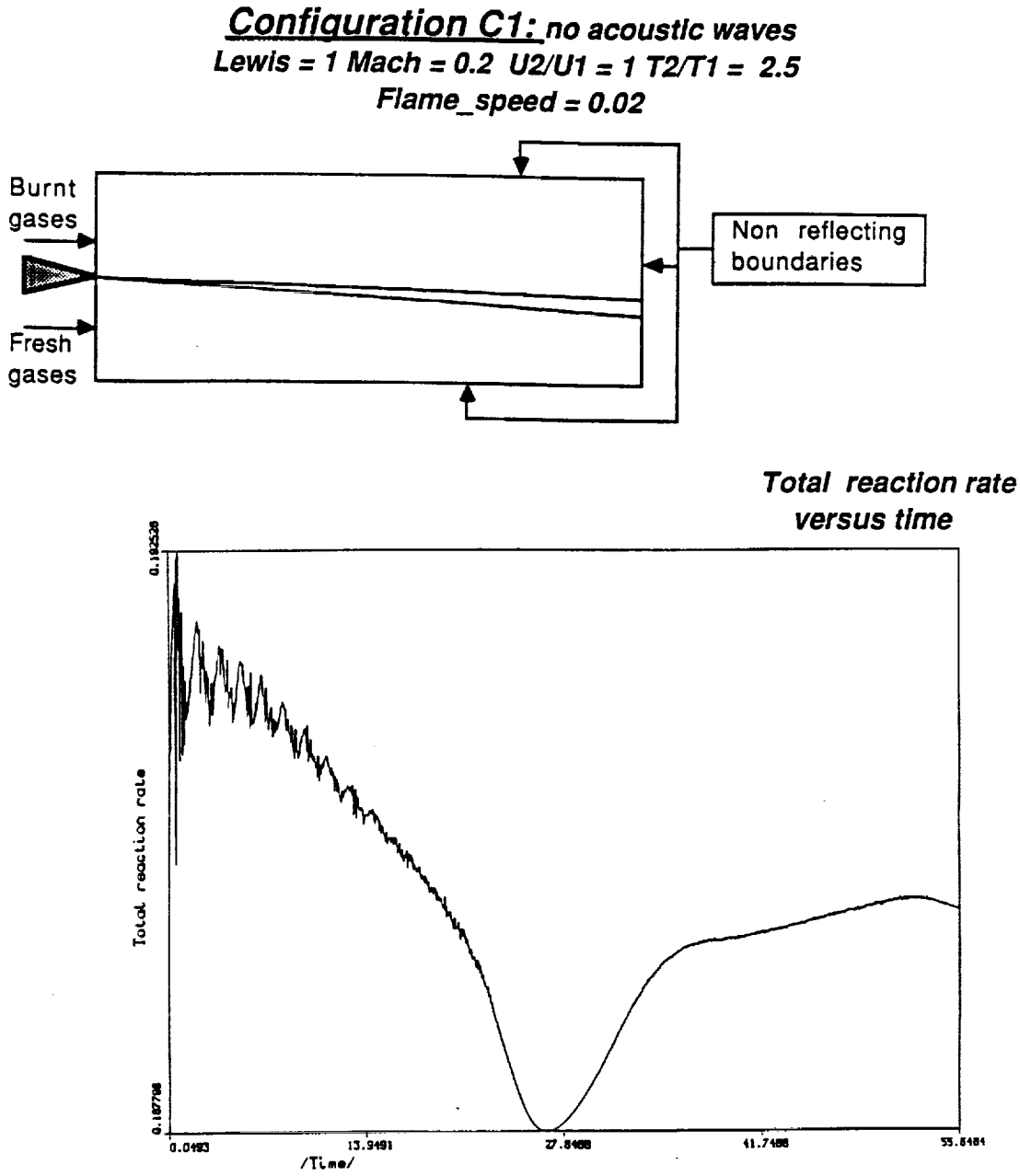

FIGURE 4. Reacting shear layer in an infinite domain.

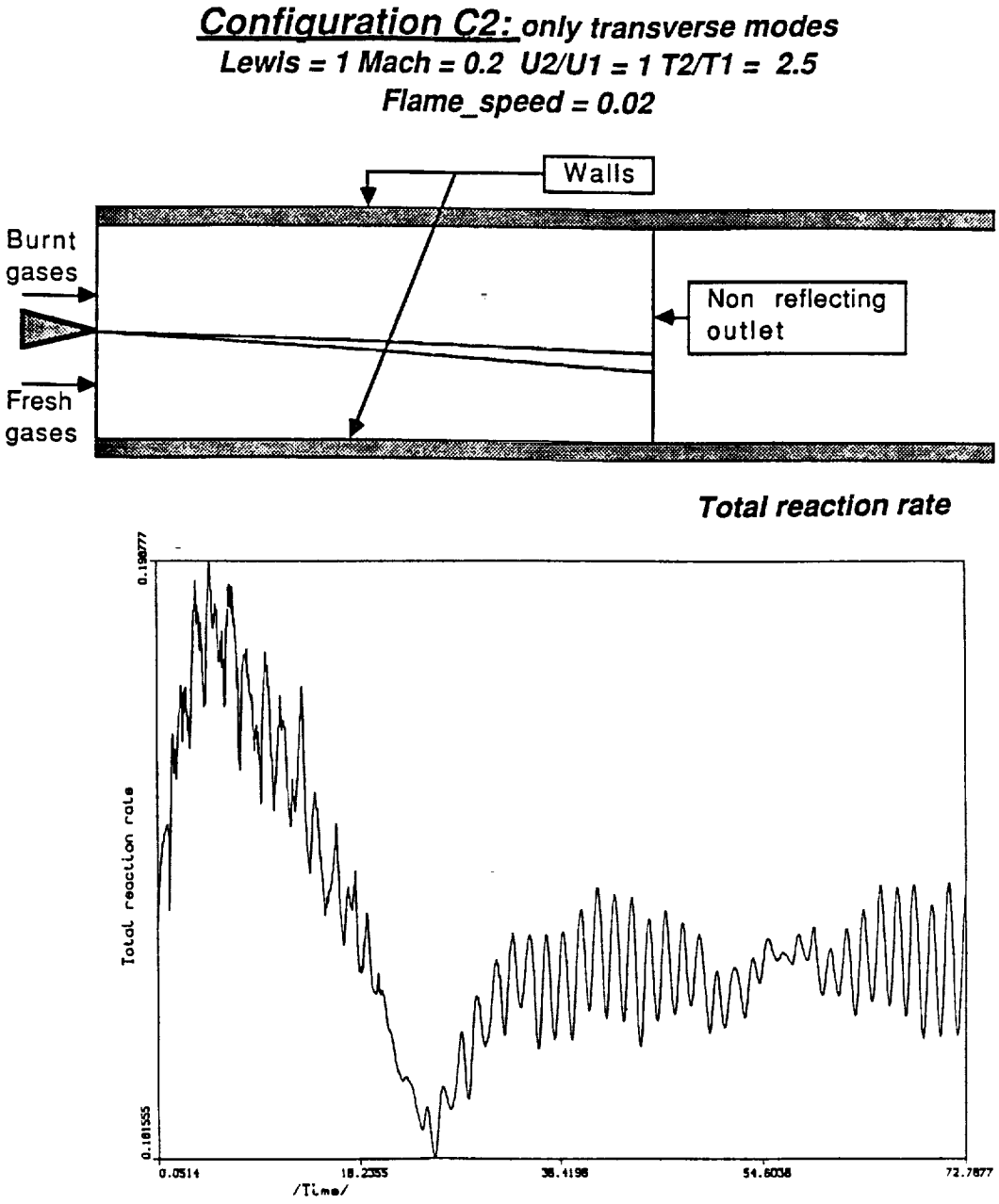

FIGURE 5. Reacting shear layer in an infinite duct.

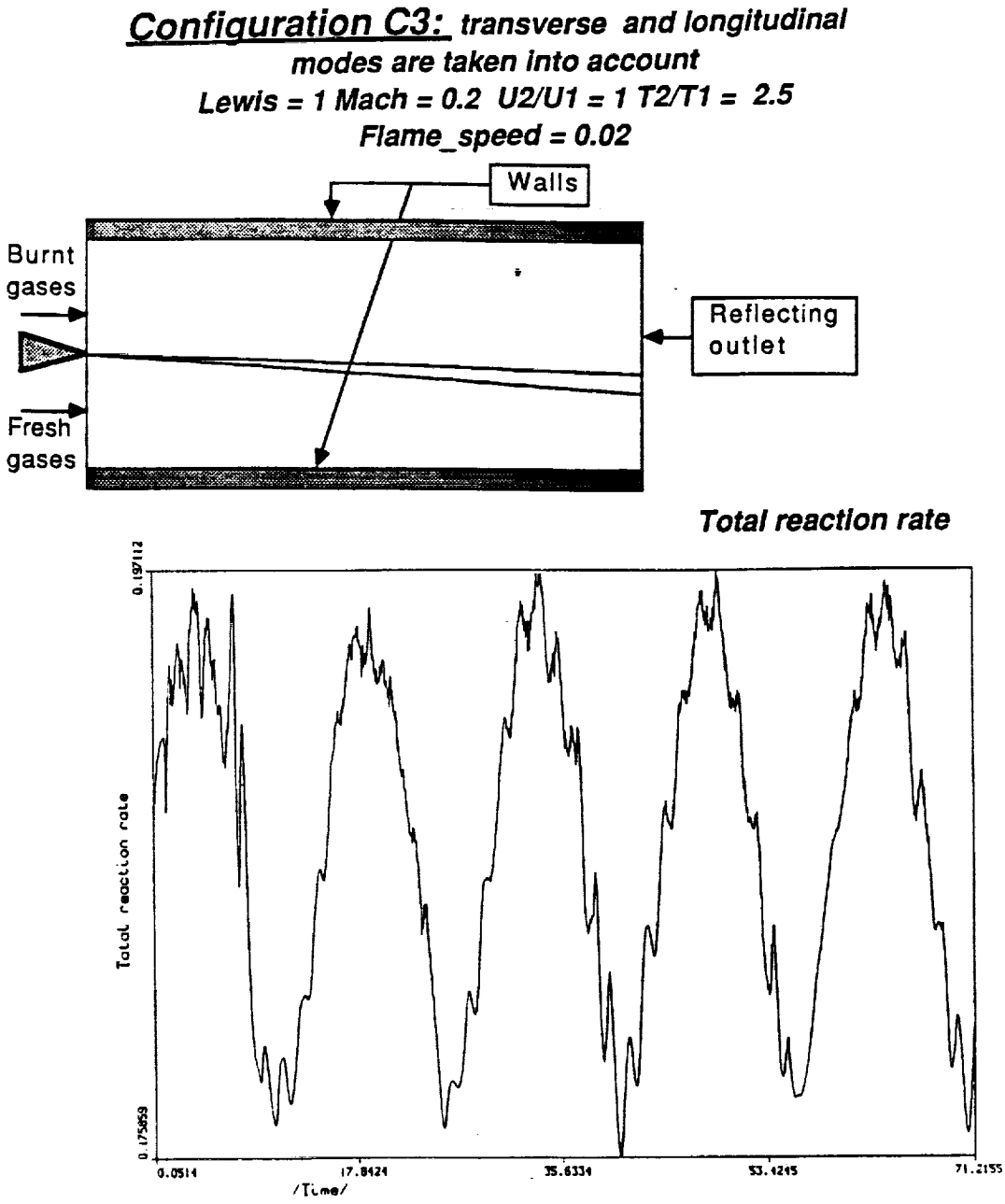

FIGURE 6. Reacting shear layer in a finite duct.

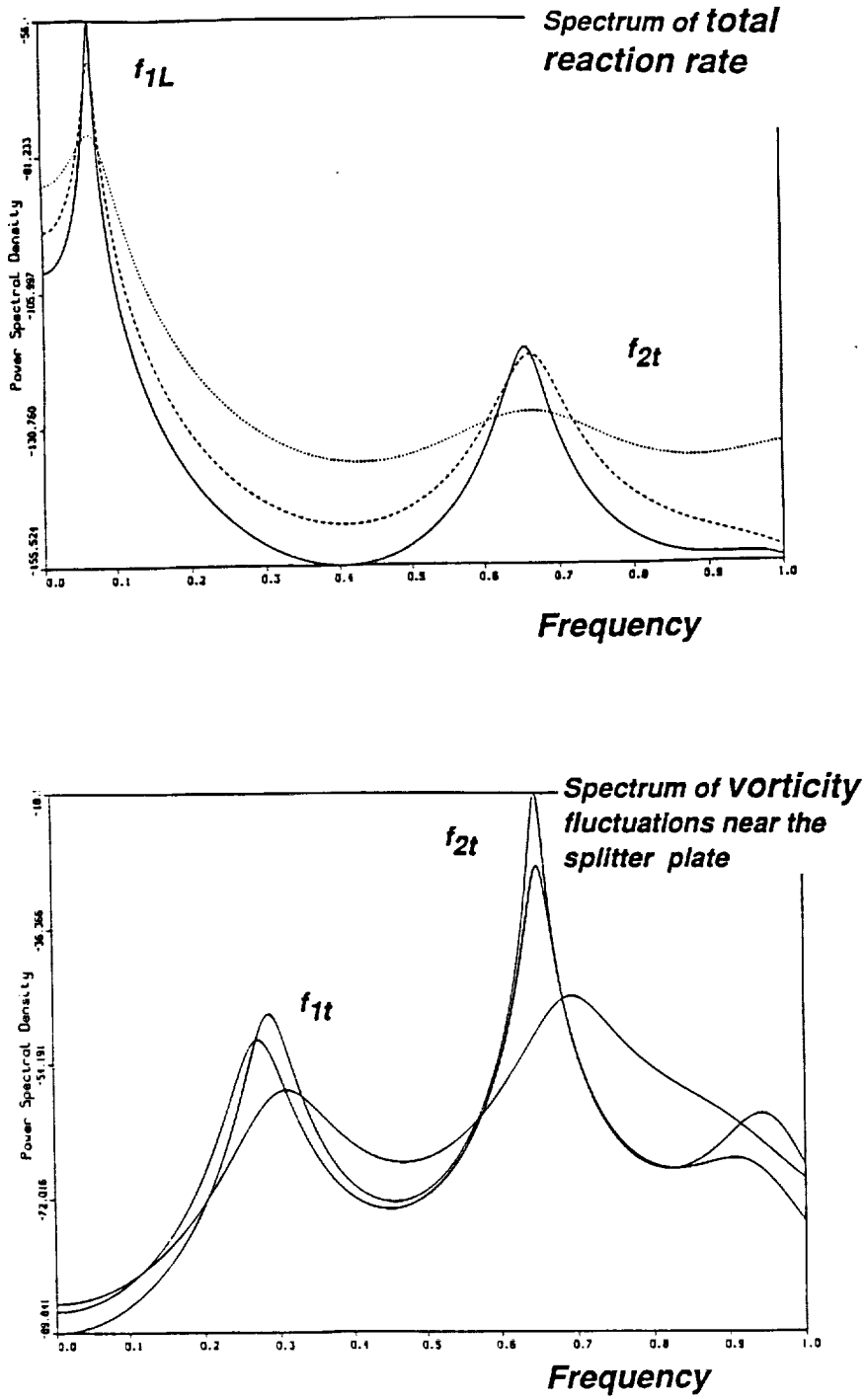

FIGURE 7. Reacting shear layer in a finite duct. Spectral analysis of total reaction rate and vorticity near the splitter plate.

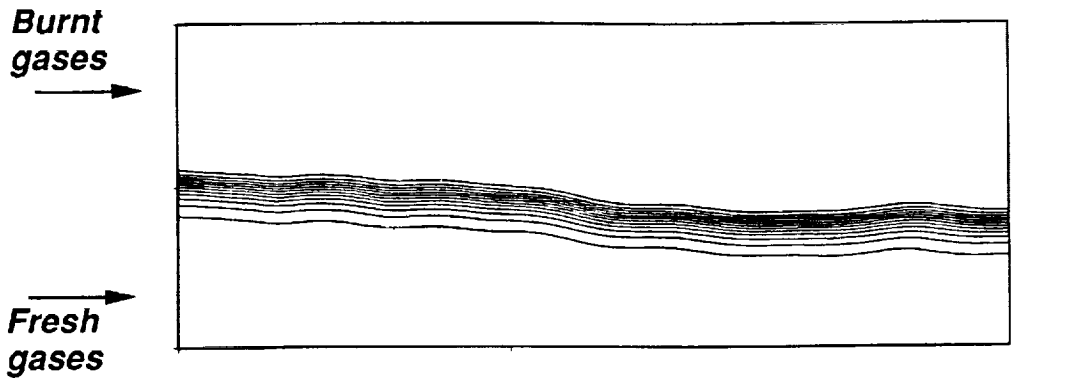

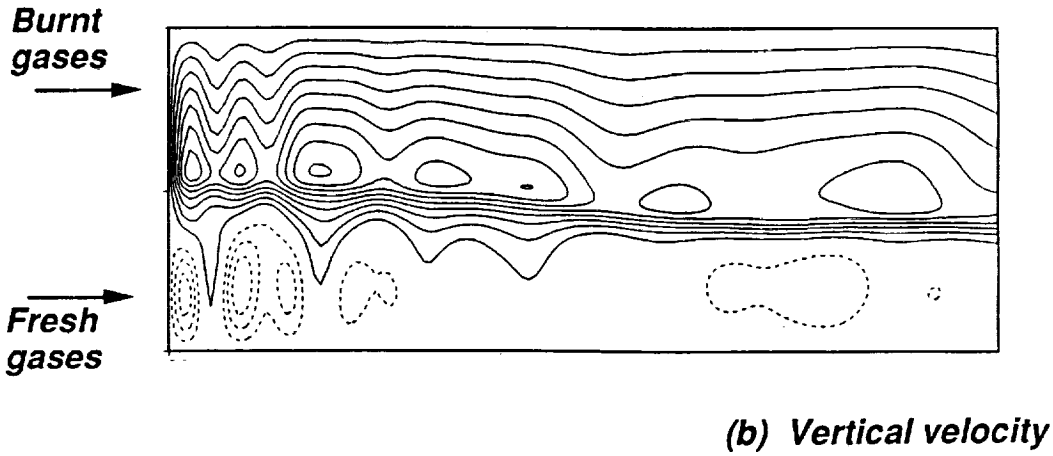

FIGURE 8. Reacting shear layer in a finite duct. Flow field at time = 70.

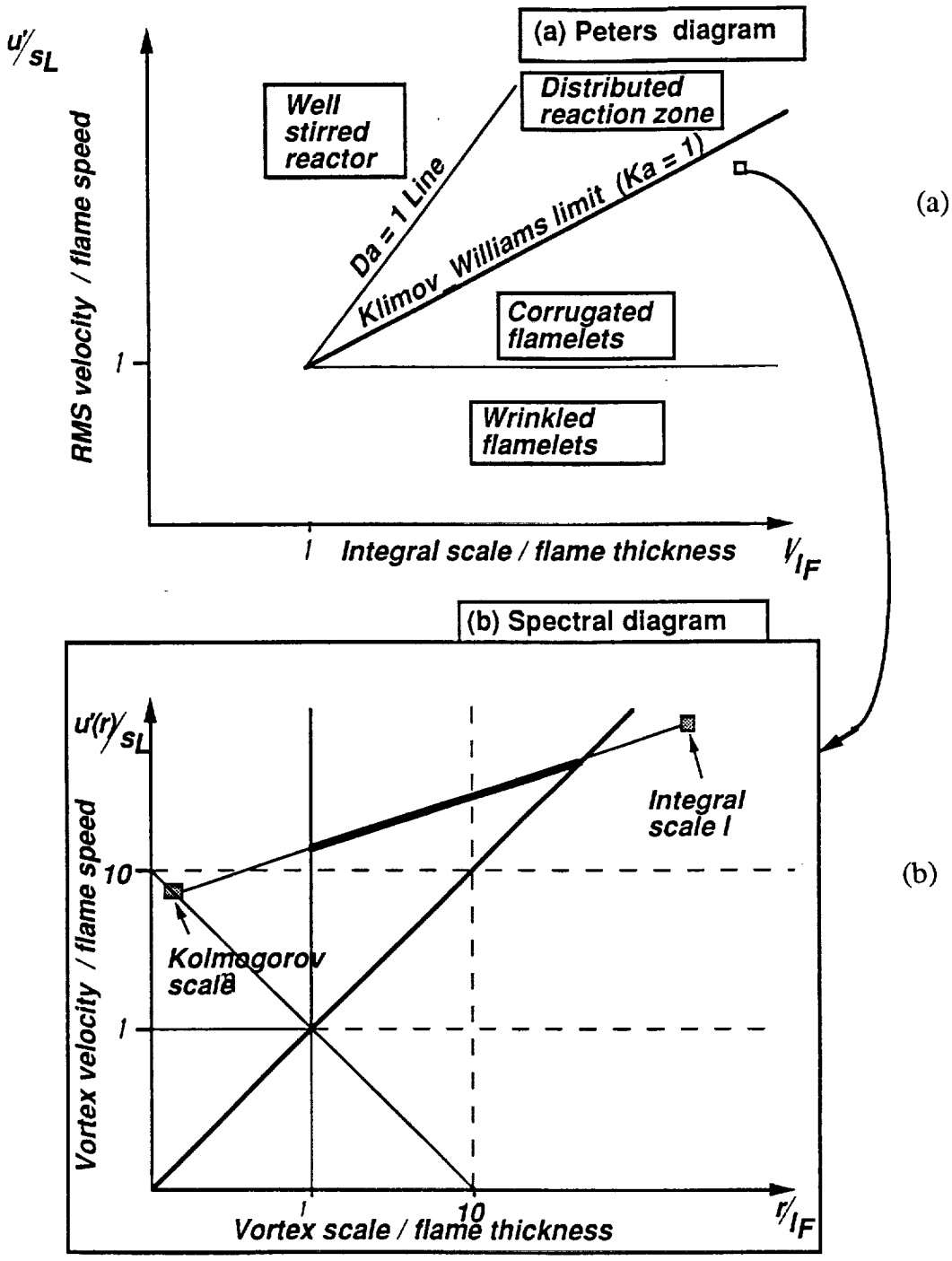

FIGURE 9. Diagrams of premixed turbulent combustion: (a) Standard diagram (with Peters notations); (b) Spectral diagram.

Using the definitions of the Taylor scale Λ and of the Kolmogorov scale η, we can construct four expressions for Ka:

$$Ka \simeq \left(\frac{(u'/s_L)^3}{l/l_F} \right)^{1/2} = \frac{\sqrt{\epsilon/\nu}}{s_L/l_F} = \left(\frac{l_F}{\eta}\right)^2 = \frac{u_K/\eta}{s_L/l_F}. \quad (3)$$

where u_K is the characteristic speed of Kolmogorov scales.

The Klimov-Williams (KW) criterion is then obtained by considering the third expression of the Ka number in Eq. (3) and stating that no flamelet should be observed in a reacting flow if the Kolmogorov scale η is smaller than the flame thickness l_F. According to the KW criterion, no flamelets would exist beyond $Ka = 1$ because their internal structure would be destroyed by stretching and quenching. The $Ka = 1$ limit is a line with a slope 1/3 in the diagram of Fig. 9a (Eq. (3)). The region below $Ka = 1$ is the flamelet region. Note from the last relation in (3) that $\frac{1}{A}\frac{dA}{dt}$ is the strain rate at the Kolmogorov scale: u_K/η. Therefore, the KW criterion is related to only one scale: the Kolmogorov scale.

• Increasing the turbulence intensity beyond the $Da = (u'/l)/(s_L/l_F) = 1$ limit leads to cases where all turbulence times are smaller than the chemical time. This regime, called the well-stirred reactor, is not well understood at the present time.

2.2.2. A spectral diagram for turbulent combustion regimes

The approach used to build diagrams in the previous section has many deficiencies: it considers only one length scale to describe turbulent combustion, it neglects all viscous and transient mechanisms as well as curvature effects. These deficiencies are especially clear when the KW criterion is derived: in Eq. (3), the KW criterion considers the Kolmogorov scales as the most active because they generate the highest strains. This approach ignores three important points:

1- Kolmogorov scales might be too small compared to the flame front thickness to stretch it.

2- Viscous effects might dissipate Kolmogorov scales before they quench the flame front.

3- Scales smaller than the flame front may induce high local curvature and thermodiffusive effects which might counteract the effects of strain.

Using direct simulation, we can derive criterions including viscous and curvature effects and take all length scales into account. The first step is to recognize that turbulent combustion diagrams are obtained through drastic simplifications and begin our analysis from a more basic point of view.

Let us consider first one flame front interacting with one 'turbulent' flow. Supposing that turbulence and chemistry are fixed, we can define a *spectral diagram* which maps the interaction between one of the turbulence scales and the flame front (Fig. 9b). There is one spectral diagram for each point of the Peters diagram.

In this spectral diagram, three classes of vortices can be isolated because they indicate important transitions: the vortices which can form pockets on the wrinkled flame front; the vortices which can quench locally the flame front; the vortices which are too small to interact with the flame zone.

It is important to emphasize that, in the same turbulent reacting flow, all three types of vortices may be found at the same time. The flow structure is the superposition of all vortices and describing it by using only one scale can not take all mechanisms into account. These three effects (pockets formation, quenching, and vortex decay) can be characterized by three non-dimensionalized numbers which depend on the length scale r (r will vary between the Kolmogorov scale η and the integral scale l):

1- $Vr(r) = u'(r)/s_L$ is the ratio of the turbulent velocity fluctuations associated with the length scale r to the laminar flame speed.

2- $Ka(r) = \frac{u'(r)/r}{l_F/s_L}$ is the Karlovitz number for the scale r. It reduces to the Karlovitz number Ka of Eq. (3) if $r = \eta$.

3- $Po(r) = \frac{r^2 s_L}{\nu l_F} = (\frac{r}{l_F})^2$ is a measure of the power of the vortex. It is the ratio of the life-time of the vortex r^2/ν to the chemical time l_F/s_L. It can also be interpreted as the ratio of the penetration length of the vortex into the flame front (before it gets dissipated by viscous effects) to the flame front thickness. It is also a good measure of the curvature effects.

In the spectral diagram, a turbulent flow field is represented by a straight line (called here 'turbulence line') bounded by the Kolmogorov and the integral scales.[a] Kolmogorov scales are located on the line $Re_\eta = u'(\eta)\eta/\nu = \frac{u'(\eta)}{s_L}\frac{\eta}{l_F} = 1$.

Each point of the turbulence line corresponds to the interaction of one length scale with the flame front (Fig. 9). Such an interaction may be computed exactly and an accurate spectral diagram may be constructed as we will show in the next section.

2.2.3. Direct simulation of vortex/flame front interactions

Many authors have studied vortex/flame interactions (Cetegen and Sirignano 1988, Ghoniem and Givi 1987, Laverdant and Candel 1988, Ashurst et al 1987). However, very few have considered all mechanisms which should be taken into account to determine turbulent combustion regimes. This is done here by solving the Navier-Stokes equations in a two-dimensional configuration using the assumptions described in Section 2.1.

The configuration is the following (Fig. 10a): at $t = 0$, two counter-rotating vortices are generated upstream of a laminar flame front. The flow is symmetrical along the $y = 0$ axis and subsequently, only the upper half is calculated and

[a] We will assume here that the turbulent reference quantities correspond to the fresh gases and that the turbulent spectrum in this part of the flow can be described by the Kolmogorov relation: $u'(r)^3/r = \epsilon$ where ϵ is the dissipation rate.

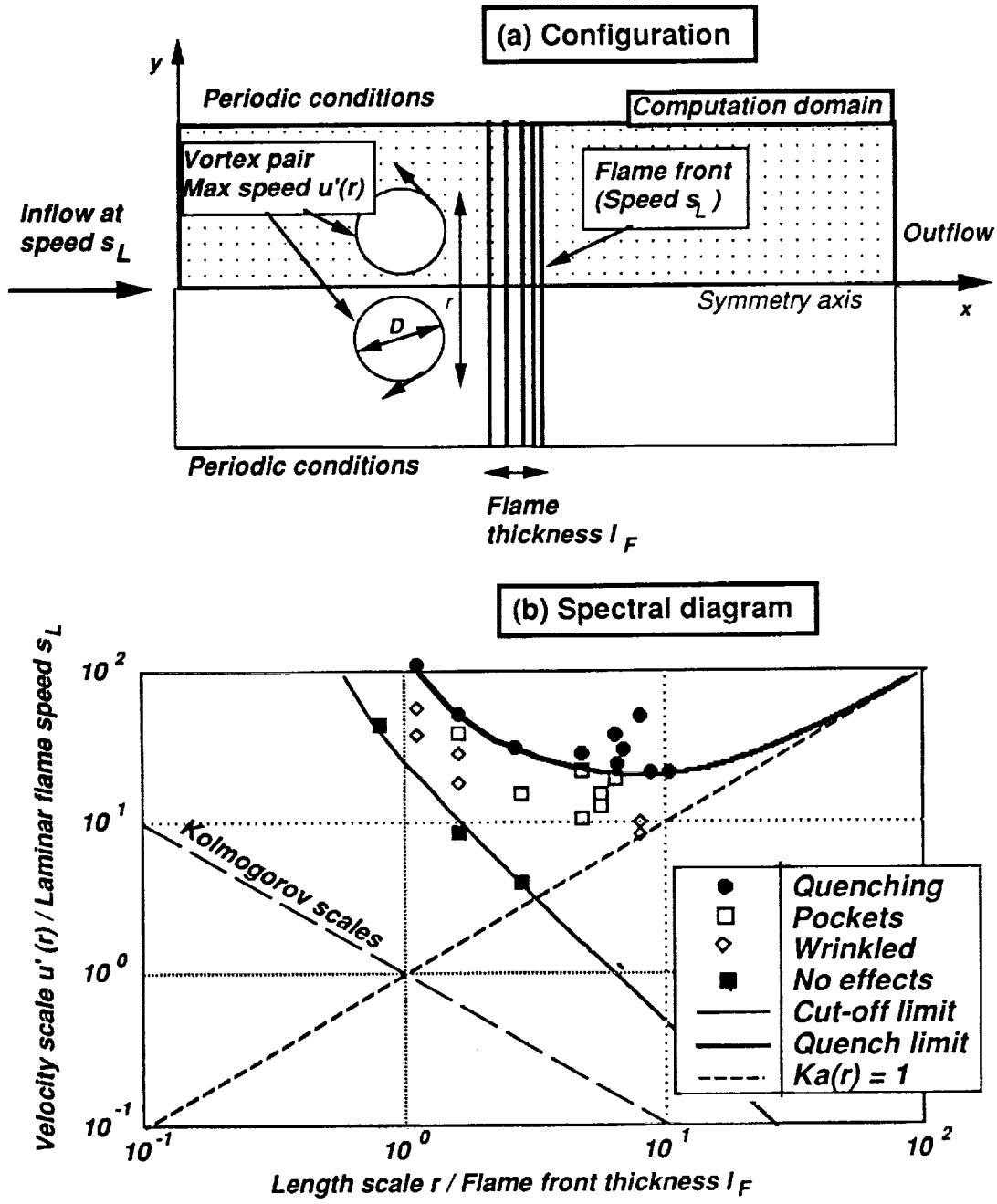

FIGURE 10. (a) Configuration for direct simulation of the interaction between a flame front and a vortex pair; (b) Spectral diagram based on direct simulation results.

displayed. The inlet flow speed is equal to the laminar flame speed so that the flame does not move when it is not perturbed. The vortex-pair configuration allows an accurate measurement of the flame stretch and speed on the axis. It also generates a high stretch and may be considered as one of the most efficient structures able to interact with the flame front because of its self-induced velocity. Finally, it is easy to generate in an experiment and some results on the interaction of a vortex pair with a flame front are available (Jarosinski et al 1988).

Simulations were performed for a flame with a temperature ratio of 4, a flame speed $s_L/c = 0.012$ and a Lewis number of 1.2 (Poinsot et al 1990). The flame front thickness l_F is $3.7\nu/s_L$. The length scale r used to characterize the vortex pair is the sum of the vortex diameter D and of the distance between vortex centers (Fig. 10a). The velocity scale $u'(r)$ is the maximum velocity induced by the pair. Tests have been performed for $0.81 < r/l_F < 11$ and $1 < u'(r)/s_L < 100$.

2.2.4. The spectral diagram and the new turbulent combustion

The resulting spectral diagram is displayed in Fig. 10b. Depending on the scale r and on the vortex pair maximum velocity $u'(r)$, computation shows that the interaction can lead to different results:

- a local quenching of the front (with or without pocket formation),
- the formation of a pocket of fresh gases in the burnt gases without quenching,
- a wrinkled flame front
- a negligible global effect without noticeable flame wrinkling or thickening.

Two lines have been constructed in this diagram: the quenching limit and the cut-off limit.

• The quenching limit indicates vortices able to quench the flame front. It was fitted among our data points for $0.81 < r/l_F < 11$ and extended for large scales $r/l_F > 11$ to match the line $Ka(r) = 1$ (Large vortices stretch the flame front like in a stagnation point flow: stretch is sustained for long times and little curvature is induced. Therefore, quenching by these structures is only determined by the ratio of vortex-induced stretch to critical flame stretch and occurs when $Ka(r) = 1$.)

• The cut-off limit corresponds to vortices inducing a modification of the total reaction rate of less than 5 percent.

From the spectral diagram, it is possible to construct a premixed turbulent combustion diagram by using the following assumptions:

(1) there are no interactions between vortices of different size,

(2) only one vortex interacts at a given time with the flame front,

(3) any structure located in the quenching zone of the spectral diagram will quench locally the flame front and induce a distributed reaction regime.

These assumptions are rather simple. The energy spectrum, for example, certainly plays an important role: scales in the quenching zone will not quench

the flame front if the energy density for these scales is too low. Therefore, assumption (3) is probably not satisfied. However, these hypothesis lead to a 'maximal' interaction diagram. Experimental results would probably lead to higher limits of $u'(r)$ for the first distributed reaction zones.

An important limitation of the present approach appears for very small and energetic scales. In this region, the effect of many small vortices on the flame front is difficult to deduce from the effect of one isolated vortex. Studying well-stirred combustion would require to take a complete turbulent field into account.

Under the assumptions listed above, the construction of a turbulent combustion diagram is straightforward. A turbulent field of type B (Fig. 11a) will contain inefficient scales (dashed line) and scales able to have some effect on the flame front but unable to quench it (solid line). Point B will, therefore, correspond to a flamelet regime. In the case of field A, even the integral scale will not be energetic enough to interact with the flame front, and the latter will remain pseudo-laminar. Turbulent field C contains scales able to quench locally the flame front (double-width solid line). Note that these scales are larger and faster than the Kolmogorov scale by orders of magnitude. C will correspond to a distributed reaction zone. The limit of distributed reaction zones is obtained by taking the tangent with a slope of 1/3 to the quenching limit of the spectral diagram. Comparing this diagram (Fig. 11b) with the Peters diagram (Fig. 9a) reveals that the domain where distributed reaction zones may be expected has moved at least of an order of magnitude towards more intense fields. The heat losses used for this computation were quite high (see Fig. 13) and in most practical cases, with lower heat losses, we expect the flamelet domain to be even larger than the present one.

Different characteristic scales may be extracted from the spectral diagram. For example, the cut-off and the quenching scales introduced by Peters (1986) can be evaluated from the quantitative data of Fig. 13 and are different by orders of magnitude when compared with the estimates given by Peters. Quenching criteria can also be derived (see Poinsot et al 1990).

2.2.5. An example of flame quenching by a vortex pair

To illustrate direct simulation results, we will describe a case where the vortex pair size and speed are high enough to induce quenching of the flame front ($r/l_F = 18$ and $u'(r)/s_L = 28$). Figures 12 and 13 display the reaction rate ($\dot{w}$) and the temperature (Θ) fields at four instants. Time is normalized by the flame time l_F/s_L: $t^+ = ts_L/l_F$.

The interaction is fast and ends after about two flame times. At $t^+ = 0.65$, the vortex pair has stretched and curved the flame but its inner structure is preserved and no quenching is observed. The Karlovitz number at this instant on the symmetry axis is around three. The fact that the flame is still burning despite such a high Karlovitz illustrates the importance of transients. At $t^+ = 1.3$, quenching appears on the downstream side of the pocket of fresh gases formed

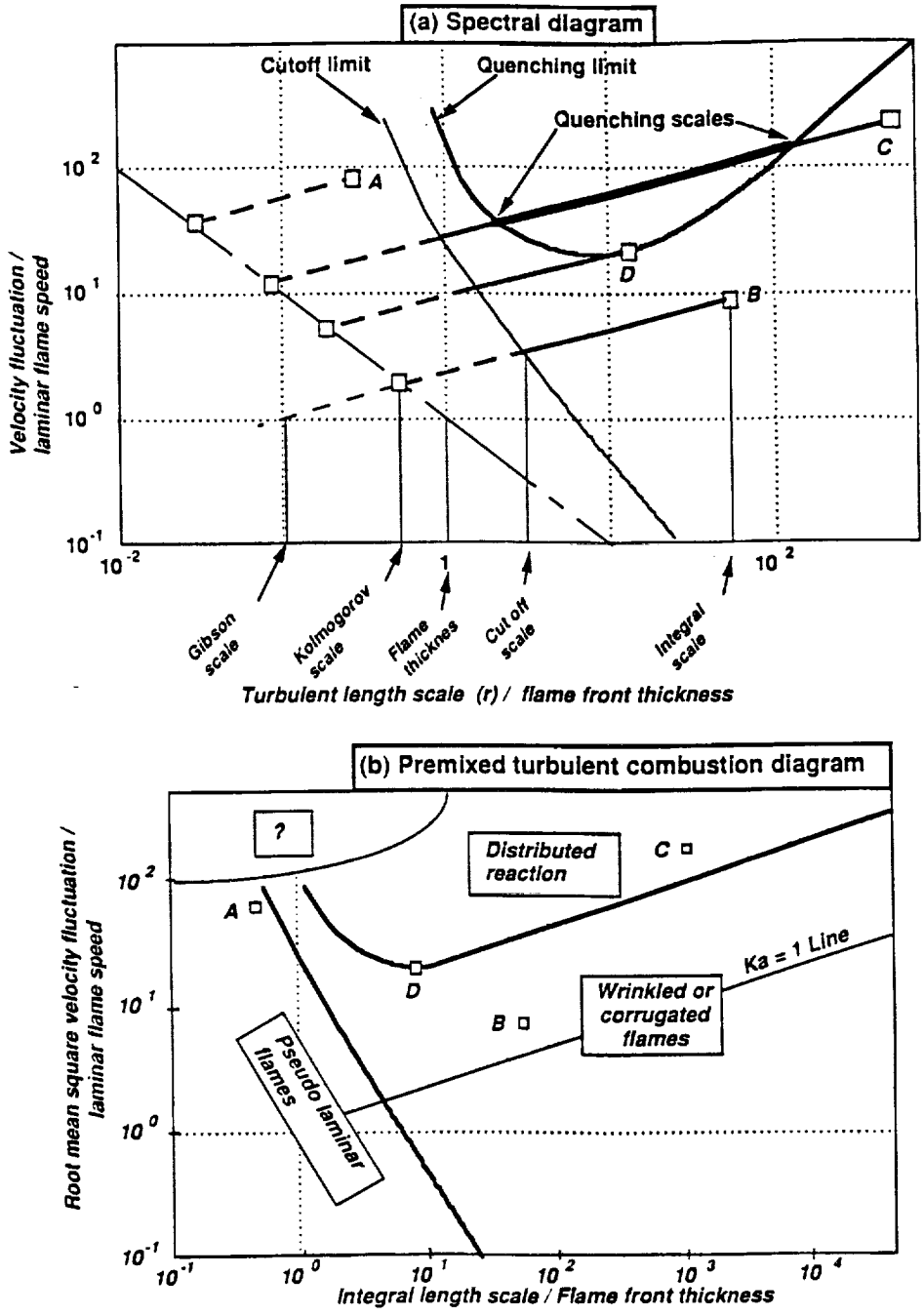

FIGURE 11. Construction of the diagram for pemixed turbulent combustion using the spectral diagram. Lewis = 1.2, strong heat losses.

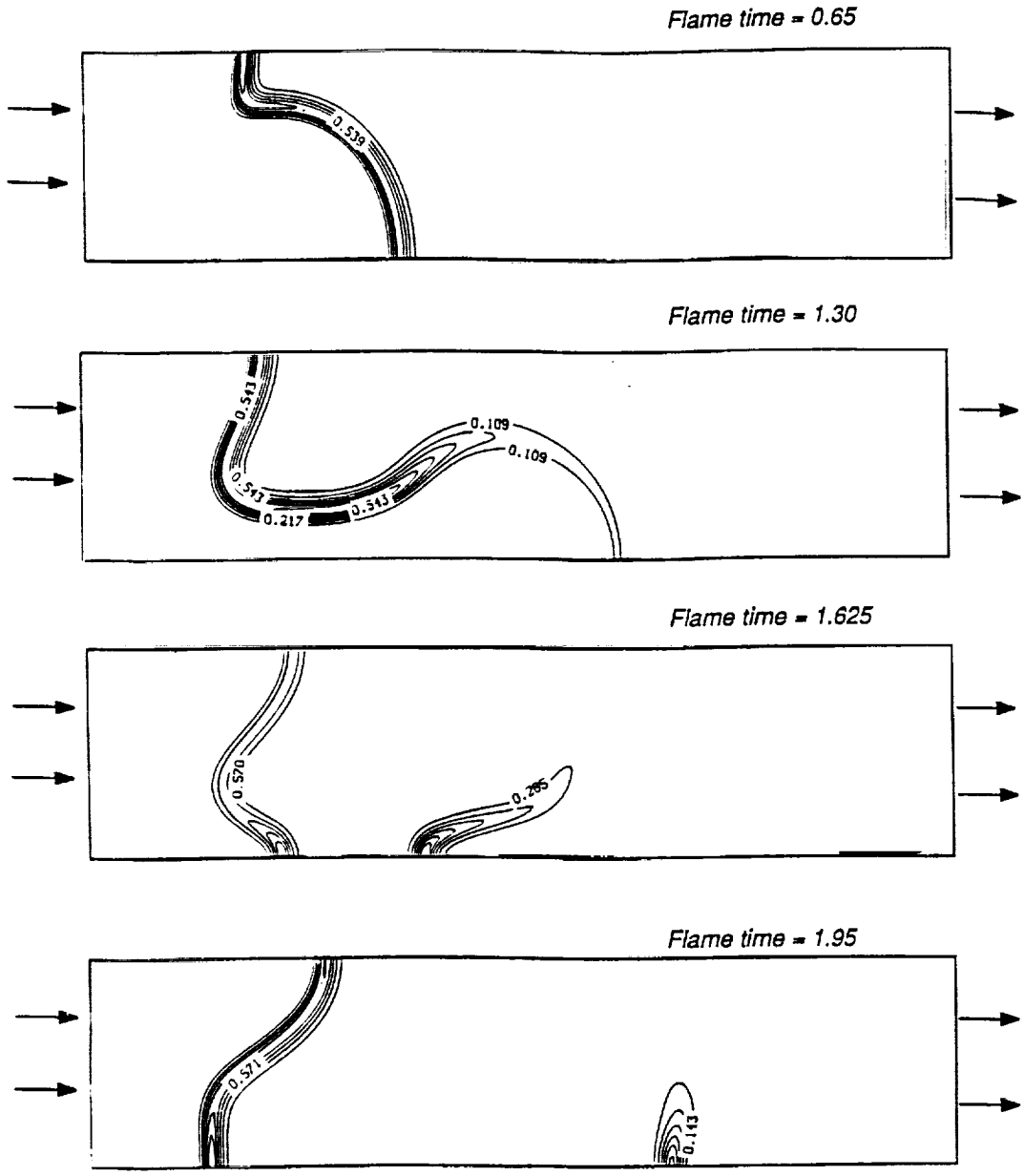

FIGURE 12. Instantaneous reaction rate fields at four instants. Quenching occurs at the tip of the flame at time = 1.30. $r/l_F = 18$ and $u'(r)/s_L = 28$.

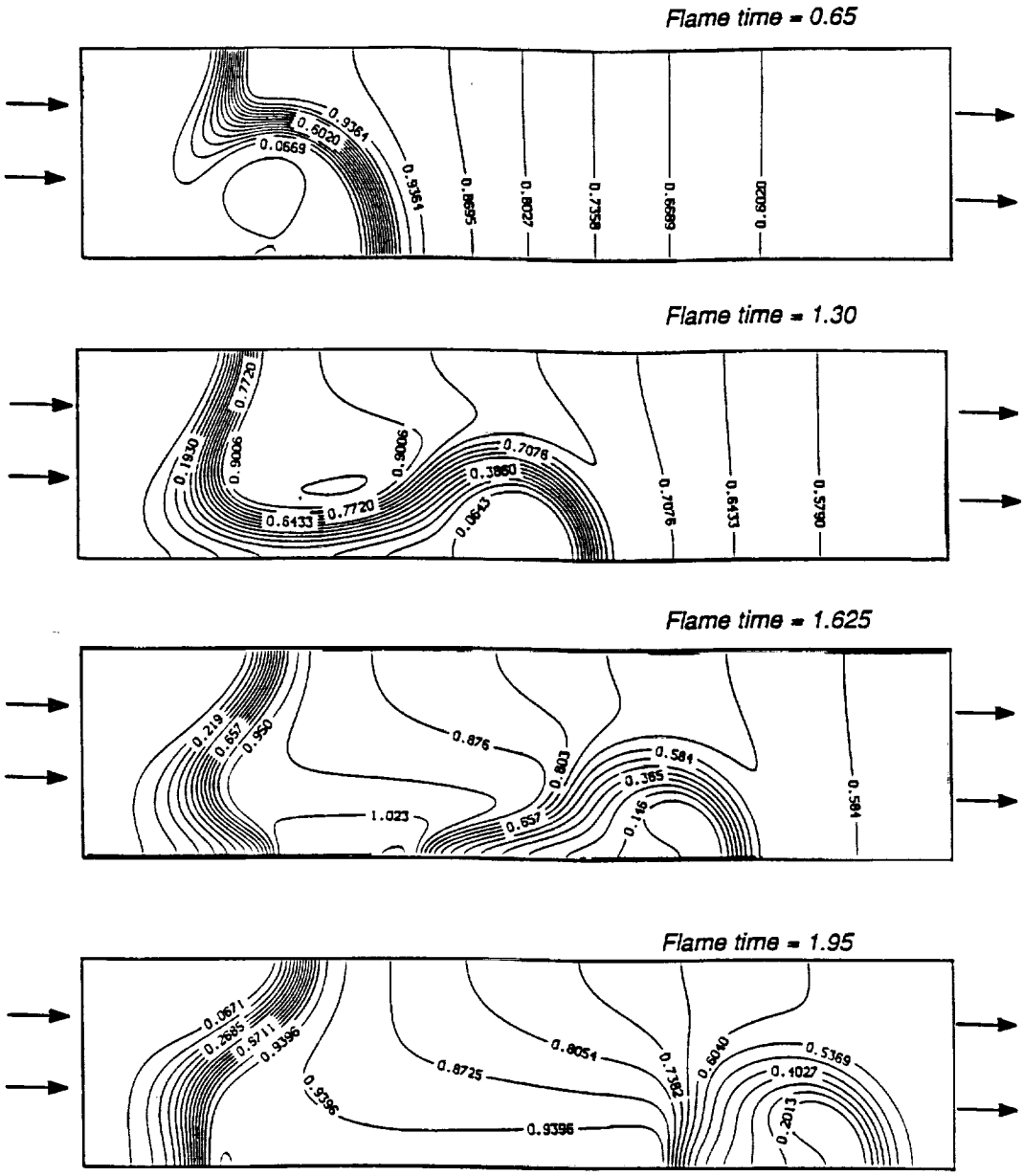

FIGURE 13. Instantaneous temperature fields at four instants. A pocket of fresh gases is formed i the stream of the burnt products. $r/l_F = 18$ and $u'(r)/s_L = 28$.

by the vortex pair. These gases are pushed rapidly into regions where the burnt gases have been cooled due to heat losses (Fig. 13). This effect, combined with the high stretch generated by the vortices, causes almost complete extinction of the pocket after it has been separated from the bulk of the fresh gases. At times $t^+ = 1.625$ and 1.95, the pocket of fresh gases is convected through the burnt gases without burning except near its tail. In this case, the flame front is not only quenched locally by the vortex pair, in addition, unburnt mixture is able to cross the flame. This mechanism may be associated with pollutant formation (i.e unburned hydrocarbons in automobile exhausts).

To conclude, the direct simulation code used in this work appears to be a powerful tool to study turbulent combustion. Possible problems to be studied in the future year include the following :

- the extension of spectral diagrams to Lewis numbers lower than unity,
- the response of the flame front to an ensemble of small energetic vortices,
- the effect of the flame front on the vorticity field.

3. The influence of curvature on premixed flame fronts

The previous section shows that curvature is an important parameter in turbulent combustion. A convenient geometry to isolate the effects of curvature in a steady reacting flow is the tip of a Bunsen burner. This zone is highly curved and depending on the chemistry and on the flow speed, the flow speed upstream of the flame front can be five to fifteen times the laminar flame speed. Many experimental studies have been performed on flame tips (see for example Mizomoto et al 1984). In a collaborative work with Dr. Mungal and T. Echeckki, who have done a flame tip experiment at Stanford, I have started computations of flame tips for different Lewis numbers and have found interesting results. In particular, for Lewis numbers lower than unity, the flame tip opening phenomenon, where the flame is quenched at the flame tip, is correctly captured by the code. This study will be pursued by writing a one-dimensional code able to predict the combined effects of stretch and curvature on a flame and comparing its results with the two-dimensional computation and with measurements.

4. The validation of flamelet models for premixed turbulent combustion

The validation of flamelet models is an important aspect of the present work. Two approaches are used.

First, the fundamental information obtained on flame / vortex interactions are incorporated in the model. The existence of quenching, the dynamics of the pockets, the effects of transients, and viscous dissipation constitute a valuable source of guidelines to construct a model. For example, the fact that scales smaller than the flame front thickness have almost no effect on the flame front (as evidenced from the spectral diagram of Fig. 11a) allows a much simpler modeling of the flame front. It also indicates which strain should be used to quantify

the flame area increase due to turbulence. Clearly the value of $\sqrt{(\epsilon/\nu)}$ which corresponds to the strain at the Kolmogorov scale overestimates the effective flame stretch. A second obvious result is that the spectral diagram obtained in Fig. 11a would be completely different if the Lewis number was lower than unity. In this case, stretch would increase the flame speed while curvature would promote extinctions. The Lewis number must be a central parameter in any turbulent combustion model. This conclusion is similar to the one obtained by Abdel-Gayed and Bradley (1985) from experimental results.

Second, once a model is built, direct simulation can be used to test it and adjust 'constants'. This was done in collaboration with Dr. D. Veynante in September 1989. The Coherent Flame Model (Candel et al 1988) and the stochastic model of Pope and Cheng (1988) were compared to direct simulation results. Realizability of both models was also considered. This study will be continued in 1990.

REFERENCES

ABDEL-GAYED R. G. & BRADLEY D. 1985 *Comb. and Flame* **62**, 61-68

ASHURST W. T., PETERS N. & SMOOKE M. D. 1987 *Combust. Sci. and Tech* **53**, 339-375

BORGHI R. 1984 *Recent Advances in Aeronautical Science*, C. Bruno, C. Caseci (Eds), Pergamon

BRAY K. N. C. 1980 *Topics in Applied Physics*, P. A. Libby and F. A. Williams ed. Springer Verlag

BUELL J. & HUERRE P. 1988 *Proceedings of the Summer Program 1988, Center for Turbulence Research* 19-27

CANDEL S., MAISTRET E., DARABIHA N., POINSOT T., VEYNANTE D. & LACAS F. 1988 Marble Symposium, CALTECH, Pasadena

CETEGEN B. & SIRIGNANO W. 1988 26th AIAA Aerospace Sciences Meeting, AIAA Paper 88-0730

GHONIEM A. AND GIVI P. 1987 25th AIAA Aerospace Sciences Meeting, AIAA Paper 87-0225

JAMESON A. & BAKER T.J 1984 AIAA 22nd Aerospace Sciences Meeting, AIAA Paper 84-0093

JAROSINSKI J., LEE J., KNYSTAUTAS R. 1988 *Twenty Second Symposium (International) on Combustion.* The Combustion Institute

MIZOMOTO M., ASAKA Y., IKAI S. & LAW C. K. 1984 *Twentieth Symposium (International) on Combustion.* p. 1933, The Combustion Institute

PETERS N. 1986 *Twenty First Symposium (International) on Combustion.* p. 1231, The Combustion Institute

POINSOT T., TROUVE A., VEYNANTE D., CANDEL S. & ESPOSITO E. 1987 *J. of Fluid Mech.* **177**, 265-292

POINSOT T. & CANDEL S. 1988 *Combus. Sci. Tech.* **61**, 121-153

POINSOT T., VEYNANTE D. & CANDEL S. 1990 submitted to the *Twenty First Symposium (International) on Combustion* The Combustion Institute

POINSOT T. & LELE S. 1989 submitted to the *J. of Comput. Phys.*

POINSOT T., COLONIUS T. & LELE S. 1989 presented at the *42nd A.P.S. Meeting* Division of Fluid Mech.

POPE S. B. & CHENG W. K. 1988*Twenty Second Symposium (International) on Combustion.* The Combustion Institute

RUTLAND C. J. & FERZIGER J. 1989 27th AIAA Aerospace Sciences Meeting. AIAA Paper 89-0127

VEYNANTE D. & CANDEL S. 1988 *Signal Processing* **14**, 295-300

VEYNANTE D., LACAS F., MAISTRET E. & CANDEL S. 1989 7th Symp. on Turbulent Shear Flows. Stanford

WILLIAMS F. A. 1985 *Combustion theory*, 2nd ed. Benjamin Cummings, Menlo Park

YANG V. & CULICK F. E. C. 1986 *Combus. Sci. Tech.* **45**, 1-25

YEE H. C. 1981 *NASA Tech Memo* 81265

Transition to turbulence in hypersonic flow

By J. J. W. van der Vegt

An outline of the project and recent progress toward the study of transition in hypersonic boundary layers is given. Aspects of the numerical method and the results of test computations are presented. At present the laminar flows over a flat plate and wedge have been computed for $M \leq 5$.

1. Motivation and objective

The prediction of transition to turbulence is of crucial importance in the design of space vehicles currently planned, such as the trans-atmospheric vehicle (TAV) and the aeroassisted transfer vehicle (AOTV). The state of the boundary layer, laminar or turbulent, has a dramatic influence on the heating of the surface and drag. Surface heating poses a bigger threat for this type of vehicles than previous ones because they do not have spherical noses and ablative heat shields. The main tools presently available for predicting transition in hypersonic flow are experiments and e^N -stability theory. Both are of great importance in the design of space vehicles, but they also suffer serious deficiencies. A serious problem with wind-tunnel experiments is noise, which causes earlier transition than in free flight. New results in the quiet Mach 3.5 pilot wind-tunnel at NASA Langley show a dramatic difference in transition compared with older, noisier tunnels, (Chen et al. 1989). Another serious problem with wind-tunnel experiments is that it is impossible to scale the chemistry effects properly. These effects are important at hypersonic speeds where the temperatures are so high that real gas effects and chemical changes become important. Therefore, in addition to wind-tunnel experiments, free flight experiments and theoretical tools are indispensable.

Among the theoretical tools, e^N-stability theory, which uses linear stability theory together with an experimentally determined N-factor, is by far the most widely used. Originally an incompressible flow method, it has been extended to compressible flow by Mack (for a review see Mack, 1984), and applied to hypersonic flow by Malik (1989) and Gasperas (1987-89). The method has as its main advantage that, for low disturbance levels and approximately parallel mean flow, it generally gives reasonable answers when accompanied with a suitable N-factor obtained by experiments. Using new results from the quiet Mach 3.5 wind-tunnel, Chen et al. (1989) showed that linear stability results compare more favorably with experiments on a cone than previous results. There are, however, problems in using linear stability theory. For instance, it cannot predict the effects of a shock on transition, which can be important in certain applications. It also fails when non-linear effects are important. Compared to incompressible

flow, however, non-linear stability theories for hypersonic flow are still in their infancy and much remains to be accomplished.

The purpose of this research is to provide additional information about transition to turbulence in hypersonic flow by using direct numerical simulation of hypersonic flows, together with non-linear stability theory. Special attention is paid to the interaction between a shock and a boundary layer, in the so-called shock layer. The two cases which will be investigated in more detail are a flat plate boundary layer and the flow about a wedge. The flat plate boundary layer is studied because it gives an opportunity to compare results with linear stability theory. The second case, the flow about a wedge, offers the opportunity to study the effects of extreme heating and shocks on transition in the shock layer.

2. Accomplishments

The main activity in 1989 has been the development of a numerical method for the solution of the compressible Navier-Stokes equations and writing and testing a computer program based on this method. In the next section the numerical method will be discussed and motivation for the choices made will be given. Results of test computations will be presented in the subsequent section.

3. Numerical method

Although the main objective of this project is to study hypersonic transition, it was decided to follow a stepwise approach to code development and test each component separately. In the design of the program and the choice of numerical method, however, the ultimate goal, hypersonic flow, was kept in mind, so the code is not necessarily optimal for intermediate problems. For instance, the program can handle an arbitrary equation of state, while in memory management extensions to larger sets of equations are anticipated.

The code must both give accurate steady state solutions with a reasonable efficiency and allow time accurate solutions. These are conflicting requirements, because for the steady case one can obtain fast convergence by adding dissipation, while one tries to minimize dissipation in time accurate calculations. Whenever there is a conflict between these requirements, time accuracy was favoured. The flow field contains both strong shocks and boundary layers, which present different problems. The addition of real gas chemistry makes the problem very stiff and puts strong limits on the time step for an explicit method, making the use of an implicit method almost mandatory. For time accurate implicit calculations, the time step cannot be too large, if all the time scales of fluid motion are to be resolved, while the faster chemical time scales are ignored by using an implicit method.

An implicit method is much more complicated than an explicit method. There are a number of implicit methods available for the compressible Navier-Stokes equations. One of the first and most widely used methods is that of Beam and

Warming (1978), which is not well suited for our problem. For time accurate solutions the approximate factorization used in the Beam and Warming algorithm adds an additional error and the viscous cross-coupling terms cannot be taken into account implicitly. In addition the method requires artificial viscosity to obtain stable solutions when there are shocks, due to the use of central differences. The Beam-Warming method is designed for obtaining steady state solutions efficiently, but is not well suited to time accurate calculations.

An alternative is a method based on splitting the non-linear terms in the Navier-Stokes equations into components related to the positive and negative eigenvalues of the operator. The method accounts for the traveling of information along the (inviscid) characteristics in the differencing. Although the flow is viscous, due to the high Reynolds number, this is not a bad approximation in most areas of the flow. Recently Montagné et al. (1989) compared various algorithms, such as flux splitting according to Steger and Warming or van Leer, approximate Riemann solvers and TVD methods for real gas equations and did not find major differences in their prediction of shock waves. Because we cannot hope to resolve the details of a shock in our simulation, we are forced to use one of these methods or central differencing with additional artificial dissipation. The choice was made to use flux splitting for the non-linear terms for its additional beneficial numerical effects, viz. a diagonally dominant matrix suited for an iterative method. In the viscous region, however, one has to be careful, because flux splitting can produce unwanted numerical dissipation, as was demonstrated by MacCormack et al. (1989). The correction to the Steger-Warming splitting proposed by MacCormack is used in regions with dominant viscous effects, whereas in a shock the Steger-Warming splitting, as described in Steger et al. (1981), is used. The fact that the flux splitting of the non-linear terms, accompanied by one sided differencing, results in a diagonally dominant matrix, which can be solved iteratively, was used to incorporate all the viscous components implicitly in the numerical method. This was impossible in the factored algorithm of Beam and Warming. It also gives more freedom in the choice of boundary conditions.

The numerical technique chosen to discretize the equations is a finite volume method because an integral formulation is better suited to flows with shocks, and it always satisfies the conservation properties of the equations. The present algorithm solves the two-dimensional compressible Navier-Stokes equations in conservation form in an arbitrary coordinate system. These can be written as:

$$\frac{\partial}{\partial t}\hat{\mathbf{U}} + \frac{\partial}{\partial \xi}(\hat{\mathbf{E}} - \hat{\mathbf{V}}_{vis_\xi}) + \frac{\partial}{\partial \eta}(\hat{\mathbf{G}} - \hat{\mathbf{V}}_{vis_\eta}) = \mathbf{0}$$

with:

$$\hat{\mathbf{U}} = \frac{\mathbf{U}}{J}; \quad \hat{\mathbf{E}} = \frac{\xi_x}{J}\mathbf{E} + \frac{\xi_z}{J}\mathbf{G}; \quad ,\hat{\mathbf{G}} = \frac{\eta_x}{J}\mathbf{E} + \frac{\eta_z}{J}\mathbf{G} \tag{1}$$

$$\hat{\mathbf{V}}_{vis_\xi} = \frac{\xi_x}{J}\mathbf{V} + \frac{\xi_z}{J}\mathbf{I}; \quad \hat{\mathbf{V}}_{vis_\eta} = \frac{\eta_x}{J}\mathbf{V} + \frac{\eta_z}{J}\mathbf{I} \tag{2}$$

and:

$$\mathbf{U} = \begin{pmatrix} \rho \\ \rho u \\ \rho w \\ e \end{pmatrix}; \quad \mathbf{E} = \begin{pmatrix} \rho u \\ \rho u^2 + p \\ \rho uw \\ (e+p)u \end{pmatrix}; \quad \mathbf{G} = \begin{pmatrix} \rho w \\ \rho uw \\ \rho w^2 + p \\ (e+p)w \end{pmatrix} \tag{3}$$

$$\mathbf{V} = \frac{1}{Re}\begin{pmatrix} 0 \\ \tau_{xx} \\ \tau_{xz} \\ u\tau_{xx} + w\tau_{xz} - \frac{q_x}{(\gamma-1)M^2 Pr} \end{pmatrix}; \quad \mathbf{I} = \frac{1}{Re}\begin{pmatrix} 0 \\ \tau_{xz} \\ \tau_{zz} \\ u\tau_{xz} + w\tau_{zz} - \frac{q_z}{(\gamma-1)M^2 Pr} \end{pmatrix} \tag{4}$$

$$\tau_{xx} = (2\mu+\lambda)\frac{\partial u}{\partial x} + \lambda\frac{\partial w}{\partial z}; \quad \tau_{xz} = \mu\left(\frac{\partial u}{\partial z} + \frac{\partial w}{\partial x}\right); \quad \tau_{zz} = (2\mu+\lambda)\frac{\partial w}{\partial z} + \lambda\frac{\partial u}{\partial x} \tag{5}$$

$$q_x = -\kappa\frac{\partial T}{\partial x}; \quad q_z = -\kappa\frac{\partial T}{\partial z} \tag{6}$$

together with the equation of state: $p = \frac{\rho c_v T}{\gamma M^2}$

Here ρ represents the density, u and v the velocity components in a Cartesian coordinate system, p the pressure, T temperature and e the total energy. The variables x and y represent the Cartesian coordinates, whereas ξ and η represent curvilinear coordinates. The coefficients M and Pr are the Mach and Prandtl numbers, whereas μ, λ and κ are the two viscosities and the thermal conductivity respectively. It is important to realize that the shear stress and heat flux components in $\mathbf{V}$ and $\mathbf{I}$ are functions of ξ and η. The equations are solved in a general coordinate system because the wedge does not allow an orthogonal coordinate system and complicated local flow phenomena, such as shocks, and boundary layers require local grid refinement. The use of generalized coordinates, however, greatly increases the complexity of the code.

The basic steps in the development of the numerical scheme will now be summarized. The first step is the choice of a time integration method. The time integration is formulated as a Padé relation, cf. Beam and Warming (1978):

$$\triangle\hat{\mathbf{U}}^n = \frac{\alpha\triangle t}{1+\beta}\frac{\partial}{\partial t}\triangle\hat{\mathbf{U}}^n + \frac{\triangle t}{1+\beta}\frac{\partial}{\partial t}\hat{\mathbf{U}}^n + \frac{\beta}{1+\beta}\hat{\mathbf{U}}^{n-1} + O[(\alpha - \frac{1}{2} - \beta)\triangle t^2 + \triangle t^3] \quad (7)$$

with: $\triangle\hat{\mathbf{U}}^n = \hat{\mathbf{U}}^{n+1} - \hat{\mathbf{U}}^n$

Here the coefficients α and β allow different time integration schemes to be obtained. For instance, $\alpha = 1$, $\beta = 0$, give the implicit Euler method, $\alpha = .5$, $\beta = 0$ give the trapezium rule and $\alpha = 1$, $\beta = 0.5$ give a three point backward scheme. The superscript n in this equation refers to the time $t = t_n$.

Introducing the compressible Navier-Stokes equations (1) into this relation yields:

$$\begin{aligned}\triangle\hat{\mathbf{U}}^n = &\frac{\alpha\triangle t}{1+\beta}\{-\frac{\partial}{\partial\xi}(\triangle\hat{\mathbf{E}}^n - \triangle\hat{\mathbf{V}}^n_{vis_\xi}) - \frac{\partial}{\partial\eta}(\triangle\hat{\mathbf{G}}^n - \triangle\hat{\mathbf{V}}^n_{vis_\eta})\} + \\ &\frac{\triangle t}{1+\beta}\{-\frac{\partial}{\partial\xi}(\hat{\mathbf{E}}^n - \hat{\mathbf{V}}^n_{vis_\xi}) - \frac{\partial}{\partial\eta}(\hat{\mathbf{G}}^n - \hat{\mathbf{V}}^n_{vis_\eta})\} + \frac{\beta}{1+\beta}\hat{\mathbf{U}}^{n-1}\end{aligned} \quad (8)$$

which is first or second order accurate in time, depending on the choice of α and β. In order to solve this set of non-linear equations for the implicit case, the flux vectors must be linearized around their value at time $t = t_n$:

$$\triangle\hat{\mathbf{E}}^n(\mathbf{U}) \cong \left(\frac{\partial\hat{\mathbf{E}}^n}{\partial\mathbf{U}}\right)_+ \triangle\mathbf{U}^n + \left(\frac{\partial\hat{\mathbf{E}}^n}{\partial\mathbf{U}}\right)_- \triangle\mathbf{U}^n \quad (9)$$

$$\triangle\hat{\mathbf{V}}^n_{vis_\xi}(\mathbf{U}) \cong \frac{\partial\hat{\mathbf{V}}^n_{vis_\xi}}{\partial\mathbf{U}}\triangle\mathbf{U}^n + \frac{\partial\hat{\mathbf{V}}^n_{vis_\xi}}{\partial\mathbf{U}_\xi}\triangle\mathbf{U}^n_\xi + \frac{\partial\hat{\mathbf{V}}^n_{vis_\xi}}{\partial\mathbf{U}_\eta}\triangle\mathbf{U}^n_\eta \quad (10)$$

with similar linearizations for the vectors $\triangle\mathbf{G}^n$ and $\triangle\hat{\mathbf{V}}^n_{vis_\eta}$. The suffices + and − on the Jacobian matrices of the inviscid flux vectors refer to the components with positive and negative eigenvalues. Introducing the linearizations of the flux vectors in (8) and integrating over a small volume gives the integral formulation for the compressible Navier-Stokes equations:

$$\frac{1}{V_{ij}}\int\limits_{V_{ij}}\frac{1}{J}\triangle\mathbf{U}^n dV+\frac{\alpha\triangle t}{1+\beta}\frac{1}{V_{ij}}\int\limits_{S_{ij}}\{n_\xi\Big(\Big(\Big(\frac{\partial\hat{\mathbf{E}}^n}{\partial\mathbf{U}}\Big)_+ +\Big(\frac{\partial\hat{\mathbf{E}}^n}{\partial\mathbf{U}}\Big)_- -\frac{\partial\hat{\mathbf{V}}^n_{vis_\xi}}{\partial\mathbf{U}}\Big)\triangle\mathbf{U}^n-$$

$$\frac{\partial\hat{\mathbf{V}}^n_{vis_\xi}}{\partial\mathbf{U}_\xi}\triangle\mathbf{U}^n_\xi-\frac{\partial\hat{\mathbf{V}}^n_{vis_\xi}}{\partial\mathbf{U}_\eta}\triangle\mathbf{U}^n_\eta\Big)+n_\eta\Big(\Big(\Big(\frac{\partial\hat{\mathbf{G}}^n}{\partial\mathbf{U}}\Big)_+ +\Big(\frac{\partial\hat{\mathbf{G}}^n}{\partial\mathbf{U}}\Big)_- -\frac{\partial\hat{\mathbf{V}}^n_{vis_\eta}}{\partial\mathbf{U}}\Big)\triangle\mathbf{U}^n-$$

$$\frac{\hat{\mathbf{V}}^n_{vis_\eta}}{\partial\mathbf{U}_\xi}\triangle\mathbf{U}^n_\xi-\frac{\hat{\mathbf{V}}^n_{vis_\eta}}{\partial\mathbf{U}_\eta}\triangle\mathbf{U}^n_\eta\Big)\}dS=$$

$$-\frac{\triangle t}{1+\beta}\frac{1}{V_{ij}}\int\limits_{S_{ij}}\{n_\xi\Big(\Big(\Big(\frac{\partial\hat{\mathbf{E}}^n}{\partial\mathbf{U}}\Big)_+ +\Big(\frac{\partial\hat{\mathbf{E}}^n}{\partial\mathbf{U}}\Big)_-\Big)\mathbf{U}^n-\hat{\mathbf{V}}^n_{vis_\xi}\Big)+n_\eta\Big(\Big(\Big(\frac{\partial\hat{\mathbf{G}}^n}{\partial\mathbf{U}}\Big)_+ +$$

$$\Big(\frac{\partial\hat{\mathbf{G}}^n}{\partial\mathbf{U}}\Big)_-\Big)\mathbf{U}^n-\hat{\mathbf{V}}^n_{vis_\eta}\Big)\}dS+\frac{\beta}{1+\beta}\frac{1}{V_{ij}}\int\limits_{V_{ij}}\frac{1}{J}\hat{\mathbf{U}}^{n-1}dV \tag{11}$$

Here V_{ij} represents a grid cell, S_{ij} a cell surface and n_ξ and n_η outward normal vectors at S_{ij}. The final step consists of approximating the fluxes across the cell surfaces S_{ij}. The positive and negative flux vectors are differenced backward and forward respectively, while the viscous terms are centrally differenced. In boundary layer regions the modifications to the differencing of the inviscid flux vectors presented by MacCormack et al. (1989) are used, whereas in a shock the Steger-Warming splitting is used, see Steger et al.(1981). After choosing proper discretizations for the components at the cell surfaces and centers, a system of linear algebraic equations is obtained:

$$\hat{A}^n_{ij}\triangle\mathbf{U}^n_{i,j}+\hat{B}^n_{ij}\triangle\mathbf{U}^n_{i,j+1}+\hat{C}^n_{ij}\triangle\mathbf{U}^n_{i,j-1}+\hat{D}^n_{ij}\triangle\mathbf{U}^n_{i+1,j}+\hat{E}^n_{ij}\triangle\mathbf{U}^n_{i-1,j}+$$

$$\hat{F}^n_{ij}\triangle\mathbf{U}^n_{i+1,j+1}+\hat{G}^n_{ij}\triangle\mathbf{U}^n_{i-1,j+1}+\hat{H}^n_{ij}\triangle\mathbf{U}^n_{i+1,j-1}+\hat{I}^n_{ij}\triangle\mathbf{U}^n_{i-1,j-1}=\hat{\mathbf{R}}^n_{ij}$$

Here $\hat{A}^n_{ij},\cdots,\hat{I}^n_{ij}$ represent the Jacobian matrices obtained after linearization of the flux vectors and $\mathbf{R}^n_{ij}$ is the right-hand side. For the compressible Navier-Stokes equations they are 4×4 matrices, but for real gases they are much larger. The details of these matrices will be published elsewhere.

The solution of this system is the most time consuming part of the numerical algorithm. The use of flux splitting for the non-linear terms makes the matrices diagonally dominant and allows the use of iterative methods. Gauss-Seidel line relaxation is used in all four directions of the fluid domain to reduce the nona-diagonal block matrix to a tri-diagonal matrix. This system of tri-diagonal matrices is usually solved with a direct inversion method because these matrices do not have a structure suitable for most iterative inversion methods. If the mean flow quantities are needed, it is not necessary to iterate this Gauss-Seidel line relaxation to convergence at each time step, but for time accurate solutions convergence to accuracy better than the truncation error must be obtained each time step. The inversion may become then prohibitively expensive. So an alternative to the direct inversion must be found. It was suggested by Dexun et al. (1989) that using the LU decomposition of the abridged matrices, consisting of only the main diagonals of the tri-diagonal block matrices, as a preconditioner and solving the tri-diagonal block matrices iteratively gives a significant improvement in computational efficiency. It is convergent for time steps very close to the maximum allowable ones of the total scheme. The fully iterative scheme so obtained converges very rapidly. In two to four Gauss-Seidel sweeps machine accuracy is obtained. The inner iteration, used to solve the block tri-diagonal matrices in each Gauss-Seidel sweep, converges in about ten to fifteen iterations for the first Gauss-Seidel sweep and in one to four the following inner iterations, thereby greatly reducing the computational time. Further tests to improve convergence by using residual correction and under- or over-relaxation did not improve the convergence rate. The improvements in the solution of the system of linear equations will be of great importance when the full real gas equations are solved because the blocks in the nona-diagonal matrix are much larger.

The outflow boundary conditions are zeroth order extrapolation, which performed well and had no noticeable upstream influence. This condition is, however, not suitable for direct simulations because of its reflective properties. The main source of trouble at the outflow boundary is the subsonic region close to the wall. The technique of setting the pressure in this region to the free-stream pressure does not work because it creates instabilities whenever the pressure becomes smaller than the free-stream pressure. The boundary conditions at the solid surface also require special attention. The set of boundary conditions used for an adiabatic wall consisted of zero velocity and heat flux at the wall, determining the pressure from the equation of state and using the continuity and energy equations to close the system. The conditions are implemented using a half cell at the solid wall, as discussed in Vinokur (1989), and works very well. Conditions such as zero normal pressure gradient and/or zero density gradient are not valid at the wall in a viscous fluid and should not be used.

4. Test results

Careful testing has been performed to investigate the accuracy of the numerical scheme and seek errors in the code. After preliminary test cases, such as uniform flow and a normal shock, the main test case was to compare the results of the computations of the flow about an adiabatic flat plate at zero angle of incidence with the analytically derived results from Crocco (1941), see also Schlichting (1979). In order to test the ability of the model to compute shocks, the case of a finite plate in a uniform flow was considered and the results at the trailing edge were compared with the boundary layer results of Crocco. This also removed the problem of choosing an inflow profile. Due to the fact that at the nose of the plate both the x- and y-derivatives are equally important, it is necessary to use small square grid cells in this region, see Fig. 1, while strong grid stretching is required in the boundary layer region. If the grid is stretched too much in one direction at the nose, divergence of the computations results. The general features of the flow field are presented in Fig. 2, which shows the pressure field at steady state for Mach number 2. The plot shows a large pressure jump at the nose of the plate, followed by an expansion around the outer edge of the boundary layer, while a weak shock originates from the nose of the plate. After the nose region the flow relaxes to a boundary layer. The temperature and velocity in the region just ahead of the trailing edge are compared with the theoretical results of Crocco. In Fig. 3 and 4 the Steger-Warming splitting and MacCormack splitting on a 42×42 grid are compared with the results of Crocco, and it is clear that the Mc Cormack splitting gives much better results; the Steger-Warming splitting is much too dissipative in the boundary layer. The results close to the wall are not bad, because this region has most of the gridpoints. It must be remarked, however, that the Steger-Warming splitting does not perform as badly as claimed by MacCormack et al. (1989). To give, however, a more definite answer about the accuracy the effects of grid refinement have to be investigated, this is currently being done.

A problem in the calculations is to define an initial field. The computations for $M = 2$ were started from a uniform flow field, but in the computations at higher Mach numbers, the Mach 2 result was used as initial field.

For all these cases, the iterative matrix inversion works without problems and is convergent for a time step very close to the stability limit of the scheme. Due to the presence of a shock and the reduction of numerical viscosity, the time step for the calculations was, however, rather restricted. This is no surprise because an analysis of implicit schemes for Burger's equation, done by Poinsot et al. (1985), shows the same result. Further tests are currently being performed on the calculation of the viscous flow about a wedge.

5. Work to be done:

• Testing the code for time accuracy. This will be done using the most unstable mode from linear stability theory and comparing growth rates. Propagation of sound waves is another interesting test case.

• Improvement of inflow and outflow boundary conditions for time accurate solutions, so that they are non-reflecting and compatible with Navier-Stokes equations.

• The results of the first two steps may show that the spatial order of the difference scheme must be increased.

• Study of transition in supersonic flow. This will be done by introducing small disturbances into the flow. It will be accompanied by the development of non-linear stability theory. Without a more advanced stability theory, it will be difficult to do a complete study of transition phenomena, due to the many parameters involved and the extremely long computation times of the simulations. Stability theory is, however, still in its infancy and will require a significant effort. Preliminary investigations show that the non-linear geometrical optics used by Artola and Majda (1989) is a good starting point.

The specific cases which will be investigated are:

Shock layer: For this case a wedge connected to a flat plate, compression corner will be used. The effects of the shock on the boundary layer can be investigated systematically as a function of wedge angle and Mach and Reynolds number.

Free stream disturbances: An important reason for inaccuracies in linear stability theory are the effects of free stream disturbances. The effects of small amplitude sound waves and free stream vorticity on the boundary layer on a cone will be studied and compared with the experiments of Chen et al. 1989, which show the effects of sound waves on transition. An important issue in this case is resonance between reflected and transmitted waves at the shock and the influence of the body. These effects on a vortex layer are also studied in Artola and Majda (1989) using non-linear geometrical optics and application of their theory to the flow on a cone or wedge will be very useful.

• Adding real gas effects to the code. This is a major, but rather straightforward extension of the program and allows the study of real gas effects on transition.

REFERENCES

ARTOLA, M. & MAJDA, A. J. 1989 Nonlinear Development of Instabilities in Supersonic Vortex Sheets II: Resonant Interaction Among Kink Modes. *SIAM Journal of Applied Mathematics.* **49**, 1310-1349.

BEAM, R. M. & WARMING, R. F. 1978 An Implicit Factored Scheme for the Compressible Navier-Stokes Equations. *AIAA Journal.* **16**, No 4, 393-402.

CHEN, F. J., MALIK, M. R. & BECKWITH, I. E. 1989 Boundary-Layer Transition on a Cone and Flat Plate at Mach 3.5. *AIAA Journal.* **27**, No. 6, 687-693.

CROCCO, L. 1941 Sullo Strato Limite Laminare Nei Gas Lungo Una Lamina Piana, Rendiconti di Matematica delle sue Applicazioni, University Rome, 139-152.

DEXUN, F. & YANWEN, M. 1989 On Efficiency and Accuracy of Numerical Methods for Solving Aerodynamic Equations, Symposium Tokyo.

GASPERAS, G. 1987 The Stability of the Compressible Boundary Layer on a Sharp Cone at Zero Angle of Attack, AIAA Conference Reno, paper AIAA-87-0494.

GASPERAS, G. 1989 Transition Prediction for Two-Dimensional Viscous Supersonic Wakes, AIAA Conference Reno, paper AIAA-89-0284.

MACCORMACK, R. W. & CANDLER, G. V. 1989 The Solution of the Navier-Stokes Equations using Gauss-Seidel Line Relaxation. *Computers and Fluids.* **17**, 135-150.

MACK, L. M. 1984 Boundary-Layer Linear Stability Theory, Special Course on Stability and Transition of Laminar Flow, AGARD Report, No. 709.

MALIK, M. R. 1989 Transition in Hypersonic Boundary Layers, AIAA Conference Reno, 1989.

MONTAGNÉ, J. L., YEE, H., C. & VINOKUR, M. 1989 Comparative Study of High-Resolution Shock-Capturing Schemes for a Real Gas. *AIAA Journal.* **27**, No.10, 1332-1346.

POINSOT, T. & CANDEL, S. M. 1986 The Influence of Differencing and CFL Number on Implicit Time-Dependent Non-Linear Calculations. *Journal of Computational Physics.* **62**, 282-296.

SCHLICHTING, H. 1979 Boundary Layer Theory, Mc Graw-Hill.

STEGER, J. L. & WARMING, R. F. 1981 Flux-Vector Splitting of the Inviscid Gasdynamic Equations with Application to Finite Difference Methods. *Journal of Computational Physics.* **40**, 263-293.

VINOKUR, M. 1989 An Analysis of Finite-Difference and Finite-Volume Formulations of Conservation Laws. *Journal of Computational Physics.* **81**, 1-52.

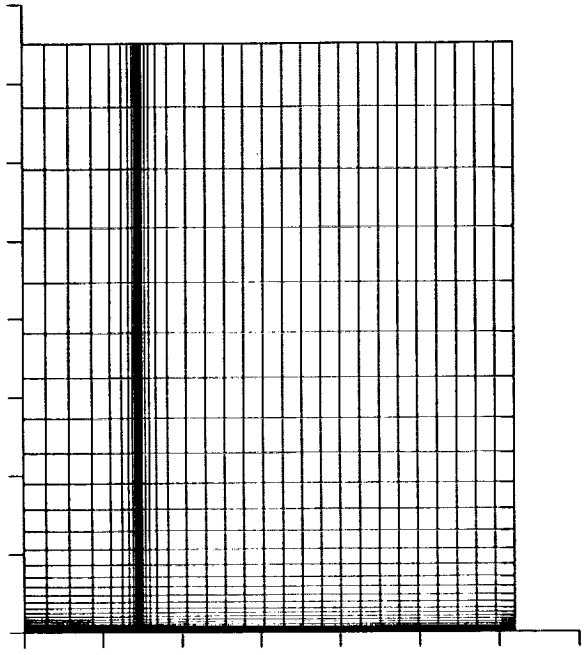

FIGURE 1. Grid for calculation of flow field above flat plate.

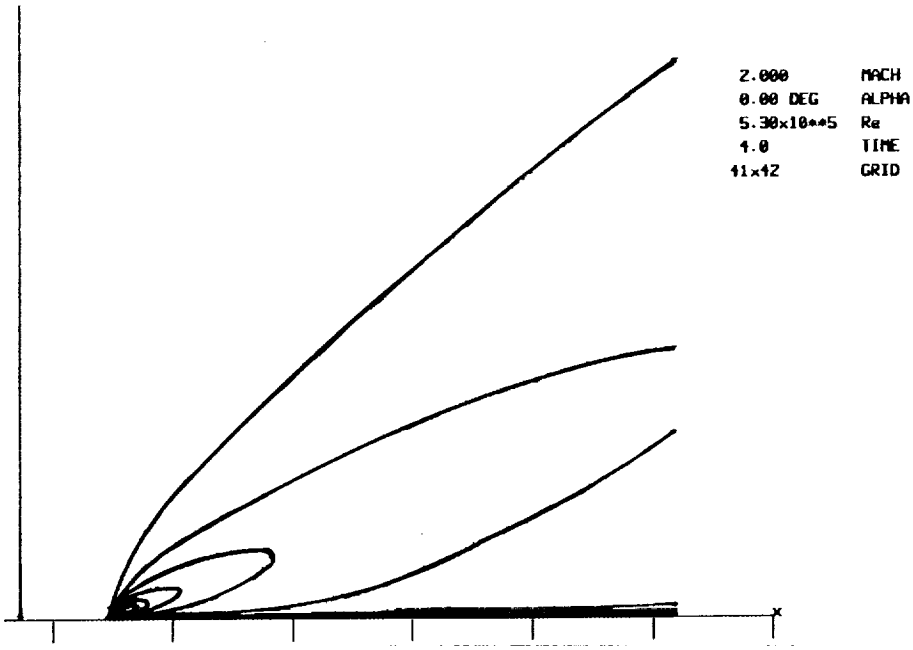

FIGURE 2. Pressure field above flat plate at Mach = 2.

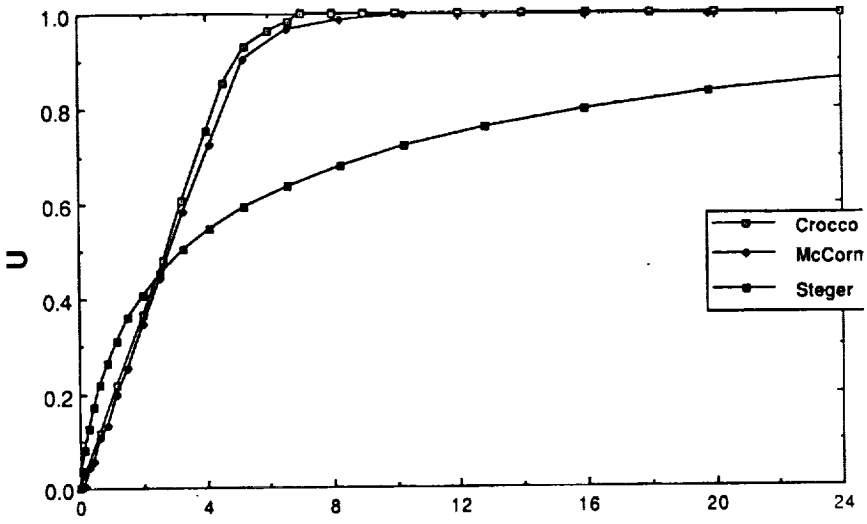

FIGURE 3. Velocity in boundary layer above flat plate at Mach = 2.

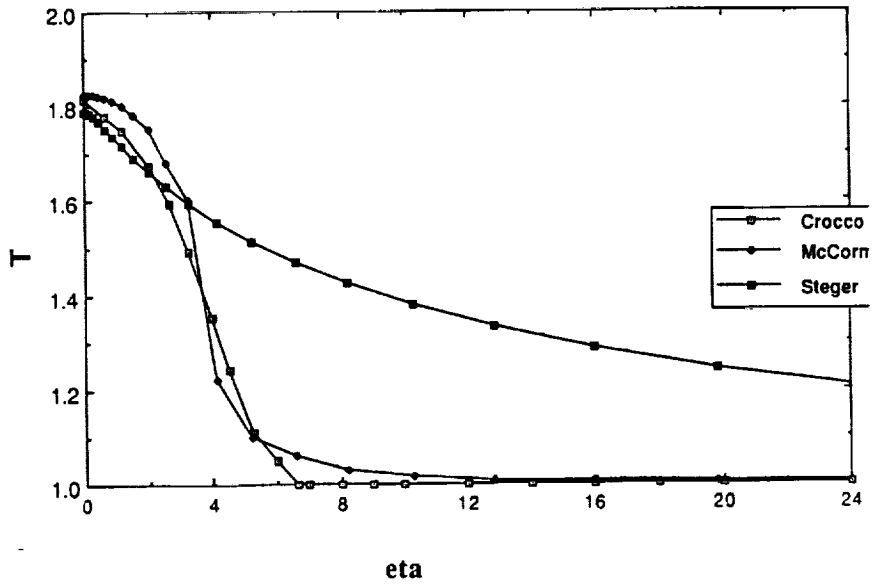

FIGURE 4. Temperature in boundary layer above flat plate at Mach = 2.

Direct simulations of wall-bounded compressible turbulence

By J. C. Buell

1. Introduction

A study has been initiated on the effects of compressibility (Mach number) on turbulent boundary layers. An understanding of both qualitative (turbulence structures, physical processes) and quantitative (turbulence statistics) effects are desired. This understanding should lead to better turbulence models for applications involving supersonic wall-bounded flows. Direct numerical simulations of an idealized problem will be used to accomplish these objectives. Among several possibilities we chose plane Couette flow with constant-temperature walls as the first problem to be studied. The lack of a mean streamwise pressure gradient plus isothermal walls implies that both horizontal directions can be assumed to be homogeneous and that the flow can reach a statistically steady state. Together, these features greatly simplify the calculations and analyses of the results.

To date, an algorithm has been developed and implemented (but not yet fully tested) for the accurate solution of the Navier-Stokes equations with the assumptions noted above. The scales we use for nondimensionalizing the problem are the channel half-width (b), half the velocity difference between the walls (U_w), average density (ρ_a), wall temperature (T_w), and the fluid viscosity evaluated at the wall temperature (μ_w). In nonconservative form, the continuity, momentum and energy equations are

$$\frac{\partial \rho}{\partial t} + \rho \frac{\partial u_j}{\partial x_j} + u_j \frac{\partial \rho}{\partial x_j} = 0,$$

$$\frac{\partial u_i}{\partial t} + u_j \frac{\partial u_i}{\partial x_j} + \frac{1}{\gamma M^2} \frac{\partial T}{\partial x_i} + \frac{T}{\gamma M^2 \rho} \frac{\partial \rho}{\partial x_i} - \frac{1}{\rho Re} \frac{\partial \tau_{ij}}{\partial x_j} = 0,$$

$$\frac{\partial T}{\partial t} + u_j \frac{\partial T}{\partial x_j} + (\gamma - 1) T \frac{\partial u_j}{\partial x_j} - \frac{\gamma(\gamma - 1) M^2}{Re} \frac{\tau_{ij}}{\rho} \frac{\partial u_i}{\partial x_j} + \frac{\gamma}{\rho \, Re \, Pr} \frac{\partial q_j}{\partial x_j} = 0,$$

where

$$\tau_{ij} = \mu \left(\frac{\partial u_i}{\partial x_j} + \frac{\partial u_j}{\partial x_i} - \frac{2}{3} \delta_{ij} \frac{\partial u_k}{\partial x_k} \right), \qquad q_j = -\mu \frac{\partial T}{\partial x_j}.$$

The ideal gas relation $\rho T = \gamma M^2 p$ was used and the Reynolds and Mach numbers are defined by $Re = \rho_a U_w b / \mu_w$ and $M^2 = U_w^2 / \gamma R T_w$. The Prandtl number $Pr = c_p \mu^* / k^*$ and c_p are assumed to be constant throughout the flow.

2. Numerical method

Unlike homogeneous and free-shear flows, the simulation of wall-bounded turbulence requires the use of an implicit time-integration scheme for the diffusive and acoustic terms because of the small grid size near the wall. Furthermore, unlike finite difference methods, an efficient implementation of a spectral method requires that the terms treated implicitly have constant coefficients. Thus, the terms that one would like to advance implicitly are broken into constant-coefficient and variable-coefficient parts by adding certain linear terms to both sides of the equations. We also let $\tau_{ij} = \mu\sigma_{ij}$ and write the diffusion terms in nonconservative form. This yields

$$\frac{\partial \rho}{\partial t} + \rho_1 \frac{\partial u_j}{\partial x_j} = -(\rho - \rho_1)\frac{\partial u_j}{\partial x_j} - u_j \frac{\partial \rho}{\partial x_j},$$

$$\frac{\partial u_i}{\partial t} + \frac{1}{\gamma M^2}\frac{\partial T}{\partial x_i} + \frac{T_0}{\gamma M^2 \rho_0}\frac{\partial \rho}{\partial x_i} - \frac{\mu_0}{\rho_0 Re}\frac{\partial \sigma_{ij}}{\partial x_j} = -u_j \frac{\partial u_i}{\partial x_j} - \frac{1}{\gamma M^2}\left(\frac{T}{\rho} - \frac{T_0}{\rho_0}\right)\frac{\partial \rho}{\partial x_i} + \frac{1}{\rho Re}\frac{d\mu}{dT}\sigma_{ij}\frac{\partial T}{\partial x_j} + \frac{1}{Re}\left(\frac{\mu}{\rho} - \frac{\mu_0}{\rho_0}\right)\frac{\partial \sigma_{ij}}{\partial x_j},$$

$$\frac{\partial T}{\partial t} + (\gamma - 1)T_0 \frac{\partial u_j}{\partial x_j} - \frac{\gamma \mu_0}{\rho_0 Re\, Pr}\frac{\partial^2 T}{\partial x_j \partial x_j} = -\left(u_j - \frac{\gamma}{Re\, Pr}\frac{1}{\rho}\frac{d\mu}{dT}\frac{\partial T}{\partial x_j}\right)\frac{\partial T}{\partial x_j} - (\gamma - 1)(T - T_0)\frac{\partial u_j}{\partial x_j} + \frac{\gamma}{Re\, Pr}\left(\frac{\mu}{\rho} - \frac{\mu_0}{\rho_0}\right)\frac{\partial^2 T}{\partial x_j \partial x_j} + \frac{\gamma(\gamma - 1)M^2}{Re}\frac{\mu \sigma_{ij}}{\rho}\frac{\partial u_i}{\partial x_j},$$

where the constants ρ_1, T_0, T_0/ρ_0, and μ_0/ρ_0 are used to optimize the stability of the time advancement scheme.

Noting that the left-hand side of these equations are to be advanced implicitly, the algorithm for solving them is as follows. First, perturbation variables T' and u_1' are defined by $T = 1 + T'$, $u_1 = U(y) + u_1'$, ($U(y)$ may be any function satisfying the boundary conditions on the velocity; we take $U(y) = y$ for the Couette flow case) so that homogeneous Dirichlet boundary conditions obtain for T', u_1', u_2 and u_3. All five variables are expanded in Fourier series in the horizontal directions, *e.g.*,

$$\rho(x, y, z) = \sum_{m=-N_x/2}^{N_x/2-1} \sum_{n=-N_z/2}^{N_z/2-1} \tilde{\rho}_{mn}(y) \exp\big(i(\alpha_m x + \beta_n z)\big),$$

where the horizontal wavenumbers are $\alpha_m = 2\pi m/L_x$ and $\beta_n = 2\pi n/L_z$. L_x and L_z are the periodic box lengths in the x and z directions, and the coefficients are assumed to be conjugate symmetric. The vertical functions are expanded using Legendre polynomials,

$$\tilde{\rho}_{mn}(y) = \sum_{l=1}^{N_y} \hat{\tilde{\rho}}_{mnl} P_{l-1}(y),$$

$$\tilde{\psi}_{mn}(y) = \sum_{l=1}^{N_y} \hat{\tilde{\psi}}_{mnl}(P_{l-1}(y) - P_{l+1}(y)),$$

where ψ denotes the four variables satisfying Dirichlet boundary conditions. The only constraint on ρ analogous to the boundary conditions on the other variables is that it satisfies global conservation of mass:

$$\int_0^{L_x} \int_{-1}^{1} \int_0^{L_z} \rho(x, y, z)\, dx\, dy\, dz = \text{constant}.$$

Using the above expansion and the Legendre orthogonality property,

$$\int_{-1}^{1} P_i(y) P_j(y)\, dy = \frac{2}{2j+1} \delta_{ij},$$

this constraint reduces to $\hat{\tilde{\rho}}_{001} = 1$. Numerically, it is imposed by simply not advancing the density equation corresponding to this mode. Ordinary differential equations in time are obtained by implementing a Galerkin method. After substituting the above expansions into the governing equations, one multiplies by the corresponding basis functions and integrates over the domain.

The method of Spalart (private communication) is used for time-integration of the ODE's. This method combines the explicit third order Runge-Kutta method of Wray (1987) with a new implicit scheme. The latter has the same structure as Crank-Nicolson applied at each substep, except it has different coefficients. Like Crank-Nicolson it is second order, but the stability properties for modes with large eigenvalues are better: instead of an amplification factor approaching -1, it has one of about 0.5 (depending on the value of a free parameter). For the implicit part, all five variables are coupled linearly. However, all the horizontal Fourier modes decouple from each other, as well as the real and imaginary parts of each mode, and the odd and even Legendre modes. This yields about $2N_xN_z$ systems of bandwidth 15 and order $\frac{5}{2}N_y$ that must be solved at each substep. Fortunately, because of symmetries involving the real and imaginary parts of the coefficients, and plus and minus z wavenumbers, only $\frac{1}{2}N_xN_z$ systems actually need to be inverted, each with four right-hand sides. One of the significant advantages of Legendre polynomials over Chebyshev is that the best formulation of the latter would yield systems with bandwidths of 20. Another is that the eigenvalues of these systems are much smaller using Legendre polynomials. This is important because numerical stability will be a limiting factor at sufficiently high Mach numbers. The nonlinear and variable-coefficient linear terms on the right-hand sides are evaluated by transforming to and from physical space and are then advanced explicitly. Note that time advancement in wavespace allows an arbitrary amount of dealiasing by using more collocation points than modes. As opposed to the incompressible case, full dealiasing is not practical since the density appears in the denominator of several terms.

The appropriate model problem to test the time advancement scheme is

$$u_t = \lambda u + \lambda \sigma u,$$

where λ is a complex constant and σ is a real constant (imaginary λ models the acoustic problem and real λ models the diffusion problem). We want to advance the first term on the right-hand side with an implicit scheme and the second with an explicit scheme. For the "standard" coefficients in the Runge-Kutta method, a straightforward stability analysis shows that as $\Delta t\lambda \to \infty$ in the complex plane, the scheme is stable as long as $-0.517 < \sigma < 0.165$. The constants ρ_1, etc., are chosen to make this so, at least in the near-wall region.

3. Linear stability

As an aid in testing the nonlinear code, as well as for its inherent interest, a linear stability code was developed. Since the viscosity of air is not constant, there is no general analytical solution for the laminar mean flow. The nonlinear equations for the mean flow are solved with the same method as above, except time advancement is replaced with an iterative scheme. The full 3-D equations are then linearized around this base state and the perturbations are assumed to be of the form $\psi(x, y, z, t) = \hat{\psi}(y) \exp i(\alpha x + \beta z + \lambda t)$. Applying the same method in y yields an eigenvalue problem of order $5N_y$ for the complex growth rate λ. This was solved using a routine from EISPACK.

Glatzel (1989) solved a simpler version of this problem. He assumed 2-D perturbations and the limit $Pr \to 0$. The latter assumption implies $T = \text{const.}$ and thus eliminates the energy equation. Although the incompressible case is stable for all Re, he found two different instabilities for supersonic Mach numbers. One is a resonance between two acoustic modes and is an inviscid instability. The other is a resonance between a viscous mode (related to Orr-Sommerfeld modes) and an acoustic mode. The lowest critical Reynolds number was 83.54 at $M = 4.11$ and $\alpha = .971$, for an acoustic-acoustic mode. Glatzel's results were reproduced with the present stability code.

Shown in Fig. 1 are the critical Reynolds number and corresponding wavenumber as a function of Mach number for air (we assume $Pr = 0.7$ and $\mu = T^{.7}$). The critical Reynolds numbers are much higher than in the case considered by Glatzel (the lowest Re_c is 1395.72 at $M = 4.18$ and $\alpha = 2.037$). Further investigation shows that increasing Pr and increasing the exponent in the temperature dependence of viscosity are both strongly stabilizing. Neither trend is understood. Intuitively, one would expect that increasing the diffusion of heat (lower Pr) would stabilize the flow. Also, the stabilizing effect of a variable viscosity is considerably greater than the amount of variation in the viscosity itself. It appears that in both cases the stabilization occurs because of changes to the mean profiles. The few 3-D perturbations tested were found to be more stable than 2-D perturbations. A more exhaustive search for unstable 3-D modes will be made.

REFERENCES

GLATZEL, W. 1989 *J. Fluid Mech.*. **202**, 515–541.

WRAY, A. A. 1987 submitted to *J. Comp. Phys.*

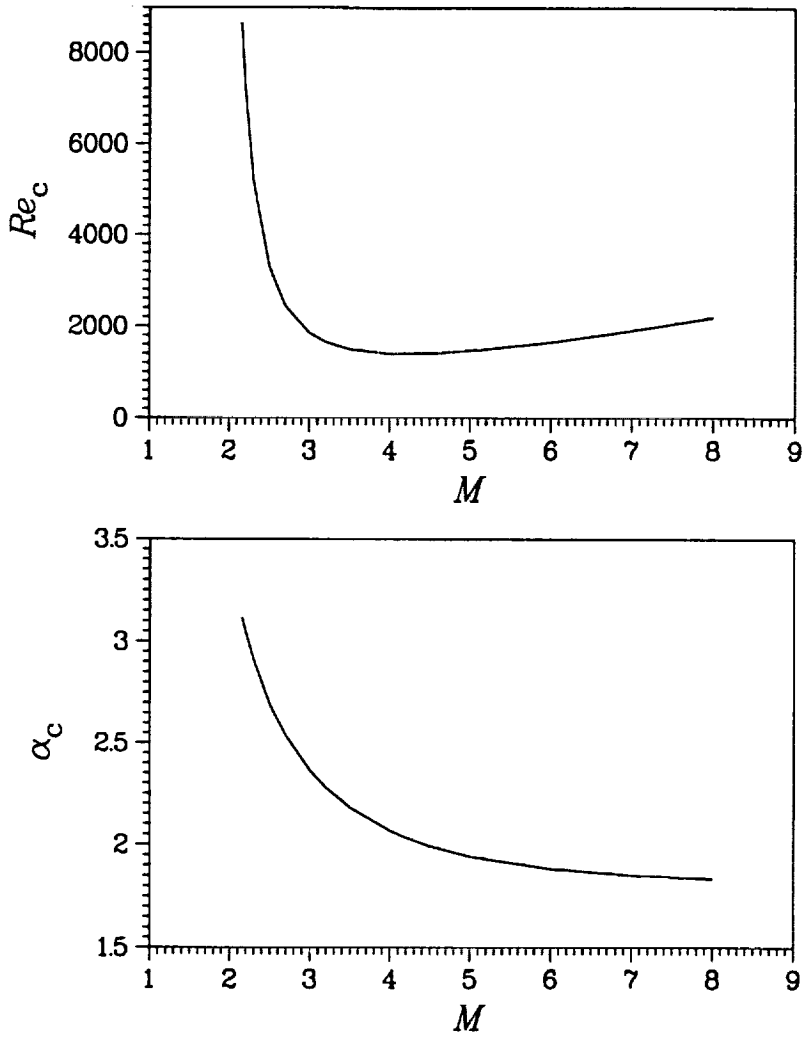

FIGURE 1. Critical Reynolds number as a function of Mach number for air (top), and corresponding critical wavenumber (bottom).

Turbulent transport in the solar nebula

By K. W. Thompson

This paper describes the current state of an ongoing project to simulate turbulent flow in a solar nebula, which is the flattened disk of dust and gas out of which a solar system forms. The goal of this project is to determine a model for the transport of mass and angular momentum in the nebula.

The nebula flow exhibits compressibility, thermal conduction, viscosity, internal heating through viscous dissipation, a stable shear due to Keplerian rotation, and a gravitational acceleration in the vertical direction which is linear with altitude. These properties combine to give flow patterns not seen in terrestrial applications.

Primordial solar systems are known to exist and are presumably undergoing an evolution similar to the early stages of our own solar system; for example, the IRAS infrared telescope has discovered such a protoplanetary system around the star Vega. Solar nebula evolution is the subject of much research in the astrophysical community. In the long run, researchers hope to gain a better understanding of planetary formation and the processes which dissipate the solar nebula with time (Black & Matthews (1985)).

1. Background

The solar nebula circled the Sun during and shortly after its formation. The nebula is thought to have formed out of the contraction of a much larger and even more diffuse molecular cloud. The nebula's central star, our Sun, also formed out of the molecular cloud matter, and it is the Sun's gravity which held the nebula together and kept it from flying apart. The combination of the Sun's gravitational field, the initial angular momentum of the molecular cloud (retained by the nebular material), and radiative cooling is believed to have confined the solar nebula to a thin disk, rather than a cloud.

Each fluid element follows a nearly Keplerian orbit around the central star. Consequently, the radial velocity of the gas decreases with increasing orbital radius r, and the nebula undergoes a shear flow. Viscosity causes friction between adjacent rings of fluid and has a braking effect on the inner ring, decreasing its total energy and causing the fluid to spiral in toward the star. The net result is to turn orbital kinetic energy into heat and to drag much of the nebular gas inward, where it ultimately becomes part of the central star. As mass is transported inward, angular momentum is transported outward.

The problem with this scenario is that molecular viscosity is too small to dissipate the nebula in a reasonable amount of time. Other effects must be invoked to explain the disappearance of the nebula, and turbulence is a logical candidate.

Turbulence may act globally much as a large viscosity, mixing fluid elements of different energy and angular momentum and augmenting the transport of mass and angular momentum.

Anticipated sources of turbulence include thermal convection (driven by the heat generated from viscous dissipation), vertical shear in the angular velocity (due to the nonuniform deviations from the central plane orbital motion of the gas with altitude), and the large velocity differential between the rotating disk matter and the infalling (non-Keplerian) molecular cloud material. Of these, turbulent convection is the focus of the current work. Turbulent convection is strongly affected by the compressibility of the flow because the density and pressure vary substantially with altitude above the nebula midplane. Hence, the study of compressible turbulence is central to this project.

The greatest obstacle to the accurate modeling of the solar nebula is the fact that the length scales on which viscous dissipation takes place (and on which the turbulent kinetic energy is turned into heat) is many orders of magnitude smaller than the size of the disk. Consequently, it is not currently possible to create a single computational model which accurately simulates both the large scale structure and the small scale dissipative processes. The objective of this project is to simulate numerically the turbulent processes on a small scale, and to obtain a parameterization of these processes which may be used in other attempts to model the large scale evolution of the nebula.

2. Previous work

The work currently being performed is closely connected with that of Cabot, Hubickyj, and Pollack (hereafter CHP), who have been using the turbulent channel flow code of Kim, Moin, & Moser (1987) to investigate incompressible turbulence in the solar nebula.

The Keplerian flow velocities are highly supersonic in the rest frame of the central star. A direct simulation of the flow in the star's rest frame is impractical, as the flow velocities dictate unworkably small time steps. A better approach is to work in a coordinate system which is comoving with the average flow in the model volume, so that the velocities are subsonic in the model's coordinate system, and the time steps are more reasonable.

CHP have relied upon a coordinate transformation based on the work of Rogallo (1981) to represent the radial shear in a form which permits the use of periodic boundary conditions in the radial direction. The Rogallo transformation eliminates the need to devise boundary conditions which properly advect turbulent flow in and out of the radial boundaries.

In the comoving frame, the gravitational acceleration varies with altitude z above the nebula midplane. The disk is very thin compared to its radial dimensions; therefore a fluid element a distance z above the central disk plane experiences a downward-directed gravitational force (due to the central star)

which is proportional to z. This linear variation of gravity has a significant effect on the convective flow. Convection in the Earth's atmosphere takes place in an altitude range over which the gravitational acceleration is essentially constant. The nebular problem has a variable acceleration with altitude, which gives rise to flow patterns not seen in constant gravity environments.

The results of CHP show that those fluid elements above the midplane which are cooler than the average temperature experience a downward acceleration which draws them toward the midplane. Although the acceleration ceases when the fluid reaches the midplane, inertia carries the fluid through the midplane and beyond, until the now-reversed gravitational acceleration robs them of momentum. Thus the zero gravity region experiences some of the most extreme motions, and the variable gravity leads to novel convection patterns.

The computational technique of Kim et al., as currently implemented by CHP, assumes an incompressible fluid. The incompressible approximation is fundamentally flawed for two reasons. First, the density varies significantly with altitude in the real nebula, and fluid elements which move in the vertical direction undergo substantial volume changes. Secondly, the incompressible code uses wall boundary conditions at the vertical boundaries, leading to boundary layer formation, while there are no such boundary layers in the solar nebula. These limitations in turn motivate the current work.

3. Current work

A compressible calculation can overcome the limitations of constant density and boundary layer effects to which an incompressible calculation is subject. Density variations and compressibility are taken care of automatically. The boundary layer problem can be alleviated by adjusting the heating profile to put a nonconvecting layer of fluid next to the walls, so that the convecting flow does not feel the walls directly and cannot form boundary layers. In the event that reflection of acoustic waves from the wall boundaries causes unacceptable perturbations to the interior solution, nonreflecting boundary conditions might be adopted to allow the acoustic waves to propagate out of the calculation, as in Thompson (1987a, 1987b, 1990).

The current work is focused on the simulation of compressible turbulent convection in three dimensions, in which the flow is subjected to a linearly varying gravitational acceleration, viscosity, thermal conduction, and a uniformly applied volume heating. The heat supplied is enough to make the fluid convectively unstable, and convection results. The current problem was formulated to be as much like the corresponding incompressible problem solved CHP as possible, with the goal of comparing the two calculations for consistency. CHP solved this problem by adopting the Boussinesq approximation, in which the flow is assumed to be incompressible and density variations are ignored except for gravitational acceleration (Chandrasekhar (1961)).

4. Numerical method

The equations to be solved are the compressible Navier-Stokes equations. They describe the time evolution of a single compressible fluid in three dimensions, and incorporate the effects of a variable gravitational field, molecular viscosity, thermal conductivity, heating through viscous dissipation, and a separately imposed volume heating.

The current calculations are performed with a code which is designed to conserve mass, energy, and local vorticity. An earlier code which was not conservative was found to become unstable after a sufficient length of time. The conservative code was written in the hope that it would be more stable, and this has proven to be the case.

The density and energy equations are written in conservative form, the conserved energy being the total (= kinetic + thermal + gravitational):

$$\frac{\partial \rho}{\partial t} + \nabla \cdot (\rho \mathbf{u}) = 0,$$

$$\frac{\partial e}{\partial t} + \nabla \cdot [(e + p)\mathbf{u} - \mathbf{u} \cdot \boldsymbol{\sigma} - \kappa \nabla T] = Q,$$

where $e = (1/2)\rho \mathbf{u} \cdot \mathbf{u} + \epsilon + \rho\Phi$; and where ρ is the density, e is the total energy density, Φ is the gravitational potential, $\mathbf{u}$ is the velocity, p is the pressure, T is the temperature, κ is the thermal conductivity, Q is the volume heating rate, $\epsilon = p/(\gamma - 1)$ is the thermal energy density, and $\boldsymbol{\sigma}$ is the viscosity tensor.

Numerical approximations to Eqs. (1–2) can be constructed which exactly conserve the total mass and energy of the system. The numerical conservation laws hold provided that suitable numerical approximations are chosen for both the volume integral of the fields and the spatial derivatives. Such approximations have been constructed, and the calculations verify that the numerical conservation laws are satisfied exactly.

The velocity equations are written in the form

$$\frac{\partial \mathbf{u}}{\partial t} - \mathbf{u} \times \boldsymbol{\omega} + \nabla \left(\frac{1}{2}\mathbf{u} \cdot \mathbf{u} + \frac{\gamma}{\gamma - 1}\frac{p}{\rho} \right) = \mathbf{g} - \frac{1}{(\gamma - 1)\rho}\left(c^2 \nabla \rho - \nabla p\right) + \frac{1}{\rho}\nabla \cdot \boldsymbol{\sigma},$$

where $\boldsymbol{\omega} = \nabla \times \mathbf{u}$ is the vorticity, c is the speed of sound, and $\mathbf{g} = -\nabla\Phi$ is the gravitational acceleration.

The viscosity tensor elements are

$$\sigma_{ij} = \mu \left(\frac{\partial u_i}{\partial x_j} + \frac{\partial u_j}{\partial x_i} - \frac{2}{3}\delta_{ij} \nabla \cdot \mathbf{u} \right),$$

where μ is the viscosity.

The pressure appears in two terms in the velocity equation, rather than as the single pressure gradient term normally seen. The reason for this formulation is

to avoid the spurious generation of vorticity by the numerical approximations. Taking the curl of the velocity equation gives

$$\frac{\partial \boldsymbol{\omega}}{\partial t} - \nabla \times (\mathbf{u} \times \boldsymbol{\omega}) = \nabla \times \left[-\frac{1}{(\gamma - 1)\rho} \left(c^2 \nabla \rho - \nabla p \right) + \frac{1}{\rho} \nabla \cdot \boldsymbol{\sigma} \right],$$

because the curl of a gradient is zero.

In the limit of zero viscosity ($\boldsymbol{\sigma} = 0$), the vorticity will remain zero at all times provided that it is zero to begin with and that the fluid is has a spatially constant entropy. (The latter condition implies $c^2 \nabla \rho - \nabla p = 0$.) The numerical approximation to the velocity equation also avoids the spurious generation of vorticity as long as the equation is cast into the form of Eq. (3). Analytically, vorticity is not generated because the curl of the gradient is zero, due to the fact that spatial derivatives commute: $\partial^2 f / \partial x \partial y - \partial^2 f / \partial y \partial x = 0$. The vorticity conservation carries over to the numerical case because the finite difference approximations to x and y derivatives also commute.

The flow is defined to be periodic in the x and y directions. Slip wall (zero stress) and constant temperature conditions are imposed at the z boundaries $z = \pm\delta$. Gravity acts only in the z direction, for which the acceleration is linear in z: $g = -g_w(z/\delta)$, where $g = g_w$ at $z = \delta$. The heating rate Q is uniform throughout the computational volume. The ratio of specific heats is $\gamma = 1.4$.

The spatial derivatives in the above equations are approximated by fourth order finite difference formulas. Suitable one-sided approximations are made at the vertical boundaries at $z = \pm\delta$, while centered approximations are made in the interior. The one-sided approximations are designed to preserve the numerical conservation of mass and energy, and are third order accurate. The complete set of derivative approximations is fourth order accurate.

The time integration is performed by the classic fourth order Runge-Kutta scheme, which is simple to implement and has excellent stability properties. The time dependent solution, therefore, has a global accuracy of fourth order and contains little numerical dissipation. Consequently, the short wavelength solution components do not undergo significant damping due to the numerical scheme.

The choice of an explicit method over an implicit method stems from the need to resolve the smallest features present in the flow. At the smallest length scales, viscosity dominates the evolution of the flow. Since we need to simulate the dissipation of kinetic energy accurately at these scales, the grid spacing and time steps necessary are set by the properties of the flow, and are the same whether explicit or implicit methods are used. The optimal grid spacing and time step are those for which the propagation and viscous Courant numbers are nearly equal. Consequently, the simpler explicit approach has been selected.

5. Results

The flow is characterized by seven numbers. These numbers have been chosen

as the scale Mach number M, the Prandtl number Pr (ratio of viscosity to conductivity), the Rayleigh number Ra (related to the volume heating Q), the density exponent α, the scale density ρ_0, the wall gravity g_w, and the wall temperature T_w. The initial state consists of an unstable static solution to which velocity perturbations are added. The temperature and density initially vary with z as $T = T_w + T_s(1 - z^2/\delta^2)$ and $\rho = \rho_0[T/(T_w + T_s)]^{\alpha-1}$, where $T_s = Q\delta^2/(2\kappa)$ is a scale temperature, α is the density exponent, and κ is the thermal conductivity.

The current simulations are defined by $M = 1$, $Pr = 0.2$, $Ra = 1.25 \times 10^5$, $\alpha = 1$, $\rho_0 = 1$, $g_w = 1000$, and $T_w = 300$. The actual flow Mach numbers are ≤ 0.3, and thus approximate an incompressible flow only in a qualitative sense. The Prandtl and Rayleigh numbers are the same as for the incompressible calculations. The density exponent α has no counterpart in the incompressible calculations and was chosen as $\alpha = 1$ to minimize the density variation. With $\alpha = 1$ the density is constant initially, but subsequently assumes an approximately Gaussian distribution with z.

Figure 1 shows the density and temperature profiles for a typical calculation. The plots represent data which is averaged both in time and in the horizontal directions, and then plotted with respect to z. Figures 2 and 3 show the spectra and autocorrelations in the x and y directions at the midplane ($z = 0$).

Figure 1 clearly shows the effects of compressibility on the solution. An incompressible flow responds to a convectively unstable state by undergoing turbulent convection, which redistributes the heat and decreases the temperature gradients from the initial perturbed state. The compressible flow not only redistributes the heat, but also the density, into a more stable distribution. In the isothermal limit where $T = T_c$, the density follows a Gaussian distribution $\rho = \rho_c e^{-z^2/2H^2}$, where $H = \sqrt{kT_c\delta/mg_w}$ is the isothermal scale height, k is Boltzmann's constant, and m is the molecular mass. The convecting flow is not isothermal, but it does exhibit smaller temperature gradients than the initial state, and the density is clearly tending to a Gaussian distribution.

The results agree qualitatively with those of CHP for the analogous incompressible problem, but show some interesting differences as well. Relative to the incompressible results, the compressible results show a higher midplane temperature which is more sharply peaked, and up by a factor of 1.6; and smaller temperature and velocity fluctuations, down by a factor of 0.7. The results should not be expected to agree exactly, as the compressible results show significant density variation, while the incompressible results do not.

6. Future directions

The next task is to study the effects of nonuniform density profiles on turbulent intensities. The current simulations began with a flat density profile in an unstable steady state, which was perturbed to initiate the growth of convection. The time averaged steady state shows a density which resembles a Gaussian

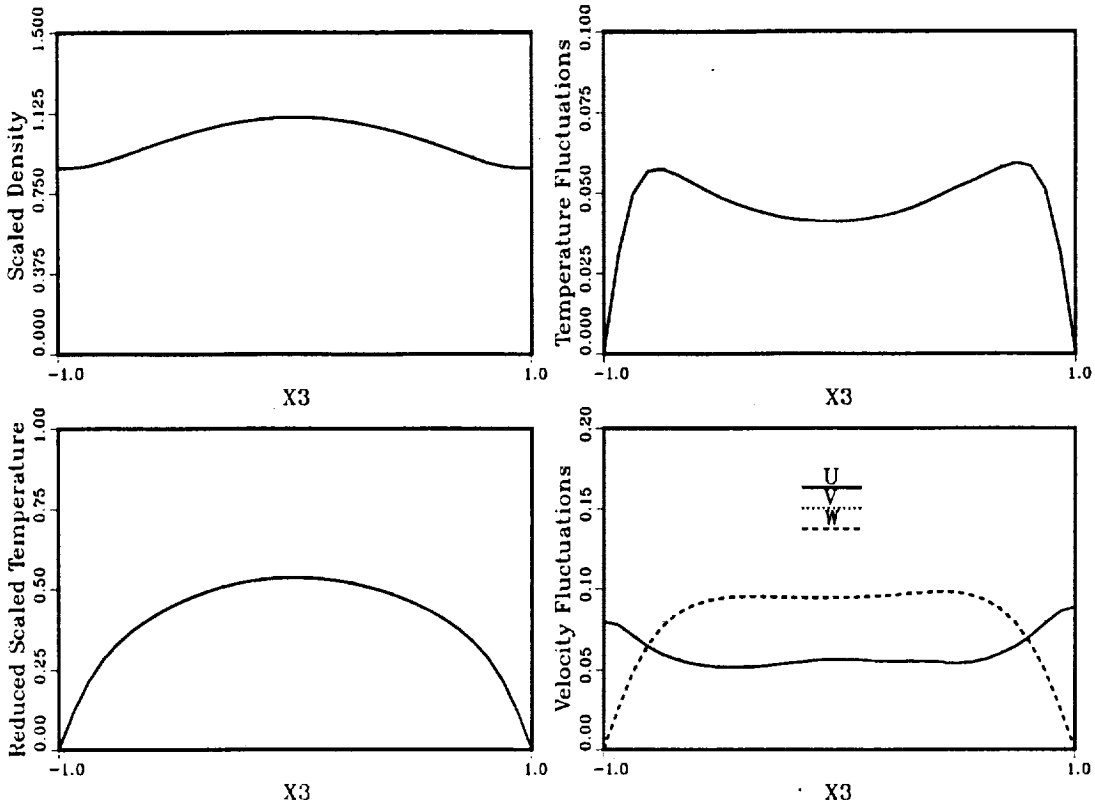

FIGURE 1. Horizontally and temporally averaged solutions for the statistical steady state, plotted versus altitude z. Density is normalized by its initial value. The temperature plot shows $(T - T_w)/T_s$. The RMS temperature and velocity fluctuations about the mean are also shown. Note: V and W curves are identical.

curve, and is peaked at the midplane. Further simulations will begin with an initial density profile which is peaked at the midplane, and should lead to a final state which shows even more density variation. Comparison of these two cases should demonstrate the dependence of turbulent intensities on the density stratification. It will be interesting to see if the incompressible results are approached as a constant density limit of the compressible results.

Some consideration is being given to the incorporation of a compressible sub-grid scale model, such as that of Zeman. Such a model might render the calculations more economical by allowing the use of a coarser grid; currently the calculations take $\approx$ 10 hours of CPU time on a Cray YMP to collect decent statistics for a single set of physical parameters. The current calculations might also serve as a test for the validity of sub-grid scale models.

Subsequent work will evolve the simulations to more accurate approximations

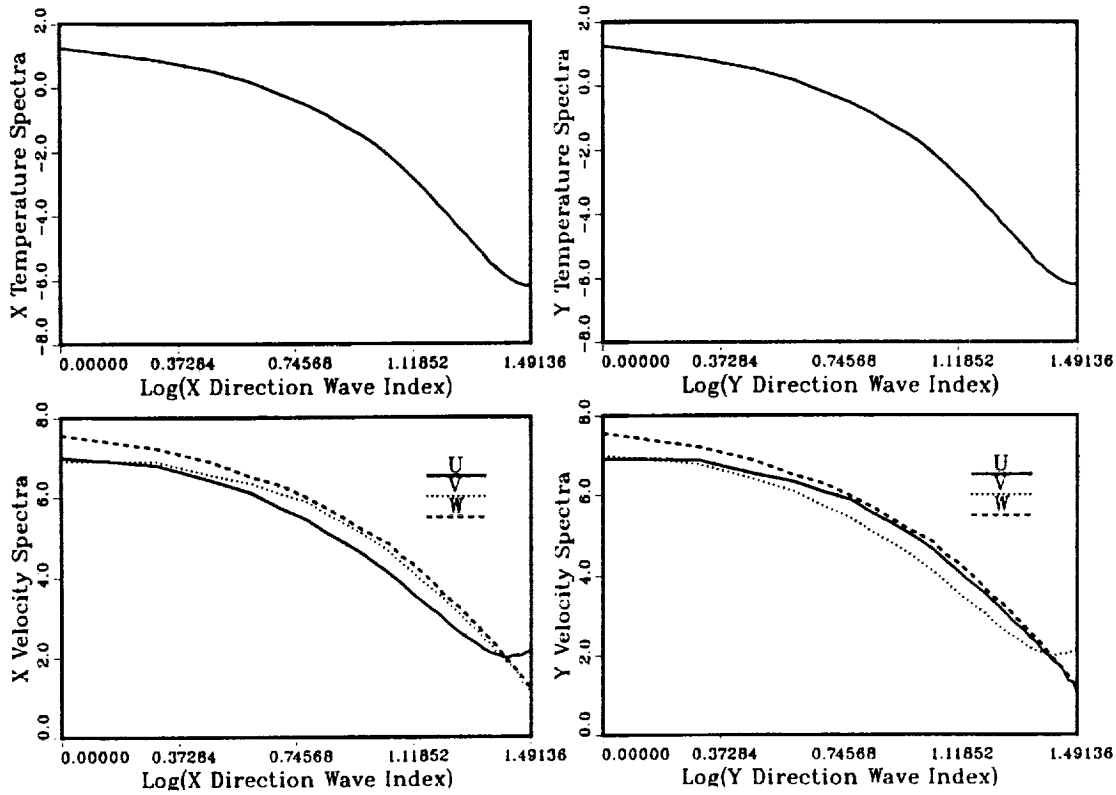

FIGURE 2. Log-log plots of the spectral intensities of the temperature and velocity fluctuations, versus the x and y direction wave numbers, at the midplane ($z = 0$).

of the actual nebula conditions. The stages to be followed will add major new physical phenomena, such as rotation, shear, and radial asymmetry.

The effects of rotation will be included by adopting a rotating coordinate system which is comoving with the flow, and in which the flow is subject to "centrifugal" forces as well as gravitational forces.

The effects of shear will be simulated by assuming a given base flow which is Keplerian, and solving for the nonlinear perturbations with respect to the base flow. The Rogallo transformation of CHP will not be used *per se*, although its useful effects will be duplicated; instead, the perturbations will be assumed to be periodic in a sheared coordinate frame, and will be mapped onto a stationary grid by appropriate coordinate transformations. This approach avoids the distortions entailed by the Rogallo transformation, in which the coordinate grid is itself sheared and must be periodically remapped to a new grid to prevent the grid

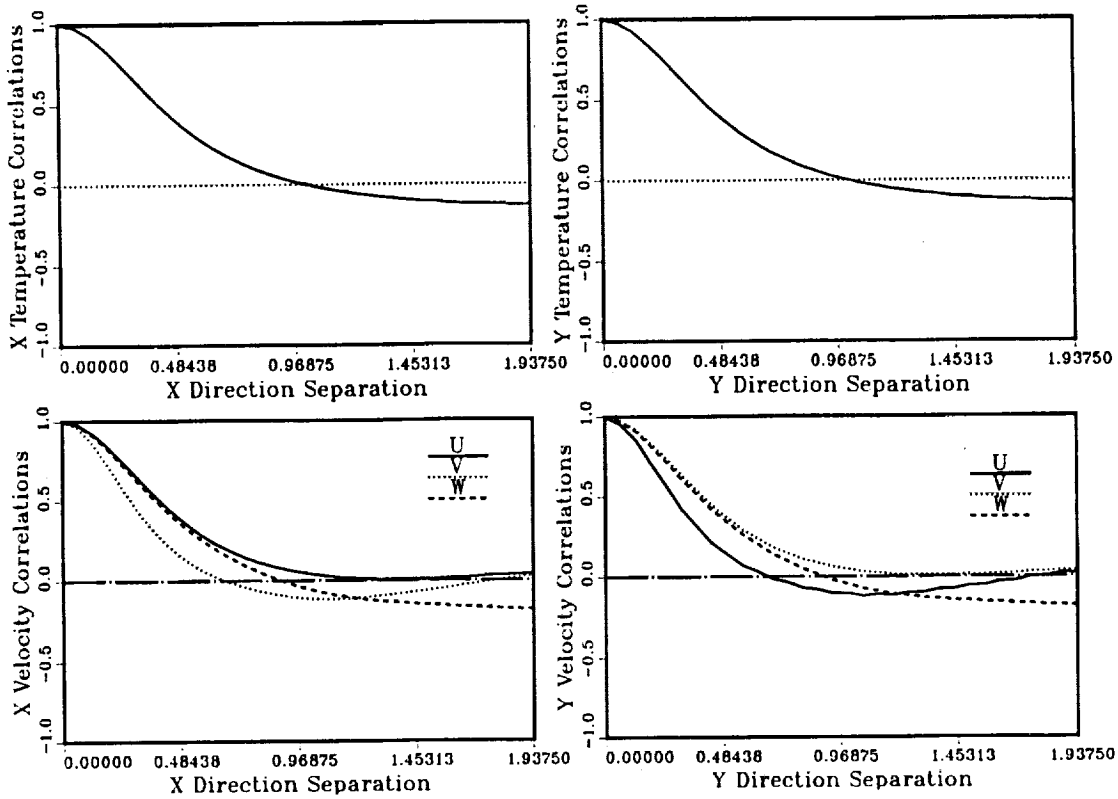

FIGURE 3. Autocorrelations of the temperature and velocity fields, versus x and y direction separations, at the midplane ($z = 0$).

from collapsing.

Radial asymmetry is ultimately required for the flow to result in a net transport of mass and angular momentum in the radial direction. Radial asymmetry renders the flow nonperiodic in the radial direction, prohibiting the use of periodic boundary conditions in this direction. It is not clear at this point how best to implement radial asymmetry. One possibility is to assume that the solution at the inner and outer boundaries consists of a known base state (from the Keplerian profile) plus a perturbation, and to assume that the perturbations at the two boundaries are related by a scaling factor. This issue will require further research.

The results of each of the above modifications will be studied carefully before proceeding to the next. By the time radial asymmetry has been implemented, we should be in a position to answer questions about the effectiveness of turbulence in transporting mass and angular momentum in the solar nebula.

REFERENCES

BLACK, D. C. & MATTHEWS, M. S. (EDITORS) 1985 *Protostars and Planets II*, University of Arizona Press. Tucson, Arizona.

CHANDRASEKHAR, S. 1961 *Hydrodynamic and Hydromagnetic Stability*, Oxford University Press (reprinted by Dover Publications, New York NY).

KIM, J., MOIN, P. & MOSER, R. 1987 Turbulence statistics in fully developed channel flow at low Reynolds number. *Journal of Fluid Mechanics.* **177**, 133.

ROGALLO, R. 1981 *Numerical Experiments in Homogeneous Turbulence*, NASA Technical Memorandum 81315.

THOMPSON, K. W. 1987a Time Dependent Boundary Conditions for Hyperbolic Systems. *Journal of Computational Physics.* **68**, 1.

THOMPSON, K. W. 1987b *Lecture Series in Computational Fluid Dynamics*, NASA Technical Memorandum 10010.

THOMPSON, K. W. 1990 Time Dependent Boundary Conditions for Hyperbolic Systems. II. *Journal of Computational Physics.* To appear.

C-3

A numerical method for prediction of compressible turbulent flows with closure models

By P. G. Huang

A new computer code to solve the time-averaged Navier-Stokes equations is developed. Many of the state-of-the-art numerical techniques and algorithms have been tested and implemented in the program in order to achieve a better numerical accuracy and code efficiency.

Various turbulence models are tested for a wide range of flows. The initial focus has been on "two-equation" eddy-viscosity models, which are the most advanced available in current compressible-flow codes. The long term goal will be to test Reynolds-Stress models and to explore their performance in the high-Mach-number range.

Although testing and improvement of turbulence models for supersonic and hypersonic flows is the primary objective of this research (70%), part of the effort (30%) has been devoted to analyzing the vortex breakdown phenomena using the new computer program. Some preliminary results on the breakdown of a vortex flow in a tube are reported. Although calculations are at the moment restricted to 2-D axisymmetric equations, an extension of this work to 3-D geometry is proposed.

1. Introduction

Traditional finite difference methods are accurate for smooth flows but give rise to over/under-shoots in region where a large gradient of the dependent variable is encountered. Although a stable solution can be obtained by adding ad-hoc artificial diffusivities, one must be careful that this solution may be corrupted, for the excessive diffusion added may smear the sharp gradient. Even in the case when one adds only enough diffusion to achieve a stable solution, slight over/under-shoots of the solution would still sometimes be observed. A mild over/under-shoot causes little difficulty in a pure Navier-Stokes calculation while it may bring about divergence of a time-averaged Navier-stokes calculation employing a closure-type of turbulence model. One possible cause of the divergence is the generation of negative turbulence quantities, such as k and ϵ.

To search for an accurate numerical scheme that will preserve the realizability property, two numerical concepts; namely TVD (Harten, 1983; Yee, 1987) and FTC (Boris and Book, 1973; Zalesak, 1979), are tested against a wide range of problems. Conclusions emerged from this investigation are reported in Section 2.

The recent interest in applying Reynolds-stress models in complex turbulent flow calculations has urged the need for a stable and efficient algorithm. The stability problem arises mainly from the stiffness of the source terms and the lack of apparent "eddy viscosity" in the mean-flow equations, while the need for numerical efficiency is due to the large number of turbulence equations that have to be solved together with the mean-flow equations and the strong coupling between the mean-flow and turbulence quantities.

While a number of numerical treatments have been proposed in some existing compressible codes to remove the source-term-related stiffness difficulties, these methods are not general and have suffered from numerical inefficiency. Moreover, although techniques involving simultaneous solution of the mean-flow and turbulence equations have open a door for handling the strong equation coupling, such methods require the inversion of a large matrix and thus are not attractive to be used in practical calculations. Last but not least, problems associated with the lack of apparent "eddy viscosity" in Reynolds-stress calculations have only begun to receive some attention and the extension of the available numerical treatments to compressible calculation is yet to be seen. Section 3 is devoted to a brief discussion of the current progress in dealing with the above-mentioned difficulties.

Section 4 presents some calculations of vortex breakdown in a tube. The importance of the boundary condition treatments is addressed in this section. Finally, a discussion on the future activities is given in Section 5.

2. Numerical schemes

Comparisons were made for the following schemes:

FCT: Zalesak (1979)

TVD (An excellent review has been provided by Yee (1987)): Harten and Yee, Yee-Roe-Davis, Roe, van Leer and Colella and Woodward

A wide range of problems have been chosen to test the numerical schemes:

1-D scalar: advection of square, Gaussian and semi-circle profiles.

2-D scalar: convection transport of a step profile and the solid body rotation of a block-profile.

2-D Euler: inviscid channel flow and oblique shock reflection.

2-D Navier-Stokes: wall-driven cavity, laminar and turbulent (two-equation model) boundary layers ($M = 0.3$, 2 and 10).

The study has shown the "Superbee" scheme by Roe emerged to be the best in terms of overall numerical performance while Harten and Yee's "Minmod" scheme is the simplest and the most stable one. Figures 1 and 2, respectively, show the predicted velocity and skin friction profiles of a laminar boundary layer. The calculation employs the Superbee scheme and shows good agreement with Blasius solution.

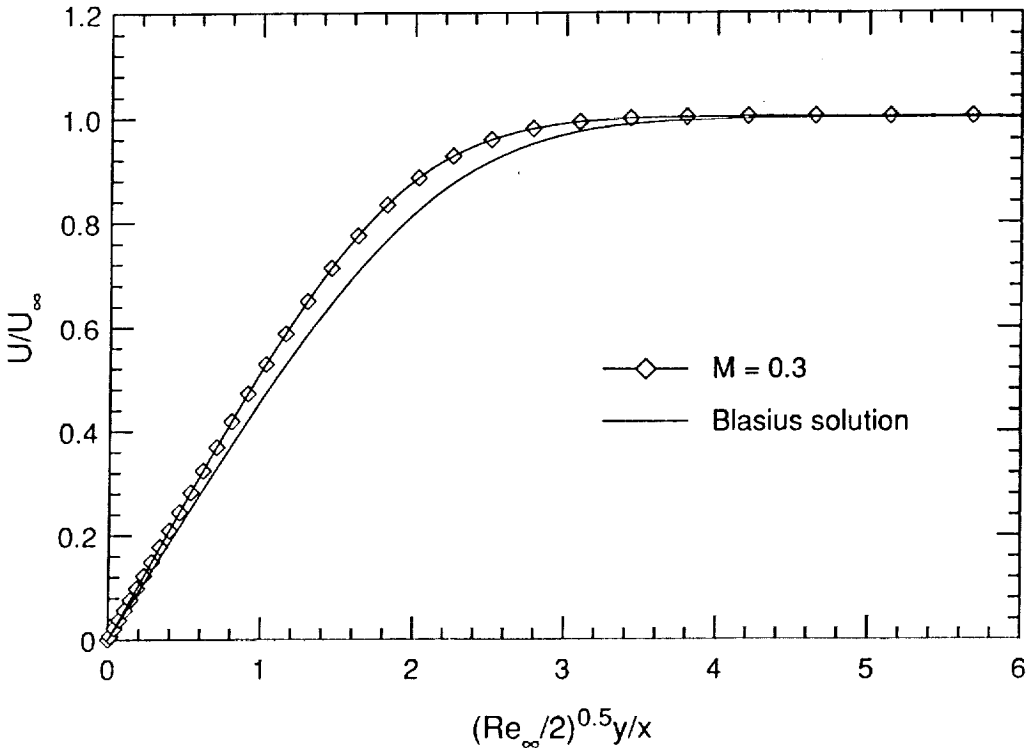

FIGURE 1. Laminar boundary layer - velocity.

3. Numerical algorithm

The lower upper symmetric successive over-relaxation method (LU-SSOR) developed by Jameson and Yoon (1986) will be the base of the present development. This algorithm is closely related to the symmetric Gauss-Seidel line relaxation method of MacCormack (1985). In our development, we show the basic equivalence between the LU-SSOR method and the Symmetric Gauss-Seidel point relaxation method (LU-SGS) (Gnoffo, 1986).

A modified version of the LU-SSOR (or LU-SGS) has been successfully implemented in the new code. The attractive features of the new code are:

(1) Solution of large block banded Matrices is not required.

(2) Vectorization of the code is possible.

(3) Relaxation can be done with infinite time step.

(4) Second-order time accuracy can be achieved with a finite time step.

(5) The operation count of the present method per iteration is only slightly greater than that of an explicit method.

(6) The method is capable of handling unstructured grids.

The code has been fully vectorized and it runs about 15 times faster than its scalar counterpart in Cray YMP.

To maintain the coupling between the mean-flow and the turbulence equations while not to involve the inversion of a big matrix, an algorithm is developed to

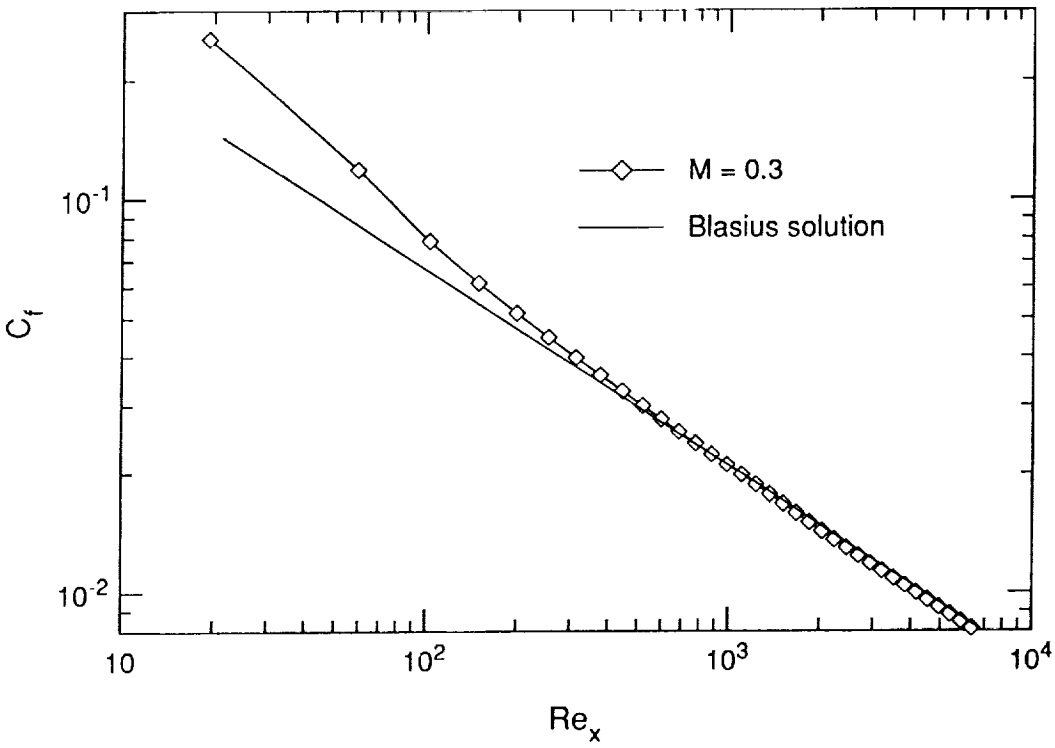

FIGURE 2. Laminar boundary layer - C_f.

obtain the solution by iterating between the mean flow and turbulence equations when performing the LU point-relaxation sweep. As a result, a large matrix is divided into two smaller matrices and they are solved sequentially in a point-by-point fashion. It has been found that this method did not give rise to numerical instability and, for a two-equation type of turbulence model, the overall computer time saving may be as high as 30%.

Because turbulence equations contain large source terms and these terms are often nonlinear, implicit treatments of the source terms are generally preferred. The approach used in the present study is similar to the stabilizing strategy of Huang and Leschziner (1986). The source is first divided into positive and negative parts. For turbulence quantities that are by nature positive, the measure is to treat the negative part of the source implicitly while the positive part is handled explicitly. The implicit treatment of the negative source is to ensure the positiveness of the solution at all time during iterations and the explicit treatment of the positive source is to preserve a diagonal domination of the matrix. This method has been found to be very robust and the overall convergence rate is satisfactory.

Figure 3 shows the predicted skin friction profiles of a Mach 2 turbulence boundary layer. Turbulence Models chosen were the $k-\epsilon$ models of Chien (1982), and Jones and Launder (1973), respectively. The results have shown

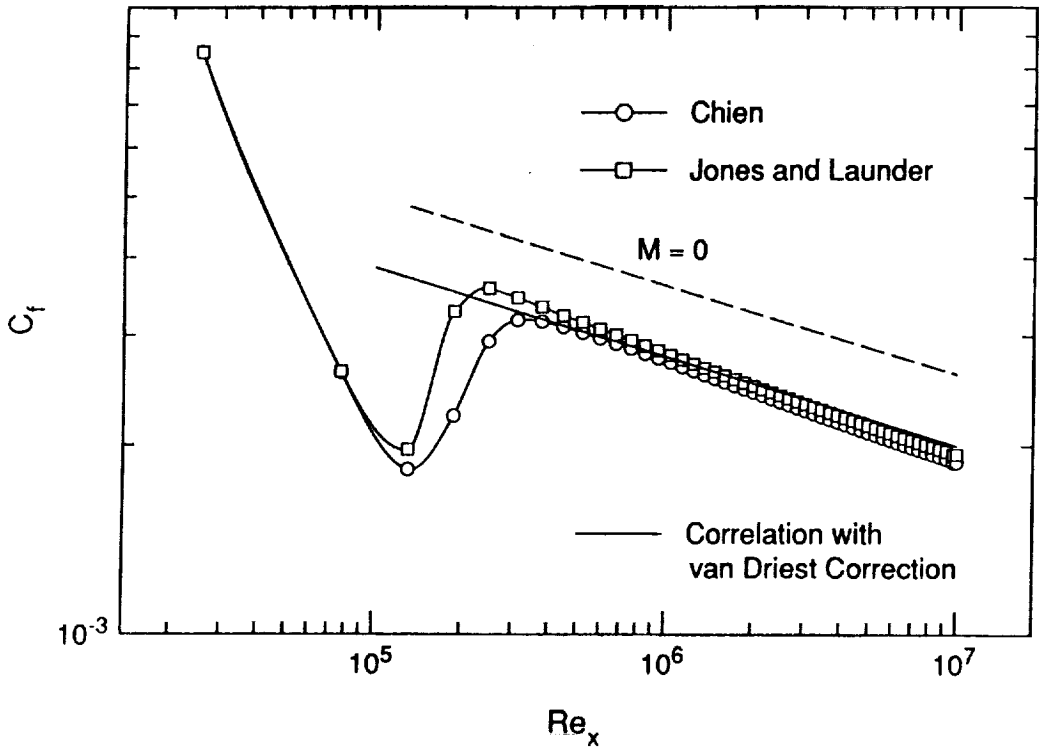

FIGURE 3. Turbulent boundary layer $-C_f$ at $M = 2$.

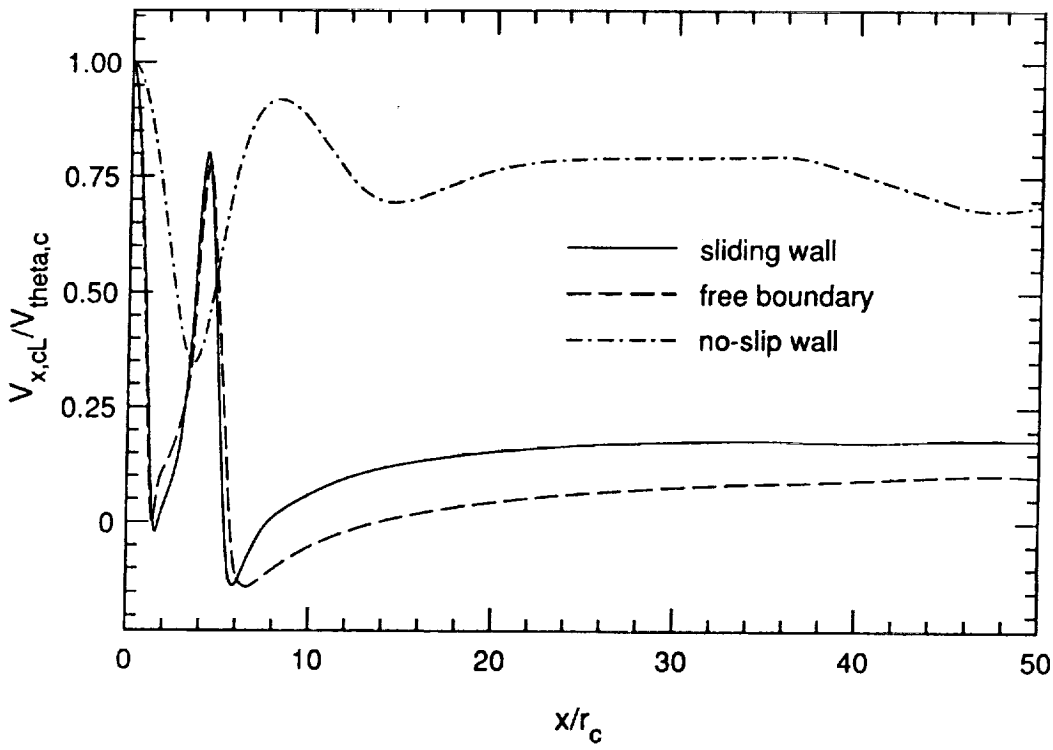

FIGURE 4. Vortex breakdown in a tube - $V_{x,cL}$.

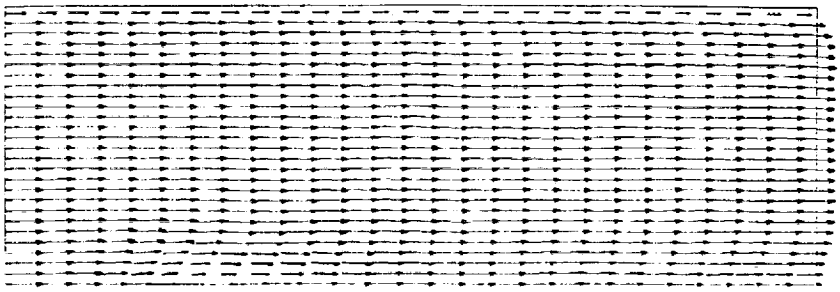

FIGURE 5. Vortex breakdown - no-slip top wall.

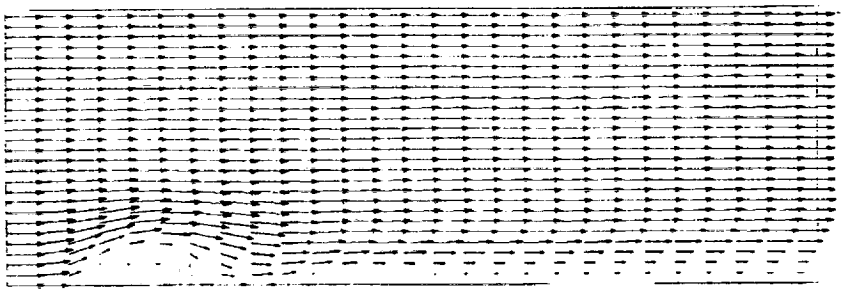

FIGURE 6. Vortex breakdown - sliding top wall.

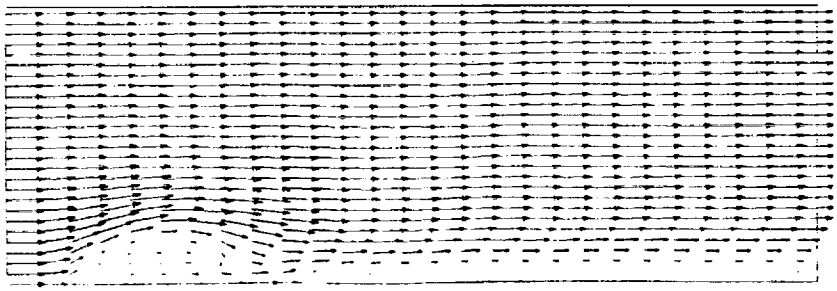

FIGURE 7. Vortex breakdown - free-stream top boundary

good agreement with experimental correlation.

4. Some preliminary results on vortex breakdown

The current investigation is restricted to the study of a vortex breakdown of the bubble-type, with the assumption of a 2-D axisymmetric flow. This problem is closely related to the one studied by Grabowski and Berger (1976) and later by Lugt and Gorski (1988).

Reynolds number, $Re = v_{\theta,max} r_c/\nu$, is chosen to be 500 based on the core radius, r_c, where the tangential velocity has its maximum value,$v_{\theta,max}$. The calculation domain is assumed to have a radius of $5r_c$ and an axial length of $50r_c$. The inlet conditions are given as follow;

$$u_x = 1/S,$$

$$v_r = 0 \text{ and} \qquad (1)$$

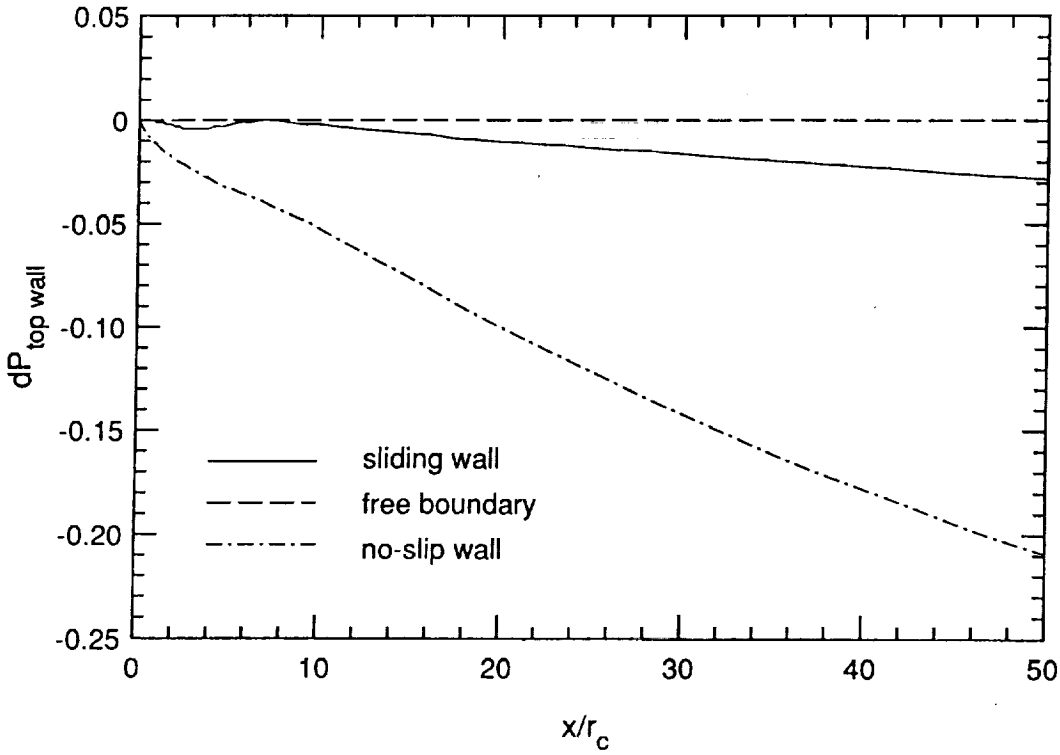

FIGURE 8. Vortex breakdown in a tube - *dp*.

$$v_\theta = \frac{1}{r}\frac{1-e^{-r^2}}{1-1/e}$$

where S, defined as $v_{\theta,max}/v_{x,inlet}$, is a swirl parameter and in the discussion that follows it is assumed to be unity. The tangential velocity is chosen to approximate a wing-tip vortex. At the axis, $v_r = v_\theta = 0.$, $\partial v_x/\partial r = 0$ and $\partial p/\partial r = 0$. The outflow conditions are $\partial/\partial x = 0$ for all variables.

In the present study, we have found that the top wall boundary-condition treatment has a very strong influence on the dynamics of breakdown suggesting that the breakdown is very sensitive to pressure gradient. Figure 4 shows the centerline axial velocity profiles for three different top wall boundary-condition treatments, no-slip, sliding ($v_{x,\text{wall}} = v_{x,\text{inlet}}$) and free-stream boundaries. It shows that the no-slip boundary introduces only slight retardation of the axial flow while the other two boundary-condition treatments give rise to flow reversal. This can be illustrated more clearly in the velocity vector plots, Figures 5 to 7. The figures show that for the sliding and the free-stream boundary treatments, the flow has formed a small well-pronounced bubble, similar in shape to that observed experimentally by Uchita et al. (1985) and Faler and Leibovich (1978).

The surprising outcome can be explained by examining the pressure distribution. Figure 8 provides a comparison of the pressure-drop profiles along the

top boundary. The figure has shown that the no-slip wall has induced a favor pressure gradient equivalent to 0.4% of inlet momentum flux, $\rho v_{z,inlet}^2$, per r_c distance. This favor pressure gradient has delayed the flow separation and thus resulted in a quite unexpected flow behavior.

5. Future plans

(1) Implement the Reynolds-stress-transport models into the new code.
(2) Compare the performance of the turbulence models.
(3) Test new pressure-strain models.
(4) Examine compressibility correction terms.
(5) Propose near-wall correction for Reynolds-Stress-transport models.
(6) Integrate to the wall or use wall functions?
(7) Investigate effects of turbulence on the dynamics of vortex breakdown.
(8) 3-D simulation of vortex breakdown.

REFERENCES

BORIS, J. P. & D. L. BOOK 1973 Flux-corrected transport I: SHASTA – a fluid transport algorithm that works. *J. Comp. Phys.* **11**, 38-69.

CHIEN, K.-Y. 1982 Predictions of channel and boundary-layer flow with a low-Reynolds-number turbulence model. *AIAA J.* **20**, 33-38.

FALER, J. H. & S. LEIBOVICH 1978 An experimental map of the internal structure of a vortex breakdown. *J. Fluid Mech.* **86**, 313-335.

GNOFFO, P. A. 1986 Application of program Laura to three dimensional AOTV flow fields. AIAA paper 86-0565.

GRABOWSKI, W. J. & S. A. BERGER 1976 Solution of the Navier-Stokes equations for vortex breakdown. *J. Fluid Mech.* **75**, 525-544.

HARTEN, A. 1983 High resolution schemes for hyperbolic conservation laws. *J. Comp. Phys.* **49**, 357-393.

HUANG, P. G. & M. A. LESCHZINER 1985 Stabilization of recirculating flow computation performed with second-moment closure and third-order discretization. 5th Symp. on Turb. Shear Flows, Cornell.

JAMESON, A. & S. YOON 1986 LU Implicit scheme with Multiple Grids for the Euler Equation. AIAA paper 86-0105.

JONES, W. P. & B. E. LAUNDER 1973 The calculation of low-Reynolds number phenomena with a two-equation model of turbulence. *Int. J. of Heat and Mass Transfer.* **16**, 1119-1130.

LUGT, H. J. & J. J. GORSKI 1988 The "bubble" concept of axisymmetric vortex breakdown with and without obstacles in the vortex core. DTRC-88/042.

MACCORMACK, R. W. 1985 Current status of numerical solutions of the

NAVIER-STOKES EQUATIONS AIAA paper 85-0032.

ROE, P. L. 1985 Some contributions to the modelling of discontinuity flows. *Lectures in Applied Mathematics*, 22, Amer. Math. Soc., Providence, R. I.

UCHIDA, S., Y. NAKAMURA & M. OHSAWA 1985 Experiments on the axisymmetric vortex breakdown in a swirling air flow. *Trans. Japan Soc. Aero. Space Sci.* **27(78)**, 206-216.

YEE, H. C. 1978 Upwind and symmetric shock capturing schemes. NASA TM-89464.

ZALESAK, S. T. 1979 Fully multidimensional flux-corrected transport algorithm for fluids. *J. Comp. Phys.* **31**, 335-362.

Incompressible spatially-developing free-shear flows

By J. C. Buell

1. Introduction

The understanding of the role of large-scale structures and the process of mixing in free shear layers has advanced rapidly since the ground-breaking work of Brown & Roshko (1974). Until recently, most of the advances came from experimental projects such as those of Konrad (1976), Bernal (1981), and Mungal & Dimotakis (1984) in gaseous layers, and Koochesfahani & Dimotakis (1986) and Lasheras *et al.* (1986) in liquid layers. For a review, the reader is referred to the article by Ho & Huerre (1984). From the visualizations given in these papers one can see the spanwise rollers, their pairings, and the geometry of the streamwise vortices (called "ribs" here). As valuable as these experiments are for investigating certain aspects of mixing layers, it is very difficult to obtain quantitative information from them about the dynamics of three-dimensional (3-D) vortical structures. Numerical simulations, on the other hand, are ideal for obtaining detailed information under well-controlled conditions. Of course, there are disadvantages, usually related to limits on the Reynolds number or on the size of the domain. Several researchers (*e.g.*, Comte *et al.* 1987, Davis & Moore 1985, and Lowery 1986) have recently simulated spatially-developing mixing layers with the goal of extracting more information than is possible in experiments. These efforts were successful to some degree, but they all suffered from either too much diffusion (either physical or numerical) or lack of resolution.

The first goal of this research is to understand the dynamics of three-dimensional vortical structures, especially the interaction of the ribs and 2-D rollers. Because of vortex stretching effects, this requires accurate and well-resolved simulations. Another goal is to distinguish temporally- and spatially-growing shear layers in terms of the dynamics and observed vortical structures. This is important since the former is much easier to compute, but the error incurred in using temporal results for certain applications is unknown. The third goal is to investigate the effects of asymmetry on passive scalar mixing and fast-chemistry product formation. In this report, a brief summary of a new numerical method is presented, followed by results for mixing layer and wake flows.

2. Numerical method

In this section we briefly describe a new algorithm for approximately solving incompressible spatially-developing free-shear problems on a domain that is infinite in the vertical (y) direction and finite in the streamwise (x) and spanwise (z)

directions. The numerical method is analyzed in more detail elsewhere (Buell 1989).

The total velocity field $\mathbf{U} = (U, V, W)$ is decomposed using

$$\begin{aligned} U(x,y,z,t) &= U_0(y) + x\,U_e(y) + u(x,y,z,t), \\ V(x,y,z,t) &= V_e(y) + v(x,y,z,t), \\ W(x,y,z,t) &= w(x,y,z,t), \end{aligned}$$

so that all components of the perturbation variable u satisfy homogeneous boundary conditions at infinity. Here, V_e is some smooth function that tends to the entrainment values at $\pm\infty$ but is otherwise arbitrary, $U_e = -\partial V_e/\partial y$, and $U_0(y)$ is the mean velocity profile at the inflow (*e.g.*, a tanh profile for mixing layers, Gaussian for wakes). The Navier-Stokes equations are cast in fourth-order form by operating on the momentum equations with $\nabla\times$ and $\nabla\times\nabla\times$, and taking the streamwise components of both. The pressure is thus eliminated and dynamical equations for the perturbation streamwise velocity and vorticity result:

$$\frac{\partial}{\partial t}\nabla^2 u = \nabla_\perp^2 H_1 - \frac{\partial^2}{\partial x \partial y} H_2 - \frac{\partial^2}{\partial x \partial z} H_3 + \frac{1}{Re}\nabla^4 U, \tag{1}$$

$$\frac{\partial}{\partial t}\omega_1 = \frac{\partial}{\partial y} H_3 - \frac{\partial}{\partial z} H_2 + \frac{1}{Re}\nabla^2 \omega_1, \tag{2}$$

where $\mathbf{H} = \mathbf{U} \times \boldsymbol{\omega}$ and the "perpendicular" Laplacian is $\nabla_\perp^2 = \partial^2/\partial y^2 + \partial^2/\partial z^2$. For mixing layers, lengths have been scaled with the inflow vorticity thickness δ_ω (the half-width for wakes) and velocities with the freestream velocity difference $U_1 - U_2$ (freestream velocity for wakes). The Reynolds number based on these scales is thus $(U_1 - U_2)\delta_\omega/\nu$. The other two nondimensional parameters of the problem are the velocity ratio $r = U_2/U_1$ (velocity deficit for wakes) and the Schmidt number $Sc = \nu/D$ where D is the diffusion coefficient of the passive scalar.

After (1) and (2) are advanced in time, the vertical and spanwise velocities v and w are recovered directly from the continuity equation and the definition of ω_1. There are two main advantages in casting the governing equations in this form. First, only two dynamical equations need to be advanced in time instead of three. Second, unlike primitive variable methods, we may allow a difference to exist (consistent with the overall accuracy of the method) between the numerical divergence of the gradient and the Laplacian operator in the Poisson equation (1). This is because we invert the continuity equation directly instead of relying on the gradient of the pressure to ensure exact conservation of mass. The second point is very important since it introduces great flexibility in the choice of numerical approximations to various operators.

Equations (1) and (2) are advanced in time explicitly using a compact third-order Runge-Kutta scheme (Wray 1988). Since the Laplacian is contained in the

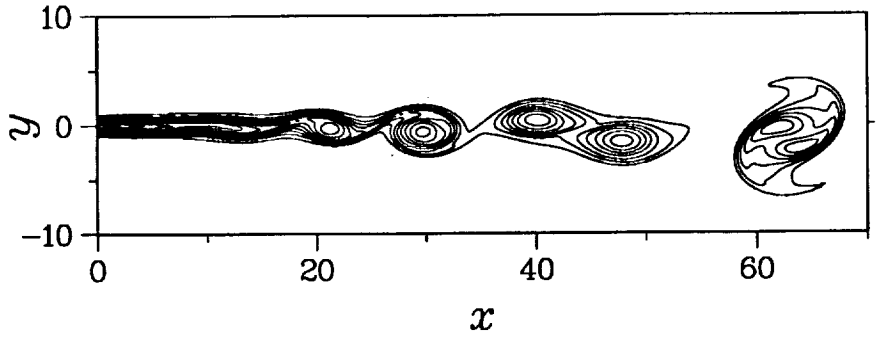

FIGURE 1. Contours of $-\omega_3$ for a 2-D mixing layer, $Re = 200$, $r = 0.2$. Contour interval is 0.1.

time-derivative term, a Poisson equation must be solved during each substep. The dependent variables are expanded in cosine (u, w) or sine (v, ω_1) series in a mapped vertical coordinate ζ (where $y = -\beta\cot(\pi\zeta)$ maps $[-\infty, \infty]$ to $[0, 1]$), and periodic Fourier series in z. The first x-derivatives in the continuity equation and in the advection terms are approximated with modified Padé finite differencing (Lele 1989). The particular approximation used here yields sixth-order accuracy for the low to moderate wavenumber components of the solution, and significantly lower dispersion errors for high wavenumbers. The second x-derivative is approximated also with a new Padé formula due to Lele (1989).

Dirichlet boundary conditions are specified for $\mathbf{u} = (u, v, w)$ at the inflow. Typically, 2-D Rayleigh equation eigenfunction profiles for a frequency near the most unstable one are used for u and v, and 3-D steady profiles for v and w are added to produce streamwise vortices. At the exit, each velocity component is required to satisfy a "convective" outflow boundary condition of the form $\partial\psi/\partial t = -c\,\partial\psi/\partial x$, where c is the nominal speed of the large structures. At infinity, $\mathbf{u} = 0$. For the mixing layer simulations, we used $V_e(y = -\infty) = .004$ and $V_e(y = \infty) = -.01$. These values were chosen to minimize the streamwise pressure gradient outside of the shear layer (this is analogous to experiments where the walls of the wind tunnel are adjusted inward).

3. Mixing layers

3.1. Dynamics of vortical structures

Our base-line case is a two-dimensional flow at $Re = 200$ and $r = 0.2$. This simulation was performed on a 192×128 mesh (grid points in x, modes in y, respectively) with 144 collocation points in y for partial dealiasing. The domain length in the streamwise direction is 70, and the vertical mapping parameter is $\beta = 8$. The layer was forced at a fundamental frequency of 0.5, although the most amplified frequency at the inflow is 0.65. This was done to compensate for the viscous thickening of the layer a short distance downstream.

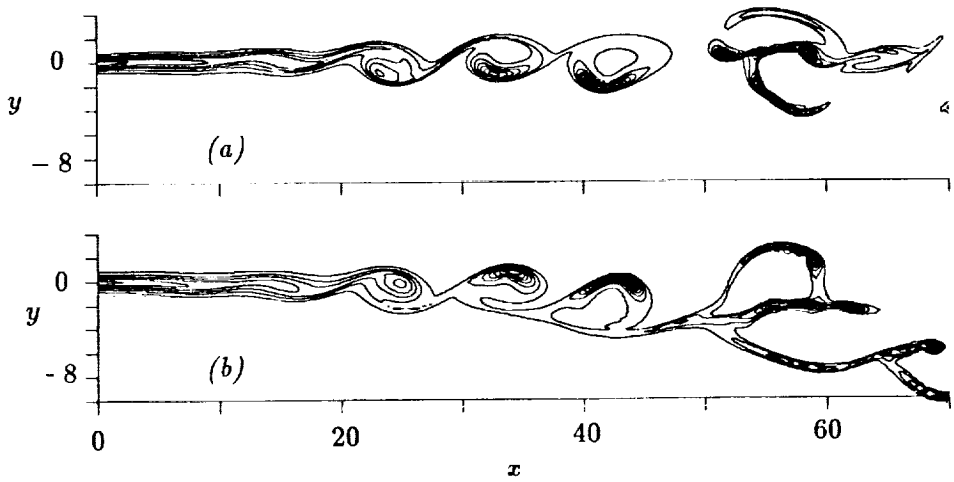

FIGURE 2. Contours of $-\omega_3$ for a 3-D mixing layer, $Re = 200$, $r = 0.2$. *(a)* $z = 0$, *(b)* $z = 2.75$. Contour interval is 0.15.

Shown in Fig. 1 are contours of vorticity (ω_3) where the fundamental was forced at an amplitude of 0.01 and the subharmonic at 0.005. The former leads to rollup and the latter to pairing of the vortices. The resulting flowfield is periodic in time with a weak nonperiodic component due to the feedback from the outflow boundary condition (Buell & Huerre 1988). The organized nature of the inflow forcing creates a "stairstep" growth of the layer downstream, where we find a high growth rate during the rollup and pairing, and small or nonexistent growth in the saturated region between.

To examine the effects of three-dimensionality, a pair of counter-rotating streamwise vortices are added at the inflow with maximum vorticity set to 5% of the maximum slope of $U_0(y)$. Between each vortex and its neighbor to either side is a symmetry plane where $\omega_1 = 0$. The Reynolds number and velocity ratio is the same as before. We set the spanwise wavelength to 5.5, or 58% of the streamwise wavelength of the rollers. This is consistent with both experiment (Huang & Ho 1989) and theory (Pierrehumbert & Widnall 1982). Due to the larger gradients that arise in the 3-D case, a finer grid was used, $256 \times 144 \times 24$ with a $y \times z$ collocation grid of 192×32 to reduce aliasing errors.

Shown in Fig. 2 are contours of spanwise vorticity (ω_3) in the two x-y symmetry planes. These plots show the initial laminar layer, development of 2-D rollers, and 3-D cup-like structures. The amplitude of the vorticity in the "cups" reaches about twice that of the maximum vorticity in the inflow profile U_0.

A 3-D visualization of the streamwise vortices (called "ribs") is shown in Fig. 3. Shown also are opposite-signed streamwise vortices inside the rollers. Note that the first pair of ribs is almost straight and nearly parallel, but the second pair is distorted and not parallel. The latter pair is very similar to the structures observed by Lasheras *et al.* (1986) in their low Reynolds number experiments in

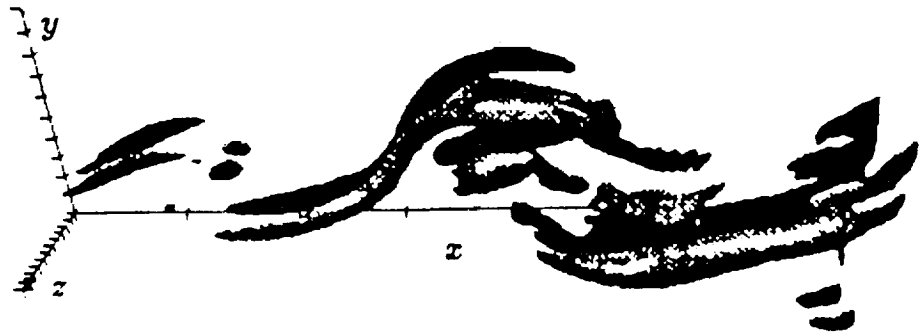

FIGURE 3. Perspective view of ω_1, contour levels ± 0.6.

water. This distortion is apparently due to self-induction effects between the ribs and the opposite-signed streamwise-vorticity structures inside the downstream roller. The ribs are intensified by the 2-D strain field of the main rollers, but this mechanism cannot increase the circulation around a rib. However, since the radius of the ribs remains about constant (or grows), the circulation increases significantly. The mechanism for this is the "conversion" of ω_3 into ω_1 by one of the "vortex stretching" terms in (2). This mechanism and quantitative measures of the circulation are discussed by Rogers & Moser (1989).

Returning to the cup-like structures shown in Fig. 2, we would like to determine their origins and the reasons for their unusual shape. First, we see that the cups that reside on the upper side of the rollers are slightly farther downstream than the lower ones. This is not a spatially-developing effect since it is also observed in the temporal case. However, the upper cups are about 25% stronger than the lower ones. This difference is not allowed by symmetry in the temporal case. The cups are clearly related to the ribs; the former lie symmetrically between the latter and slightly towards the middle of the layer. Furthermore, the sense of rotation of the ribs causes a positive spanwise strain in the regions occupied by the cups and thus creates a mechanism for the enhancement of spanwise vorticity.

However, this mechanism does not explain why the cups are concave on their inner sides, why they are strongest on the opposite side (in the streamwise sense) of the roller from the associated ribs, and why they are not convected away by the downwash (in the case of the upper cups) between the ribs. These questions are answered by examining Fig. 4. Shown there are y-z cuts of ω_3 and ω_1 at the x-location corresponding to the maximum of ω_3 in the upper cup. The ω_1 plot shows three pairs of counter-rotating structures: from top to bottom these are ribs connected to the upstream roller, opposite-signed vortices in the core

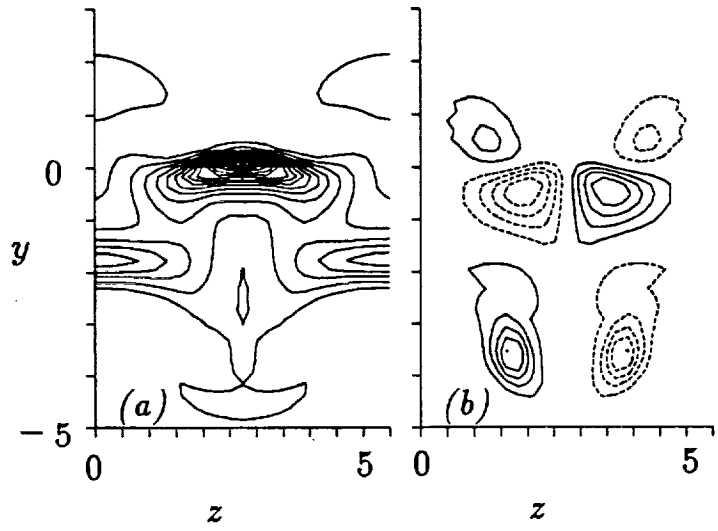

FIGURE 4. Spanwise cuts of vorticity through the roller at $x = 44$. The contour interval is 0.15, and negative values are represented by dashed lines. *(a)* $-\omega_3$, *(b)* ω_1.

of the roller (which we call "legs", a term which will become self-explanatory later), and another pair of ribs connected to the downstream roller. Each of the cups resides in the middle of a quadrapole formed by the legs and one or the other pair of ribs. The maximum amplitude of the legs is located very near the upper cup, contributing most to the positive strain there. The role of the ribs thus appears to be secondary; they contribute less to the strain, but are needed to produce a stagnation point in the vertical velocity so that the cups are not convected away and can continue to get strained. The convective effect of the strong vertical velocity created by the legs also explains the concave structure of the cups.

One would expect the upper and lower cups to be connected by vortex lines, and that these lines would show a streamwise tilt corresponding to the streamwise offset of the two cups. This is not quite true. Shown in Fig. 5 are two views of two sets of vortex lines, each set initiated in the region of maximum spanwise vorticity in each cup. A "hairpin" structure is formed by the lines, where the cups form the ends of the hairpin, and the regions between (consisting mostly of ω_1 and ω_2) are the "legs". We see that the two sets are definitely disjoint, although there is one vortex bundle (not shown) that goes from the vicinity of the downstream edge of the upper cup to the upstream edge of the lower cup. Consistent with this, all the lines are inclined by about $45-50°$, whereas a line connecting the middle of one cup to the middle of the other would be inclined

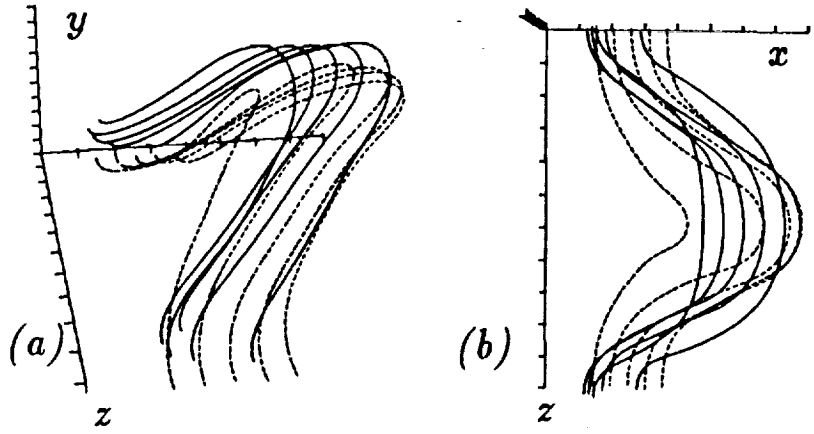

FIGURE 5. Vortex lines in the roller near $x = 42$. Dashed lines start from lower cup, solid lines from upper cup. *(a)* Perspective view, *(b)* top view.

only about 30° from the vertical. The lines emanating from the lower cup (for example) go up and forward of the upper cup so that the legs produce counter-rotating vortices just below the upper cup. Thus, vortex lines from each cup produces a strain field to enhance the other.

3.2 Passive scalar mixing

For the results discussed in this section, a passive scalar profile is specified at the inflow that is zero on the low-speed side, one on the high-speed side and has the same tanh profile as U_0 in the shear layer. It is often observed that a 2-D spatially-developing mixing layer will entrain more high-speed fluid than low-speed. The process by which this happens is shown by the passive scalar contours in Fig. 6, where $Re = 500$ and $Sc = 0.8$. When two vortices pair, they initially form an oblong structure.

As this structure turns end over end, it efficiently "engulfs" a large amount of pure fluid from both streams in the form of "tongues". We note that the low-speed tongue is narrower than the high-speed one because the proximity of an unpaired roller just upstream creates a blockage effect not present on the downstream side of the paired structure.

Furthermore, the existence of a stagnation point (in the frame moving with the vortices) between the vortices implies that the velocities associated with the tongues should be similar. Dimotakis (1986) used these arguments along with experimental data to estimate the ratio of the amount of high-speed to low-speed fluid entrained in the layer as $E = 1 + 3.9 d\delta_\omega/dx$. While it is very difficult to measure this quantity directly, the simulations show no inconsistency with it (for

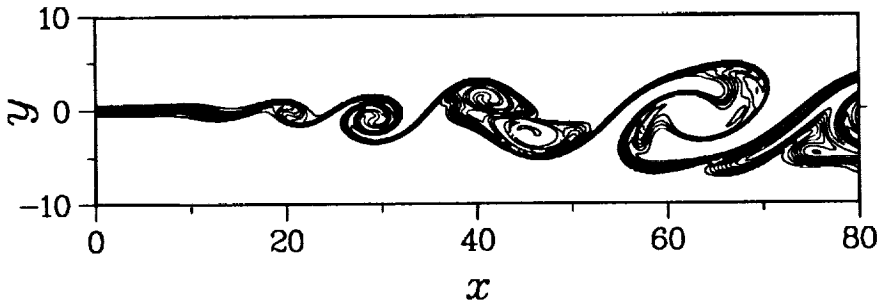

FIGURE 6. Contours of passive scalar ϕ for a 2-D mixing layer, $Re = 500$, $r = 0.2$, $Sc = 0.8$. Contour interval is 0.1.

the results reported here, $d\delta_\omega/dx \simeq 0.087$). Passive scalar contours at $Re = 200$ show similar features, although the tongues are not as distinct because of the increased diffusion.

For the 3-D case, we plot contours of the passive scalar in three $y-z$ cuts through three different braid regions in Fig. 7. This sequence shows the effect of the development of the ribs on the scalar field. In the terminology of Lin & Corcos (1984), the ribs start off in a "noncollapsed" state and only produce a mild bending of the scalar contours. After they have strengthened farther downstream, the ribs "collapse" and produce mushroom-shaped structures.

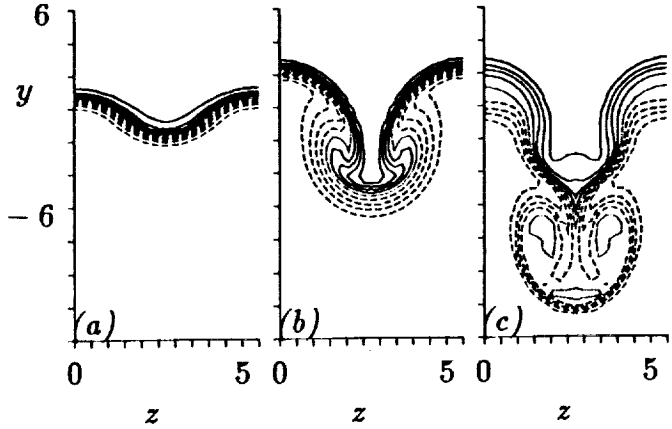

FIGURE 7. Contours of passive scalar in y-z cuts at *(a)* $x = 28$, *(b)* $x = 48$, and *(c)* $x = 63$. Contour interval is 0.1. Solid lines, $0.6 \leq \phi \leq 0.9$; dots, $\phi = 0.5$; dashes, $0.1 \leq \phi \leq 0.4$.

Analogous features are seen in the experiments of Bernal (1981). We see that there are two different kinds of mushroom structures: one falling and the other rising (which requires a periodic extension of the plots to see fully). Due to the

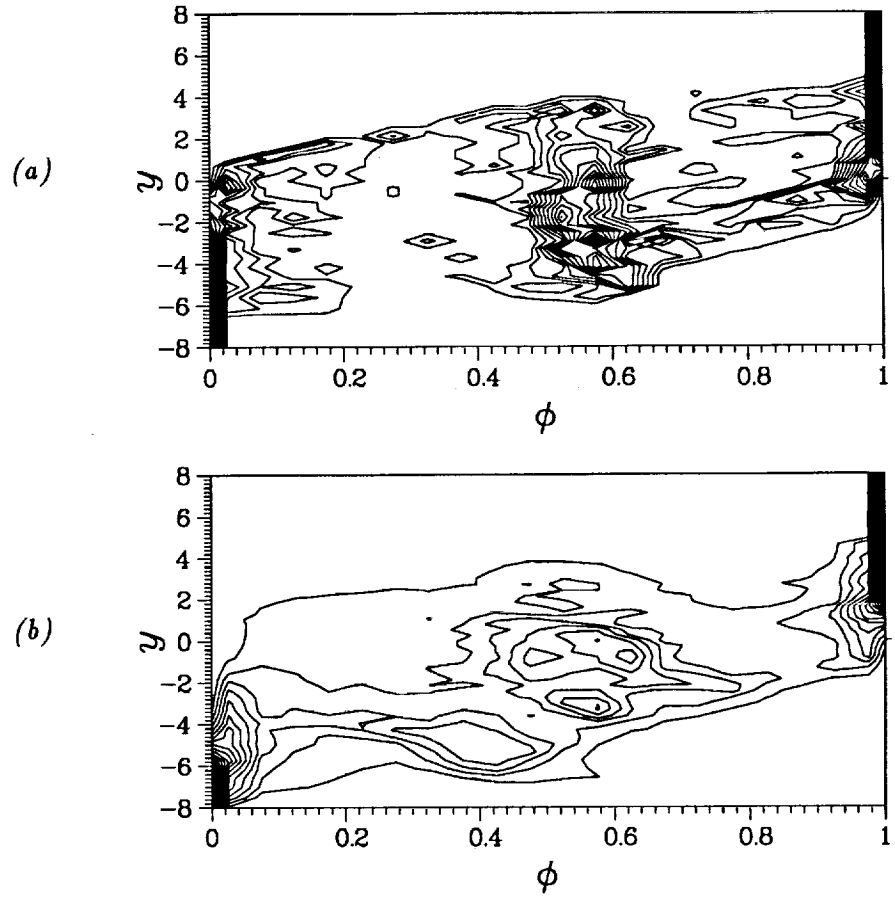

FIGURE 8. Contours of the probability density function for the passive scalar at $x = 57$. Contour difference is 0.02. *(a)* 2-D case, *(b)* 3-D case.

asymmetry of the layer, the pair of ribs associated with the latter tend to be closer together than the other pair.

This, together with the low Reynolds number of the flow, tends to "cut-off" high-speed fluid from penetrating into the core of the descending mushroom. At higher Reynolds numbers, the ribs do not interact diffusively. From the last two plots, it is clear that the ribs cause the layer to have more surface area on the low-speed side than the high-speed side. The last plot shows more low-speed fluid being entrained into the ribs and that the average value of the scalar in the core of the ribs is well below 0.5.

Statistics of the passive scalar (also called the "conserved" scalar) can be used to calculate fast-chemistry reactions. Following the analysis of Mungal & Dimotakis (1984), we assume a simple reaction $A + B \rightarrow 2P$ where the diffusivities of both reactants and the product are all equal and the reaction is very fast

compared to hydrodynamic or diffusive time scales. The equivalence ratio is defined as $\eta = c_{02}/c_{01}$, where c_{02} and c_{01} are the reactant concentrations in the low-speed and high-speed streams, respectively. The concentrations of the two reactants and the product are all related to the conserved scalar, ϕ. For the above inflow conditions, stoichiometry occurs when the conserved scalar has the value $\phi_s = \eta/(1+\eta)$. This value is called the stoichiometric mixture fraction and is also the point where the product concentration reaches a maximum. Given a probability distribution function (pdf) $p(x, y, \phi)$ of the conserved scalar, Mungal & Dimotakis (1984) showed how several quantities of interest (such as the product, product thickness, and mixture fraction derived from a "flip" experiment) can be calculated. (The pdf gives the probability that the value of the conserved scalar at (x, y) is ϕ, averaged over z and time.)

Shown in Fig. 8 are contours of pdf's for the 2-D and 3-D cases at $x = 57$. Several features are evident. Pure fluid with probability one is seen at the top-right and bottom-left of both plots. Homogeneously-mixed fluid is shown in the middle where the pdf's reach maxima between 0.5 and 0.6. In the temporal case the maxima must occur at 0.5 by symmetry. The asymmetry here is due to the 2-D "engulfment" discussed above. These maxima are nearly independent of y, as in the model of Broadwell & Breidenthal (1982). Between the homogeneous fluid in the middle and the pure fluid are "wings" in the pdfs. These are due to the strained flame sheets between the two pure fluids or between one pure fluid and the homogeneous fluid. The main difference between the 2-D and 3-D pdf's is a second maximum in the latter near $\phi = 0.4$ and for $y < 0$. This is related to the entrainment of low-speed fluid by the ribs, and (as discussed in connection with Fig. 7) is undoubtably a low Reynolds number effect.

In Fig. 9 product thickness (δ_P) normalized by the 1% visual thickness (δ_1) is plotted for the two cases. The downturn for large x for the 2-D case is due to the faster growth of the visual thickness there, while in the 3-D case the structures continue to mix the two fluids as fast as the layer grows, creating a plateau. The average mixture fraction is plotted in Fig. 10. In the laminar region (small x) the layer diffuses into the low-speed side faster than the high-speed side, lowering $\bar{\phi}$ below 0.5. At higher Reynolds numbers this quantity would be much closer to 0.5 (the difference between the two cases in this region is probably due to the thinness of the layer there and thus poor statistics). Farther downstream, the 2-D case achieves a value in the vicinity of that predicted by the Broadwell-Breidenthal model (about 0.535), while in the 3-D case $\bar{\phi}$ falls below 0.5. The latter effect is directly associated with the ribs and the second maximum in the pdf. At higher Reynolds numbers we expect that the ribs would mix fluid more symmetrically and that the second maximum would be close to 0.5. This was confirmed by a recent simulation at $Re = 400$. In this case $\bar{\phi}$ is between 0.5 and the 2-D case.

The product thickness as a function of the stoichiometric mixture fraction at

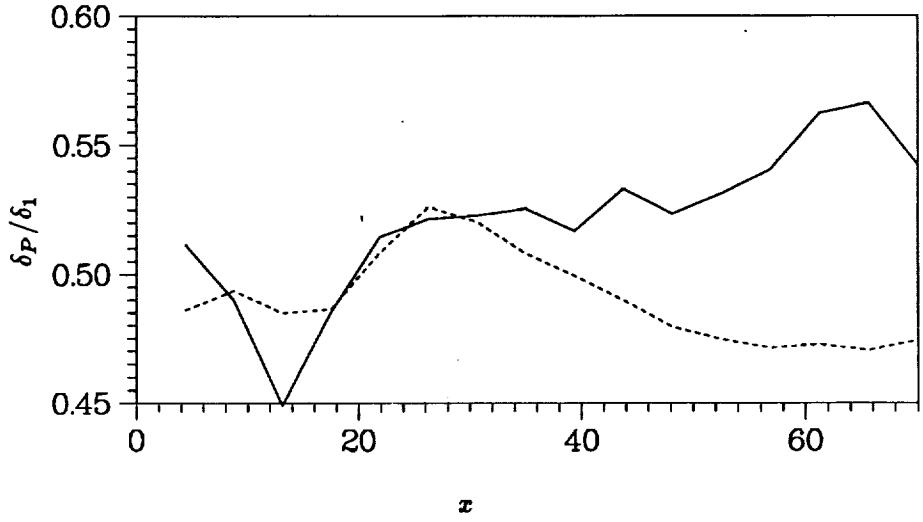

FIGURE 9. Product thickness normalized by visual thickness. Solid line, 2-D; dashed line, 3-D.

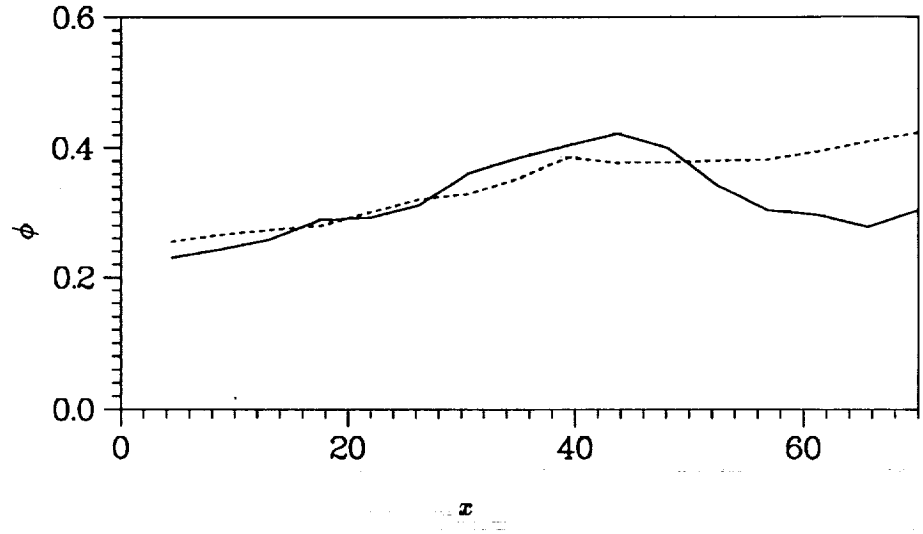

FIGURE 10. Mixture fraction. Solid line, 2-D; dashed line, 3-D.

$x = 57$ is compared to the experimental results (at $r = 0.38$) of Mungal & Dimotakis (1984) in Fig. 11. The 2-D results are just slightly below the experimental measurements for all values of ϕ_s, while the 3-D results are above. For small ϕ_s (low-speed reactant lean), excessive product is created in the latter case due to the effect of the ribs. It is not clear to what extent the close comparison in the

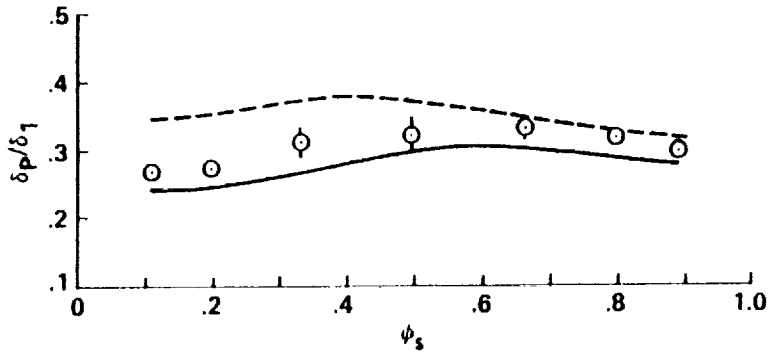

FIGURE 11. Product thickness/visual thickness vs. stoichiometric mixture fraction. Solid line, 2-D; dashed line, 3-D; symbols, experimental data from Mungal & Dimotakis (1984).

2-D case is fortuituous; the extra diffusion from the low Reynolds number here appears to balance the small-scale motion and mixing in the turbulent experiments. The $Re = 400$ product thickness (not shown) is closer to the experiments than the lower Re results, especially for small ϕ_s.

4. Wakes

In this section some results from simulations of spatially-developing wakes will be discussed. We will concentrate on the effects of 3-D perturbations on a plane Gaussian wake at a moderate Reynolds number. Very few 3-D simulations of wakes have been performed in the past. Riley & Metcalfe (1980) performed a direct numerical simulation of the temporally-developing turbulent wake of an axisymmetric body using experimental data for the initial conditions. Although the mesh was coarse, low-order statistics compared well with the experiments. Meiburg & Lasheras (1988) reported results from wake experiments with different types of spanwise forcing and computed the flow using inviscid vortex dynamics calculations. It is difficult to use the latter to study small-scale details of free-shear flows, but they were able to reproduce the large-scale features of the experiments. More recently, Chen *et al.* (1989) performed well-resolved simulations of a compressible plane wake. Their main goal was to determine the effect of Mach number on the development of the wake, but they also described the development of 3-D structures which should be similar to the incompressible case.

In this work we present results for a relatively simple case where two different kinds of perturbations are added to a Gaussian mean inflow profile. The first is a two-dimensional (2-D) time-periodic forcing where the profiles for u and v are the eigenfunctions of the corresponding Rayleigh equations. Any frequency near the most amplified one produces the classical Kármán vortex street. The second kind of perturbation is a spanwise-periodic array of counter-rotating streamwise

vortices. These are assumed to be steady as they might be in a wind tunnel with small nonuniformities in the last screen. As in the mixing layer and other shear flows, the streamwise vortices (*ribs*) are amplified by the strain field of the 2-D spanwise vortices (*rollers*). When the ribs become sufficiently strong, they distort the rollers through advection and strain effects. These effects will be contrasted with a 2-D simulation *sans* ribs. In addition, a passive scalar with a Gaussian profile is introduced at the inflow. It is often assumed in the experimental literature that smoke or heat introduced in the wake will follow the vorticity. The degree to which this is true will be tested in both the 2-D and 3-D simulations.

The Reynolds number is $Re = U_0\delta/\nu = 400$, where δ is the half-width of the layer at the inflow. The inflow profile is defined by $\bar{U}(y) = 1 - \lambda \exp(-.69315y^2)$, where $\lambda = 0.692$ is the velocity defect (corresponding to the experiments of Sato & Kuriki 1961). The Schmidt number is $Sc = 1$. The 2-D forcing is applied at a frequency of 0.5 and an amplitude of 0.06. The maximum growth rate occurs at a frequency of 0.614, but the lower value was used to compensate for the viscous thickening of the wake downstream. For the 3-D simulation steady profiles for v and the spanwise velocity w are added at the inflow to produce streamwise vorticity with an amplitude of 0.1 and a spanwise wavelength of 6. As with the mixing layer calculations, each velocity component is required to satisfy a convective outflow boundary condition, except here we use $c = 0.9$. At infinity, all perturbations are set to zero. The length of the computational domain is $L_x = 70$ and the vertical mapping parameter is $\beta = 6$. The mesh is $384 \times 128 \times 24$ (grid points in x, Fourier modes in y and z). Most of the aliasing errors were eliminated by using a collocation grid in the spectral directions of 160×32.

Shown in Fig. 12 are contours of spanwise vorticity (ω_3) for the base-line 2-D case. The formation of a vortex street consisting of alternating-sign vortices (rollers) is clearly seen. A consequence of conservation of angular momentum is the formation of "spiral arms" around each vortex; not all the vorticity can roll up into the vortex cores. Farther downstream these arms diffuse away, leaving nearly circular vortex cores. Note also the near-symmetry between the upper and lower vortices.

Contours of ω_3 for the 3-D case are plotted in Fig. 13 in the two x-y symmetry planes (where $\omega_1 = 0$). These planes are each between a pair of counter-rotating streamwise vortices. Qualitatively the same structures appear as in the 2-D case, but there are important quantitative differences. Considering the row of vortices along the top (negative ω_3), we see that the flow starts off very much like the 2-D flow, but by $x = 20$ significant distortion in z appears. At $z = 0$ the peak vorticity is on the inside edge of the rollers, while at $z = 3$ the peak vorticity is on the outside edge. This cannot be an advection effect since by $x \simeq 40$ the peak value of ω_3 reaches -0.8 (at the inflow it is about -0.5). Thus the variation in z must be due to vortex stretching effects. This enhancement

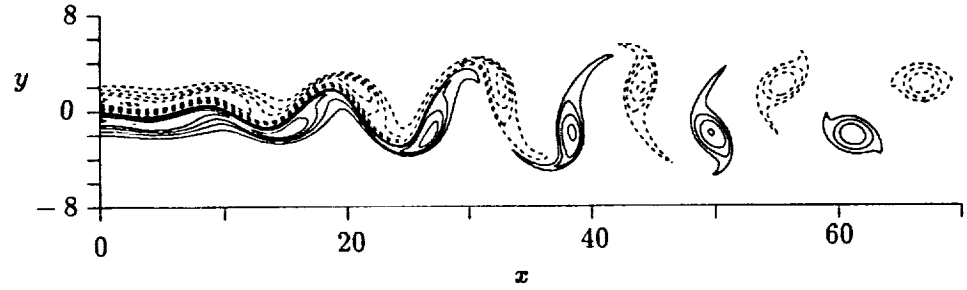

FIGURE 12. Contours of spanwise vorticity for the 2-D case. Contour interval is 0.1. Dashed lines denote negative levels, solid lines denote positive levels.

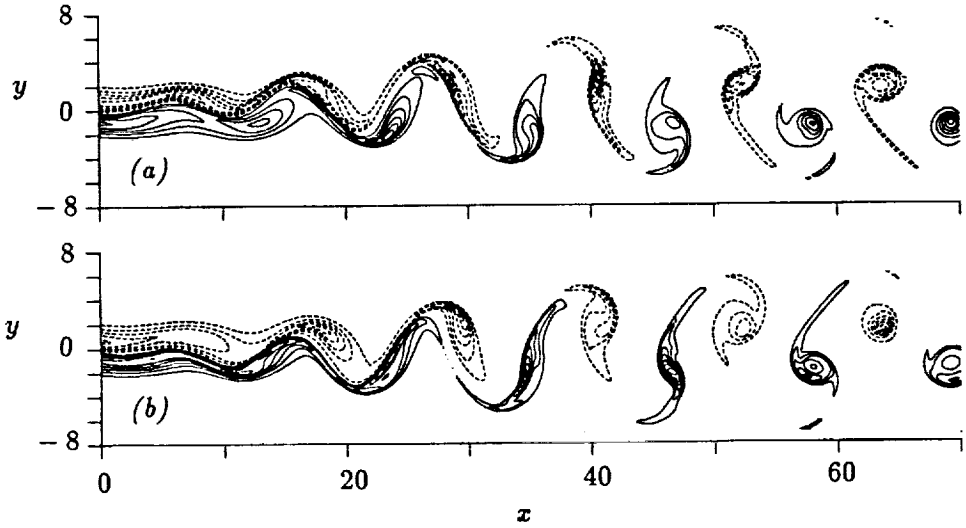

FIGURE 13. Contours of spanwise vorticity for the 3-D case at *(a)* $z = 0$ and *(b)* $z = 3$. Contour interval is 0.1.

of vorticity occurs at all z locations but is most pronounced at $z = 0$. Beyond $x \simeq 35$, a different process from the one responsible for the above enhancement becomes dominant. At $z = 3$, the maximum vorticity amplitude drops suddenly by $x = 40$, then rises to nearly its previous level by $x = 60$. At $z = 0$, a small, intense and nearly symmetric elliptic roller forms by $x = 40$. This is followed by a suppression of vorticity on one side of the center of the roller so that a nearly irrotational region is imbedded inside the roller by $x = 60$. Because of the symmetry in the inflow conditions, all of the above comments for the upper row of vortices at $z = 0$ and $z = 3$ apply to the mirror image in y of the lower row at $z = 3$ and $z = 0$, respectively.

Some of the mechanisms for the enhancement and suppression of ω_3 in certain regions are evident from an examination of the streamwise (ω_1) and vertical (ω_2)

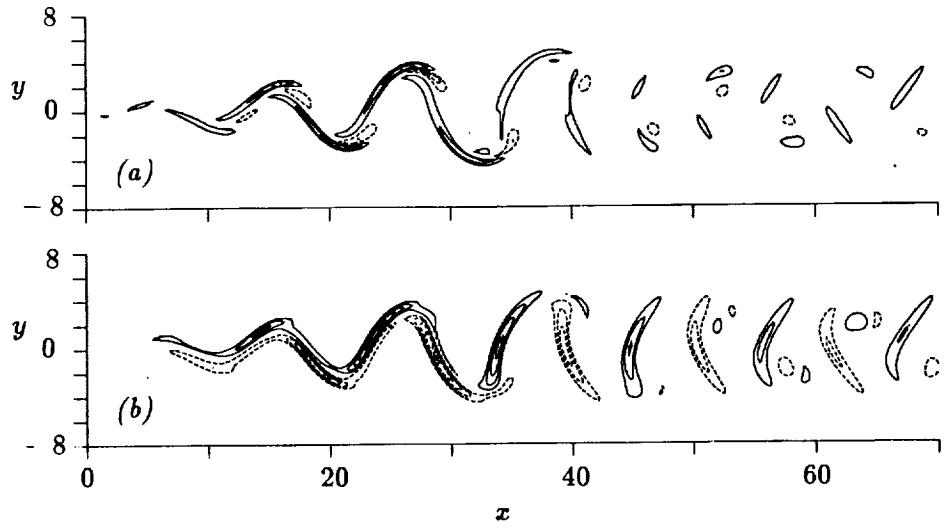

FIGURE 14. Contours of *(a)* streamwise vorticity and *(b)* vertical (cross-stream) vorticity corresponding to Fig. 2 at $z = 1.5$ Contour interval is 0.1.

components of vorticity, shown in Fig. 14 at $z = 1.5$. Both components develop very quickly up to about $x = 25$, then decay slowly thereafter. At $z = 1.5$, ω_1 is positive at the inflow and leads directly to the formation of ribs with the same sign. These ribs can be divided into two sets; those with positive ω_2 and those with negative. For $x < 20$ the former are clearly associated with the upper rollers and the latter with the lower rollers. During the growth phase of the ribs, they connect spanwise vortices of like sign (see Chen *et al.* 1989).

As in mixing layers, the ribs are intensified by the 2-D strain field of the main rollers, but again this mechanism cannot increase the circulation around a rib. We find that the same mechanism as in the mixing layer is responsible for converting ω_3 into ω_1. However, the process is less efficient as the layer develops since the 2-D strain field between rollers is weakened by the presence of both signs of ω_3 in alternate rollers. In Fig. 13 note that the main effect of the 3-D distortion of ω_3 for $x < 35$ is the enhancement of vorticity along one side of a roller and suppression along the opposite side (both due to the vortex stretching terms produced by the ribs), thus shifting the peak vorticity towards one side. In the z-plane on the other side of a particular streamwise vortex, the peak vorticity is shifted to the other side of the same spanwise roller. Due to this distortion, the vortex lines in the rollers will have an x (as well as a y) component. Farther downstream, one end of each rib becomes increasingly associated with a roller on the opposite side of the wake. Also, they tend to stand nearly vertical, in contrast to a typical rib angle of 45° for $x < 25$ and for mixing layers. This transition coincides with the end of the growth of the ribs and the beginning of their decay.

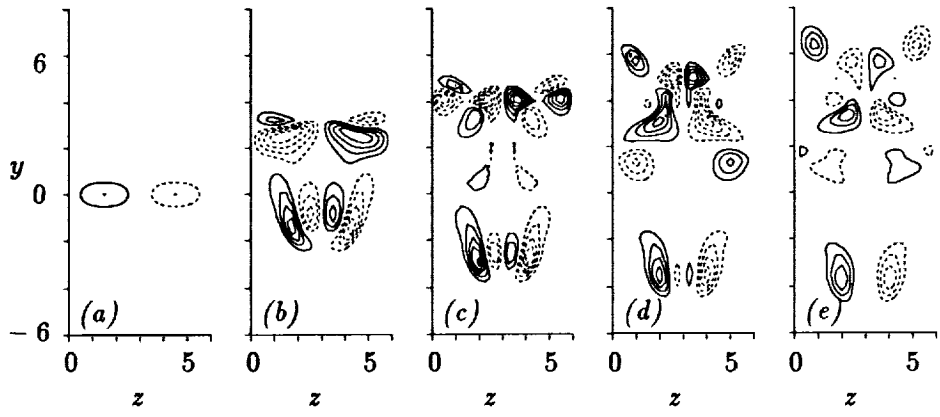

FIGURE 15. Contours of streamwise vorticity in z-y planes at *(a)* $x = 0$, *(b)* $x = 29$, *(c)* $x = 40.5$, *(d)* $x = 52$, and *(e)* $x = 63.5$. Contour interval is 0.05.

Shown in Fig. 15 are spanwise (z-y) cuts of ω_1 at five x locations. The first plot shows the inflow forcing, and the others show cuts through the upper rollers. Note that in either half of the domain (*e.g.*, $0 \leq z \leq 3$), the magnitudes of the positive and negative streamwise vorticity are about the same even though there is only one sign at the inflow. For $x < 40$ the ribs (the lowest and highest pairs of vortices in Figs. 15(*b-e*)) have the characteristic shape of "non-collapsed" vortices – elliptical and tilted from the horizontal (see Lin & Corcos 1984). This is a relatively stable state. Farther downstream they begin to show signs of collapse to small, round and more intense vortices (however, a higher Reynolds number is needed to see this clearly). Comparing Figs. 14(*a*) and 14(*b*) at $x = 29$ to Fig. 15(*b*) we note that the regions of enhanced ω_3 are located in the middle of positive strain regions created by ω_1-quadrapoles. Similarly, regions of ω_3 suppression are also located in the middle of quadrapoles, but where the strain is negative. Further, half of the ω_1 vorticity involved is associated with ribs while the other half is due to the distortion of the rollers. By $x = 40$ (Fig. 15(*c*)), several changes in the structure of the flow have occurred. The ribs and rollers have moved away from one another so that the former are not a part of one of the above-mentioned quadrapoles and do not appear to significantly contribute to the strain in the vicinity of the rollers. Instead, new ω_1 is created within the rollers, which are then strained in a different manner than before. One can follow the evolution of ω_1 and see that the quadrapoles it forms are responsible for the changing distribution and intensity of ω_3.

A perspective view (Fig. 16) of the rollers located between $x = 40$ and $x = 60$ shows part of the evolution of ω_3. In Fig. 17 two perspective views of vortex lines initiated in the ribs located at $x = 28$ and $x = 34$ show the formation of vortex loops. Since both signs of ω_3 are needed to close the loops, the ribs must connect opposite-signed vortices. Farther upstream, vortex lines continue all the way across the span and are not closed, suggesting the ribs connect vortices

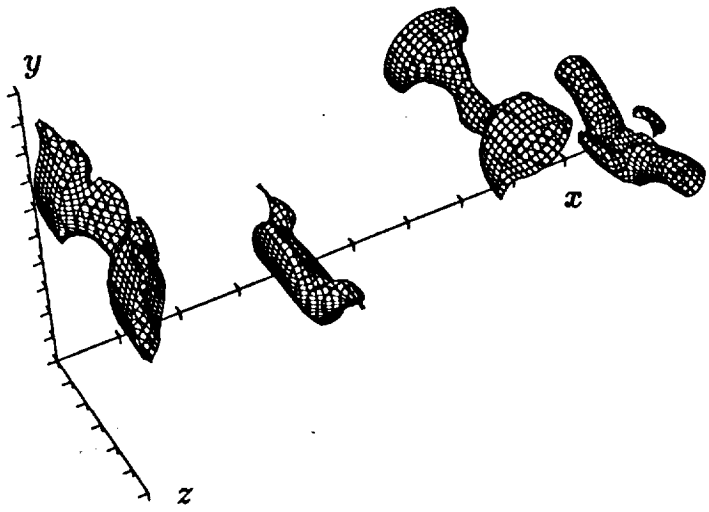

FIGURE 16. Perspective view of $|\omega_3|$ corresponding to figure 14 in the range $40 \leq x \leq 60$. Contour level is 0.35.

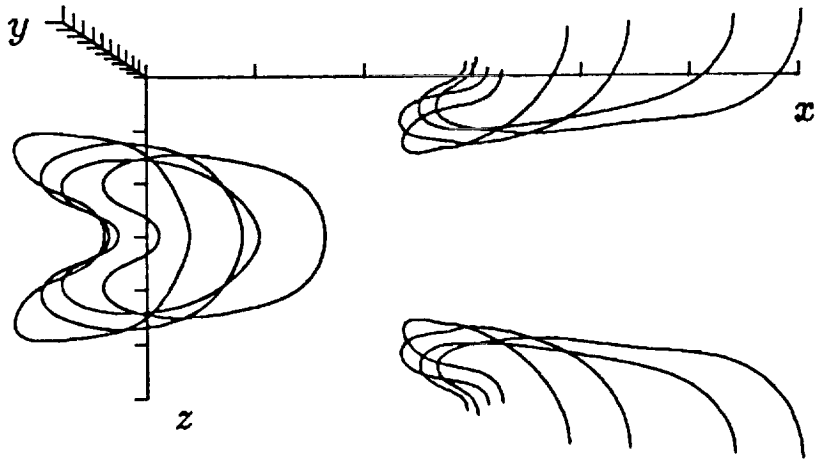

FIGURE 17. Top view of vortex lines initiated in the ribs at $x = 28$ and $x = 34$. x axis extent is $28 \leq x \leq 40$.

of like sign. We note also that the vortex loops originally associated with the bottom half of the wake (one of which is shown at the left in the plots of Fig. 17) are all lined up and centered at $z = 3$ while the upper ones are centered at $z = 0$

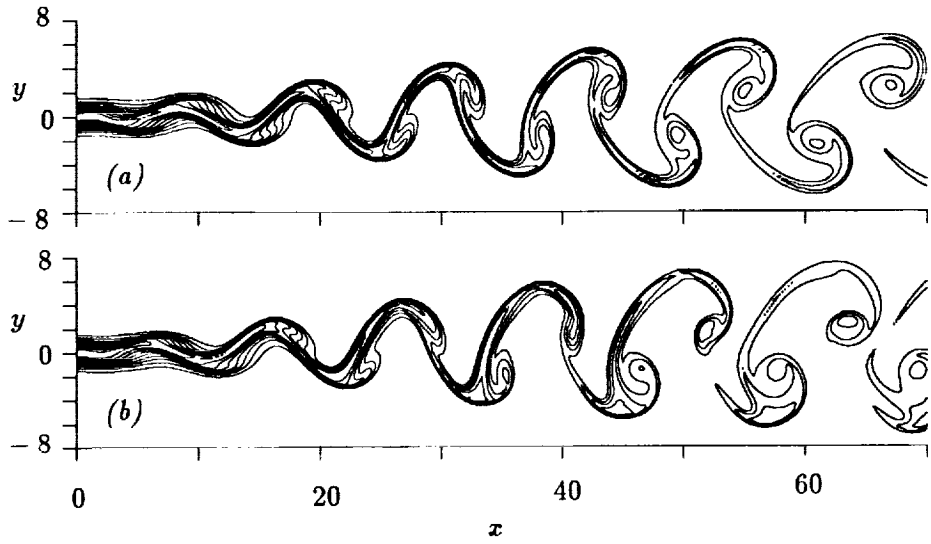

FIGURE 18. Passive scalar contours for the *(a)* 2-D case, and *(b)* 3-D case at $z = 0$. Contour interval is 0.1.

(or, equivalently, $z = 6$). Introducing time-periodicity into ω_1 at the inflow will create other patterns of loops.

Experimentally, one often introduces smoke or heat as a passive scalar into the wake in order to trace the vorticity. Of course, this is only an approximation unless the flow is 2-D, the Schmidt number is unity, and the inflow passive scalar profile is identical to the vorticity profile. We tested this approximation here for both the 2-D and 3-D cases, using a Gaussian profile (with half-width 0.833) to model the injection of a passive scalar. Shown in Fig. 18 are the results for the 2-D case and for the 3-D case at $z = 0$. Comparing Figs. 12 and 18(a) we see significant differences. However, for $x > 45$, the maxima of the passive scalar lie very close to the extrema in vorticity, but with no consistent relative offset. For the 3-D case, a comparison of Figs. 14(a) and 18(b) shows larger differences. In particular, the upper and lower sides are less similar in the passive scalar than in the vorticity. Also, while there is a local maxima in the passive scalar near each roller, there are also concentrations of scalar in nearly irrotational areas as well. This may be an indication of history effects; the passive scalar may concentrate in regions of high vorticity, and then be left behind as the vorticity moves elsewhere through vortex-stretching effects.

REFERENCES

BERNAL, L. P. 1981 thesis, California Institute of Technology, Pasadena, CA.

BROADWELL, J. E. & BREIDENTHAL, R. E. 1982 *J. Fluid Mech.* **125**, 397–410.

BROWN, G. L. & ROSHKO, A. 1974 *J. Fluid Mech.* **64**, 775–816.

BUELL, J. C. 1989 submitted to *J. Comp. Phys.*

BUELL, J. C. & HUERRE, P. 1988 in *Proceedings of the 1988 Summer Program*, Center for Turbulence Research, p. 19.

CHEN, J. H., CANTWELL, B. J. & MANSOUR, N. N. 1989 AIAA Paper No. 89-0285, Reno.

COMTE, P., LESIEUR, M., LAROCHE, H. & NORMAND, X. 1987 in *Turbulent Shear Flows VI*, Springer-Verlag.

DAVIS, R. W. & MOORE, E. F. 1985 *Phys. Fluids* **28**, 1626–1635.

DIMOTAKIS, P. E. 1986 *AIAA J.* **24**, 1791–1796.

HO, C.-M. & HUERRE, P. 1984 *Ann. Rev. Fluid Mech.* **16**, 365–424.

HUANG, L. S. & HO, C.-M. 1989 submitted to *J. Fluid Mech.*

KONRAD, J. H. 1976 thesis, California Institute of Technology, Pasadena, CA.

KOOCHESFAHANI, M. M. & DIMOTAKIS, P. E. 1986 *J. Fluid Mech.* **170**, 83–112.

LASHERAS, J. C., CHO, J. S. & MAXWORTHY, T. 1986 *J. Fluid Mech.* **172**, 231–258.

LELE, S. K. 1989 submitted to *J. Comp. Phys.*

LIN, S. J. & CORCOS, G. M. 1984 *J. Fluid Mech.* **141**, 139–178.

LOWERY, P. S. 1986 thesis, Stanford University, Stanford, CA.

MEIBURG, E. & LASHERAS, J. C. 1988 *J. Fluid Mech.* **190**, 1–37.

MUNGAL, M. G. & DIMOTAKIS, P. E. 1984 *J. Fluid Mech.* **148**, 349–382.

PIERREHUMBERT, R. T. & WIDNALL, S. E. 1982 *J. Fluid Mech.* **114**, 59–82.

ROGERS, M. M. & MOSER, R. D. 1989 Proceedings of the Seventh Symposium on Turbulent Shear Flows, Stanford, CA.

RILEY, J. J. & METCALFE, R. W. 1980 Turbulent Shear Flows 2, 78–97.

SATO, H. & KURIKI, K. 1961 *J. Fluid Mech.* **11**, , 321–352.

WRAY, A. A. 1988 submitted to *J. Comp. Phys.*

Center for Turbulence Research
Annual Research Briefs - 1989

A numerical method for direct simulation of turbulence in complex geometries

By P. Orlandi

1. Introduction

Direct simulation has often been applied to describe flow fields within regions described by simple coordinate systems. Spectral methods have been used because of their higher accuracy compared to finite differences (Moser et al. 1983). For complex geometries, implementation of spectral methods is not generally efficient; modifications of these methods, such as spectral element methods (Korczac and Patera), can be applied but the accuracy is greatly reduced. In this paper we describe a finite difference method for incompressible flows with geometrical complexities in two dimensions and periodic conditions in the third direction.

In contrast to Cartesian coordinates, the choice of the best system of velocity components when curvilinear coordinates are used is not unique. We have shown that an accurate and simple formulation can be obtained when the Navier-Stokes equations are written in terms of fluxes. As with Cartesian coordinates (Harlow and Welch), the fluxes are staggered and pressure is located at the cell center. This scheme is compact and the solenoidal field is easily obtained.

We have derived the equations for the fluxes directly from the equations for the Cartesian components in the"new" coordinate system. This is done in the discrete space by multiplying the equations by the metric quantities at the same cell positions where the fluxes are defined. This procedure requires definitions of the metric quantities at the center of the cell faces, at the center of the cell, and at the corners.

A fractional step method has been used for the time advancement. When generalized coordinate are used, the method requires modifications of the method used in Cartesian coordinates (Kim and Moin, 1985). The major difference resides in the "pressure" calculation; while in Cartesian coordinates "pressure" is obtained by Fourier methods, in general curvilinear coordinates and for a large number of grid points the pressure solution requires iterative schemes. The usual iterative schemes have convergence rates dependent on the number of mesh points. A modified multigrid method appropriate for general curvilinear coordinates (Orlandi and Esposito, 1989) has been developed. At present it has been demonstrated that the method has very good convergence properties for 2-D but requires improved relaxation scheme for 3-D.

The ultimate goal of this work is to study the flow inside a channel with riblets on one of the two walls. The method has been tested for 2-D flows in

the presence of bodies with a geometrical singularity and for 3-D flows inside domains described by Cartesian coordinates. The results have been compared with previous numerical simulations and with experimental results.

The cases considered are:

a) the growth of Orr-Sommerfield waves in plane Poiseuille flow,

b) the flow over a backward-facing step,

c) the flow past a wedge,

d) the flow inside a narrow channel.

Finally the case of a channel with two large riblets on a wall has been simulated. In this case a limited number of grid points is sufficient, and in spite of the slow convergence for the pressure solver, one is able to obtain solutions with a reasonable CPU time. At present solutions with very fine grids in all three directions can not been obtained, due to the lack of a fast "pressure" solver for general curvilinear coordinates. Data analysis aimed at finding reasons for drag reduction will be the subject of a future study.

2. Physical model

Different formulations can be obtained of the Navier-Stokes equations in a system of generalized curvilinear coordinates x^i (defined by $y^j = y^j(x^i)$, with y^j the Cartesian coordinates) depending whether Cartesian covariant and contravariant velocity components are employed. In this word flux variables are used. The relation among the Cartesian components v^j and the fluxes q^i is

$$v^j = q^i c_i^j / g \tag{1}$$

where the metric quantities c_i^j are

$$c_i^j = \frac{\partial y^j}{\partial x^i} \tag{2}$$

The other metric quantities necessary for writing the Navier-Stokes equations in generalized coordinates are the a^{ji} (the inverse of $a_{ji} = c_j^l c_i^l$) and the Jacobian of the coordinate transformation $g = \sqrt{a}$ with $(a = \| a_{ij} \|)$.

The continuity equation in terms of fluxes is

$$div(\vec{v}) = \frac{1}{g} \frac{\partial q^i}{\partial x^i} = 0 \tag{3}$$

a form very similar to the expression in Cartesian coordinates. With Cartesian coordinates, numerical methods based on velocity staggering have a very compact form for the discrete *div* and *grad* operators, and well-structured matrices readily yield solenoidal velocity fields within round-off errors. The extension of velocity staggering to curvilinear coordinates is highly desirable.

The momentum equations in the x^j coordinate system are

$$\frac{\partial v^i}{\partial t} + (v^i u^j)_{/j} = -\frac{\partial p}{\partial y^i} + \frac{1}{Re}(v^i)_{/ij} \tag{4}$$

First- and second-covariant derivatives expressed in conservative form are

$$(v^i u^j)_{/j} = \frac{1}{g}\frac{\partial v^i q^j}{\partial x^j} \tag{5}$$

$$(v^i)_{/ij} = \frac{1}{g}\frac{\partial}{\partial x^i}\alpha^{ij}\frac{\partial v^i}{\partial x^j} \tag{6}$$

where $\alpha^{ij} = a^{ij}g$. The pressure gradient is

$$\frac{\partial p}{\partial y^i} = (c^i_j)^{-1}\frac{\partial p}{\partial x^j} \tag{7}$$

Flowfields periodic in one direction and with geometrical complexities in the other directions can be solved by introducing the coordinate transformation $y^j = y^j(x^i), j, i = 1, 2$, and $y^3 \equiv x^3$. This transformation reduces the number of terms in Eqs.(4-6) because $a_{i3} = 0$ for $i \neq 3$. It is worthwhile to introduce the fluxes q^1, q^2 in the plane of geometrical complexity and to use the Cartesian component $q^3 \equiv v^3$ in the third direction. The fluxes q^j are related to the Cartesian components by $q^1 = v^1 c^2_2 - v^2 c^2_2$ and $q^2 = v^2 c^1_1 - v^1 c^2_1$. The equation for q^j is derived in the discrete space which requires the definition of the metric quantities at several points of the cell. The equations for the fluxes have a large number of terms which can be gathered in five groups: nonlinear term, H^l, pressure term, P^l, and three diffusive terms, D^l, $D^{l,r}(r \neq l)$, and $D^{l,r,i,j}$. Let

$$Q^{kl}_m = q^k c^l_m / g \quad , \quad \gamma^n_l = (c^l_n)^{-1} g \tag{8}$$

Each term in the q^l equation can be expressed as

$$H^l = \frac{1}{g}(\gamma^l_n \frac{\partial q^j Q^{mn}_m}{\partial x^j}) + \frac{\partial q^l q^3}{\partial x^3} \quad ; \quad j, m, n = 1, 2 \tag{9}$$

$$P^l = \alpha^{lj}\frac{\partial p}{\partial x^j} \quad ; \quad j = 1, 2 \tag{10}$$

$$D^l = \frac{1}{g}(\gamma^l_n \frac{\partial}{\partial x^j}\alpha^{jj}\frac{\partial Q^{ln}_l}{\partial x^j}) + \frac{\partial^2 q^l}{\partial x^2_3} \quad ; \quad j, n = 1, 2 \tag{11}$$

$$D^{l,r} = \frac{1}{g}(\gamma^l_n \frac{\partial}{\partial x^j}\alpha^{jj}\frac{\partial Q^{rn}_r}{\partial x^j}) \quad ; \quad j, n = 1, 2, r \neq l \tag{12}$$

$$D^{l,r,j,i} = \frac{1}{g}(\gamma^l_n \frac{\partial}{\partial x^j}\alpha^{ji}\frac{\partial Q^{rn}_r}{\partial x^i}) \quad ; \quad j \neq i = 1, 2; \quad r, n = 1, 2 \tag{13}$$

The terms in the equation for q^3 are

$$H^3 = \frac{1}{g}\left(\frac{\partial q^j q^3}{\partial x^j}\right) + \frac{\partial q^3 q^3}{\partial x^3} \quad ; \quad j = 1,2 \tag{14}$$

$$P^3 = \frac{\partial p}{\partial x^3} \tag{15}$$

$$D^3 = \frac{1}{g}\left(\frac{\partial}{\partial x^j}\alpha^{jj}\frac{\partial q^3}{\partial x^j}\right) + \frac{\partial^2 q^3}{\partial x_3^2} \quad ; \quad j = 1,2 \tag{16}$$

$$D^{3,3,i,j} = \frac{1}{g}\left(\frac{\partial}{\partial x^j}\alpha^{ji}\frac{\partial q^3}{\partial x^i}\right) \quad ; \quad j \neq i = 1,2 \tag{17}$$

The general form for the momentum equations is

$$\frac{\partial q^i}{\partial t} - \frac{1}{Re}D^i = -P^i - H^i + \frac{1}{Re}(\mid \epsilon_{3ir} \mid D^{i,r} + \mid \epsilon_{3kj} \mid D^{i,r,k,j}) \quad ; \quad r,k,j = 1,2 \tag{18}$$

where ϵ_{kil} denotes the usual permutation tensor. The boundary conditions for q^i are obtained from the Cartesian velocities.

The second order accurate central differencing is used for nonlinear and viscous terms. The discretized equations for the component q^i can be written as

$$\frac{\partial q^i}{\partial t} - \frac{1}{Re}D^i = -P^i - R^i \tag{19}$$

where the nonlinear term and the diffusive terms of Eqs. (12, 13, 17) have been included in R^i.

The systems of equations were solved by the fractional step method with the pressure at the previous time step introduced in evaluating the non-solenoidal velocity field $\hat{q}^i$. Accuracy of time advancement was second-order and the time step, Δt, was chosen such that $\Delta t \mid \frac{1}{g}\frac{q^1}{\Delta x^1} + \frac{q^3}{\Delta x^3} \mid_{max} < 1$.

The fractional step method requires a second step to evaluate the solenoidal field $(q^i)^{n+1}$ by

$$\frac{(q^i)^{n+1} - \hat{q}^i}{\Delta t} = -\frac{1}{2}(\Phi^i) \tag{20}$$

Φ^i is given by Eq.(10) and Eq.(15) where the scalar Φ is substituted for p.

The "pressure" is calculated from an elliptic equation obtained by substituting the fluxes $(q^i)^{n+1}$ of Eq.(20) in the continuity equation, yielding

$$\frac{1}{g}\left(\frac{\delta}{\delta x^m}\alpha^{mn}\frac{\delta\Phi}{\delta x^n}\right) + \frac{\delta^2\Phi}{\delta x_3^2} = \hat{Q} \quad ; \quad m,n = 1,2 \tag{21}$$

Equation (21) is evaluated at the center of the cell.

For incompressible flows, it is desirable that Eq.(21) be solved to be within round-off errors. Usually with iterative schemes like line SOR and point SOR

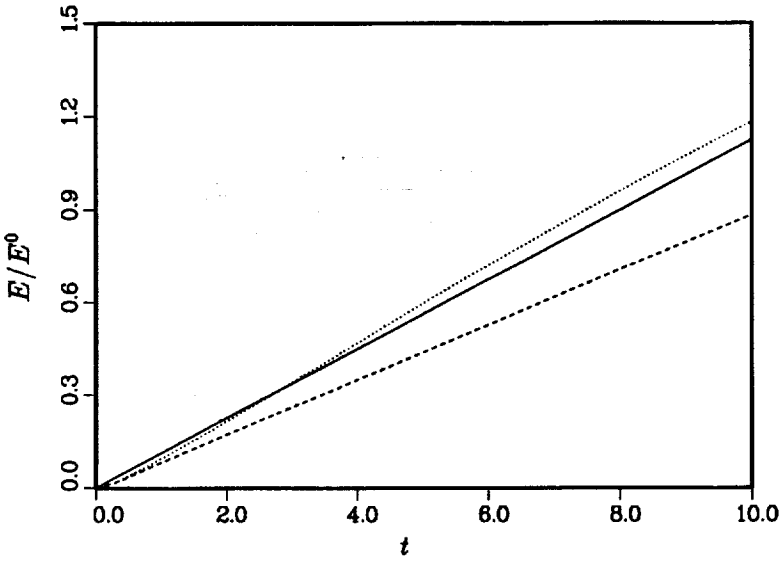

FIGURE 1. Energy growth rate: ——— linear theory; ····· centered Jacobian; — - - — averaged Jacobian.

the convergence error is not reduced to round-off levels. However, these schemes together with a multigrid algorithm are able to provide a fast convergence. In order to vectorize the code a four-color checker-board scheme with over-relaxation was used. The method and the treatment near the boundaries is described in the paper of Orlandi and Esposito (1989). From the Φ the pressure, necessary in Eq.(19), can be calculated by (see Kim and Moin, 1985)

$$p^{n+1} = p^n + \frac{1}{2}(\Phi - \frac{\Delta t}{2Re}(\frac{1}{g}\frac{\delta}{\delta x^j}\alpha^{jj}\frac{\delta\Phi}{\delta x^j} + \frac{\delta^2\Phi}{\delta x_3^2})), \qquad j = 1,2 \qquad (22)$$

The numerical algorithm requires the coordinate transformation $y^j = y^j(x^i)$. This transformation is usually given by an analytical relation; however, for some complex geometries the transformation has been obtained numerically by using the code GRIDGEN2D of J. P. Steinbrenner (1986).

3. Results and discussion

Evolution of small disturbances

A useful test for the accuracy of numerical methods is accurate prediction of the evolution of small disturbances.

The time evolution of small perturbations in the plane Poiseuille flow at $Re = 7500$, with the initial perturbation obtained from solutions to the Orr-Sommerfield eigenvalue problem, has been used by Canuto et al. (1987) and Rai and Moin (1988) to measure the accuracy of different numerical methods

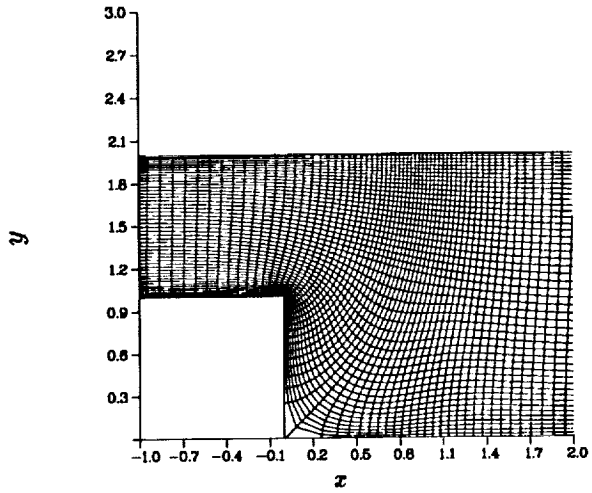

FIGURE 2. Computational grid for a backward-facing step.

with different resolutions. We have computed this case using a 98 × 48 grid. Computed energy growth is shown in Fig. 1 and shows an agreement with linear theory. To emphasize how the calculation is influenced by the calculation of metric quantities, the energy growth evaluating the Jacobian g in the diffusive terms by averaging two neighbor values is also shown (dashed line). The averaging significantly reduces the accuracy of the numerical scheme.

Flow over a backward-facing step

This flow has been considered for the geometrical singularity and because solutions are available in literature. First, the numerical method was tested using a Cartesian grid. For this case convective boundary conditions at the outflow and a parabolic profile at the inflow were prescribed. With a grid of 96 × 48 at $Re = U_c h/\nu = 600$ the present simulation predicts the reattachment location of the main separation region at $X_{1r} = 10.4$, which compares well with the values $X_{1r} = 10.5$ obtained by Kim and Moin (1985) using a finer grid in the vertical direction. In the case of cartesian coordinates the characteristic points of the separation regions reach their final values in a short time of integration.

To obtain the solution in a domain which considers also the upstream section, the domain is mapped into a Cartesian computational domain by an analytical expression based on a conformal transformation. Stretching functions resulting in a finer resolution near the walls and corners are used. In the case of a mesh 128 × 48, the grid distribution in the region of the step is given in Fig.2. The simulation in general curvilinear coordinates was performed with several meshes and different grid distributions without finding appreciable differences. Fig.3 shows the convergence of the characteristic points of the separation regions to their steady values. Convergence is achieved in a longer time than the time

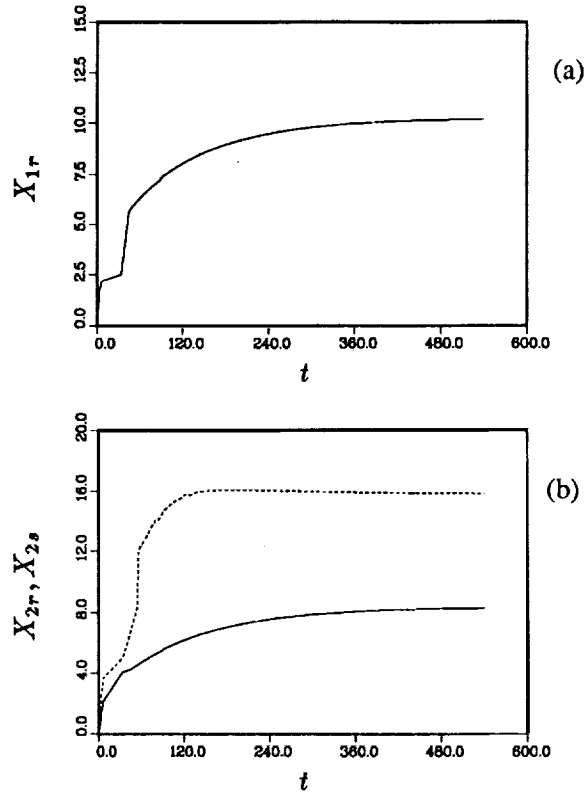

FIGURE 3. Time evolution of characteristic points of separation regions at $Re = 450$. Computations were performed using generalized coordinates. (a) Reattachment length of the primary separation bubble; (b) separation and reattachment locations of the secondary separation bubble.

necessary in Cartesian coordinates. Moreover, the final values are slightly lower.

The values obtained by general curvilinear coordinates are $X_{1r} = 10.1$, $X_{2s} = 8.2$, $X_{2r} = 15.9$, while those by Cartesian coordinates are $X_{1r} = 10.4$, $X_{2s} = 8.6$, $X_{2r} = 16.1$. Here X_{2r} and X_{2s} denote the location of separation and reattachment, respectively, of the secondary separation bubble at the upper wall.

Flow past a 2-D wedge

This case has been studied experimentally by Pullin and Perry (1980) using detailed flow visualization to describe the motion of the vortex generated at the vertex of the wedge. The flow was driven by a piston to the left of the wedge (see Fig. 4). They considered several cases varying the Re number, the velocity of the piston, and the shape of the wedge. In the present case we did the simulation only for the 60deg wedge and at two Re. This case has been considered especially because the geometry of the body is very similar to the geometry of the riblets.

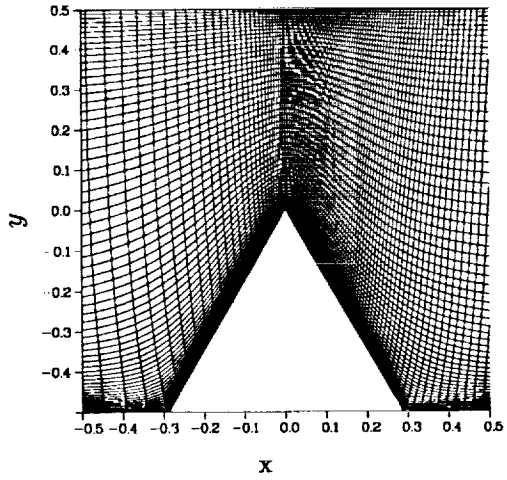

FIGURE 4. Computation grid for the wedge.

The grid has been obtained by using the GRIDGEN2D code.

In the case of a 60 deg wedge with a 128×64 mesh, the grid distribution in the wedge region is given in Fig.4. Different shapes of the velocity profile at the inlet have been used. No appreciable differences on the trajectory of the vortex were observed when prescribing a slug velocity profile or profiles with different boundary layer thickness at the inlet. At the outflow a convective boundary condition was employed.

Fig.5 shows the time evolution of the horizontal position of the center of the vortex at $Re = 1560$ and $Re = 3687$ compared with the measurements of Pullin and Perry (1980). In the present case, the center of the vortex has been obtained by evaluating the position of minimum pressure, while in the experiment the position was obtained by dye flow visualizations. At the beginning the agreement is very good, while at later times there are differences.

In the numerical simulation, the ramp-like trajectory is due to the fact that the position of the vortex center has been calculated without introducing an accurate interpolation scheme. The difference with the experimental results is in part due to the fact that dye concentrations do not perfectly coincide with vorticity concentrations. A further reason for the difference may be due to three-dimensional effects which have not been considered in the present numerical simulation.

Turbulent channel flow

Rai and Moin (1990) have shown that the finite difference schemes are capable of generating results very accurate and comparable with those obtained by pseudospectral methods. They simulated the full channel capturing several spanwise structures. Following Jimenez and Moin, in this work we have simulated the

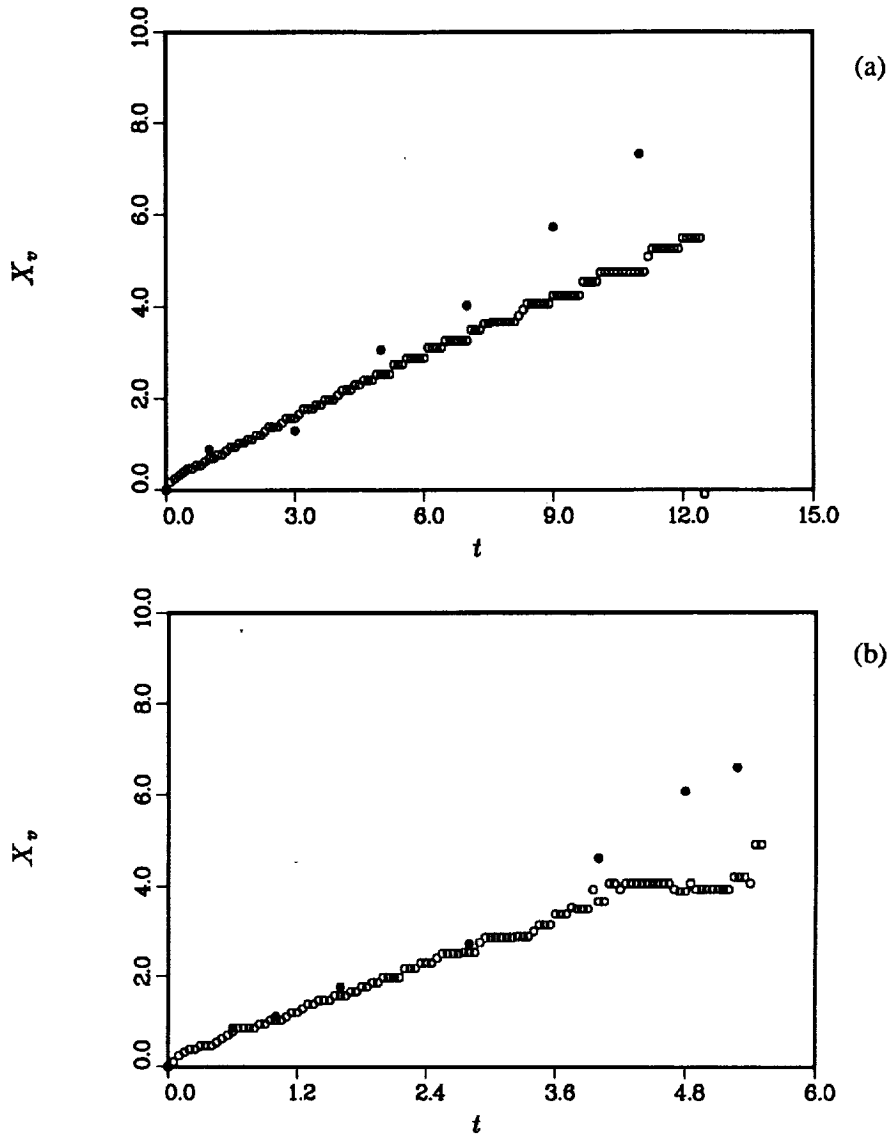

FIGURE 5. Horizontal position of the vortex center relative to the wedge-apex. a) $Re = 1560$; b)$Re = 3687$ (o numerical, • experiments).

case of a narrow channel with a spanwise dimension sufficient to capture one or two streaks. The solution obtained by this calculation is then used as initial condition for the case with riblets. In this case, a large number of grid points is necessary to represent accurately the geometrical complexity of the riblets.

The calculations were initialized with random perturbations with amplitude of up to 25% of the centerline velocity superimposed on the parabolic velocity profile. This large perturbation was chosen because the Reynolds number ($Re =$

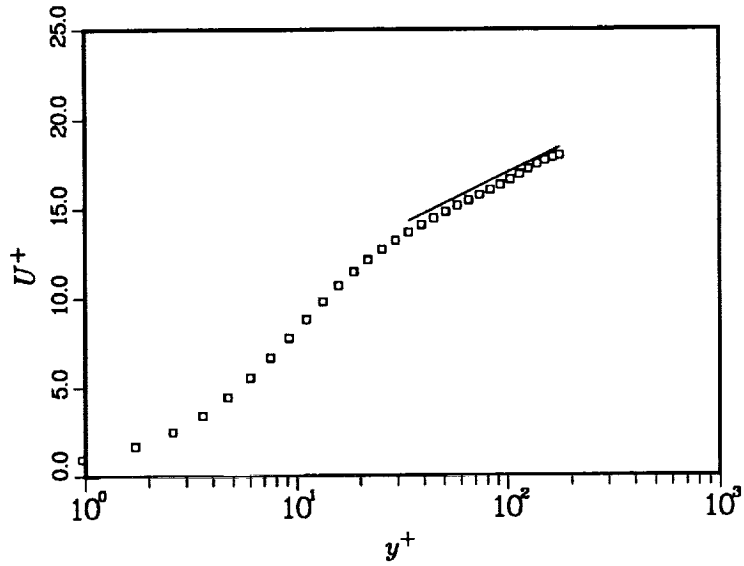

FIGURE 6. Mean velocity profile, $\frac{1}{.4}lny^+ + 5.5$

$U_c\delta/\nu = 4200$) is subcritical. The small spanwise dimension is used with $L_z = .289\pi\delta$. This dimension has been chosen because at this Re, $R_\tau = u_\tau\delta/\nu = 180$ is obtained. Eight riblets can be located in the channel with $s/h = 1$ and $h^+ = 20$.

In these calculations, the "pressure" field was obtained by a direct method which uses Fourier expansions in the streamwise and spanwise directions. For a $16 \times 64 \times 16$ grid, calculations require half second for each time step on the CRAY-YMP. The calculation done with finer grids in the spanwise direction resulted in no appreciable difference in the mean velocity and Reynolds stress distributions.

Figs.6-9 show the profiles of mean velocity and turbulent intensities obtained by averaging the instantaneous quantities for a period of time $tu_\tau/\delta = 15$. In the near-wall region, the agreement with the results obtained by spectral calculation for the large channel is very good. The pseudospectral numerical simulation was shown by Kim et al. (1987) to be in very good agreement with experimental results. In the central region, the present results show a larger normal stress with respect to the spanwise stress; this behavior does not depend on the numerical method but depends on the narrow channel assumption (Jimenez and Moin, 1990).

Turbulent channel flow in the presence of riblets

As mentioned before, the iterative pressure solver is not efficient in three dimensions. In some cases, we were not even able to obtain convergence. This constraint limited the present study to the geometry in Fig. 10, which has a limited number of grid points in the streamwise and spanwise directions.

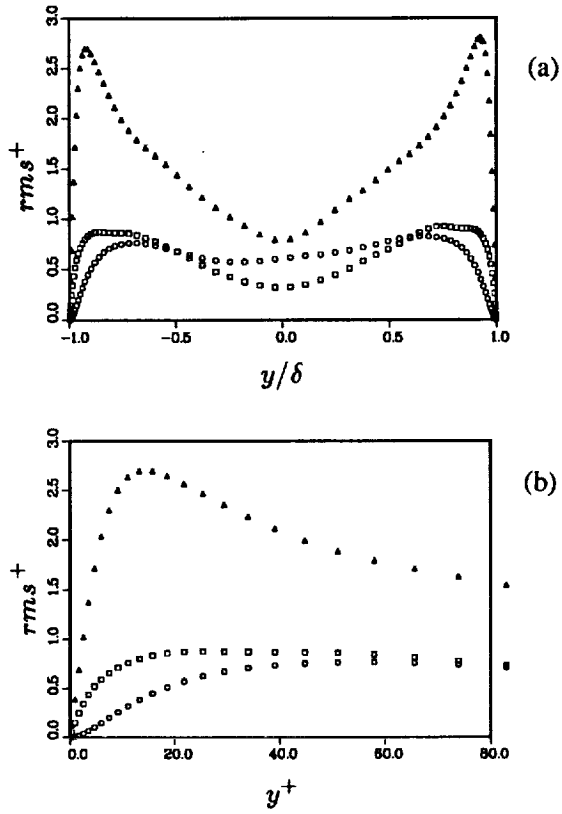

FIGURE 7. Root-mean-square velocity fluctuations normalized with the wall shear velocity. $\triangle$ q^3_{rms} streamwise, $\square$ q^1_{rms} spanwise, $\circ$ q^2_{rms} vertical. a) In global coordinates; b) in wall coordinates.

The initial velocity field was obtained from a turbulent plain channel simulation. The riblets were introduced gradually using a continuous transformation in time.

Figs.11-12 show mean velocity and rms profiles in the valley and tip regions respectively. The usual averaging in the $x-$ direction and over a time of $t = 10\delta/u_\tau$ was performed.

These preliminary results show that riblets cause modifications of velocity and the rms profiles. In the valley (Fig. 11) of the riblets, there is a weak reduction of the streamwise intensities, while the other stresses are not affected. At the tip of the riblets (Fig. 12) the profile are similar to those of the flat wall. At the center of the channel, the flow is not strongly affected by the riblets. The computation of channel with riblets reported here is of highly preliminary nature. However, it has been demonstrated that such a computation is feasible. In the coming year we will refine these computations and use the resulting data to examine the phenomenon of drag reduction.

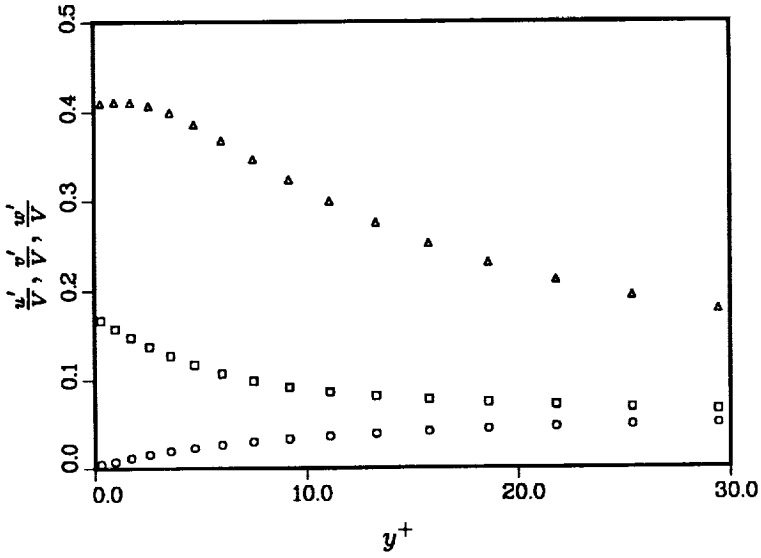

FIGURE 8. Turbulence intensities near the wall normalized by the local mean velocities. △ streamwise, □ spanwise, ○ vertical.

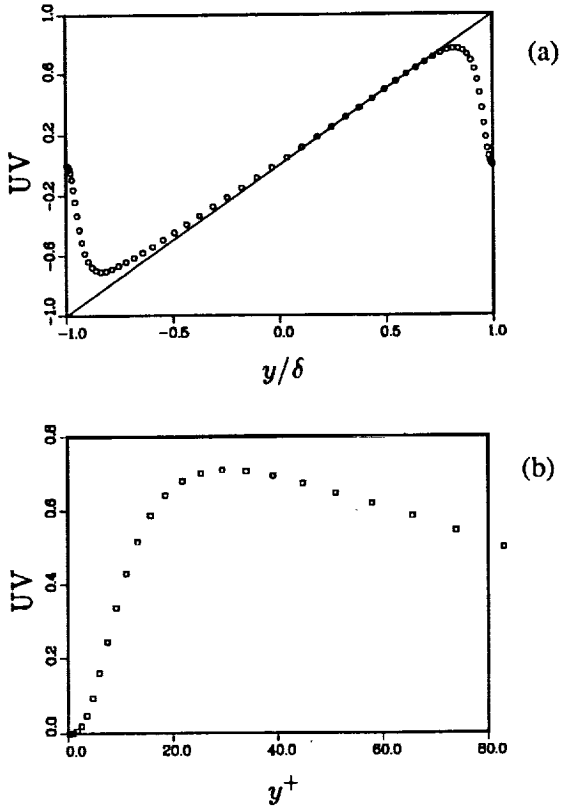

FIGURE 9. Reynolds shear stress normalized by the wall shear stress a) in global coordinates , b) in wall coordinates.

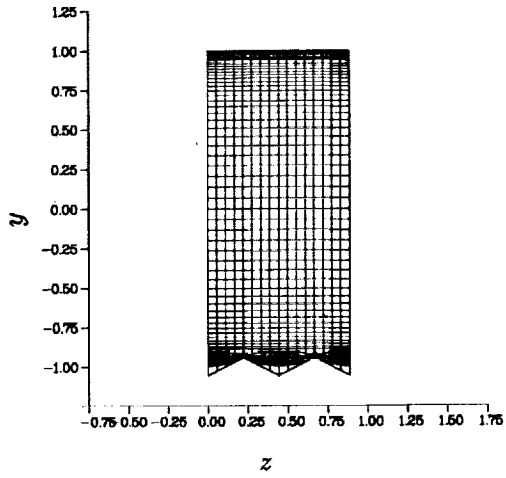

FIGURE 10. Computational grid in a vertical section of a channel with two riblets.

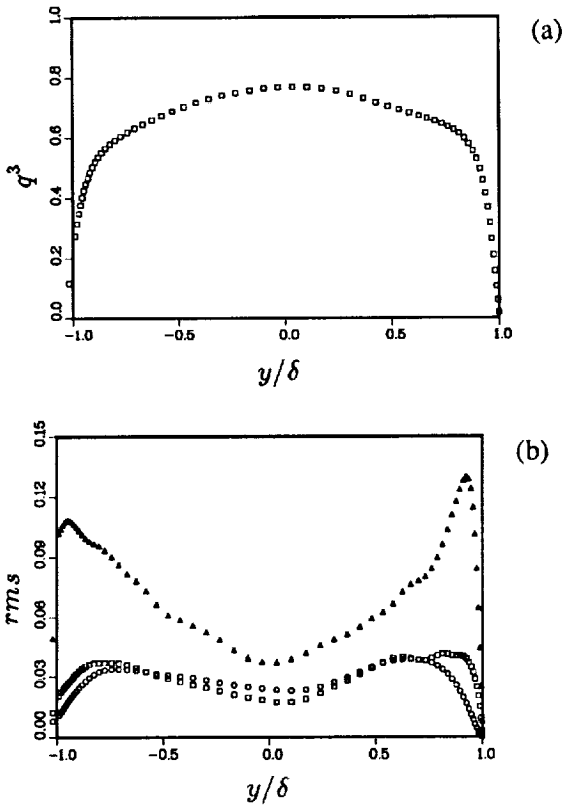

FIGURE 11. a) Mean velocity profile and b) root-mean-square velocity fluctuations, in global coordinates at the riblets valley.

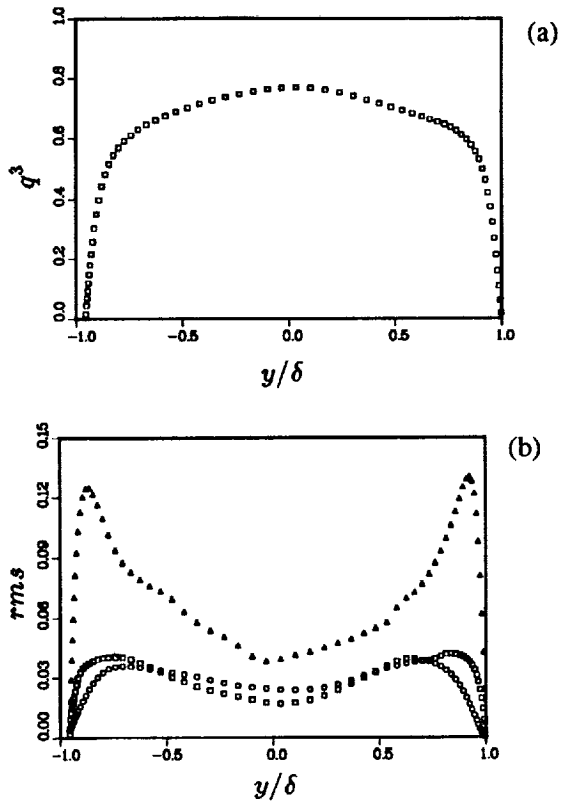

FIGURE 12. a) Mean velocity profile and b) root-mean-square velocity fluctuations, in global coordinates at the riblets tip.

Acknowledgment

We are indebted to Drs. K. Shariff and J. Jimenez for useful discussions.

REFERENCES

CANUTO, C., HUSSAINI, M. Y., QUARTERONI, A.,& ZANG, T. A. 1987 Spectral Methods in Fluid Dynamics Springer Series in Computational Physics.

HARLOW, F. H., & WELCH, J. E. 1965 Numerical calculation of time-dependent viscous incompressible flow of fluid with free surface. *Physics of Fluids.* **8**, 2182-2189.

JIMENEZ, J. & MOIN, P. 1990 The minimal flow unit in near wall turbulence, Center for Turbulence Research Manuscript 105.

KIM, J., & MOIN, P. 1985 Application of a fractional-step method to incompressible Navier-Stokes equations. *J. Comput. Physics.* **59**, 308-323.

KIM, J., MOIN, P.,& MOSER, R. D. 1985 Turbulence statistics in fully developed channel flow at low Reynolds number. *J. Fluid Mech.* **177**, 133.

KORCZAC, K. Z., & PATERA, A. T. 1986 An isoparametric spectral element method for the solution of the Navier-Stokes equations in complex geometries. *J. Comput. Physics.* **62**, 361-382.

MOSER, R. D., MOIN, P., & LEONARD A. 1983 A spectral numerical method for the Navier-Stokes equations with applications to Taylor-Couette flow. *J. Comput. Physics.* **48**, 524-544.

ORLANDI, P., ESPOSITO, P. G. 1989 A multigrid solver for the pressure equation for incompressible Navier-Stokes equations in general curvilinear coordinates (unpublished paper).

PULLIN, D. I. & PERRY, A. E. 1980 Some flow visualization experiments on the starting vortex. *J. Fluid Mech.* **97**, 239-255.

RAI, M. M., MOIN, P. 1988 Direct simulations of turbulent flow using finite difference schemes. *AIAA paper 89-0369 27th Aerospace Sciences Meeting, Reno.*

STEINBRENNER, J. P. 1986 Gridgen2d. *General Dynamics CFD Report 063-4-8601.*

Center for Turbulence Research
Annual Research Briefs - 1989

The large-scale structures in turbulent plane Couette flow

By M. J. Lee

Turbulent plane Couette flow has been numerically simulated at a Reynolds number, $\mathrm{Re} = U_w h/\nu = 6{,}000$. Preliminary examination of the instantaneous velocity and vorticity fields revealed the existence of large-scale eddies which grow in the flow direction with time and have the spanwise scale as large as the channel-height. The persistence of the longitudinal eddies was not observed when the small scales in the spanwise direction were not well resolved, indicating that the growth of the large-scale longitudinal eddies requires the contribution from the small-scale motions in the spanwise direction. The statistical correlations in the flow agree well with the experimental results.

1. Introduction: motivation and objectives

An important fluid-mechanical aspect of a fully-developed plane Couette flow is that the flow has a constant shear stress across the entire channel height, be it laminar or turbulent. The constancy of shear stress, $\tau/\rho = \nu\, dU/dy - \overline{uv}$ (equal to its value at the wall, $\tau_w/\rho = \nu\, dU/dy|_w$), is a direct consequence of zero mean pressure gradient in the flow as it is driven by shear generated at two plane, solid boundaries in rectilinear, parallel movement (at speed U_w) relative to each other (see Figure 1). Here, (x, y, z) denote the coordinates in the flow direction, in the normal direction to the center plane of the channel (i.e. $-1 \le y/h \le 1$, where h is the channel half-height) and in the spanwise direction, respectively. In a fully-developed plane Couette flow, turbulence statistics are uniform in a horizontal xz-plane. Because of its simple flow geometry and the existence of the constant shear-stress region, turbulent plane Couette flow has been considered as one of the building-block flows for study of wall-bounded turbulent shear flows.

Another characteristic of plane Couette flow is that both the mean vorticity (or mean shear, $S = dU/dy$) and turbulent shear stress ($-\rho\,\overline{uv}$) are symmetric about the center plane ($y/h = 0$), in contrast with pressure-driven Poiseuille flow that has profiles antisymmetric about $y/h = 0$. Because of the resulting finite production rate, $-S\,\overline{uv}$, even in the core region (say, $0.2\text{–}0.5 \le y_\perp/h \le 1$, where $y_\perp$ is the distance normal to a nearest wall) the shapes of the turbulence intensity profiles ($\overline{u^2}$, $\overline{v^2}$, $\overline{w^2}$) differ significantly among the three components (see El Telbany & Reynolds 1982), indicating the existence of a high degree of anisotropy in the flow. Therefore, we conjecture (or hypothesize) that instantaneous turbulence structures in the core region of plane Couette flow would be quite different from those of Poiseuille flow. This question has not been addressed before. However, in the vicinity of the walls (e.g. $y_\perp/h \le 0.1\text{–}0.2$), turbulence structures

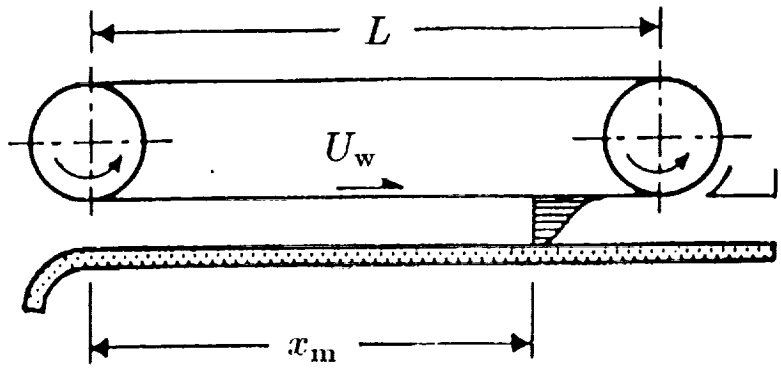

FIGURE 1. Schematic diagram of a typical experimental setup of turbulent plane Couette flow. Because the belt is prone to deform at high speeds, the length of the shearing boundary has to be limited, resulting in a rather short flow-development length (or time), $x_m/h = 10$–300.

of the two flows are expected to be similar, since the near-wall dynamics of a turbulent shear flow is primarily controlled by a mechanism universally represented by the 'law of the wall.' For instance, the near-wall turbulence structures in boundary layer and plane Poiseuille flow appear to be identical even though the outer structures of the two flows are significantly different.

Despite its apparent importance as a paradigm of wall-bounded turbulent shear flows, plane Couette flow has not been studied extensively. In most previous experiments (Reichardt 1956, 1959; Robertson 1959; Robertson & Johnson 1970; Leutheusser & Chu 1971; El Telbany & Reynolds 1980, 1981), the boundary shearing was realized by employing either a (flexible) moving belt or a fluid interface, which is prone to deform at high speeds (or at high Reynolds numbers, $\mathrm{Re} = U_w h/\nu$). To alleviate this problem, the length of the shearing boundary had to be made short, which resulted in a rather short flow-development length (or time): $x_m/h = 10$–300 (x_m is the distance from the entrance to the location of the principal measuring station). Because of the difficulties arising from the movement of the shearing boundary, only the profiles of mean velocity, turbulence intensities and turbulent shear stress were obtained in most experiments, and measurements of energy spectra and two-point velocity correlations were limited in the streamwise direction only (Robertson & Johnson 1970; Aydin & Leutheusser 1979, 1989).

The present study aims at two main objectives. First, we would like to identify turbulence structures in plane Couette flow and examine differences from those in plane Poiseuille flow. Previous works showed that the core region of

plane Poiseuille flow is dominated by hairpin-shaped vortical eddies (Moin & Kim 1985; Kim & Moin 1985). It is our goal to understand the mechanism by which the boundary shearing produces turbulence structures different from those generated in a pressure-driven flow. Second, we would like to test the capability of existing turbulence models (and scaling laws) in describing the turbulence characteristics of plane Couette flow. Because most near-wall turbulence models have been developed by assuming that the wall layer is of constant-stress equilibrium (Townsend 1976, §5), there is an intrinsic interest to examine the performance of existing models.

To achieve these objectives, turbulent plane Couette flow has been numerically simulated by integrating the Navier-Stokes equations in time (for a brief description, see §2.1). Using the database obtained from the direct numerical simulation, the existence of large-scale eddies in plane Couette flow was found. In this report, special attention is focused on the large-scale motions that develop in the flow direction with time and that have the cross-stream dimensions as large as the channel-height, $2h$. A discussion of the statistical correlations follows the examination of the instantaneous structures.

2. Accomplishments

2.1. Direct numerical simulation

For the present study, the flow Reynolds number ($U_w h/\nu$) of 6,000 was selected. Note that the chosen value of the Reynolds number is higher than the range of the reported critical transition Reynolds numbers, 1,000–2,000. The numerical algorithm of the present code is identical to that used in the computation of Kim, Moin & Moser (1987), except the wall boundary conditions. A spectral method (Fourier in the horizontal xz-plane and Chebyshev in the vertical y-direction) for the spatial differentiations and an Adams-Bashforth/Crank-Nicolson algorithm for time advancement were used.

Direct numerical simulation (DNS hereinafter) of a turbulent flow is meaningful only when all the essential scales in the flow under consideration are properly represented in the computation. As shown in Table 1, computations have been carried out with three different sizes (i.e. horizontal dimensions, B_x and B_z) of the computational domain (or box): $B_x/h = 4\pi$, 8π and 16π. In all the cases reported here, the number of the Chebyshev modes used for the vertical direction was 65, and the spanwise dimension was half the streamwise dimension: $B_z/B_x = \frac{1}{2}$. The largest computational domain (for runs Q1, Q2, Q3) has a high streamwise-to-vertical aspect ratio, $B_x/(2h) \simeq 25$.

A computation on a box of a given size was started on a coarse mesh with horizontal modes (NX,NZ) of 32×32, which was successively expanded up to 128×128 modes. The expansion of the horizontal modes was done after the flow reached a 'quasi-steady' state as determined by inspection of such statistics as the

Case	B_x/h	B_z/h	NX	NZ	$\Delta x/h$	$\Delta z/h$
B1	4π	2π	32	32	0.393	0.196
D1	8π	4π	32	32	0.785	0.393
D2			64	64	0.393	0.196
D3			128	128	0.196	0.0982
Q1	16π	8π	32	32	1.57	0.785
Q2			64	64	0.785	0.393
Q3			128	128	0.393	0.196

TABLE 1. Specifications of the computational box and the horizontal Fourier modes for plane Couette flow simulations. For all the runs, the number of the vertical Chebyshev modes was 65 and $\mathrm{Re} = U_w h/\nu = 6000$.

mean velocity, turbulent kinetic energy, shear stresses, two-point velocity correlations and energy spectra. Table 1 also shows the corresponding horizontal grid spacings, $(\Delta x, \Delta z)$. When the flow reached a 'quasi-steady' state the Reynolds number, $\mathrm{Re}_\tau = U_\tau h/\nu$, based on the wall-shear velocity, $U_\tau = (\nu\, dU/dy|_w)^{1/2}$, and channel half-height, h, was about 180. (Laminar Couette flow at this flow Reynolds number has $\mathrm{Re}_\tau \simeq 55$.) The size of the biggest computational domain was $B_x^+ \simeq 9{,}000$, $B_z^+ \simeq 4{,}500$, where the superscript + denotes a quantity made dimensionless by the viscous length scale, $\ell_\nu = \nu/U_\tau$.

2.2. *The large-scale structures*

The streamwise two-point correlations of fluctuating velocity components, (u, v, w), at the center of the channel $(y/h = 0)$ from the computation on the smallest box size, $(B_x, B_z)/h = (4\pi, 2\pi)$ are shown in Figure 2. The significant correlation of the streamwise velocity component, u, at the streamwise separations near $r_x/h = 2\pi$ indicates that the size of the computational domain is not sufficient for the largest eddies. Therefore, it was decided that the computation must be performed on a bigger computational domain.

Figure 3 shows the streamwise two-point correlations at the center plane $(y/h = 0)$ from the computation with a bigger box, $(B_x, B_z)/h = (8\pi, 4\pi)$. When the number of the horizontal modes was small with the grid spacing $(\Delta x, \Delta z)/h = (0.785, 0.393)$, the bigger box size appeared to be sufficient enough to contain large-scale motions in the flow, as indicated by the negligible correlations at large streamwise separations in Fig. 3(*a*). However, as the number of the horizontal modes increased so that the grid spacing became $(\Delta x, \Delta z)/h = (0.393, 0.196)$, the correlation of the streamwise velocity, u, was high again (see Fig. 3*b*). Comparison of the computations on the same box size but with different numbers of the horizontal modes (especially the spanwise modes) suggests

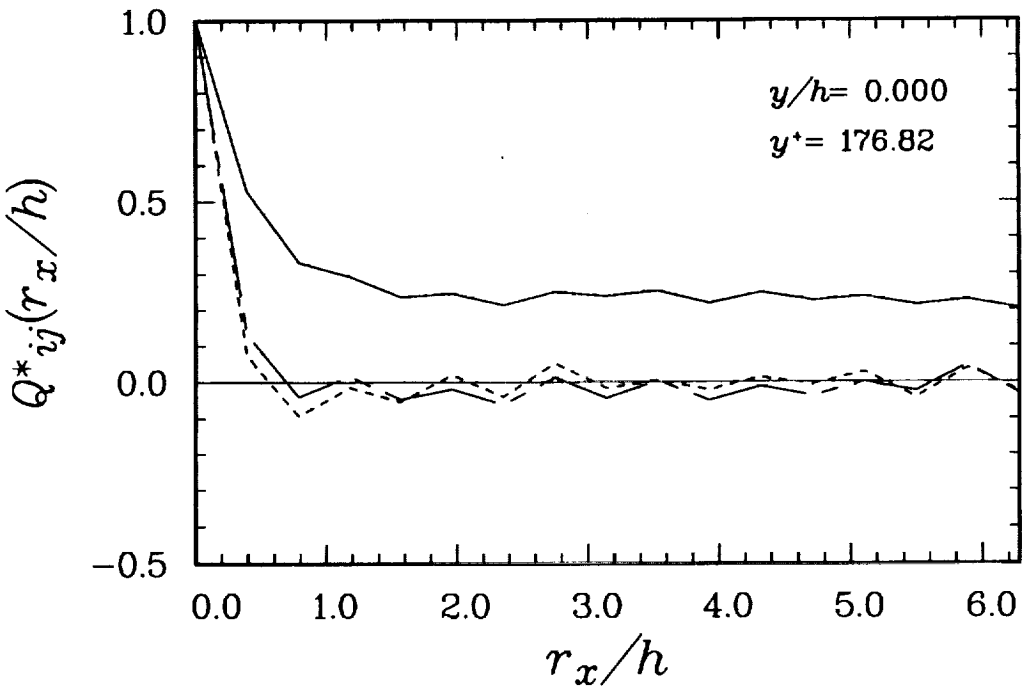

FIGURE 2. The streamwise two-point correlations of velocity at $y/h = 0$ from the computation with the smallest box, $(B_x, B_z)/h = (4\pi, 2\pi)$. ——, $Q^*_{uu}(r_x/h)$; ----, $Q^*_{vv}(r_x/h)$; ——, $Q^*_{ww}(r_x/h)$. The significant correlation at the streamwise separation, $r_x/h = 2\pi$, indicates that the box size is insufficient to contain largest eddies in the flow. The grid spacing is $(\Delta x, \Delta z)/h = (0.393, 0.196)$.

that the growth of the longitudinal eddies requires the contribution from small-scale motions in the spanwise direction.

Inspection of the spanwise energy spectra, $E_{uu}(k_z)$, of the streamwise velocity (Figure 4, run case D3) revealed that with the contributions from small scales a definite peak develops in times at $k_z h \simeq 1$, which is an order-of-magnitude higher than the density at other scales. The presence of the sharp peak indicates the existence of a finite spanwise scale of the energetic eddies. The generating mechanism of these large-scale eddies differs significantly from that of the streaky structures in the near-wall region (sublayer) and in homogeneous shear flows (Lee, Kim & Moin 1987). The streaky turbulence structures are selectively amplified by the high mean shear rate ($S^* = Sq^2/\epsilon \gg 1$), a linear mechanism in which transfer of energy between different scales is absent (Lee & Hunt 1989).

Some details of the instantaneous structures in the computed flow are discussed below. Figure 5 shows the contours of the streamwise velocity fluctuations, u, plotted on the center plane ($y/h = 0$). The contours on the center

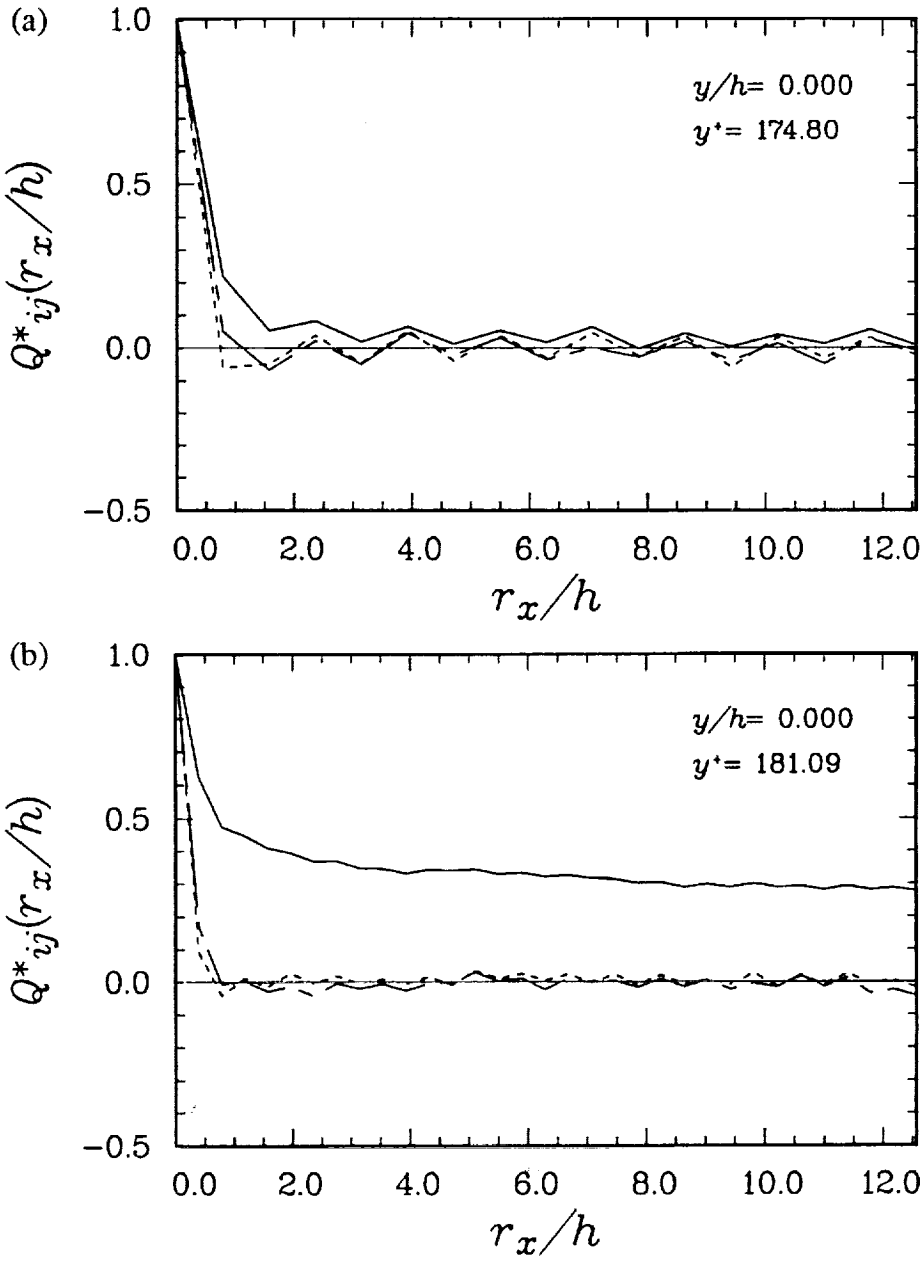

FIGURE 3. Comparison of the streamwise two-point correlations at $y/h = 0$ from the computations with different number of horizontal modes (NX,NZ) on the bigger box, $(B_x, B_z)/h = (8\pi, 4\pi)$: (*a*) (NX,NZ) = (32,32); (*b*) (NX,NZ) = (64,64). ——, $Q^*_{uu}(r_x/h)$; ----, $Q^*_{vv}(r_x/h)$; —·—, $Q^*_{ww}(r_x/h)$. The development of high correlation with the increase of the number of the spanwise modes suggests that the growth of the large eddies in plane Couette flow requires contributions from the small-scale spanwise motions.

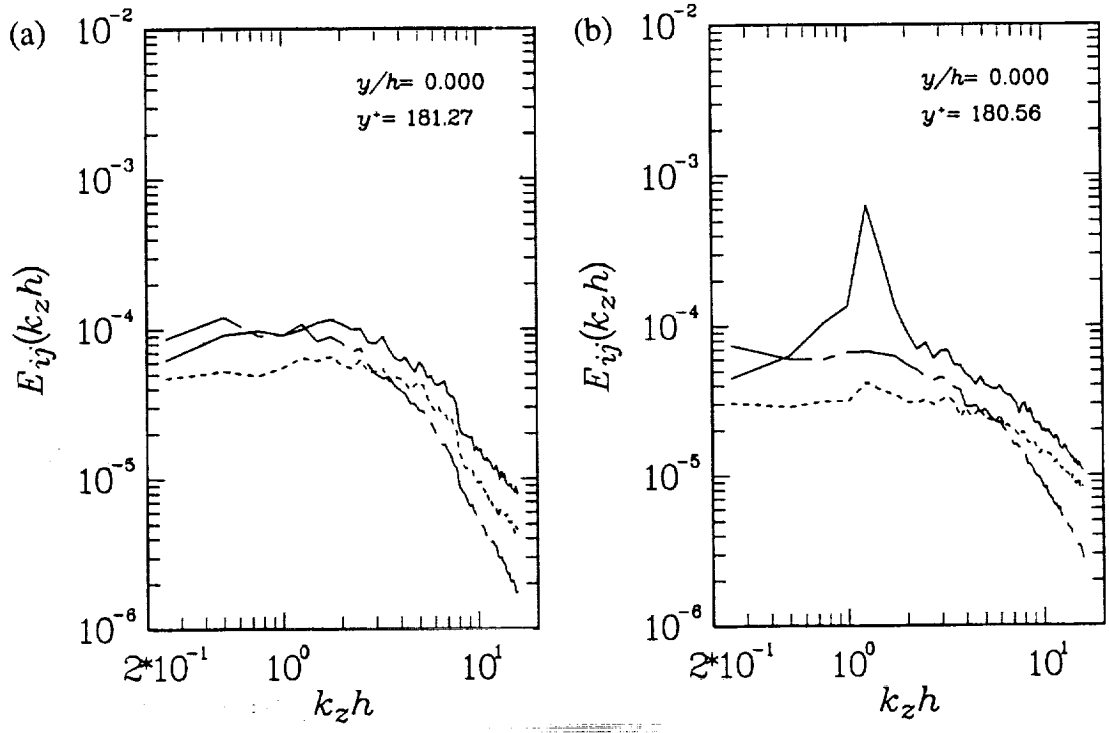

FIGURE 4. Evolution of the spanwise energy spectra at the center of the channel ($y/h = 0$), showing that the development of a peak of the streamwise component at the wavenumber $k_zh \simeq 1$: (a) earlier time, t_0; (b) later time, $(t - t_0)U_w/h \simeq$ 500–1000. ——, $E_{uu}(k_zh)$; ----, $E_{vv}(k_zh)$; ——, $E_{ww}(k_zh)$.

plane clearly show the existence of organized large-scale eddies in the flow. The topological configuration of these structures may appear to be similar to that of the near-wall streaky structures in that the low- and high-speed flow regions are highly elongated in the flow direction and alternate in the spanwise direction. However, the length scales, Λ_x and Λ_z, of the structures in the core region are much larger than those, λ_x and λ_z, of the streaks in the sublayer: $\Lambda_x^+ \simeq 5{,}000$–$7{,}000$, $\Lambda_z^+ \simeq 900$, $\lambda_x^+ \simeq 1{,}000$, $\lambda_z^+ \simeq 100$, where the subscripts x and z denote the streamwise and spanwise directions, respectively. This difference in scales also suggests that the generating mechanism for the large-scale structures in the Couette flow is different from that responsible for generating the wall-layer streaks. Contours of the other velocity components (v and w), vorticity and pressure are not as much elongated, and they are more intermittent and localized in space (not shown here).

The spatial distribution of u near the two walls are different (see Figure 6). Near the bottom wall where the mean fluid speed is larger than the wall speed, the distribution of u is positively skewed, and the converse is true near the top

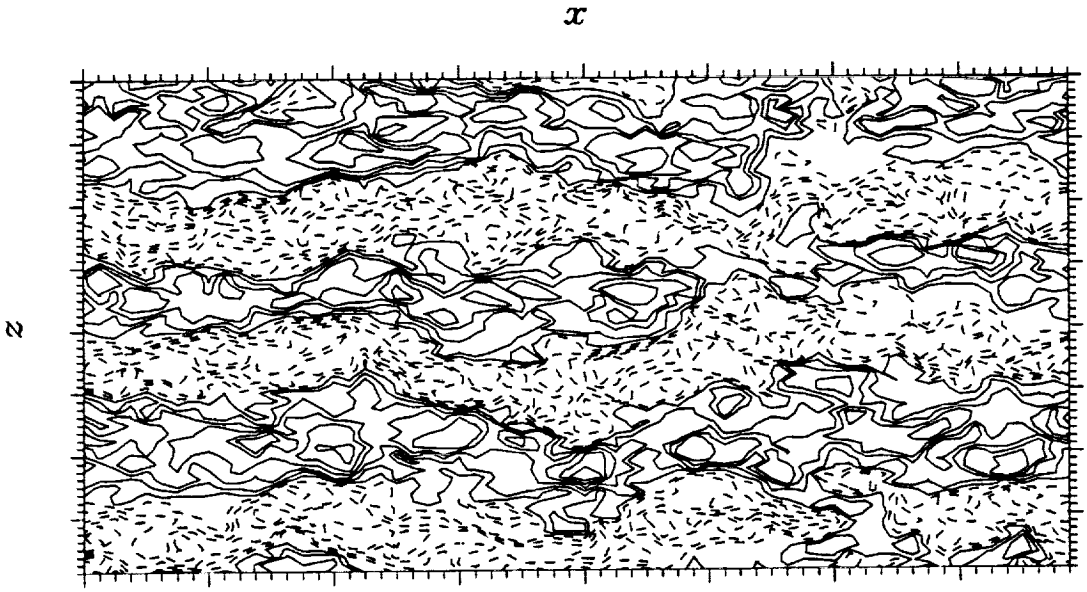

FIGURE 5. Contours of the streamwise velocity fluctuations, u, at the center of the channel ($y/h = 0$), showing the existence of large-scale structures developing in the core region. ——, $u > 0$; ----, $u < 0$.

wall. In contrast, the respective distributions of other components of velocity (v, w) and the streamwise and vertical vorticity components (ω_x, ω_y) are not as much different near the two opposite walls as the u distribution, and have skewness factors much less than that of u. However, the spanwise vorticity (ω_z) has a high negative skewness factor near the both walls.

The vertical extent of the eddy structures is shown by the contour plot of u on a yz-plane (an end view) in Figure 7. (The vertical direction is magnified by a factor of $2\frac{1}{2}$ for visual clarity near the walls; $L_z = 4\pi h$ and $Ly = 2h$.) The vertical extent of the large eddies is as big as the channel height, $2h$. The spanwise spacing between the low- or high-speed regions as determined from an inspection of contour plots such as Figure 7 is about $4h$. This is consistent with the spanwise two-point correlation of the streamwise velocity fluctuations, $Q^*_{uu}(r_z)$, that has distinct negative dips at separations $r_z/h \simeq 2$, 6 and positive peaks at $r_z/h \simeq 4$. If the computational domain were larger, the dips and peaks would appear at the separations $r_z/h = 4n - 2$ and $4n$, respectively ($n = 1, 2, \ldots$). However, the near-wall regions consist of small-scales structures.

2.3. Statistical correlations

Here, the statistical properties of plane Couette flow computed from the simulation with the best resolution are presented. In Figure 8(a), the computed

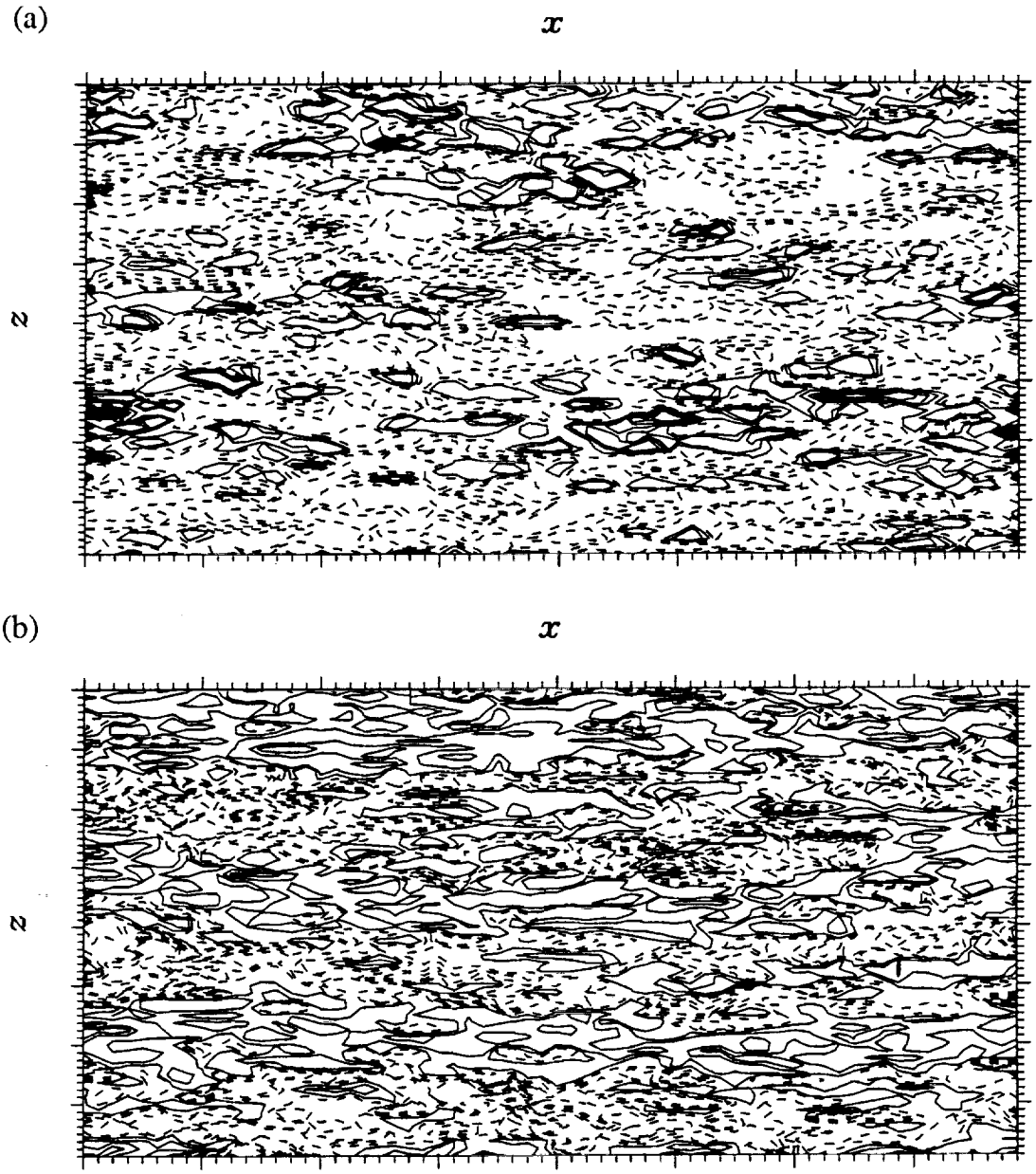

FIGURE 6. Comparison of distribution of the streamwise velocity fluctuations (*a*) near the bottom wall, $y/h = -0.98$ ($y^+ = 3.5$); (*b*) near the top wall, $y/h = +0.98$ ($y^+ = 3.5$). ——, $u > 0$; ----, $u < 0$. Note that the u-distribution is positively skewed near the bottom wall and the converse is true near the top wall.

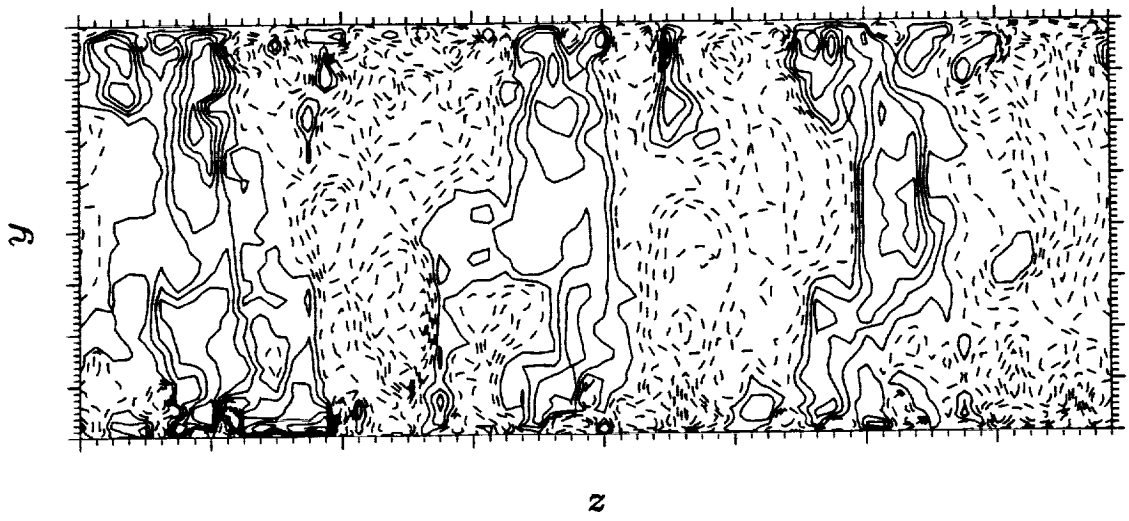

FIGURE 7. Contours of the streamwise velocity fluctuations on a yz-plane (an end view), showing that the vertical extent of the large eddies is almost the channel height ($2h$) and the spanwise spacing (or the size) of a pair is about $4h$. ——, $u > 0$; ----, $u < 0$. (Note that the vertical direction is magnified by a factor of $2\frac{1}{2}$ for visual clarity near the walls.)

mean velocity profile across the channel is compared with the experiments conducted at different flow Reynolds numbers (Re = 2,900, Reichardt 1959; Re $\simeq 2 \times 10^4$–4×10^4, El Telbany & Reynolds 1980). It should be noticed that at high Reynolds numbers the velocity profile changes rapidly within a narrow region near the wall ($y_\perp/h \leq 0.1$), and that it has a constant slope over the half channel-height around the center ($-0.5 \leq y/h \leq 0.5$). The mean velocity gradient at the boundary, $S_w = dU/dy|_w$, grows substantially with the Reynolds number, whereas that at the center plane, $S_c = dU/dy|_{y=0}$, decreases with increasing Reynolds numbers. The mean velocity gradient (or mean shear rate) in the core region is about 5% of the wall value (or total stress) and it is about 30% of the value for a laminar flow with a linear velocity profile. Thus, the total shear stress in the turbulent case is about 10 times higher than the laminar equivalent.

The near-wall profile, U^+, made dimensionless by the wall-shear velocity (U_τ), *vs.* y^+, the distance normal to the wall scaled by the viscous length ($\ell_\nu = \nu/U_\tau$) is shown in Figure 8(b). The solid and chain-dashed lines are the profiles near the lower and upper walls, respectively. The dashed and dotted lines denote the universal law of the wall: $U^+ = y^+$ and $U^+ = (1/\kappa)\ln y^+ + B$ ($\kappa = 0.4$ and $B = 5.5$), respectively, which fits the experimental data at a high Reynolds number (El Telbany & Reynolds 1980). The data from the present simulation

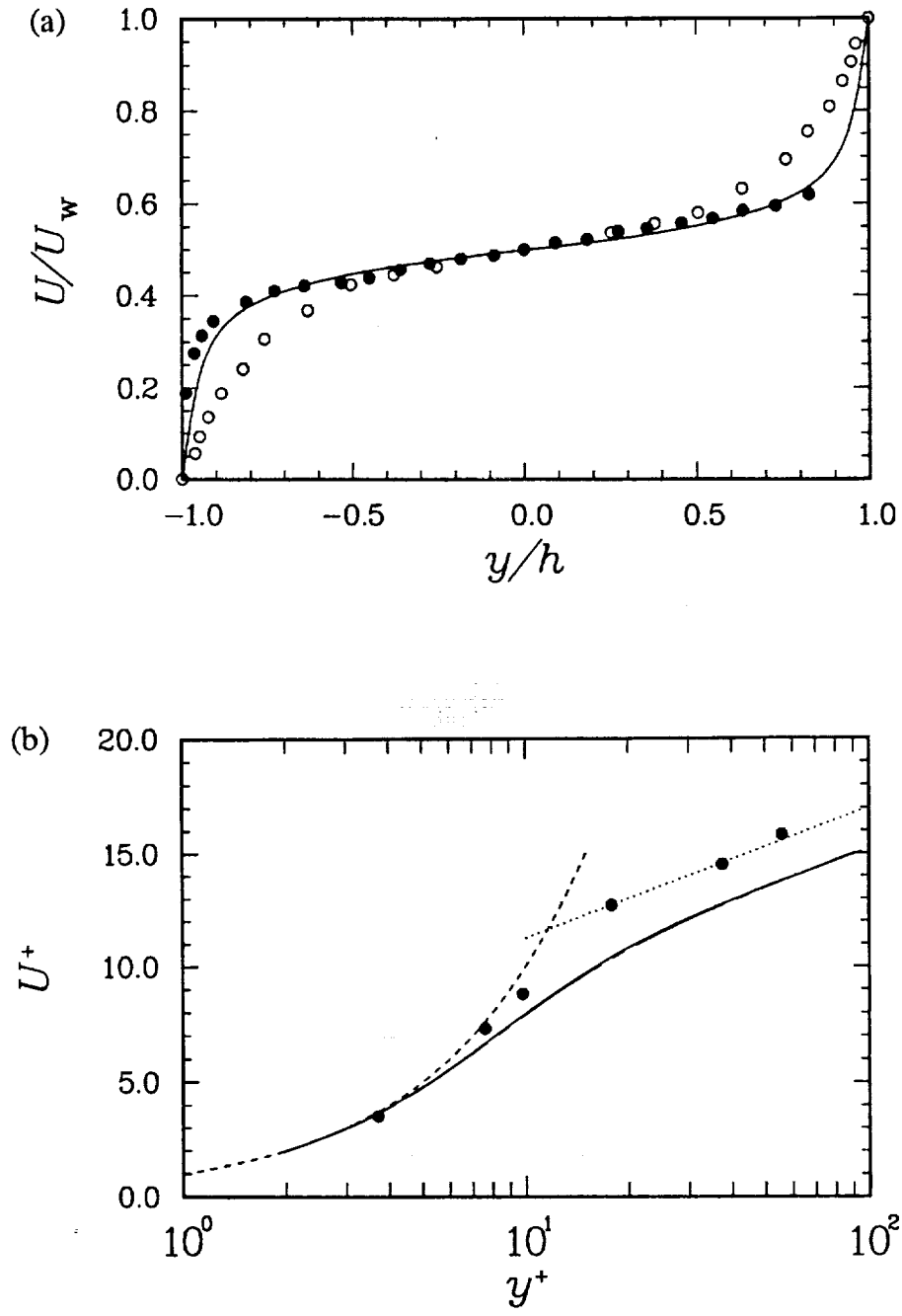

FIGURE 8. Mean velocity profile in plane Couette flow: (*a*) global profile, U/U_w *vs.* y/h; (*b*) near-wall profile, U^+ *vs.* y^+. ——, present result; ○, Reichardt (1959); ●, El Telbany & Reynolds (1980); ----, $U^+ = y^+$; ·····, $U^+ = (1/\kappa)\ln y^+ + B$ ($\kappa = 0.4$ and $B = 5.5$); In (*b*), the solid and chain-dashed lines are the profiles for the lower and upper walls, respectively.

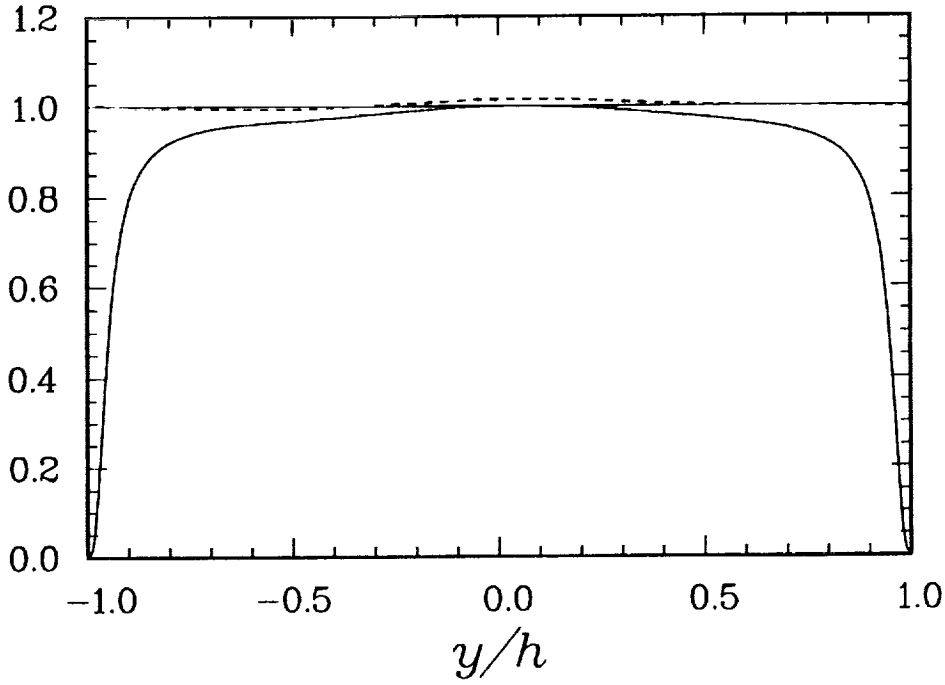

FIGURE 9. Profile of shear stresses in plane Couette flow: ——, turbulent shear stress ($-\rho\overline{uv}/\tau_w$); ----, total shear stress (τ/τ_w).

show $B = 3.5$, a lower value than that for high Reynolds numbers ($B = 5.5$). This is counter to the usual dependence on the Reynolds number.

Figure 9 shows the profiles of turbulent and total shear stresses. The total shear stress is nearly uniform across the whole channel height. In the near-wall region, the turbulent shear stress increases rapidly with the distance from the wall: it attains $0.9\tau_w$ at $y_\perp/h = 0.2$. (The small deviation of τ/τ_w from unity is due to the insufficient number of the sample fields used for average.)

The turbulence intensities (u'^+, v'^+, w'^+) scaled by the wall-shear velocity (U_τ) in Figure 10(a) show good agreement with the experimental results at higher Reynolds numbers (El Telbany & Reynolds 1981). Compared with those in a plane Poiseuille flow at comparable Reynolds numbers (Fig. 10b, Kim *et al.* 1987), the intensities in Couette flow are significantly higher at most locations in the channel, except in the vicinity of the wall ($y^+ \leq 30$) where the Couette-flow values are higher only slightly. This marked contrast is a direct consequence of the constancy of total shear stress, $\tau = \mu\, dU/dy - \rho\overline{uv}$, across the channel in the flow. (In a plane Poiseuille flow, the total shear stress has a linear profile $\tau/|\tau_w| = -y/h$, and $dU/dy = 0$ and $\overline{uv} = 0$ at the channel center, $y/h = 0$, by symmetry.)

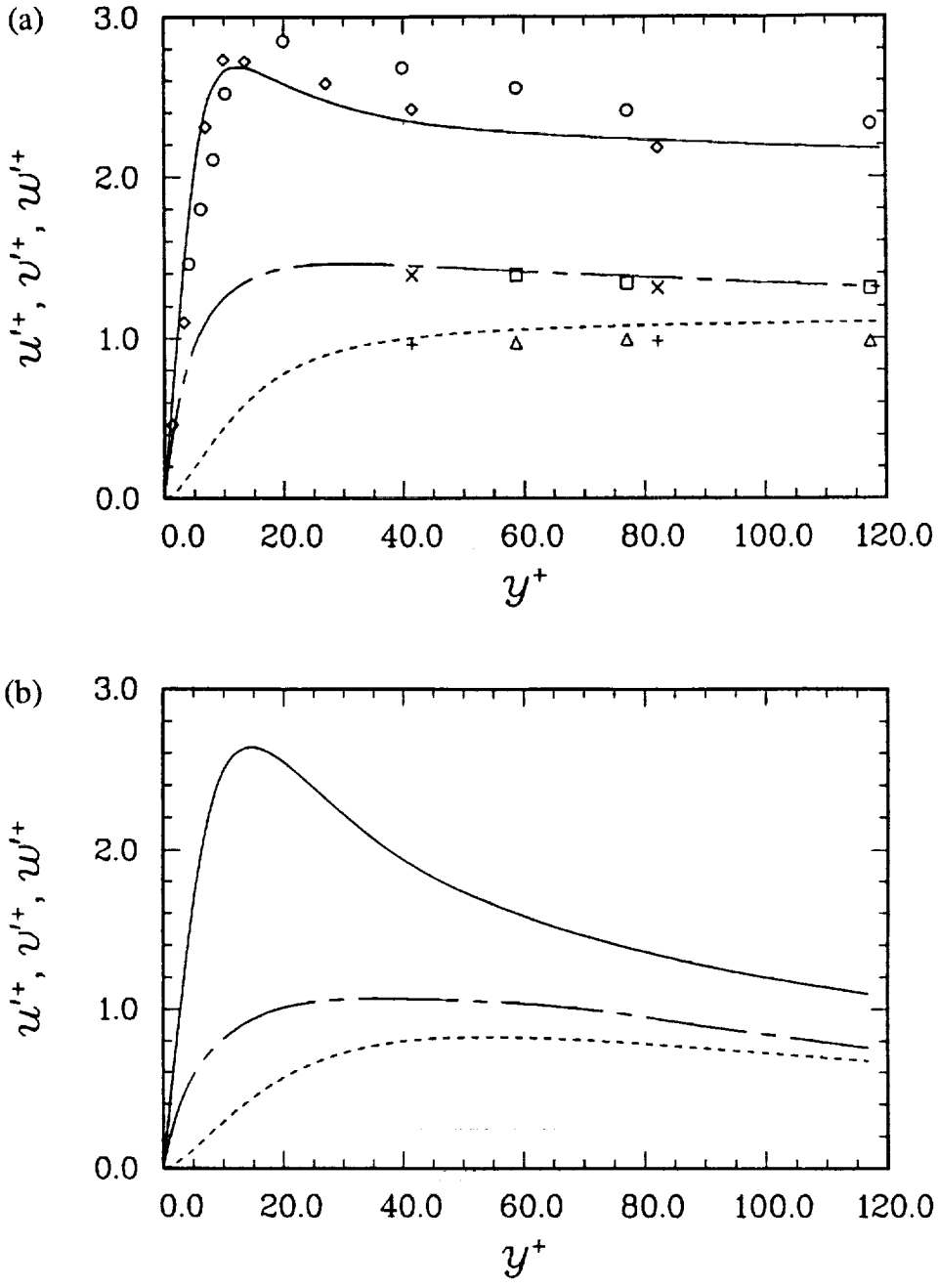

FIGURE 10. Near-wall profiles of the turbulence intensities: (u'^+, v'^+, w'^+) *vs.* y^+: (*a*) plane Couette flow; (*b*) plane Poiseuille flow. Lines are from the computations: ——, u'^+; ----, v'^+; — — —, w'^+. Symbols are the measured data from El Telbany & Reynolds (1981).

Figure 10(a) also shows that the turbulence structure in the core region has strong anisotropy, i.e. $\overline{u^2} : \overline{v^2} : \overline{w^2} \simeq 6 : 1 : 2$. The mean velocity profile is approximately linear in the core region, indicating that turbulence statistics are uniform there as would be in homogeneous turbulent flows.

3. Summary

In this report, preliminary results are presented on the existence of the large-scale structures in turbulent plane Couette flow. The structures are primarily associated with the streamwise velocity fluctuations in the core region (say, $y_\perp/h > 0.2$). These eddies develop in the flow direction in time and grow to fill the whole channel in the cross-stream plane. Analysis of the two-point correlations and spectra shows that the spanwise scale of the individual eddies is about the channel height ($2h$). The generating mechanism of these large-scale eddies differs from that of the streaky structures found in flows at high shear rate.

There is an intrinsic interest in studying plane Couette flow from the modeling point of view because this flow has a constant total shear stress across the channel. We plan to analyze turbulence statistics including the Reynolds-stress transport budget to examine the capability of the existing turbulence models. Comparison of these with those in plane Poiseuille flow would reveal the differences and similarities of the two flows in how the wall layer is affected by the structures in the core region.

REFERENCES

AYDIN, M. & LEUTHEUSSER, H. J. 1979 Novel experimental facility for the study of plane Couette flow. *Rev. Sci. Instr.* **50**, 1362–1366.

AYDIN, E. M. & LEUTHEUSSER, H. J. 1987 Experimental investigation of turbulent plane-Couette flow. *Forum on Turbulent Flows–1987*, FED vol. 51, 1987 ASME Applied Mech., Bioeng. & Fluids Eng. Conf., Cincinnati, Ohio, June 14–17, 1987 (ed. W. W. Bower), pp. 51–54. Amer. Soc. Mech. Eng.: New York.

AYDIN, E. M. & LEUTHEUSSER, H. J. 1989 Plane-Couette flow between smooth and rough walls. *J. Fluid Mech.* (*sub judice*)

EL TELBANY, M. M. M. & REYNOLDS, A. J. 1980 Velocity distributions in plane turbulent channel flows. *J. Fluid Mech.* **100**, 1–29.

EL TELBANY, M. M. M. & REYNOLDS, A. J. 1981 Turbulence in plane channel flows. *J. Fluid Mech.* **111**, 283–318.

EL TELBANY, M. M. M. & REYNOLDS, A. J. 1982 The structure of turbulent plane Couette flow. *Trans. ASME J. Fluids Eng.* **104**, 367–372.

KIM, J., MOIN, P. & MOSER, R. D. 1987 Turbulent statistics in fully developed channel flow at low Reynolds number. *J. Fluid Mech.* **177**, 133–166.

KIM, J. & MOIN, P. 1986 The structure of the vorticity field in turbulent channel flow. Part 2. Study of ensemble-averaged fields. *J. Fluid Mech.* **162**, 339–363.

KLINE, S. J., REYNOLDS, W. C., SCHRAUB, F. A. & RUNSTADLER, P. W. 1967 The structure of turbulent boundary layers. *J. Fluid Mech.* **30**, 741–773.

KREPLIN, H. & ECKELMANN, H. 1979 Behavior of the three fluctuating velocity components in the wall region of a turbulent channel flow. *Phys. Fluids* **22**, 1233.

LEE, M. J. & HUNT, J. C. R. 1989 The structure of sheared turbulence near a plane boundary. *Seventh Symp. on Turbulent Shear Flows*, Stanford University, Stanford Calif., Aug. 21–23, 1989 (ed. F. Durst *et al.*), pp. 8.1.1–8.1.6.

LEE, M. J., KIM, J. & MOIN, P. 1987 Turbulence structure at high shear rate. *Sixth Symp. on Turbulent Shear Flows*, Toulouse, France, Sept. 7–9, 1987 (ed. F. Durst *et al.*), pp. 26.6.1–26.6.6; To appear in *J. Fluid Mech.*

LEUTHEUSSER, H. J. & CHU, V. H. 1971 Experiments on plane Couette flow. *Proc. ASCE J. Hydr. Div.* **97** (HY9), 1269–1284.

MOIN, P. & KIM, J. 1985 The structure of the vorticity field in turbulent channel flow. Part 1. Analysis of instantaneous fields and statistical correlations. *J. Fluid Mech.* **162**, 339–363.

REICHARDT, H. 1956 Über die Geschwindigkeitsverteilung in einer geradlinigen turbulenten Couetteströmung. *Zeit. angew. Math. Mech.* **36**, Sonderheft 26–29.

REICHARDT, H. 1959 Gesetzmäßigkeiten der geradlinigen turbulenten Couetteströmung. *Mitteil.* No. 22. Max-Planck-Inst. Strömungsforschung und Aerodynamischen Versuchsanstalt: Göttingen.

ROBERTSON, J. M. 1959 On turbulent plane-Couette flow. *Proc. Sixth Midwestern Conf. Fluid Mech.*, Univ. of Texas, Austin, Texas, Sept. 9–11, 1959, pp. 169–182.

ROBERTSON, J. M. & JOHNSON, H. F. 1970 Turbulence structure in plane Couette flow. *Proc. ASCE J. Eng. Mech. Div.* **96** (EM6), 1171–1182.

TOWNSEND, A. A. 1976 *The structure of turbulent shear flow.* 2nd edn. Cambridge University Press: Cambridge, England.

Turbulent thermal convection in a differentially rotating channel

By W. Cabot

1. Motivation and objectives

Differentially rotating disks of gases and solids occur in several astrophysical systems, in particular in the inner parts of protostellar nebulae, of which our own solar system is thought to be a relic (see reviews in Black & Matthews, 1985). These "accretion disks" (see review by Pringle, 1981) are characterized by near centrifugal balance (i.e. nearly Keplerian orbits), a small vertical-to-radial aspect ratio, highly supersonic rotation speeds (the rotation rate being the dominant timescale), and very low effective Prandtl numbers due to very low densities that give rise to high radiative emissivities. Accretion disks are deduced to evolve on timescales many orders of magnitude faster than can be accounted for by angular momentum transport by molecular viscosity. Other mechanisms — like turbulent Reynolds stresses — are thus hypothesized to account for angular momentum transport. Turbulence is suspected because any sustained large-scale disturbance in the disk will have a very high Reynolds number. Unfortunately, there are as yet no reliable models to describe accretion disk turbulence, nor even many testable constraints from present astronomical observations. It is not even agreed on which mechanism is most responsible for generating and sustaining the postulated turbulence: mechanical stirring by infalling material, or thermodynamic instabilities, such as thermal convection, or magnetohydrodynamic instabilities (more than one may apply at different epochs in the protostellar evolution). The shear for Keplerian rotation is stable, and by itself cannot drive the turbulence, but in the presence of an instability it can generate Reynolds stresses that transport mass and angular momentum. As a result, as material in the disk falls down the gravitational well of the central body, gravitational potential energy becomes available to drive turbulence in a self-sustaining manner.

Lin & Papaloizou (1980) and Cabot et al. (1987) proposed *ad hoc* — and mutually incompatible — models of Reynolds stress production in protostellar disks due to thermal convection, and it is this particular problem that motivated the work described here. We have undertaken a program of making numerical "experiments" to test various models of Reynolds stress production and convective heat transfer in differentially rotating thermal convection, and to develop better models if need be. (This problem in principle has a wider interest than the astrophysical one, for it involves the complicated interactions of thermal convection, rapid rotation, and shear in a turbulent, compressible

medium, which should provide a severe test for many turbulence models.) We also wish to determine if thermal convection can indeed generate self-sustaining turbulence in an accretion disk environment. Our objectives are (1) to study localized turbulence in circumstances approximating those found accretion disks using previously existing expertise in performing *direct numerical simulations* of turbulent, incompressible channel flows with low Reynolds number, (2) to determine the limitations of such calculations, and (3) to extend the type of numerical simulation (e.g., to include density stratification and compressibility effects and to accommodate higher Reynolds numbers with subgrid-scale modelling) so that the relevant physical effects are realistically captured.

2. Direct numerical simulations

The direct numerical simulation code of Kim et al. (1987) for an incompressible, semi-infinite channel flow was modified as described previously by Cabot (1989). The flow is homogeneous in the horizontal (x, z) directions (with periodic boundaries assumed) and inhomogeneous in the vertical (y) direction, bounded by impermeable walls. The simulation code now allows buoyancy in the vertical direction in the Boussinesq approximation; gravity can be uniform or variable. The flow must be either externally or internally heated, as the heat dissipation of kinetic energy is neglected in the internal energy equation in the incompressible limit. For the accretion disk problem, the flow is given a gravity proportional to the distance from midchannel and an imposed uniform internal heat source. The code includes imposed differential rotation about the vertical axis by integrating the governing equations in a comoving frame with a (locally) linear shear profile using Rogallo's (1981) transformation to remesh the distorted numerical grid. The boundary conditions imposed on the walls are that the vertical velocity component (v) vanishes, that the potential temperature (θ) is fixed, and that the horizontal velocity components (u, w), or their normal derivatives, vanish (no-slip or no-stress conditions, respectively). No-stress wall conditions are used almost exclusively for the accretion disk problem, as they produce weaker viscous boundary layers. (A few simulations performed with internal heating featuring an interior source and exterior sinks are observed to further reduce the viscous boundary layers.)

3. Current progress

3.1. Unsheared thermal convection

Direct numerical simulations of non-rotating thermal convection have been performed for external and internal heat sources, uniform gravity, and no-slip walls and compared favorably to prior laboratory and numerical simulation data. Sequences of simulations for different rates of uniform rotation were performed for internal heating, linearly varying gravity, and both no-slip and no-stress walls; the results of these simulations are described in Cabot et al. (1990).

The rotational (and viscous) stabilization of the thermal convection is found to agree well with linear stability analysis. Turbulence is transported efficiently through the midchannel region where gravity vanishes, leading us to model the convective heat flux by modifying mixing length models for Bénard convection with a reduced effective Rayleigh number to account for the variable gravity and with rotational stabilization based on linear analysis. The models give the correct qualitative effects of rotation, but with poorer quantitative agreement with heat fluxes and turbulence intensities, missing by as much as factors of 2.

I have begun to apply some second-order closure models (e.g., k-ε and Reynolds stress models) to the case of thermal convection with no rotation, uniform gravity, uniform internal heating, and no-slip walls, which is convectively unstable on one side and stable on the other and features an entrainment region much like planetary boundary layers (PBLs). I have therefore focused on closure models successfully applied to PBLs, e.g., Zeman & Lumley (ZL, 1976), although there are some difficulties with all such models. In contrast to the channel simulation, PBLs have an impermeable, no-slip lower surface with fixed heat fluxes and a moving, no-stress upper surface; they also feature very high Reynolds numbers. This channel simulation therefore resembles a viscous PBL with a lid on top. Aside from requiring low Reynolds number corrections, this poses a problem in applying boundary conditions using the ZL model. As matching conditions in the near-wall vicinity to the inviscid interior, ZL use similarity solutions based on the distance from the fixed wall and the positive buoyancy production term; but this approach breaks down near a fixed wall with negative buoyancy production, as occurs in the channel. I am currently exploring other ways to specify matching conditions. A related problem with some second-order closures (generally attributed to deficiencies in modelling the pressure terms) is their inability to predict realistic near-wall horizontal velocity intensities that peak due to deflection by an impermeable wall ("the splatting effect").

3.2. Differentially rotating thermal convection

Sequences of simulations with differential rotation, internal heating, linearly varying gravity, and no-stress walls have been performed most recently with (1) fixed epicyclic frequency $\kappa \equiv [2\Omega(2\Omega + S)]^{1/2}$ (measuring the mean angular momentum gradient) while varying the ratio of shear rate S to rotation rate Ω, and (2) a fixed Keplerian ratio of S to Ω $(-3/2)$ while varying κ. The orientation of the rotation, shear, and gravity are depicted in Figure 1. The latter sequences for Keplerian rotation are being performed at three different Reynolds/Prandtl numbers with fixed Péclét number to determine the effects of different viscosities for the same heating. Statistical samples are extracted when the numerical grid is orthogonal, which occurs once per b_{33}/S, where $b_{33} \geq 1$ is the ratio of the streamwise to spanwise box size. This limits us to perform simulations with moderate to rapid shear rates in terms of convective scale times.

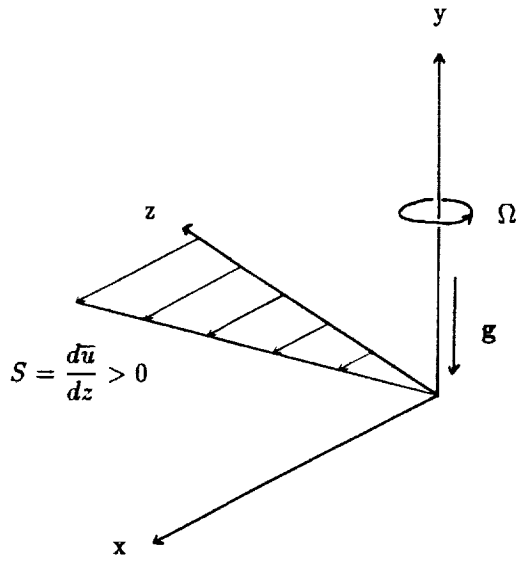

FIGURE 1. Orientation of rotation Ω, (positive) linear shear S, and gravity $\mathbf{g}$ with respect to numerical simulation coordinates.

3.2.1. Fixed κ, Re; varying S/Ω

Simulations with scale Reynolds number $Re = 559$, scale Péclét number $Pe = 112$, and scale epicyclic frequency $\kappa = 0.14$ (i.e., with fixed convective and centrifugal stabilization properties) were performed for $s \equiv S/2\Omega = 0$, -0.25, -0.50, -0.75, and -0.90 ($s = -1$ being the critical value for marginal centrifugal stability). The roughly uniform vertical profile of the Reynolds stress $-\overline{uw}$ for this value of κ is found to increase nearly homologously with shear, and its correlation $\overline{uw}/u_{rms}w_{rms}$ increases from 0 to about 0.28 for $s = 0 \rightarrow -1$; $\overline{uw}$ varies roughly as $|S|^{1/2}$ in this range ($S = \kappa s/[1+s]^{1/2}$). The cause of this apparent scaling is not yet known. Despite different degrees of elongation of convective cells in the streamwise direction and other anisotropy characteristics of u and w, statistical convection properties, such as the vertical convective heat flux, the buoyancy production rate, the convection correlation $\overline{\theta v}/\theta_{rms}v_{rms}$, and the vertical velocity variance, are only slightly affected by the presence of the shear; the turbulence time scale $\tau = q^2/\varepsilon \approx 10$ (where q^2 is twice the turbulent kinetic energy) also varies little. However, the shear-to-turbulence ratio $|S|\tau$ is only about 0.5 to 4 in these simulations, and most of the variation is seen at the high end of this range. It may therefore be instructive to do another fixed-κ sequence with higher shear rates. A characteristic of more rapid rotation and shear rates is that $\overline{uw}$ becomes negative in regions near midchannel and at the walls, and a fixed-κ sequence in this regime would especially test the homology of the Reynolds stress profile for different values of s.

3.2.2. Fixed (Keplerian) S/Ω; varying κ, Re

Three sequences of Keplerian rotation simulations with $Re = 559$, 1000, and 1789 were performed for $\kappa = 0.14$, 0.25, 0.45, 0.61, and 0.80. The scale Péclét number $Pe = 112$ for all simulations. It was necessary to increase the mesh size from $64 \times 33 \times 64$ for $Re = 559$ (where 33 is the vertical) to $96 \times 49 \times 96$ for $Re = 1000$ and $128 \times 65 \times 128$ for $Re = 1789$. (Some runs are still in progress, and some results are presented for more coarsely meshed grids than indicated above and/or with minimal statistics.)

There are two distinct trends that are evident from these simulations. The first is tendency for the Reynolds stress $-\overline{uw}$ to change sign near the wall and midplane regions for rapid rotation, where there is significant rotational stabilization of the convective flow, such that the net shear production of turbulent kinetic energy becomes negative. This is seen in Figure 2, which depicts the ratio of net shear to net buoyancy production in the channel and the average Reynolds stress correlation versus epicyclic frequency. The epicyclic frequency κ_o where the Reynolds stress changes sign is seen to be a sensitive function of Re. The rough progression of $\kappa_o \approx 0.4$, 0.6, 0.7 for $Re = 559$, 1000, 1789 may suggest asymptotic dependences for κ_o like $\alpha \exp(-\beta/Re)$ with $\alpha \approx 1$ and $\beta \approx 500$ or $a/[1 + (b/Re)^2]$ with $a \approx 0.75$ and $b \approx 500$, which imply that there is always negative net shear production for $\kappa > 1$ at this value of Pe. However, higher-Re data is needed to confirm the accuracy of this estimate, and runs with different Pe are needed to determine its dependence on convective efficiency.

The second major trend seen in these sequences of simulations is the tendency of the channel flow to become two-dimensional (but still three-component) for $\kappa > \kappa_1$, where $\kappa_1 \leq 0.8$ regardless of the value of Re. In such simulations the streamwise autocorrelation functions for v and θ (and u and w at some depths in the channel) remain constant and large (typically ≥ 0.6) at large separations; namely, most of the power in these variables is found at (or very near) $k_x = 0$. Increasing the box size in the streamwise direction has no ameliorating effect on the autocorrelation functions. As a result, the spectral code is unable to resolve the streamwise direction, making any statistics therefrom untrustworthy. The energy spectra in the spanwise direction tend to have a lot of power concentrated at a particular (finite) value of k_z. The onset of this regime is perhaps governed by a critical Richardson number of some sort composed of the shear rate and a convective time scale (perhaps depending on Pe). The shear causes the flow to become two-dimensional in the linear analysis, and it is only the effect of buoyancy production of turbulence that counters that trend. The shear-to-turbulence ratio $|S|\tau$ appears to be between about 7 and 9 (depending on Re) at the onset of two-dimensionality.

Note from Figure 2b that the maximal Reynolds stress correlations appear to be not much greater than 0.2 (and probably less than 0.25) for all cases, although the maxima are not that well defined by the simulation data. Vertical

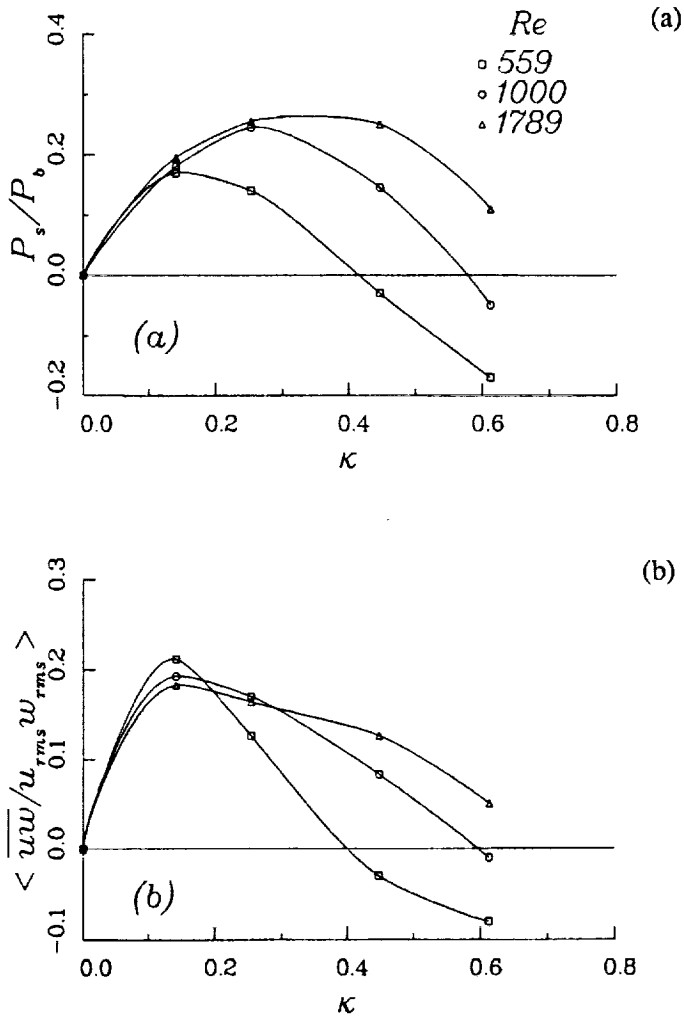

FIGURE 2. (a) The ratio of volume-averaged shear production rate P_s to buoyancy production rate P_b and (b) the volume-averaged Reynolds stress correlations at different epicyclic frequencies κ for Keplerian rotation (shear rate $S = -1.5\kappa$).

profiles of the Reynolds stress correlation are shown in Figure 3a for $Re = 559$ at different κ, in which the progression of positive to negative values at the walls and midchannel is seen. Note the region of positive values around $y = \pm 0.6$, which persists for all shear rates; this is probably not directly related to the buoyancy production peaks at about $y = \pm 0.7$, but is rather a reaction to impermeable walls, like "splatting", regulated by pressure effects. The regions of positive $\overline{uw}$ move to $y = \pm 0.7$ for $Re = 1789$, and the wall regions of negative $\overline{uw}$ have thicknesses that scale roughly as $Re^{-1/2}$ and are comparable to the

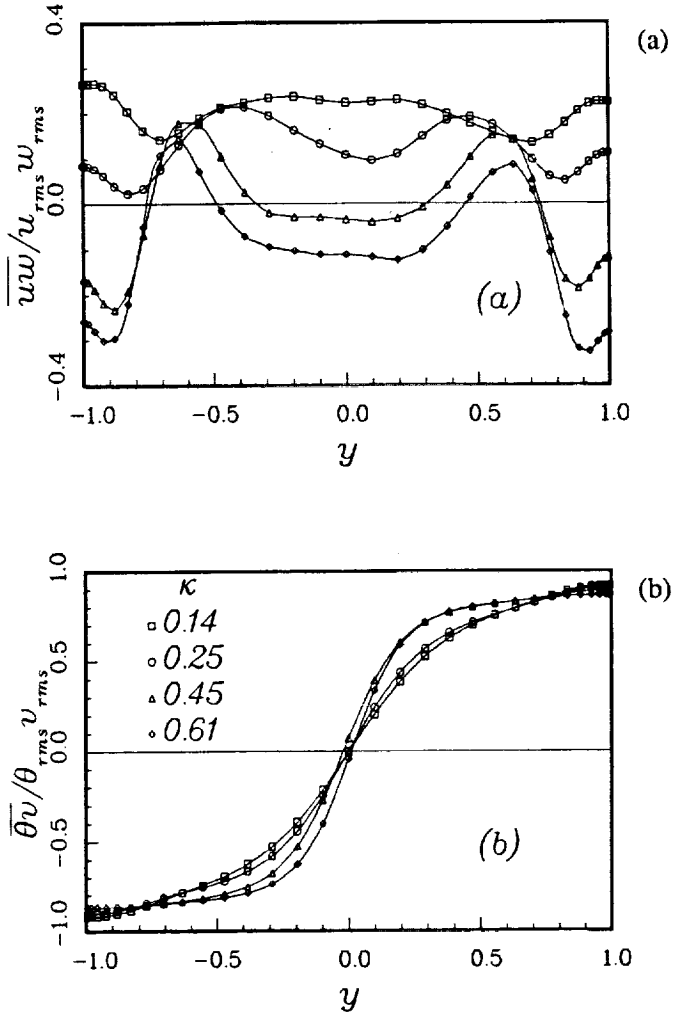

FIGURE 3. Vertical profiles of (a) Reynolds stress and (b) convective flux correlations for Keplerian rotation and $Re = 559$.

viscous length $(\nu q^2/\varepsilon)^{1/2} = (\tau/Re)^{1/2}$. We also note again that properties of vertical heat convection are not greatly altered by the Keplerian shear. For example, Figure 3b shows the vertical profiles of the convection correlations for the same cases as Figure 3a.

Statistics for terms in the governing equations of $\overline{uu}$, $\overline{vv}$, $\overline{ww}$, and $\overline{uw}$ are being accumulated, which include pressure-strain rates. The normal pressure-strain components tend to become concentrated near the walls for larger rotation/shear rates. The pressure-strain component for $\overline{uw}$ remains more evenly distributed and largely balances the production term in the interior; about a viscous length from the walls the production features positive peaks that are

not balanced by pressure-strain (but rather by diffusion), and this appears to be directly related to the positive-$\overline{uw}$ regions seen in Figure 3a. I have yet to explain adequately what controls the appearance of the negative-$\overline{uw}$ regions, especially in the interior where we expect (hope) that wall effects are minimal. It is clear, though, that near-wall models will be crucial for an accurate overall representation of such flows. The dissipation rates for the normal velocity components follow the trends of the normal velocities; this is also true for $\overline{uw}$ at lowest Re, with $\overline{uw}$ and its dissipation becoming negative at the walls, but at the higher Re the dissipation rate stays positive definite, even though $\overline{uw}$ goes negative, and is distributed like dissipation rates for $\overline{uu}$ and $\overline{ww}$. This has implications for modelling, for it shows how the low-Re component of dissipation behaves differently than the high-Re asymptote.

4. Discussion

From the preceding work, we are able to make a few tentative conclusions about the nature of thermal convection in a differentially rotating, centrifugally balanced disk, although there are several deficiencies in the incompressible simulations when it comes to describing the actual physics in protostellar accretion disks. The incompressible calculations have, however, provided a number of insights into the course that future endeavor should take.

4.1. Present conclusions

Most of the properties of vertical heat transport by convection are not drastically affected by the rotational shear (at least in the regime of three-dimensional turbulence), which means that results from simulations with uniform rotation can be used more widely for differential rotation cases with the same epicyclic frequency κ. Since $\kappa \geq 1$ in protostellar disks, we conclude that convective efficiencies are much less (by over an order of magnitude) than for no rotation, as was assumed in the mixing length models by Lin & Papaloizou (1980).

Turbulent shear stresses that can, in principle, transport angular momentum are produced by thermal convection in the presence of differential rotation, but they are found to be very sensitive to the rotation and shear rates, as well as the viscosity. There is a possibility that the flow may develop negative shear production of turbulent kinetic energy, which is a pathological (i.e. unsustainable) situation in accretion disks, as well as becoming nearly two-dimensional. Some of this behavior is undoubtedly due to weakening of the thermal convection by rotational stabilization, but there are also clearly strong viscous/wall effects that need to be disentangled. Nevertheless, the present simulations suggest that the conversion of thermal convection to Reynolds stress is less efficient than commonly assumed in protostellar disk models with a maximal Reynolds stress correlation for thermal convection of about 0.25 and a maximal value of $\overline{uw}/q^2$ of about 0.06, which is an order of magnitude less than in the standard solar nebula model of Lin & Papaloizou.

4.2. Deficiencies in the numerical simulations

4.2.1. Incompressible flows

Codes that simulate incompressible flows, including those in the Boussinesq approximation, cannot take into account the large density variations and acoustic waves that occur in nature. In accretion disks the regions of interest cover several density scaleheights, and some disturbances are likely to develop strong acoustic components, if not weak shocks. Another property of density stratification is the occurrence of convectively stable exterior regions where radiation-dominated emissivities grow as ρ^{-2} and cause the temperature gradient to decline to subadiabatic levels; this stable buffer zone in principle can damp exterior disturbances and make them less susceptible to less-than-physical (i.e. numerically convenient) boundary conditions. This would mitigate the direct effects of impermeable walls on the turbulence properties, which has already been seen to be a problem in the incompressible simulations.

4.2.2. Low Reynolds numbers

Accretion disks feature very large Reynolds numbers (but moderate Péclét numbers), and this means that direct numerical simulations are susceptible to unrealistic viscous effects. Low Reynolds numbers also stabilize convection in the direct numerical simulations at lower rotation rates than are expected in accretion disks. It is therefore desirable to attain higher Reynolds numbers (preferably in conjunction with more realistic boundaries) in order to minimize viscous effects, as well as to provide more stringent tests on asymptotic relations, such as for the Reynolds stress production in §3.2. In order to accomplish this goal, modelling of the subgrid scales is required.

4.2.3. Self-consistent energy balance in protostellar disks

An important question for convective accretion disks is whether or not they can quasistatically sustain thermal convection by tapping the gravitational energy released from torqued disk material, and what internal heating distribution arises. In the incompressible governing equations, terms in the internal energy equation involving the adiabatic temperature gradient, the pressure work, and the heat dissipation of kinetic energy are formally neglected. Internal heating is imposed on the flow. This makes it impossible to determine consistently the energy balance in the disk.

For simulations of thermal convection in a compressible channel flow (e.g., see Thompson, 1989), where all of the previously neglected internal energy terms are included, there is still a problem in making a realistic, self-sustaining balance. The heating distribution in the channel with no imposed heat source will equal the heat dissipation of turbulent kinetic energy less the pressure work, with net heating equal to the net shear production, since the pressure-work precisely balances the buoyancy production of turbulent kinetic energy. The energy source

(sink) for a positive (negative) net shear production is supplied in the channel by the work done to maintain the imposed rotational shear rate. It is not clear what vertical profile of heating would result, nor even if a self-sustaining state exists. The problem is that one cannot relate this heating to the release of gravitational energy, which depends on the radial (spanwise) gradient of the stress, when the spanwise direction is assumed to be homogeneous in the channel flow. In a real accretion disk, the local heating is supplied by a combination of comparable amounts of gravitational energy and annular stresses that maintain the Keplerian rotation. To do this problem consistently, we clearly need to abandon homogeneity in the spanwise direction.

4.3. Future directions

4.3.1. Modelling

I am pursuing second-order (Reynolds-stress) modelling of the incompressible simulation results, starting at the simple case of uniform gravity and uniform heating in the channel (with the attempted development of better wall matching conditions and near-wall models). Next I plan to move to cases with vertically varying gravity, initially testing the simple replacement of derivatives of the convective flux with derivatives of the buoyancy production rate containing the variable buoyancy term. If these prove successful, then modelling of cases with uniform rotation and differential rotation can proceed. Such tests should be useful for testing the limits of current models and, if reasonably successful, could be used to approximate some properties of accretion disks. Since simplified forms of second-order closure models are commonly used as subgrid-scale models, these tests could conceivably help to verify or improve them.

In principle, density stratification in the Boussinesq approximation can be included in a straightforward way in the modelling, but general compressible effects will require careful consideration of dilitation and shock effects, like the model proposed by Zeman in this volume.

It must also be determined if two-dimensional flows occurring at rapid shear rates can be made tractable to (perhaps simpler) modelling or different numerical simulation techniques.

4.3.2. Direct numerical simulations

Although useful direct numerical simulations of the incompressible flow for application to protostellar disks have been nearly exhausted, there are a few trial runs that could prove interesting. First, a few simulations with uniform rotation have been done with a centrally peaked heat source and large heat sinks near the walls (approximating the effects of a large adiabatic gradient), which provides a convectively stable exterior and greatly weakened viscous wall layers. It would be interesting to repeat some of these simulations with differential rotation and compare the production of turbulent shear stress to simulations with uniform heating in order to gauge the qualitative effects of the walls. Second, to test

for self-sustaining states, simulations could be attempted for developed, internally heated convection in which the imposed internal heat source is replaced with some function whose net heating is comparable to it, but which is directly proportional to the shear production rate. The same test with a compressible channel code can be made more easily, since the frictional heating due to turbulence is already consistently included, and once the imposed internal heat source is turned off the convection can conceivably feed off of the work done to impose the constant shear.

Once the compressible channel code being developed by Thompson (1989) is in production, we will be able to repeat similar sequences in parameter space that have been done with the incompressible code, and we will be able to assess realistic density stratification and compressibility effects in protostellar disks. As noted above, though, the exact energy balance in a real protostellar disk requires relaxation of spanwise homogeneity, and the concomitant use of periodic boundary conditions, in order to generate torques. A scheme needs to be devised to specify spanwise (radial) gradients in a consistent way. It may also not be much more trouble to include previously neglected curvature terms.

Finally, a wider range simulations with density stratification and/or compressibility, not confined to such a narrow application as discussed here, would prove useful fodder for, e.g., second-order closure models. We would have more confidence in applying or extending those models that have proven themselves under a wide range of circumstances.

4.3.3. Large-eddy simulations

In order to obtain more realistically high Reynolds numbers and to make determine better high-Re asymptotic behavior, we must inevitably perform large-eddy simulations in which the smallest scales are modelled rather than resolved. For buoyancy-driven (incompressible) flows, commonly used subgrid-scale (SGS) models are ones based on second-order closure models (e.g., Schmidt & Schumann, 1989) and on buoyancy-modified Smagorinsky models (e.g., Mason, 1989). It would be of interest to incorporate these into numerical simulations for Boussinesq convection in order to gain expertise with SGS modelling and to extend our results to higher Reynolds numbers. Because we are interested in very low Prandtl number flows, thermal fluctuations become unimportant at much lower wavenumbers than velocity fluctuations, which could either cause resolution problems due to the scale dichotomy or simplify matters by allowing resolution of all relevant thermal scales and modelling of smaller velocity scales.

An important consideration is testing the ability of SGS models to provide accurate results at moderate to high Reynolds numbers. Unfortunately, there are no astrophysical flows that can be resolved well enough to provide accurate data for such testing. (This is why we're using numerical simulations in the first place!) For buoyancy-driven flows, planetary boundary layers have received a

lot of attention, and data exists for internally heated fluids in a uniform gravity. Laboratory experiments with rotating Bénard convection have also been performed. Other terrestrial or laboratory flow fields with rotation and shear effects need to be found or devised to test SGS models.

The development and testing of *compressible* SGS models is crucial to simulating accretion disks and other astrophysical systems in which acoustic waves are believed to transport energy to rarefied regions and deposit heat through shocks. Shocks in low-viscosity media by nature are narrow and difficult to resolve numerically. Again finding pertinent, terrestrially realizable test-cases will be the rub.

4.3.4. Magnetohydrodynamics

Finally, magnetic fields are known to be important in stars, energetic accretion disks, and in the collapse of molecular clouds to protostars. The importance of magnetic fields in protostellar disks is still problematic. Simulating the interaction of magnetic fields with convected and/or sheared turbulent flow in different systems is thus of fundamental interest, but something that has been largely neglected heretofore.

Acknowledgements

This work is being done in collaboration with J. B. Pollack and P. Cassen (NASA-Ames) and K. W. Thompson (CTR).

REFERENCES

BLACK, D. C. & MATTHEWS, M. S. 1985 *Protostars & Planets II*, University of Arizona Press, Tucson.

CABOT , W. 1989 Direct numerical simulations of turbulent convection with a variable gravity and Keplerian rotation. *CTR Annual Research Briefs - 1988.* , 121–125.

CABOT, W., CANUTO, V. M., HUBICKYJ, O. & POLLACK, J. B. 1987 The role of turbulent convection in the primitive solar nebula. *Icarus.* **69**, 387–422, 423–457.

CABOT, W., HUBICKYJ, O., POLLACK, J. B., CASSEN, P.& CANUTO, V. M. 1990 Direct numerical simulations of turbulent convection: I. Variable gravity and uniform rotation. *Geophys. Astrophys. Fluid Dyn.* in press.

KIM, J., MOIN, P. & MOSER, R. 1987 Turbulence statistics in fully developed channel flow at low Reynolds number. *J. Fluid Mech.* **177**, 133–166.

LIN, D. N. C. & PAPALOIZOU, J. 1980 On the structure and evolution of the primordial solar nebula. *Mon. Not. R. Astron. Soc..* **191**, 37–48.

MASON, P. J. 1989 Large-eddy simulation of the convective atmospheric boundary layer. *J. Atmos. Sci.*. **46**, 1492–1516.

PRINGLE, J. E. 1981 Accretion discs in astrophysics. *Ann. Rev. Astron. Astrophys.* **19**, 137–162.

ROGALLO, R. S. 1981 Numerical experiments in homogeneous turbulence. *NASA Tech. Mem.* 81315.

SCHMIDT, H. & SCHUMANN, U. 1989 Coherent structure of the convective boundary layer derived from large-eddy simulations. *J. Fluid Mech.* **200**, 511–562.

THOMPSON, K. W. 1989 Turbulent transport in the solar nebula. *CTR Annual Research Briefs - 1988.* 107–114.

ZEMAN, O. & LUMLEY, J. L. 1976 Modeling buoyancy driven mixed layers. *J. Atmos. Sci.* **33**, 1974–1988.

Patterns in simulated turbulent channel flow

By D. Stretch

1. Motivation and objectives

The arrival of direct numerical simulations as a practical research tool for studying the fundamental physics of turbulent flow has provided data of unprecedented detail. The volume of data available, however, presents its own difficulties and has generated a need for new methods of interrogating the available data and extracting information of physical importance.

The detailed nature of databases from numerical simulations makes them ideally suited to studying the spatial structure or topology of the flow kinematics. The identification of organized motions or coherent structures in turbulent flows is a controversial area of research. The key difficulty is the specification of appropriate criteria for the identification of these structures. In particular, the subjectivity often associated with such choices is a major drawback. One consequence of this is that different researchers, using different criteria, have "discovered" a variety of structures, and it remains unclear how they are related to one another. For example, flow visualization experiments have shown that elongated low and high speed streaks are characteristic of the flow near the wall (e.g. Kline et al, 1967), while inclined horseshoe or hairpin shaped vortices have apparently been observed in the outer flow (e.g Head & Bandyopadhyay, 1981). Similar vortices have also been observed in the near wall region (e.g. Britter & Stretch, 1985; Robinson et al, 1989). Conditional sampling analyses have shown that protruding shear layers are common features of the near wall flow, and are associated with a large contribution to turbulence production (Johansson et al, 1987). Analysis of the flow kinematics using the method of proper orthogonal decomposition, which employs a global optimization criterion, has also been carried out to yield quasi-streamwise vortices in the near wall region, with attached double-roller eddies spanning the flow (Moin & Moser, 1989).

The surface stress is a key diagnostic in wall-bounded turbulent flows. Large fluctuations in the stress are believed to be associated with intermittent "bursting" events during which a large proportion of the turbulence production takes place. If this is so, then a detailed investigation of the structure of the surface stress and its spatial relationship to events within the flow could have wide application in drag reduction and other aspects of flow control. The initial phase of this research project, therefore, concentrated on the surface stress field.

The main objectives of the research project may be summarized as follows.

(a) Carry out a statistical analysis of the instantaneous surface stress in a simulated turbulent channel flow, including comparison with multi-point experimental data from a zero pressure gradient turbulent boundary layer (Britter

and Stretch, 1985).

(b) Apply a simple pattern-recognition procedure to educe the characteristic spatial structure of various flow diagnostics. Initially attention was focused on the instantaneous streamwise component of the surface stress. The objective was to investigate the relationship between characteristics features of the surface stress and dynamically significant events occurring within the flow.

(c) As initially implemented the pattern analysis was restricted to investigating the structure of a scalar diagnostic (such as the streamwise surface stress fluctuations) in two spatial dimensions. A final objective of this program was to extend the pattern recognition analysis to examine the whole 3-D structure of the flow. One of the main questions we wished to address was "What are the spatial relationships among the many different kinematic structures that have been proposed by previous investigators?".

2. Outline of the pattern recognition methodology

The pattern recognition method used for the present study is based on work by Townsend (1979), Savill (1979) and (particularly) Mumford (1982,1983). Recent applications of this pattern analysis method have been reported by Ferre and Giralt (1989a,b). These studies were all concerned with the analysis of multipoint experimental measurements in turbulent wakes and boundary layers, and were confined to locating flow patterns in a 2-dimensional plane of data. The present study seems to be the first application of this type of approach to data from numerically simulated turbulent flow. This has allowed the full 3-D structure of the flow to be studied using an extension of the method employed by the above-mentioned authors. The low Reynolds number simulation of turbulent channel flow by Kim, Moin and Moser (1987) was the primary source of data for the present study ($Re_\theta = 287$).

In general terms the objective of the pattern recognition analysis is to educe a statistically significant spatial organization of a given flow diagnostic. For example, suppose the flow diagnostic is smoke or dye concentrations resulting from injection into the sublayer of a turbulent boundary layer. If an ensemble of photographs showing the structure of the smoke (dye) concentration field just downstream of the injection position is examined, it is clear that a streaky pattern would be recognized as the most probable spatial organization of that flow diagnostic. Note that in order to recognize this, a translational invariant pattern recognition method is required, since the streaks may be at different spanwise locations at the instant of each photograph.

Details of the pattern recognition strategy may be outlined as follows. Consider a field of data $D(\mathbf{x})$, which for present purposes is assumed to be a scalar function of a position vector $\mathbf{x} \in \mathbf{R}^3$.

$$D(\mathbf{x}) = \{d(i,j,k),\ 0 \le i \le n_1,\ 0 \le j \le n_2,\ 0 \le k \le n_3\}$$

In the present context D is some chosen diagnostic of the turbulent field. Note that the pattern analysis procedure can easily be generalized to include time evolution and vector functioned diagnostics. We now define a pattern field $P(\hat{\mathbf{x}})$, a scalar function of the position vector $\hat{\mathbf{x}} \in \mathbf{R}^3$.

$$P(\hat{\mathbf{x}}) = \{p(i,j,k),\ 0 \leq i \leq m_1,\ 0 \leq j \leq m_2,\ 0 \leq k \leq m_3\}$$

where $m_1,\ m_2,\ m_3 \leq n_1,\ n_2,\ n_3$.

The first step in the pattern analysis is to initialize the pattern field $P(\hat{\mathbf{x}}) = P_0(\hat{\mathbf{x}})$. Next a convolution is performed between the pattern and the data fields.

$$C(\mathbf{x}) = P(\hat{\mathbf{x}}) * D(\mathbf{x})$$

Patterns which have a shape similar to the input pattern P are then located in the data field D by searching for all the local maxima in the convolution function C. Note that there is no threshold criterion used in the pattern selection (although it is, of course, simple to include one if desired). Once the patterns have been located in the data they are extracted and ensemble averaged to yield an updated estimate of P, and the process is repeated. The iterative procedure results in a pattern P which on average has the best correlation with the instantaneous patterns located in the data field D.

Note that the pattern recognition method does not employ an absolute criterion for locating patterns. The pattern selection depends on a relative criterion, namely that locally the flow kinematics are more similar to the reference pattern P than elsewhere in that neighbourhood, where the measure of similarity is the magnitude of the convolution (or cross-correlation) between the reference pattern and the data. The use of convolution for pattern recognition is a well established and tested method (see e.g. Duda and Hart, 1973)

The pattern analysis procedure outlined above has translational invariance but not scale or rotational invariance; it is assumed that the patterns can occur at any position $\mathbf{x}$ in the data, but the orientation and size of the patterns is always assumed to be the same. It is possible to include scale and rotational invariance in pattern recognition schemes such as this one, but it involves considerable complication of the analysis, and thus has not been implemented to date.

It shall be shown later (by examples) that the results of the pattern search do not appear to be sensitive to the choice of initial pattern P_0. In the present investigation P_0 was usually specified so that the first iteration simply performed a spatial averaging operation in one plane of the 3-D data field.

The results of the pattern analysis may be assessed in a variety of objective tests. For example, the statistical significance of the ensemble averaged patterns P may be tested using standard methods from sampling theory. The proportion of the data volume occupied by the patterns and the similarity between the ensemble averaged pattern P and the instantaneous flow field is information available directly from the pattern recognition algorithm.

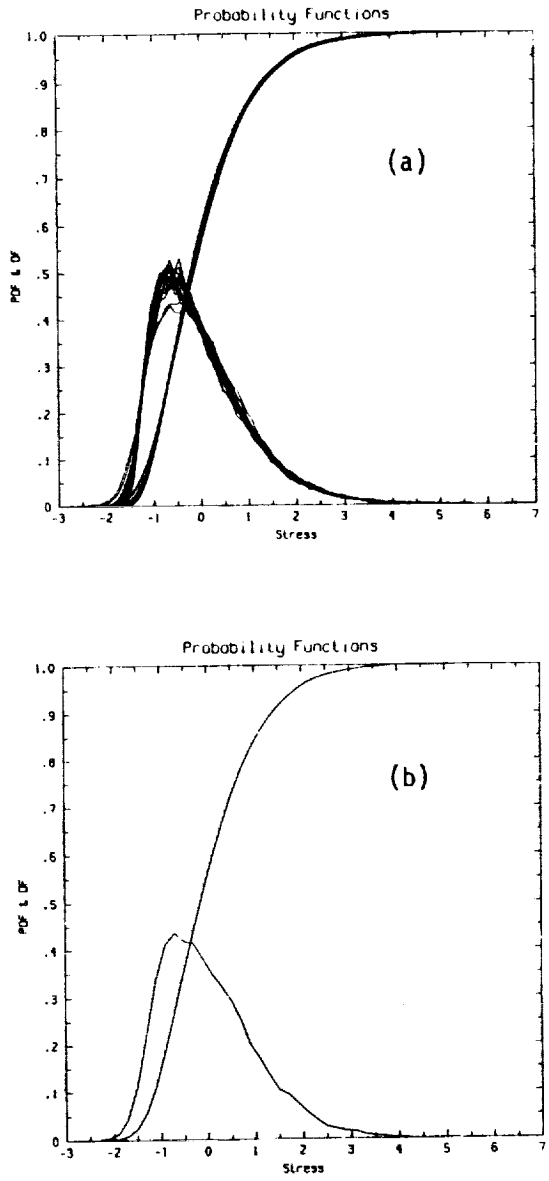

FIGURE 1. Probability density and distribution functions for the streamwise surface stress fluctuations : (a) experimental data $915 \leq Re_\theta \leq 2140$, (b) simulation data $Re_\theta = 287$. The stress fluctuations are normalized by their rms values.

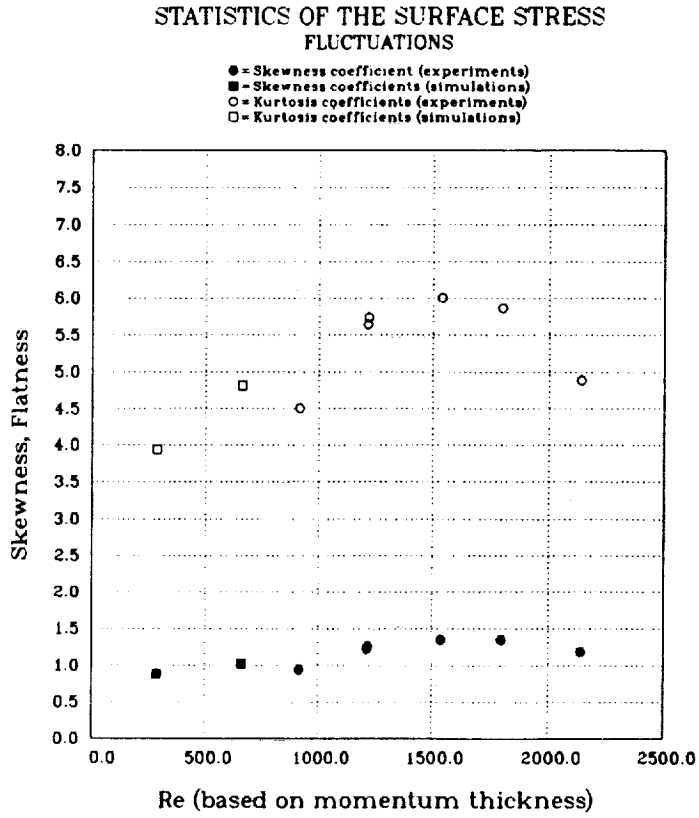

FIGURE 2. Skewness and kurtosis coefficients of the streamwise surface stress fluctuations from experiments and simulations.

3. Summary of results

3.1 One-point statistics

The basic 1-point statistics for the streamwise surface stress fluctuations from both the simulations and experiments are shown in figures 1 and 2. The probability density functions of the stress fluctuations are positively skewed and have a kurtosis somewhat higher than a Gaussian distribution. Values for the skewness and kurtosis coefficients $S = \overline{\tau^3}/\tau'^3$, $F = \overline{\tau^4}/\tau'^4$ from the experimental measurements are in the range $1.0 \leq S \leq 1.6$ and $4.0 \leq F \leq 6.0$, which may be compared with the Gaussian values $S = 0$ and $F = 3$. The experimental data show a slight increase with Reynolds number. The simulation results of $S = 0.88$, $F = 3.9$ at a low Reynolds number $Re_\theta \simeq 287$ are consistent with this trend. Preliminary simulation results at $Re_\theta \simeq 660$ (also shown in fig 1) are $S = 1.06$ and $F = 5.04$, which is also consistent with the experiments. The skewness in the surface stress is apparently caused by the way the low and high stress regions

are generated. High surface stresses are associated with the "sweep" (or fourth quadrant, Q4) event during which high-speed fluid moves toward the wall. Low stresses are associated with the "burst" (or second quadrant, Q2) event during which low speed fluid moves away from the wall. The low speed fluid involved in the burst must be drawn from regions near the wall and at the sides of the event, a motion which is apposed by the strong viscous stresses in the sub-layer.

The ratio of the root mean square streamwise stress fluctuations to the mean wall stress was experimentally determined to be $\tau'/\overline{\tau} = 0.4 \pm 0.1$, increasing slightly with Reynolds number. The simulation results are 0.36 and 0.39 at $Re_\theta = 287, 660$ respectively, again in reasonable agreement with the experiments.

From the probability density function, it can be seen that the instantaneous streamwise surface stress is less than the mean value for 55 – 60% of the time (increasing with Reynolds number). The most probable value is approximately $0.5\tau'$ below the mean. The pdf drops off sharply at $2.0\tau'$ below the mean. Note that since $\tau'/\overline{\tau} \simeq 0.4$, stress fluctuations exceeding $2.5\tau'$ below the mean would imply reversed flow adjacent to the wall. From the pdf's it appears that the instantaneous (near) surface streamlines are topologically free of critical points, or at least that their occurrence is extremely rare.

3.2 Two-point statistics

Two-point correlation functions for streamwise and transverse separations are shown in figure 3. The experimental data and simulation results are shown with separations scaled on wall variables ν and $u_\star$. A streamwise advection velocity of $10u_\star$ for the stress fluctuations was measured experimentally using two-point measurements with streamwise separations. This value is consistent with those obtained from previous analyses of the simulation data bases (Alfredsson et al (1988), Johansson et al (1987), Guezennec et al (1987), Hussain et al (1987), Swearingen et al 1987). If this advection velocity is used to convert the time series experimental measurements to a spatial analog there is surprisingly good agreement with the simulation results. Conclusions regarding the scaling of the two-point correlations on wall variables should, however, be made with care, since the range of Reynolds number covered by the data is limited.

The two-point correlations for spanwise separations do not scale as well as those for streamwise separations; there is a decrease in the magnitude of the negative loop for $\triangle z^+ \geq 40$ with increasing Reynolds number. This trend has been tentatively confirmed by the preliminary channel simulations at $Re_\theta \simeq 660$ and by the boundary layer simulations of Spalart (1988). The reason for this effect is not clear, but it probably reflects the broader range of scales in the higher Reynolds number cases.

3.3 Results of 2-D pattern analyses

The application of the pattern analysis to the simulation data was begun using 2-D data comprising the streamwise component of the fluctuating surface

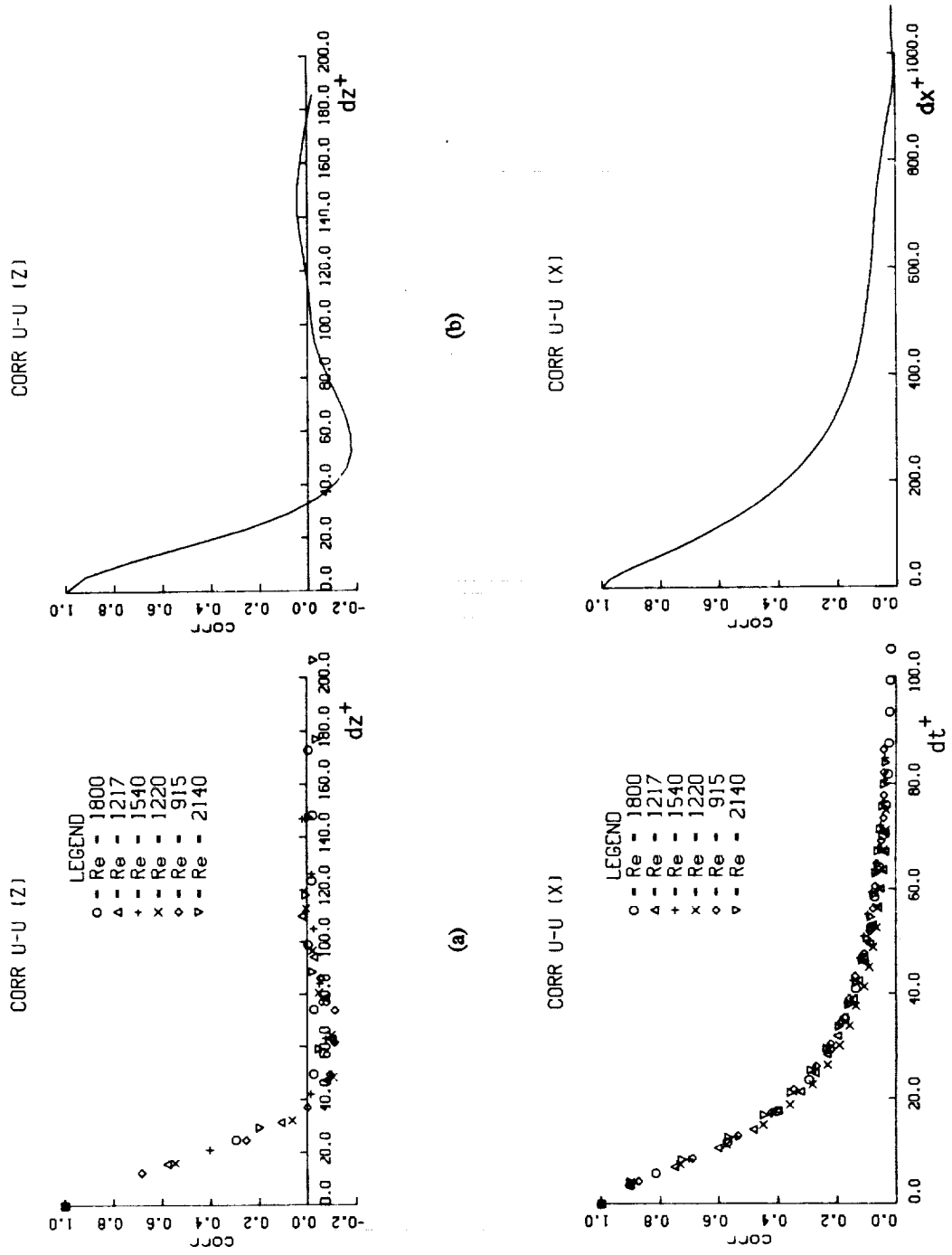

FIGURE 3. Two point correlation functions of the streamwise surface stress fluctuations : (a) experiments, (b) simulations.

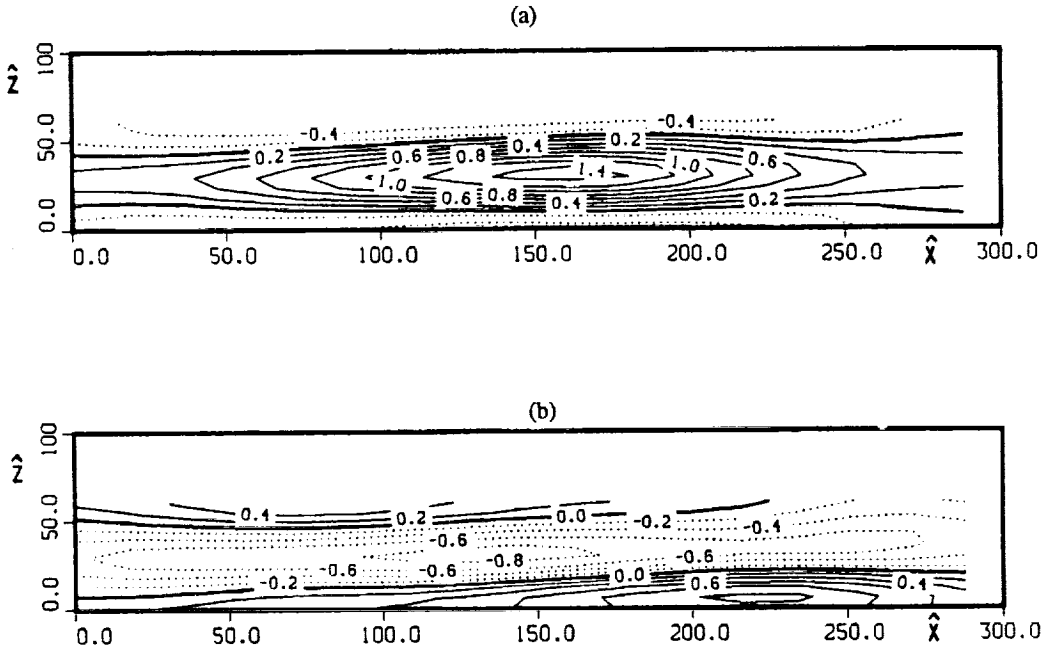

FIGURE 4. Results from a 2-D pattern analysis of the streamwise surface stress fluctuations : (a) high stress regions, (b) low stress regions. The stress fluctuations are normalized their rms values. Dotted lines are used for negative values.

stress at the wall. Several data fields consisting of 128×128 values of the stress, spaced as $\Delta x^+ = 18.0$, $\Delta z^+ = 6.0$, were used for the analyses. The results were compared with those from similar analyses of multi-point experimental measurements.

Using a simple spatial filter as the initial pattern for the iterative pattern analysis, the structure of locally high and low stress regions were investigated. For example, initial patterns defined by

$$p_0(i,j,k) = \begin{cases} \pm 1, & \text{if } 7 \le i \le 11,\ j = 1,\ 3 \le k \le 9; \\ 0, & \text{otherwise.} \end{cases}$$

where the pattern size was $m_1 = 17$, $m_2 = 1$, $m_3 = 11$, were used to obtain the results shown in figure 4. Five iterations were performed to obtain this result, although there was little variation after the second iteration.

The high- and low-stress patches have some distinct characteristics. High stress regions have a larger amplitude and are somewhat more localized in space than the low stress regions. Non-dimensionalized with the inner variables ν and $u_\star$, the amplitudes and scales of these stress patterns have been found to be broadly consistent with those educed from experimental data.

3.4 Results of 3-D pattern analyses

The data used for the 3-D pattern analysis comprised fields of $128 \times 128 \times 16$ values in the x, z, and y directions respectively, spaced as $\Delta x^+ = 18.0$, $\Delta z^+ = 6.0$ and $\Delta y^+ \simeq 10.0 \pm 0.1$.

Pattern analyses for a range of different flow diagnostics and initial patterns P_0 have been performed. The examples described below illustrate some of the main results. Note that all references to lengths or positions are non-dimensionalized using the length scale $\nu/u_\star$. Velocities are non-dimensionalized with $u_\star$, and vorticity by the scale $u_\star/\delta$, where δ is the channel half-width (dividing by 180 gives values of the vorticity scaled by ${u_\star}^2/\nu$). Furthermore, co-ordinates x, y and z refer to the data space D, while $\hat{x}$, $\hat{y}$ and $\hat{z}$ refer to the pattern space P.

Example 1 : Diagnostic = streamwise velocity fluctuations.

In this example, a simple initial pattern P_0, which was designed to select near-wall shear layers in the first iteration, was used. That is

$$p_0(i,j,k) = \begin{cases} +1, & \text{if } 10 \le i \le 15,\ j = 2,\ 3 \le k \le 13; \\ -1, & \text{if } 17 \le i \le 22,\ j = 2,\ 3 \le k \le 13; \\ 0, & \text{otherwise.} \end{cases}$$

where the pattern size was $m_1 = 31$, $m_2 = 15$, $m_3 = 15$. Note that the indices i, j, and k refer here to the streamwise ($\hat{x}$), normal ($\hat{y}$), and spanwise ($\hat{z}$) directions respectively. Only horizontal translations were allowed in this pattern search.

The results of the pattern eduction are shown in figure 5. After 4 iterations, the educed pattern is seen to comprise asymmetric high and low speed regions in the xz plane at $\hat{y}^+ = 10$. Note the occurrence of smaller scale high and low peaks within the elongated "streaks". These high/low pairs seem to occur alongside one another separated by $\Delta\hat{z}^+ \simeq 50$. An xy cross-section through the pattern at $\hat{z}^+ = 42$ is also shown in figure 5. An elevated shear layer typical of those obtained by conditional sampling methods can be seen.

Ensemble averages of flow diagnostics other than the streamwise velocity fluctuations were examined in the regions centered around the located patterns. The streamwise vorticity is shown in the yz plane at $\hat{x}^+ = 270$ (figure 5c), and in the xy plane at $\hat{z}^+ = 42$ (figure 5d). It can be seen that a single dominant positive streamwise vortex is associated with the near-wall high/low peaks in the u field.

In this example, 57 patterns were identified in a single data field D. The average value of the normalized cross-correlation coefficient between the final ensemble averaged pattern and the 57 instantaneous patterns was 0.36. The data used to obtain the ensemble average comprised 82% of the whole $128 \times 128 \times 16$ data field. These figures are typical of all the cases described here.

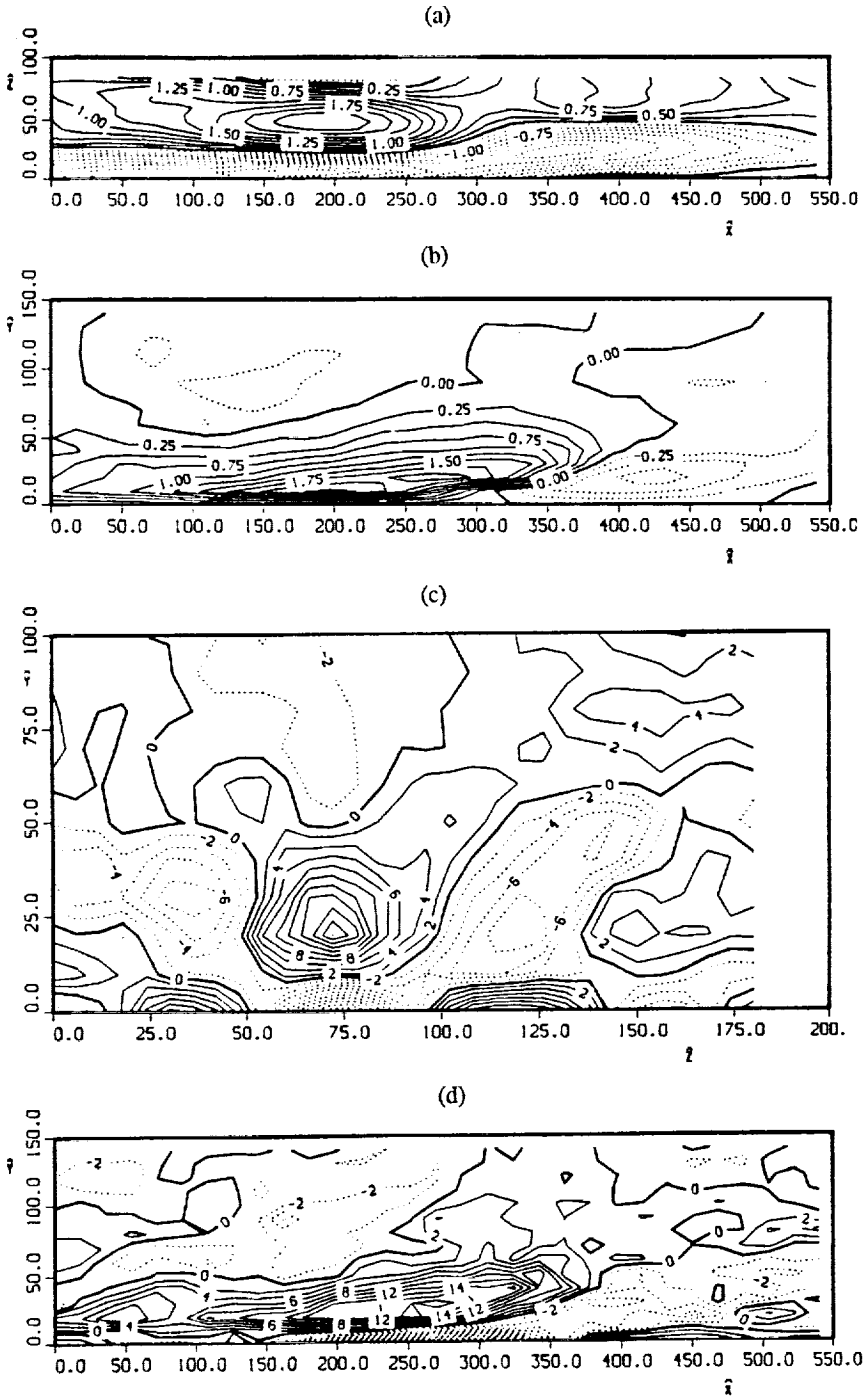

FIGURE 5. Results from example 1 of the 3-D pattern analysis: (a) u field in xz plane at $\hat{y}^+ = 10$, (b) u field in xy plane at $\hat{z}^+ = 42$, (c) ω_x field in zy plane at $\hat{x}^+ = 270$, (d) ω_x field in xy plane at $\hat{z}^+ = 50$. Velocity fluctuations are normalized by $u_\star$ and vorticity fluctuations by $u_\star/\delta$. Dotted lines are used for negative values.

Example 2 : Diagnostic = streamwise vorticity (near wall).

In this example the initial pattern field P_0 was chosen to perform a simple spatial averaging in the yz plane. That is

$$p_0(i,j,k) = \begin{cases} +1, & \text{if } i = 8,\ 2 \leq j \leq 4,\ 2 \leq k \leq 8; \\ 0, & \text{otherwise.} \end{cases}$$

where the pattern size was $m_1 = 15$, $m_2 = 5$, $m_3 = 9$. Vertical translations were allowed in the pattern search, but were constrained so that the center of the pattern was in the region $20 \leq y^+ \leq 60$. The objective was to locate and examine quasi-streamwise vortices in the near-wall region of the flow.

Results of the pattern eduction are shown in figure 6. The pattern comprises a vortex inclined at a small angle to the horizontal axis, roughly 15 degrees. There is only weak evidence of spanwise pairing of opposite signed vortices. However, there is strong negative vorticity underneath and downstream of the primary positive vortex. Near the wall this arises to satisfy the no-slip boundary condition. Note, however, that the region of negative vorticity is also inclined to the wall and appears to separate from the wall sufficiently far downstream. This is further illustrated in example 3 below.

The ensemble averaged streamwise and vertical velocity fluctuations associated with the patterns are also shown in figures 6c and 6d. The streamwise velocity field has the same features as were found in example 1. The vertical velocity field shows the expected upwelling over the low speed "streak" and flow towards the wall over the high speed region.

Example 3 : Diagnostic = streamwise vorticity (outer flow).

In this example, the initial pattern field P_0 was identical to the previous example, except that vertical translations in the pattern search were constrained to the region $80 \leq y^+ \leq 130$ in order to examine the structure of the streamwise vorticity in the outer part of the flow.

Results of the pattern eduction are shown in figure 7. As in example 2, the pattern comprises inclined vortices. The scale of the vortices seems to have increased, as has the inclination angle. Once again we note how the primary pairing of opposite sign vortices is in the vertical and streamwise directions, but not in the spanwise direction.

Example 4 : Diagnostic = spanwise velocity fluctuations.

A simple attached eddy of the type proposed by Townsend (1976) may be expected to give rise to transverse velocity fluctuations of the same sign in elongated regions extending from the wall to the outer flow. Preliminary study of the instantaneous velocity fields from the simulations suggested that such features were indeed present. This motivated a pattern analysis using the w velocity field as the flow diagnostic. The initial pattern was designed to select (after spatial

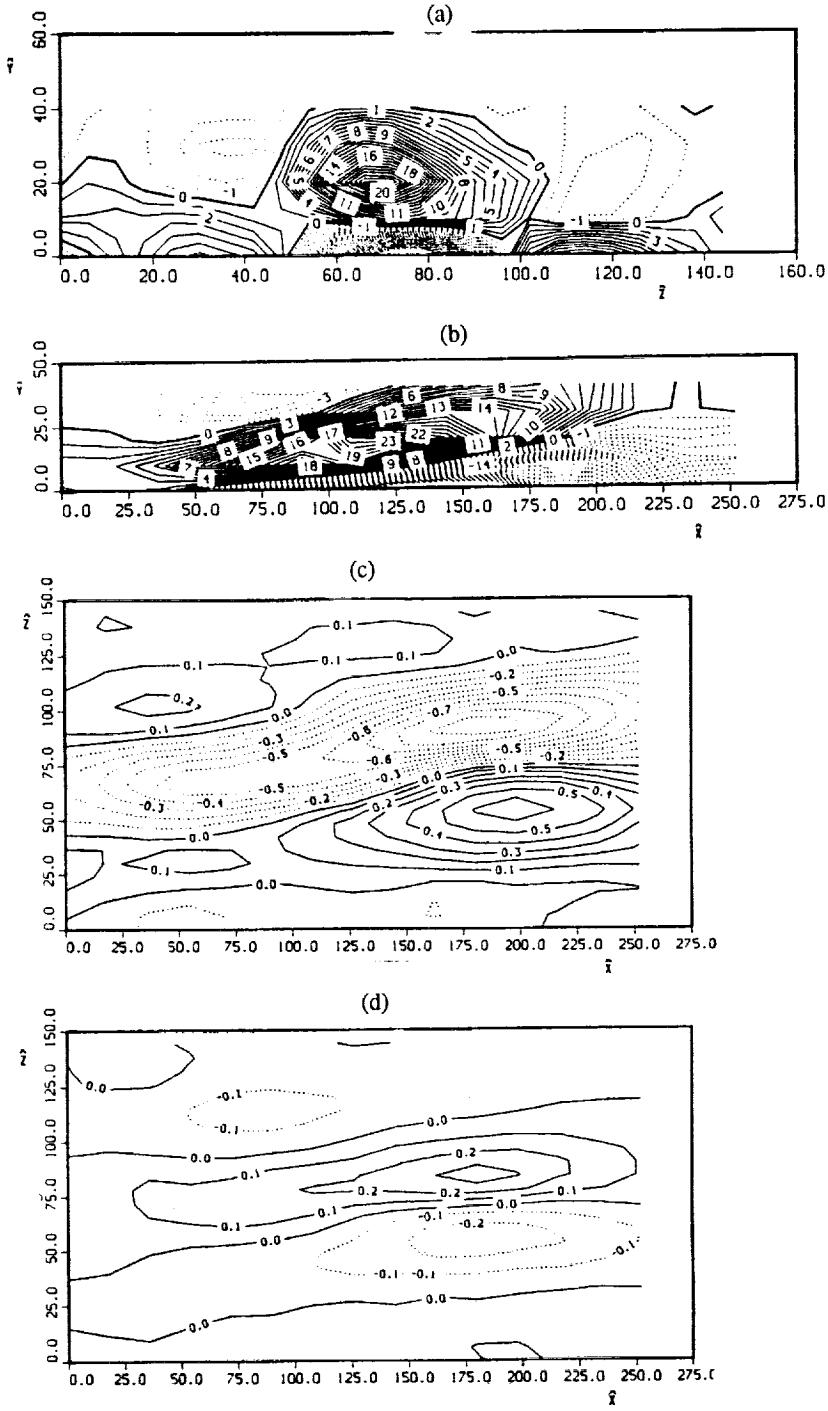

FIGURE 6. Results from example 2 of the 3-D pattern analysis: (a) ω_x field in xy plane at $\hat{x}^+ = 126$, (b) ω_x field in xy plane at $\hat{z}^+ = 72$, (c) u field in xz plane at $\hat{y}^+ = 0$, (d) v field in xz plane at $\hat{y}^+ = 0$. Normalization of the data as for figure 5.

smoothing) regions of locally high transverse velocity in the outer part of the flow ($y^+ \simeq 100$). That is

$$p_0(i,j,k) = \begin{cases} +1, & \text{if } 3 \leq i \leq 7,\ 10 \leq j \leq 12,\ 5 \leq k \leq 11; \\ 0, & \text{otherwise.} \end{cases}$$

where the pattern size was $m_1 = 9$, $m_2 = 15$, $m_3 = 15$. Only horizontal translations were allowed in the pattern search.

A result from this pattern analysis is shown in figure 8a. The educed pattern for the w field comprises elongated positive and negative (paired) regions extending from the wall to the outer part of the flow (the channel half width is at $y^+ = 180$). Examination of other flow diagnostics has shown how these paired w fluctuations are linked to the shear layers near the wall. In figure 8b, data of the instantaneous w field in an xy plane is shown as an example of an occurrence of the educed w pattern.

Summary

The main contribution of the pattern analysis has been to clarify the spatial relationships among various flow structures. In particular, we have used the method to investigate the relationships among between near-wall high/low speed streaks, near-wall shear layers, and quasi-streamwise vortices (or vortex pairs). These structures have been observed or educed from flow visualization and/or conditional sampling analyses by many previous investigators, so their presence in the patterns obtained in the present investigation is neither new nor surprising. However, the unification of all these observations seems to be a particular achievement of the present analysis. A summary of the main conclusions is presented schematically in figure 9.

4. Future plans

The major objectives of this research project as outlined in section 1 above have been achieved. In particular, a pattern recognition procedure for analysing scalar fields in two or three spatial dimensions has been successfully implemented and used to study the structure of simulated turbulent channel flow. The full results of this work are currently being written up for publication.

There are several ways in which the present research project may evolve, and the following are some in progress and planned for the immediate future.

4.1 Pattern analysis

Application to additional flow diagnostics

To date the pattern analysis has been limited to the study of the streamwise and spanwise velocity fluctuations and the streamwise vorticity, although the structure of other flow diagnostics at the pattern locations have also been examined. There are obvious extensions of the work in applying the pattern

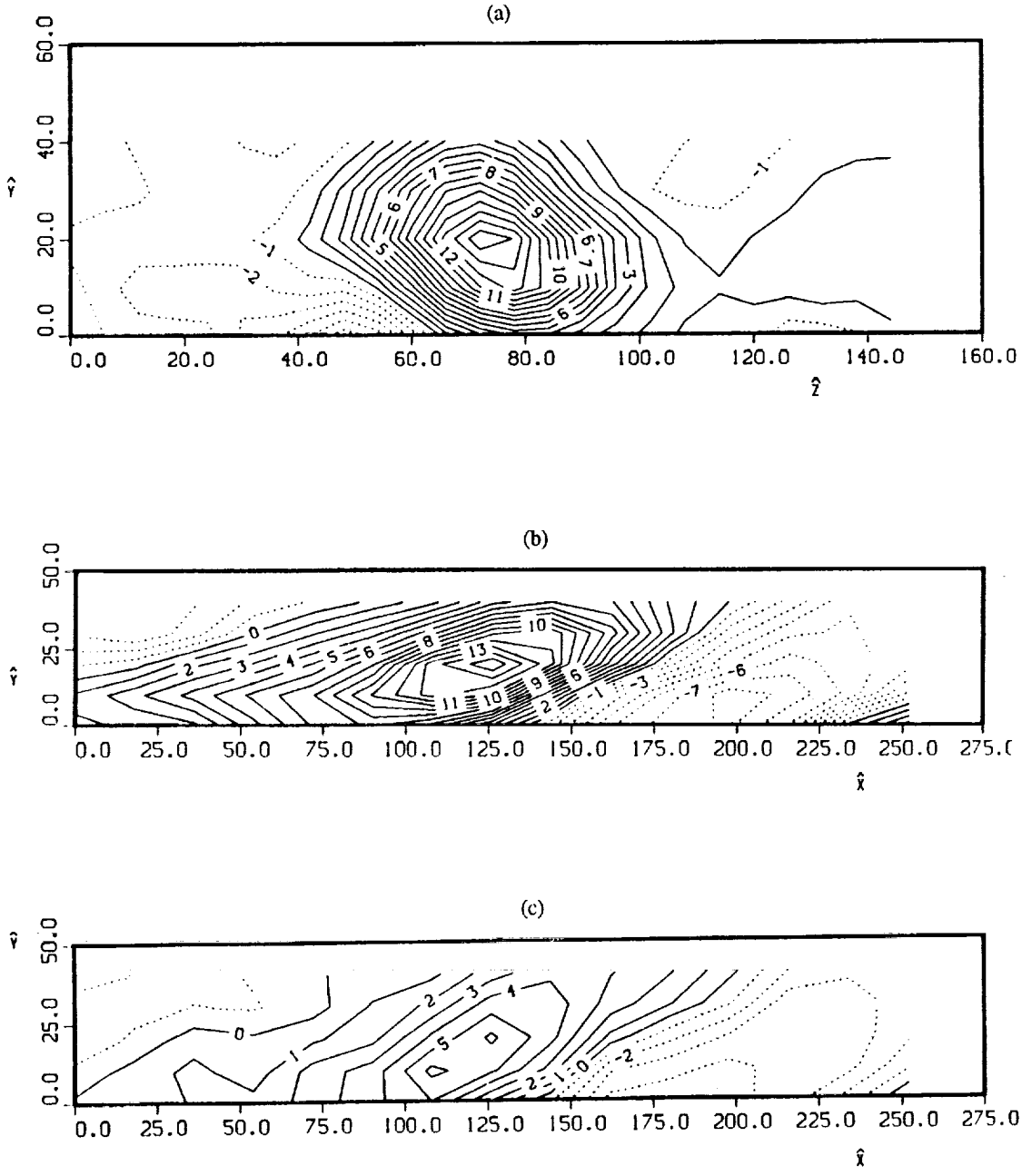

FIGURE 7. Results from example 3 of the pattern analysis: (a) ω_x field in zy plane at $\hat{x}^+ = 126$, (b) ω_z field in xy plane at $\hat{z}^+ = 72$, (c) ω_y field in xy plane at $\hat{z}^+ = 72$. Normalization of the data as for figure 5.

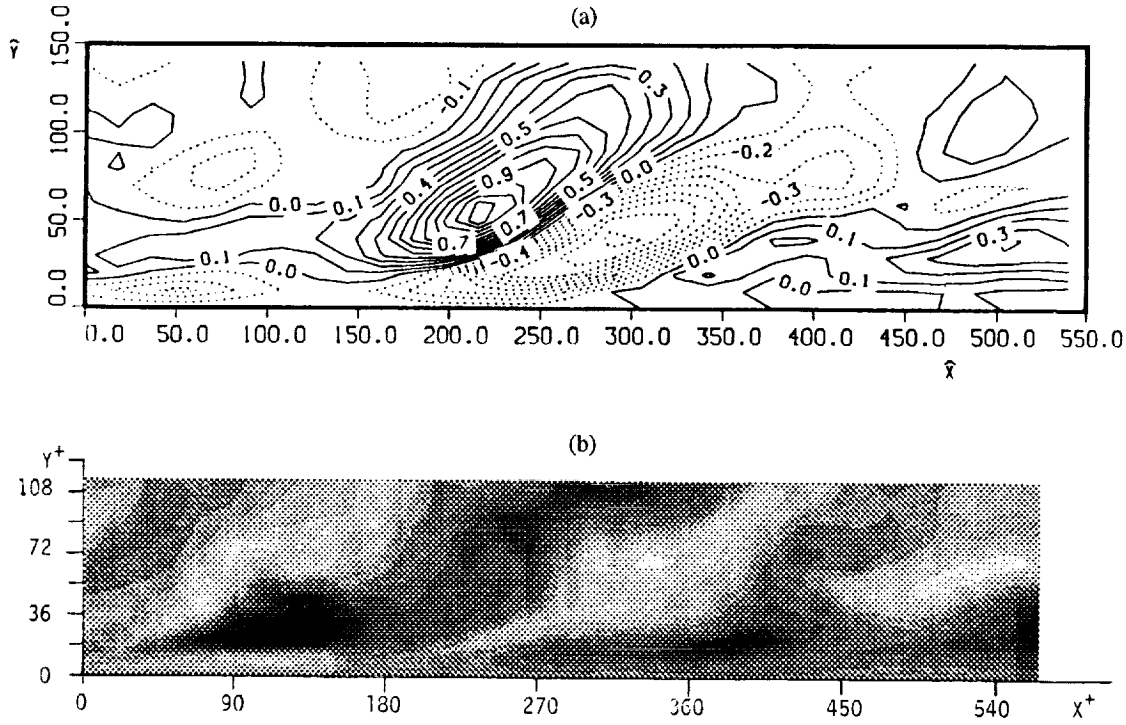

FIGURE 8. Results from example 4 of the pattern analysis: (a) w field in xy plane at pattern center, (b) example of an instantaneous w field in an xy plane. The w velocity fluctuations are normalized with $u_\star$, and dotted lines are used for negative values in (a), and shades of gray are used in (b).

recognition to further diagnostics of the flow directly. Examples which have not yet been analysed are the instantaneous Reynolds stresses, vertical velocity fluctuations, and components other than streamwise of the vorticity field. In addition, the structure of the helicity density and the local dissipation rates may also be investigated. The pattern recognition approach is particularly useful in cases where the spatial shapes of features and/or their spatial relationships are required.

An analysis presently in progress is to use the product of the pressure and the vorticity as a diagnostic intended for detecting vortices (as distinct from simply vorticity). Vortices which display roughly circular streamlines in a plane perpendicular to their axes characteristically have low pressure regions in their cores (Robinson et al, 1989). Alternatively, the pattern analysis procedure may be used to examine the spatial structure of the eddy, streaming, and convergence zones defined by Hunt et al, 1988.

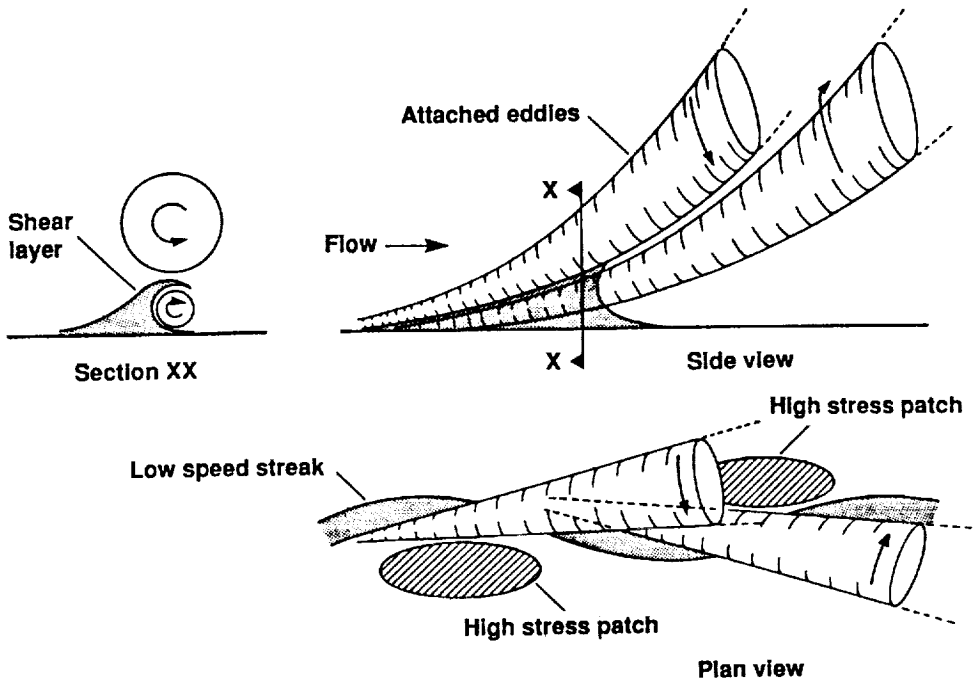

FIGURE 9. Sketch giving a simplified summary of the pattern analysis results.

Application to simulated boundary layer data

An interesting extension of the present research would be the application of the pattern analysis to the simulated boundary-layer data of Spalart (1988). While it is expected that the near-wall structure of the boundary-layer and channel flows is at least qualitatively similar, significant differences may be present in the outer flow structure. Application of the pattern analysis to investigating these differences is straightforward. The boundary-layer data also covers a wider range of Reynolds number than the currently available channel flow data, with $225 \leq Re_\theta \leq 1410$. This may enable Reynolds number effects to be assessed, at least within the limited parameter range available. Application of the pattern analysis to the higher Reynolds number channel flow data, when they are available, is also planned.

4.2 Dynamics of the turbulence structures

While the pattern recognition analysis has proven to be useful for extracting information on the kinematics of the turbulence, it is limited in its ability to

provide dynamical information. It is possible to study temporal evolution using the pattern analysis, but the volume of data required increases dramatically and the details of the dynamics may in any event be unacceptably smeared by the ensemble averaging process. Furthermore, the absence of scale and rotational invariance in the pattern analysis scheme (as it is currently implemented) may also be a drawback in that context. For example, it is expected that changes in scale are an important aspect of the evolution of the vortex structures.

A more promising approach for studying the dynamics of the flow may be the analysis of simplified initial value problems. Research based on the use of linearized Rapid Distortion Theory to study the evolution of localized 3-D disturbances in a strong shear (with and without the presence of a boundary) is planned for continuing work. Previous work at CTR by Lee & Hunt (1988) and Lee, Kim & Moin (1989) has shown how prolonged straining of initially isotropic turbulence by strong shear gives rise to a "streaky" structure in the flow (a 1-component, 3-D flow in the limit of rapid and large strains). The scaling of the resulting structure, however, is unclear from the above-mentioned work. There were two length scales in the problem considered: L_0, the initial characteristic length scale of the turbulence, and $(\nu/S)^{\frac{1}{2}}$, a length scale based on the viscosity ν and the shear rate S. This issue may be analytically resolvable and efforts are underway. Furthermore, it may be worth noting that work by Jang, Benney & Gran (1986), and developments thereof currently in progress at CTR (by J. Kim), have suggested that a "direct resonance" mechanism may explain the observed scaling of the near wall streaks and the origin of associated quasi-streamwise vortices. These "resonant" modes, which have algebraic growth rates, also appear to be present in uniform shear flow. An interesting question, therefore, arises concerning the effect of curvature in the mean velocity profile on these modes. Curvature gives rise to a class of solutions comprising propogating, wave-like disturbances in the flow, as distinct from the purely convected disturbances in the absence of curvature.

Flow visualization experiments (Britter & Stretch, 1985) have suggested that a wake-like "instability" or roll-up of vertical (and transverse) vorticity associated with the low and high speed streaks may be involved in the generation of quasi-streamwise vortices near the wall. A similar mechanism has been proposed and studied by Swearingen and Blackwelder (1987). An investigation of this proposal using linearized initial value problems is planned.

4.3 Channel flow manipulation using buoyancy effects

Previous experiments by the author (Stretch, 1985 ; Britter & Stretch, 1985) have suggested that a weak stable stratification can have a profound effect on the structure of turbulent boundary layers. In particular, rapid and dramatic decreases in turbulence mass and momentum transport can occur with increasing stable stratification to the extent that it seems possible to partially laminarize the flow. These experimental observations (involving both flow visualization

and quantitative measurements) suggest that the stratification effects are closely focused on the fundamentally important dynamics of the flow. In addition to obvious applications in flow control, it thus appears that the use of stratification as a manipulative tool may be a revealing way to study the dynamics of the turbulence. It is planned to perform simulations of a stably stratified turbulent channel flow in order to study these effects.

Acknowledgements

The author is indebted to John Mumford of Cambridge University for explaining his pattern recognition strategy. Josep Ferre from the University of Barcelona also assisted with some initial analysis of the experimental data. It is a pleasure to acknowledge the contributions of Rex Britter from Cambridge University, who visited CTR this summer to collaborate with me on some of the work outlined here. I am grateful to John Kim of CTR for providing simulation data and for helpful comments on the work. Finally, I would like to acknowledge the support of the Center for Turbulence Research.

REFERENCES

ALFREDSSON, P. H., JOHANSSON, A. V., & KIM, J. 1988 Turbulence production near walls: the role of flow structures with spanwise asymmetry. Report CTR-S88, Proceedings of the 1988 Summer Program, Center for Turbulence Research.

BRITTER, R. E. & STRETCH, D. D. 1985 On the structure of turbulent boundary layers. Report for TOPEXPRESS Ltd., Cambridge, UK, June 1985.

BRITTER, R. E. & STRETCH, D. D. 1985 Flow visualization of a stably stratified boundary layer. IUTAM Symp. on Mixing in Stratified Fluids, Margaret River, Western Australia, 25-28 Aug., 1985.

DUDA, R. O. & HART, P. E. 1973 *Pattern Classification and Scene Analysis.* J. Wiley & Sons.

FERRE, J. A. & GIRALT, F. 1989a Pattern-recognition analysis of the velocity field in plane turbulent wakes. *J. Fluid Mech.* **198**, 27-64.

GUEZENNEC, Y. G., PIOMELLI, U., & KIM, J. 1987 Conditionally-averaged structures in wall-bounded turbulent flows. Report CTR-S87, Proceedings of the 1987 Summer Program, Center for Turbulence Research.

HEAD, M. R. & BANDYOPADHYAY, P. 1981 New aspects of turbulent boundary-layer structure. *J. Fluid Mech.* **107**, 297-338.

HUNT, J. C. R., WRAY, A. A., & MOIN, P. 1988 Eddies, streams, and convergence zones in turbulent flows. Report CTR-S88, Proceedings of the Summer Program, Center for Turbulence Research.

HUSSAIN, A. K. M. F., JEONG, J., & KIM, J. 1987 Structure of turbulent shear flows. Report CTR-S87, Proceedings of the 1987 Summer Program, Center for Turbulence Research.

JANG P. S., BENNEY, D. J., & GRAN, R. L. 1986 On the origin of streamwise vortices in a turbulent boundary layer. *J. Fluid Mech.* **169**, 109-123.

JOHANSSON, A. V., ALFREDSSON, P. H., & KIM, J. 1987 Shear-layer structures in near-wall turbulence. Report CTR-S87, Proceedings of the 1987 Summer Program, Center for Turbulence Research.

KIM, J., MOIN, P., & MOSER, R. 1987 Turbulence statistics in fully developed channel flow at low Reynolds number. *J. Fluid Mech.* **177**, 133-166.

LEE, M. J. & HUNT, J. C. R. 1988 The structure of sheared turbulence near a plane boundary. Report CTR-S88, Proceedings of the Summer Program, Center for Turbulence Research.

LEE, M. J., KIM, J., & MOIN, P. 1989 Structure of turbulence at high shear rate. Unpublished manuscript.

MOIN, P. & MOSER, R. D. 1989 Characteristic-eddy decomposition of turbulence in a channel. *J. Fluid Mech.* **200**, 471-509.

MUMFORD, J. C. 1982 The structure of large eddies in fully developed turbulent shear flows. Part 2. The plane wake. *J. Fluid Mech.* **137**, 447-456.

ROBINSON, S. K., KLINE, S. J., & SPALART, P. R. 1989 A Review of Quasi-Coherent Structures in a Numerically Simulated Boundary Layer. NASA TM-102191.

SAVILL, A. M. 1979 Effects on turbulence of curved or distorting mean flow. Ph.D. thesis, University of Cambridge.

SPALART, P. R. 1988 Direct numerical simulation of a turbulent boundary layer up to $R_\theta = 1410$. *J. Fluid Mech.*. **187**, 61-98.

STRETCH, D. D. 1986 The dispersion of slightly dense contaminants in a turbulent boundary layers. Ph.D. thesis, University of Cambridge.

SWEARINGEN, J. D., BLACKWELDER, R. F., & SPALART, P. S. 1987 Inflectional instabilities in the wall region of bounded turbulent shear flows. Report CTR-S87, Proceedings of the 1987 Summer Program, Center for Turbulence Research.

TOWNSEND, A. A. 1976 *The Structure of Turbulent Shear Flows.* C. U. P.

TOWNSEND, A. A. 1979 Flow patterns of large eddies in a wake and in a boundary layers.. *J. Fluid Mech.* **95** 3, 515-537.

OMIT TO END

APPENDIX
CENTER FOR TURBULENCE RESEARCH
1989 ROSTER

NAME/TERM		AREA OF RESEARCH
POSTDOCTORAL FELLOWS		
BELL, Dr. James H. 3/89 - 1/90	Ph.D. Aeronautics and Astronautics, 1989, Stanford	Experimental studies of secondary vortex structure in mixing layers
BUELL, Dr. Jeffrey C. 1/89 - present	Ph.D. Mechanical Engineering, 1986, UCLA	Direct simulations of wall-bounded compressible turbulence Incompressible spatially-developing free-shear flows
CABOT, Dr. William H. 3/88 - present	Ph.D. Physics, 1983, University of Rochester	Turbulent thermal convection in a differentially rotating channel
HUANG, George 3/89 - present	Ph.D. Mechanical Engineering, 1986, University of Manchester	Numerical prediction of turbulent flows with closure models
LEE, Dr. Moon J. 12/87 - present	Ph.D. Mechanical Engineering, 1985, Stanford	Turbulence physics and modeling
MENEVEAU, Dr. Charles 9/89 - present	Ph.D. Mechanical Engineering, 1989, Yale	Turbulence dynamics in the wavelet representation
POINSOT, Dr. Thierry 9/88 - present	Docteur es Sciences, Mechanical Engr., 1987, Univ. d'Orsay, France	Direct simulation of turbulent combustion
SHIH, Dr. Tsan Hsing 4/87 - present	Ph.D Mechanical Engineering, 1984, Cornell University	Turbulence modeling: near-wall turbulence and effects of rotation on turbulence
SMITH, Dr. Leslie M. 9/88 - present	Ph.D. Applied Mathematics, 1988, Massachusetts Institute of Technology	Development of renormalization group analysis of turbulence
STRETCH, Dr. Derek D. 1/89 - present	Ph.D. Engineering, 1986, Cambridge	Patterns in simulated turbulent channel flow
THOMPSON, Dr. Kevin W. 6/87 - present	Ph.D. Physics, 1985, Princeton	Turbulent transport in the solar nebula

NAME/TERM		AREA OF RESEARCH
VASTANO, Dr. John A. 9/88 - present	Ph.D. Physics, 1988, University of Texas at Austin	Short-time Lyapunov exponent analysis
VEERAVALLI, Dr. Srinivas 9/89 - present	Ph.D. Mechanical Engineering, 1989, Cornell University	An experimental study of the effects of rapid rotation on turbulence
VEGT, Dr. Jaap van der 9/88 - present	Ph.D. Mathematics, 1988, Delft Univ. of Technology, The Netherlands	Transition to turbulence in hypersonic flow
WALEFFE, Dr. Fabian A. 9/89 - present	Ph.D. Applied Mathematics, 1989, MIT	Organized motions underlying turbulent shear flows
WATMUFF, Dr. Jonathan H. 11/87 - present	Ph.D. Mechanical Engineering, 1979, University of Melbourne, Australia	An experimental investigation of a low Reynolds number turbulent boundry layer subject to an adverse pressure gradient
SENIOR FELLOWS		
HUNT, Julian C. R. 11/89	Professor, DAMTP, University of Cambridge	Classification of turbulent flow regions.
JIMENEZ, Javier 6/89 - 12/89	Professor of Aeronautics, Universidad Politecnics, Madrid	Stability and structure of wall-bounded flows
ORLANDI, Paolo 6/89 - 11/89	Professor, Dept of Mechanics and Aeronautics, University of Rome	A numerical method for direct simulation of turbulence in complex geometries
SENIOR RESEARCH ASSOCIATE		
ZEMAN, Otto 3/89 - present	Ph.D. Aerospace Engineering, 1975, Pennsylvania State Univ.	Modeling of compressible turbulence

NAME/TERM	AREA OF RESEARCH
GRADUATE STUDENTS	
BEAUDAN, Patrick 10/87 - present	Numerical methods in complex geometry
KARASSO, Paris S. 7/89 - present	Mixing in curved shear layers
KASSINOS, Stavros 10/88 - present	Reynolds averaged turbulence modeling
LE, Hung 4/88 - present	Direct numerical simulation of flow over a backward facing step
LIN, Tony Y.-C. 10/89 - present	3D & unsteady geophysical flows

1989 ADVISORY COMMITTEE

Dr. Dennis M. Bushnell
NASA Langley Research Center

Dr. Marvin E. Goldstein
NASA Lewis Research Center

Dr. Randolph A. Graves, Jr. (Ex-officio)
NASA Headquarters

Dr. Jack Herring
National Center for Atmospheric Research

Prof. Fazle Hussain
University of Houston

Prof. Paul A. Libby
University of California at San Diego

Prof. John L. Lumley
Cornell University

Dr. James M. McMichael
Air Force Office of Scientific Research

Dr. Jack Nielsen (Ex-officio)
NASA Ames Research Center

Prof. Steven A. Orszag
Princeton University

Prof. Anatol Roshko
California Institute of Technology

Dr. Robert E. Singleton
U. S. Army Research Office

Dr. Ronald Smelt (Chairman)

Dr. Michael J. Werle
United Technologies Corporation

Dr. Robert Whitehead
NASA Headquarters

STEERING COMMITTEE

Prof. Dean R. Chapman
Dept. of Aeronautics & Astronautics
and Mechanical Engineering, Stanford University

Dr. Sanford S. Davis
Chief, Fluid Dynamics Research Branch, NASA Ames Research Center

Prof. Javier Jimenez
Senior Visiting Fellow, Center for Turbulence Research, 6/89-12/89
Professor, Fluid Mechanics, University of Madrid

Dr. John J. Kim
Ames Coordinator, Center for Turbulence Research
Head, Turbulence Physics Section, NASA Ames Research Center

Mr. Joseph G. Marvin
Chief, Experimental Fluid Dynamics Branch, NASA Ames Research Center

Prof. Parviz Moin
Director, Center for Turbulence Research
Professor, Dept. of Mechanical Engineering, Stanford
Senior Staff Scientist, NASA Ames Research Center

Prof. William C. Reynolds
Program Coordinator, Center for Turbulence Research
Professor and Chairman, Dept. of Mechanical Engineering, Stanford
Senior Staff Scientist, NASA Ames Research Center